



Yahya, Najeeb Ali (2015) Failure analysis of bonded steel/CFRP laminate connections. PhD thesis,

<http://theses.gla.ac.uk/6659/>

Copyright and moral rights for this thesis are retained by the author

A copy can be downloaded for personal non-commercial research or study, without prior permission or charge

This thesis cannot be reproduced or quoted extensively from without first obtaining permission in writing from the Author

The content must not be changed in any way or sold commercially in any format or medium without the formal permission of the Author

When referring to this work, full bibliographic details including the author, title, awarding institution and date of the thesis must be given



Failure analysis of bonded steel/CFRP laminate connections

By

Najeeb Ali Yahya

Submitted in fulfilment of the requirements for the
Degree of Doctor of Philosophy (PhD)

System, Power & Energy Research Division
School of Engineering
College of Science and Engineering
University of Glasgow
Glasgow, UK

May 2015

Abstract

Adhesive-bonded applications are widely used in industry, because of significant advantages such as uniform stress distribution, design flexibility and suitability to bond similar and dissimilar structural materials. This study focuses the adhesive-bonded long overlap of steel/carbon fibre reinforced polymer (CFRP) composite double lap shear (DLS) joints.

The purpose of the work is to predict and assess the structural failure and behaviour of the DLS joint, including delamination of the composite, and to determine the effects of the design parameters of adherend thickness, overlap length and fabric orientation on the joint's failure. There are different ways for such a joint to fail, which makes predicting failure very difficult. Another important difference is the failure mode of composites, where the relatively low interlaminar shear or tensile strength of the resin system causes failure of the composite before failure of the adhesive bondline occurs.

Both experimental and numerical methods were used for the analysis. The experimental programme includes fabrication, mechanical testing and failure examinations of various joints. The numerical methods are based on 2D models, using strength of materials and cohesive zone modelling (CZM) approaches. In order to model adhesive joints accurately and efficiently, fracture tests were implemented to determine the fracture criteria. Mode-I and mode-II fracture energies were obtained by double cantilever beam (DCB) and end notched flexure (ENF) tests. An inverse method was used to define the cohesive parameters of the bilinear relation, fitting the numerical and experimental load-displacement curves.

The DLS model has been created in Abaqus software, and results for each approach have been presented. Critical locations of stress concentrations in the DLS joint were identified, and the CZM successfully predicted the delamination initiation and propagation region observed in the experiment. As a result, it was concluded that the data obtained from the analysis showed good agreement with the experimental results, and in addition to the fibre orientation angles of the CFRP laminate markedly affecting the failure load of joints, the failure mode and stress distributions appeared in adhesive and composite.

Furthermore, the study shows that the cohesive elements enable the numerical results to be obtained in shorter simulation times than the strength of materials approach, which should encourage use of CZM to analyse large structural applications.

Acknowledgements

All praise be to Allah (God), the Most Merciful and Beneficent. I would like to take this opportunity to express my sincere thanks to my supervisor, Dr Safa Hashim. Without his continued support, supervision and encouragement during the whole period, this research would not have been possible.

I would also like to thank Mr. John Davidson for his assistance with the experimental testing.

I give special thanks to my colleagues, friends and the department staff for their generous help and assistance.

My special gratitude goes to the Libyan government, especially the Ministry of Higher Education and Scientific Research for nominating me to study aboard and supporting me and my family with a fully-funded scholarship. I would also like to acknowledge the funding provided by the School of Engineering, University of Glasgow, in support of conferences attendance.

I am most appreciative of my father, mother, brother and sisters for their continuing support. Special thanks to my wife for her patience and providing me comfort and my children, Mohamed, Sara and Ali, for their affectionate support and love during this period of study.

Declaration

This thesis is entirely my own work, except where mentioned and acknowledged. This work has not been previously submitted for any other degree or qualification in any university.

Najeeb Ali Yahya

May 2015

Table of contents

Abstract.....	ii
Acknowledgements.....	iii
Declaration.....	iv
Table of contents	v
List of Figures.....	x
List of Tables	xvii
Nomenclature.....	xix
Abbreviation	xxi
Chapter 1	1
1 Introduction.....	1
1.1 Motivation and scope	1
1.2 Aims and objectives	4
1.3 Outline of the thesis.....	5
Chapter 2	7
2 Literature review.....	7
2.1 Introduction	7
2.2 Composite materials	7
2.2.1 Matrices.....	8
2.2.2 Fibres.....	9
2.2.3 Fibre Orientation	10
2.2.4 Unidirectional Lamina	10
2.2.5 Cross ply Laminate	11
2.3 Carbon fibre reinforced polymers	12
2.4 Moulding processes	12
2.4.1 Infusion moulding	13
2.4.2 Autoclave moulding	13
2.5 Adhesive bonding.....	14
2.5.1 Adhesion	14
2.5.2 Surface preparation	16

2.6	CFRP and adhesive bonding applications	17
2.7	Adhesive joint design	22
2.7.1	Effects of adherend thickness.....	22
2.7.2	Joint geometry effects	24
2.7.3	Behaviour of composite adherends	25
2.7.4	Influence of fibre architecture on joint strength	25
2.8	Previous work on hybrid connections	27
2.9	Analytical solutions of adhesive joints.....	30
2.10	Numerical solutions of adhesive joints	33
2.10.1	Strength of materials approach.....	33
2.10.2	Damage mechanics approach.....	34
2.10.2.1	Cohesive zone model.....	35
2.10.2.2	Determination of cohesive zone parameters.....	37
2.11	Comparing cohesive zone model with strength of material approach	40
2.12	Failure mechanisms of composite adhesive joint.....	41
2.13	Delamination failure of composite	43
2.14	Summary of the literature review	45
Chapter 3	48
3	Experimental work (Material properties)	48
3.1	Introduction	48
3.2	Composite material properties.....	48
3.2.1	Resin system - Epoxy resin LY3505/Hardener XB3405	49
3.2.2	Fibre properties	49
3.2.3	Unidirectional composite material coordinates.....	50
3.2.4	Rules of mixture	51
3.3	Adhesive properties	53
3.3.1	Adhesive selection	53
3.3.2	Tensile testing of adhesive butt-joint specimens	54
3.3.3	Extrapolation of data	55
3.3.4	Thick adherend shear test (TAST)	57
3.4	Damage and fracture experiments	59
3.4.1	Double cantilever beam experiments	59
3.4.1.1	Specimen Preparation	60

3.4.1.2	Test results of DCB specimen bonded with adhesive 2015	63
3.4.1.3	Test results of DCB specimen bonded with resin LY3505/XB3405	64
3.4.1.4	Mode I Fracture Energy of Adhesive 2015, G_{Ic}	65
3.4.1.5	Mode I Fracture Energy of Resin LY3505/XB3405, G_{Ic}	68
3.4.2	The end notched flexure specimen (ENF)	69
3.4.2.1	Specimen preparation	70
3.4.2.2	Test processing of ENF specimen	71
3.4.2.3	Test results of ENF specimen bonded with adhesive 2015	71
3.4.2.4	Test results of ENF specimen bonded with resin LY3505/XB3405	73
3.4.2.5	Data analysis	74
3.5	Comments	75
Chapter 4	76
4	Experimental investigations of DLS joint	76
4.1	Introduction	76
4.2	DLS joint preparation	76
4.2.1	Surface preparation	77
4.2.2	Adhesive application	78
4.2.3	Clamping	79
4.2.4	Curing	80
4.3	DLS joints testing procedure	80
4.3.1	Tensile testing Set-up	82
4.3.2	Test Results	83
4.3.2.1	Effect of fibre orientation	83
4.3.2.2	Effect of overlap length	85
4.3.2.3	Effect of CFRP adherend thickness	87
4.4	Testing of DLS joint using the strain gauges	88
4.5	Testing of DLS joint using high speed camera	90
Chapter 5	93
5	Numerical analysis of DLS joint based on strength of material approach	93
5.1	Introduction	93
5.2	Geometry and boundary conditions	93
5.3	Meshing Methodology	94
5.4	Material properties	96

5.5	Mesh convergence	99
5.6	Stress distributions	102
5.6.1	Effect of stacking sequence.....	103
5.6.2	Effect of overlap length.....	111
5.6.3	Effect of outer adherend thickness	112
5.7	Summary	115
Chapter 6	116
6	Numerical investigation of pure mode I and II	116
6.1	Introduction	116
6.2	Cohesive zone model concept	116
6.3	Numerical modelling using cohesive elements	119
6.3.1	Traction separation relations	121
6.3.1.1	Linear elastic response	122
6.3.1.2	Damage initiation criterion.....	123
6.3.1.3	Damage evolution.....	123
6.3.2	Characteristic of the models.....	125
6.4	Numerical simulation of the DCB specimen.....	126
6.4.1	Deducing the normal cohesive strength for bilinear CZM.....	127
6.4.2	Varying mode I fracture energy, G_{IC} using bilinear CZM.....	130
6.5	Numerical simulation of the ENF specimen	131
6.6	Length of the cohesive zone	136
6.7	Viscous regularisation	140
6.8	Summary	143
Chapter 7	144
7	Numerical analysis of DLS joint based on cohesive zone model.....	144
7.1	Introduction	144
7.2	Modelling parameters and details.....	144
7.2.1	Geometry and boundary conditions of model.....	144
7.2.2	Mesh of model	145
7.2.3	Material properties of model.....	146
7.2.4	Cohesive zone model parameters.....	147
7.3	The effect of cohesive zone position	149
7.4	Damage parameters sensitivity on DLS numerical results.....	150

7.5	Damage initiation and growth	151
7.6	Parametric studies.....	153
7.6.1	Effect of stacking sequence.....	153
7.6.2	Effect of adherend thickness	155
7.6.3	Effect of overlap length.....	156
7.7	Conclusions	158
Chapter 8	159
8	Discussion, conclusions and future work	159
8.1	Discussion	159
8.1.1	Properties of materials.....	159
8.1.2	DCB and ENF tests	160
8.1.3	Numerical modelling of DCB and ENF	162
8.1.4	Cohesive interface element technique.....	164
8.1.5	Verification of interface element model	165
8.1.6	DLS joint modelling.....	165
8.1.7	Prediction of failure of DLS joints.....	168
8.1.7.1	Effect of fibre orientation	170
8.1.7.2	Effect of overlap length	171
8.1.7.3	Effect of adherend thickness	172
8.1.8	General modelling and experimental issues.....	174
8.2	Summary and conclusions.....	175
8.3	Future work	177
References	179
Appendices	199
Appendix A:	Technical data sheet (Araldite LY3505/Hardeners XB3405)	199
Appendix B:	Technical data sheet (Araldite 2015).....	204
Appendix C:	Technical specification of Vishay strain gauges	210
Appendix D:	Technical data sheet of strain gauge adhesive (M-bond AE-10)	211
Appendix E:	Failure Criteria.....	212
Publications	215

List of Figures

Figure 2.1: Fibre arrangement patterns in the layer of a fibre-reinforced composite [25]...	10
Figure 2.2: Unidirectional lamina lay-up to produce cross ply laminates	11
Figure 2.3: Illustration of a) the lay-up of a 5 layer cross ply laminate and b) optical micrograph of layer cross ply laminate [26]	11
Figure 2.4: Vacuum infusion moulding showing the vacuum bag, sealant, outlet to vacuum pump, inlet to resin supply and the preform surrounded by peel ply.....	13
Figure 2.5: Prepreg moulding showing the vacuum bag, sealant, outlet to vacuum pump and the preform surrounded by peel ply	14
Figure 2.6: Mechanical Inter-locking [37]	15
Figure 2.7: Adhesive bonding applications at the new AIRBUS A380 [60]	18
Figure 2.8: A fuselage section of the A350	19
Figure 2.9: Composite deck adhesively bonded to steel hull [69]	20
Figure 2.10: CFRP used to strengthen bridges [70].....	20
Figure 2.11: World's largest carbon composite bridge in Paris (left) and Composite bridge on UK motorway (right) [70]	21
Figure 2.12: External strengthening of concrete structures [70].....	21
Figure 2.13: Different joint geometry of adhesive joints [72]	22
Figure 2.14: Joint geometry effects [74]	23
Figure 2.15: Deformations in single lap shear joints with elastic adherends [94]	30
Figure 2.16: Deformations in single lap joints predicted with Goland and Reissner's model [94]	31
Figure 2.17: Adhesive shear stress distribution when the stress free condition at the ends of the overlap is verified [97]	32
Figure 2.18: Schematic of bilinear, exponential and trapezoidal CZM [128]	36
Figure 2.19: Double Cantilever Beam (a) and End Notch Flexure (b) specimens for measurement of the pure Mode I and II cohesive laws.....	38
Figure 2.20: Mixed Mode Bending specimen [137]	39
Figure 2.21: Modified Arcan test specimen and loading fixture [138].....	39
Figure 2.22: Major fracture types [60]	42
Figure 2.23: Possible failure modes in a CFRP bonded to steel system [158]	43

Figure 2.24: Stages of delamination failure [73]	44
Figure 3.1: Composite ply coordinate system.....	50
Figure 3.2: Steel butt joint.....	54
Figure 3.3: Stress strain curves from steel butt joint.....	55
Figure 3.4: Stress-strain curves for Araldite 2015 [175].....	55
Figure 3.5: Geometry and dimensions (in mm) of the thick adherend shear test	57
Figure 3.6: Thick adherend shear test specimen	57
Figure 3.7: Load-displacement curves of the TAST specimen bonded with Araldite 2015	58
Figure 3.8: Failure of TAST specimen	58
Figure 3.9: Fracture modes	59
Figure 3.10: Illustration of DCB specimen	60
Figure 3.11: DCB Specimen preparation and bonding in jig.....	61
Figure 3.12: Steel adherends with PTFE sheet and the resin LY3505/XB3405	61
Figure 3.13: DCB specimen and loading blocks.....	62
Figure 3.14: Experimental setup using a travelling microscope	62
Figure 3.15: Load-displacement curves of DCB specimen bonded with Adhesive 2015 ...	63
Figure 3.16: Failure surfaces from DCB test	64
Figure 3.17: Load-displacement curves of DCB specimen bonded with Resin LY3505/XB3405	64
Figure 3.18: Failure surfaces of DCB test with resin LY3505/XB3405	65
Figure 3.19: Linear regression data used for CBT method.....	66
Figure 3.20: Linear regression data used for ECM method	67
Figure 3.21: R-Curve for adhesive 2015 using SBT, CBT and ECM	67
Figure 3.22: R-Curve for Resin LY3505/XB3405 using SBT, CBT and ECM	68
Figure 3.23: Illustration of ENF specimen.....	69
Figure 3.24: The ENF specimen preparation and bonding in jig.....	70
Figure 3.25: ENF specimen.....	70
Figure 3.26: Photograph of ENF test setup	71
Figure 3.27: Load-displacement curves of ENF specimen bonded with Adhesive 2015	72
Figure 3.28: Failure surfaces of ENF test	72
Figure 3.29: Load-displacement curves of ENF specimen bonded with Resin LY3505/XB3405	73
Figure 3.30: Failure surfaces of ENF test with resin LY3505/XB3405	73

Figure 4.1: DLS Joint (Steel/CFRP)	77
Figure 4.2: Grit blasting used to treat steel adherends	77
Figure 4.3: Acetone used to clean the adherends surfaces of DLS joint before bonding	78
Figure 4.4: Picture of applying adhesive to adherends	79
Figure 4.5: Two test specimens clamped in the jig, ready for curing	79
Figure 4.6: Laboratory oven used to cure the adhesive joints.....	80
Figure 4.7: DLS Joint geometry and dimensions	81
Figure 4.8: Bonded specimens showing $[0^\circ, 90^\circ]_6$ specimens with various overlap lengths	81
Figure 4.9: Tensile test of $[0^\circ, 90^\circ]_6$ specimen with 75 mm overlap length	83
Figure 4.10: Failure shapes: a) S-shape, b) U-shape.....	83
Figure 4.11: Load displacement curves for different orientation angle with 75 mm overlap length and 3 mm thickness of CFRP adherend	84
Figure 4.12: Experimental fracture surfaces for: (a) $[0^\circ, 90^\circ]_6$ specimen, (b) $[90^\circ, 0^\circ]_6$ specimen and (c) $[+45^\circ, -45^\circ]_6$ specimen	84
Figure 4.13: Load-displacement curves for $[0^\circ, 90^\circ]_6$ specimens at varying overlap lengths	86
Figure 4.14: Load-displacement curves for $[90^\circ, 0^\circ]_6$ specimens at varying overlap lengths	86
Figure 4.15: Influence of the overlap length on the failure load for $[0^\circ, 90^\circ]_6$ specimens ..	87
Figure 4.16: Load-displacement curves for specimens with different outer adherend thickness	87
Figure 4.17: Failure surfaces for: a) $[90^\circ, 0^\circ]_6$ specimen, b) $[90^\circ, 0^\circ]_{12}$ specimen.....	88
Figure 4.18: The location of strain gauges on $[0^\circ, 90^\circ]_6$ specimen with 75 mm overlap length	89
Figure 4.19: Strain gauges positions and test set up	89
Figure 4.20: Typical curves of load vs. strain measurement for $[0^\circ, 90^\circ]_6$ specimen with 75 mm overlap length as experimentally registered on adherends. (Figure 4.18) .	90
Figure 4.21: Setup for experimental investigation	91
Figure 4.22: Failure initiation and growth in the DLS joint	92
Figure 5.1: Loading and boundary conditions of the DLS joint	94
Figure 5.2: Image of $[0^\circ, 90^\circ]_6$ CFRP laminate (a) using Normasky microscope, (b) modelled in Abaqus.....	95
Figure 5.3: Finite element mesh of the DLS joint.....	95

Figure 5.4: Schematic illustrations of laminates with various layup sequences	96
Figure 5.5: Illustration of shear strain produced by tensile loading of a fibre composite.....	97
Figure 5.6: Mesh distribution in regions LHS and RHS for the $[0^\circ, 90^\circ]_6$ model, element ratio 0.5 (mesh 1).....	99
Figure 5.7: Mesh distribution in regions LHS and RHS for the $[0^\circ, 90^\circ]_6$ model, element ratio 1(mesh 2).....	100
Figure 5.8: Mesh distribution in regions LHS and RHS for the $[0^\circ, 90^\circ]_6$ model (mesh 3)	100
Figure 5.9: Maximum principal stress distributions along the centre of adhesive layer for $[0^\circ, 90^\circ]_6$ model with 50 mm overlap at different meshes.	101
Figure 5.10: Shear stress distributions along the centre of adhesive layer for $[0^\circ, 90^\circ]_6$ model with 50 mm overlap at different meshes.	101
Figure 5.11: Peel stress distributions along the centre of adhesive layer for $[0^\circ, 90^\circ]_6$ model with 50 mm overlap at different meshes.	102
Figure 5.12: Contours of maximum principal stress in the CFRP for different models with 75 mm overlap: (a) $[0^\circ, 90^\circ]_6$, (b) $[90^\circ, 0^\circ]_6$ and (c) $[+45^\circ, -45^\circ]_6$ at failure loads (50 kN, 47.5 kN and 17 kN) respectively	103
Figure 5.13: Maximum principal stress distribution along the upper of adhesive layer for various models with 75 mm overlap at failure loads	104
Figure 5.14: Stresses distribution along the centerline of the ply next to the bondline for $[0^\circ, 90^\circ]_6$ model at failure load (50 kN).....	105
Figure 5.15: Stresses distribution along the centerline of the ply next to the bondline for $[90^\circ, 0^\circ]_6$ model at failure load (47.5 kN)	105
Figure 5.16: Stresses distribution along the centerline of the ply next to the bondline for $[+45^\circ, -45^\circ]_6$ model at failure load (17 kN)	106
Figure 5.17: Data path through the thickness of the adhesive and CFRP laminate (at RHS)	106
Figure 5.18: Stress distributions through the thickness of adhesive and CFRP laminate of $[0^\circ, 90^\circ]_6$ model; (a)Tensile stress (S11) , (b)Peel stress (S22) and Shear stress (S12) at data path (Figure 5.17)	108
Figure 5.19: Stress distributions through the thickness of adhesive and CFRP laminate of $[90^\circ, 0^\circ]_6$ model; (a)Tensile stress (S11) , (b)Peel stress (S22) and Shear stress (S12) at data path (Figure 5.17)	109

Figure 5.20: Stress distributions through the thickness of adhesive and CFRP laminate of $[+45^{\circ}, -45^{\circ}]_6$ model; (a) Tensile stress (S11) , (b) Peel stress (S22) and Shear stress (S12) at data path (Figure 5.17)	110
Figure 5.21: Shear stress distributions along the upper of adhesive layer for different values of overlap length for $[0^{\circ}, 90^{\circ}]_6$ models at failure loads.....	112
Figure 5.22: Maximum principal stresses distribution along the upper adhesive layer for different outer adherend thickness	113
Figure 5.23: Shear stresses distribution along the upper adhesive layer for different outer adherend thickness	114
Figure 5.24: Peel stresses distribution along the upper adhesive layer for different outer adherend thickness	114
Figure 6.1: Illustration of cohesive zone model concept [128], at first a linear elastic material response prevails (1), as the load increases the crack initiates ($T=\sigma_0$) (2) and then, governed by the nonlinear cohesive law, it evolves from initiation to complete failure (3) with the appearance of new traction free crack surfaces ($\Delta=\Delta_f$) (4).	118
Figure 6.2: Independent meshes with tie constraints [201].....	120
Figure 6.3: Diagram of the three most commonly used relations [128]	121
Figure 6.4: Bilinear traction-separation law.....	124
Figure 6.5: a) Geometry and dimensions (in mm) of the DCB model and boundary conditions, b) DCB mesh used with single row of cohesive elements to represent the adhesive thickness	127
Figure 6.6: Study on effect of varying normal strength of Araldite 2015	128
Figure 6.7: Study on effect of varying normal strength of Resin LY3505/XB3405	129
Figure 6.8: Study on the effect of the varying mode I fracture energy of Araldite 2015 ..	130
Figure 6.9: Study on effect of the varying mode I fracture energy of Resin LY3505/XB3405	131
Figure 6.10: a) Geometry and dimensions (in mm) of the ENF model and boundary conditions, b) ENF mesh used with single row of cohesive elements to represent the adhesive thickness	132
Figure 6.11: Deformed 2D model of ENF mesh after crack propagation in the adhesive.	132
Figure 6.12: Cohesive failure in the adhesive for ENF model using the bilinear CZM	133

Figure 6.13: Influence of the cohesive strength on the response of ENF numerical results of Araldite 2015.....	133
Figure 6.14: Influence of the fracture energy on the response of ENF numerical results of Araldite 2015.....	134
Figure 6.15: Influence of the cohesive strength on the response of ENF numerical results of resin LY3505/XB3405	135
Figure 6.16: Influence of the fracture energy on the response of ENF numerical results of resin LY3505/XB3405	135
Figure 6.17: length of the cohesive zone	136
Figure 6.18: Illustration of S22 traction ahead of crack tip, with very fine mesh used to capture cohesive zone length.....	138
Figure 6.19: The effect of cohesive element length on the predicted load–displacement curve of DCB model	139
Figure 6.20: The effect of cohesive element length on the predicted load–displacement curve of ENF model	140
Figure 6.21: The effect of viscous regularisation factor on the predicted load–displacement curve of DCB model	142
Figure 6.22: The effect of viscous regularisation factor on the predicted load–displacement curve of ENF model	142
Figure 7.1: Geometry of DLS joint model and boundary conditions	145
Figure 7.2: Finite element mesh of DLS joint.....	146
Figure 7.3: Cohesive elements to simulate failure paths in adhesive bond; (a) Adhesive-cohesive model and (b) cohesive model	149
Figure 7.4: Comparison of Load-displacement curves of different failure models	150
Figure 7.5: Numerical results sensitivity to 10% increase in constitutive damage parametres	151
Figure 7.6: Contour, showing failure prediction of the $[0^\circ, 90^\circ]_6$ model: (a) damage initiation at the RHS (b) and propagation to the end of bond.....	152
Figure 7.7: Stiffness degradation curves at various percentage of maximum failure load (50 kN) for the $[0^\circ, 90^\circ]_6$ model with 75 mm overlap length	153
Figure 7.8: Contour, showing failure prediction of DLS joint in the adhesive and resin layers for the $[90^\circ, 0^\circ]_6$ model at load 48 kN	154

Figure 7.9: Contour, showing failure prediction of DLS joint in the adhesive and resin layers for the $[+45^{\circ}, -45^{\circ}]_6$ model at load 17 kN.....	154
Figure 7.10: Stiffness degradation of the first element to fail in three models.....	155
Figure 7.11: Numerical load displacement curves for models with different thickness....	156
Figure 7.12: Influence of overlap length on the load-displacement curve.....	157
Figure 7.13: Numerical loads prediction for different overlap length	157
Figure 8.1: Variation of CPU time with overlap length of the $[0^{\circ}, 90^{\circ}]_6$ models for both the strength of material and the CZM approaches.	167
Figure 8.2: Comparison of the load versus strain curves for $[0^{\circ}, 90^{\circ}]_6$ specimens and models with overlap length of 75 mm	169
Figure 8.3: Comparison between the experimental and numerical curves for $[0^{\circ}, 90^{\circ}]_6$ joint with different overlap length, experimental from Figure 4.15 and numerical from Figure 7.13	172
Figure 8.4: Comparison between the experimental and numerical curves for $[0^{\circ}, 90^{\circ}]$ joint with different laminate thickness	173

List of Tables

Table 2.1: Comparison of resin properties [23, 24]	9
Table 3.1: Properties for LY3505 epoxy with hardener XB3405 [176]	49
Table 3.2: Properties of single carbon fibre [177]	50
Table 3.3: Material properties of CFRP laminate	53
Table 3.4: Plastic properties of Araldite 2015	56
Table 3.5: Results of the DCB experiments of Adhesive 2015	68
Table 3.6: Results of the DCB experiments of resin LY3505/XB3405.....	69
Table 3.7: Results of the ENF experiments of Adhesive 2015 and resin LY3505/XB340575	
Table 4.1: Type and number of specimens	82
Table 5.1: Material properties of carbon-epoxy composite, adhesives and mild steel,	98
Table 5.2: Properties of Araldite 2015 in the plastic region	99
Table 5.3: Stress results through the adhesive layer at failure loads (Figure 5.12), the numbers in bold indicate maximum critical stresses.....	107
Table 5.4: Stress results through the laminate and resin layers from numerical analysis at failure load (Figure 5.12), the numbers in bold indicate maximum critical stresses.....	107
Table 5.5: Stress results through the adhesive layer at a load of 50 kN, the numbers in bold indicate maximum critical stresses.....	113
Table 6.1: Young's modulus (E) and Poisson's ratio (ν) used for the CPE4R elements..	125
Table 6.2: Young's modulus (E), shear modulus (G), normal cohesive strength (σ_o), shear cohesive strength (τ_o), normal fracture energy (G_{IC}) and shear fracture energy (G_{IIC}) used for the COH2D4 cohesive elements	125
Table 6.3: Cohesive parameters deduced from data fitting for mode I.....	131
Table 6.4: Cohesive parameters used for traction-separation modelling using CZM.....	136
Table 6.5: Different values of the parameter M in literature [205].....	137
Table 7.1: Type of models	145
Table 7.2: Elastic properties of the adhesive and resin layers	148
Table 7.3: Damage initiation (Quads Damage).....	148
Table 7.4: Damage propagation (Damage Evolution)	148
Table 7.5: Effect of overlap length on the failure load in the $[0^\circ, 90^\circ]_6$ model.....	157

Table 8.1: Percent saving in simulation time between strength of material and CZM approaches for the $[0^\circ, 90^\circ]_6$ models with different overlap lengths.....	168
-------------------------------------------------------------------------------------------------------------------------------------------------------------------------	-----

Nomenclature

Symbols	Description	Units
B	Width of the specimen	mm
E	Young's Modulus	GPa
E _a	Young's modulus of adhesive	GPa
E _c	Young's Modulus of composite	GPa
E _f	Young's Modulus of fibre	GPa
E _m	Young's Modulus of matrix	GPa
E ₁₁	Young's Modulus of composite along x-axis	GPa
E ₂₂	Young's Modulus of composite along y-axis	GPa
E ₃₃	Young's Modulus of composite along z-axis	GPa
E _{LL}	Young's Modulus of composite parallel to the fiber direction	GPa
E _{TT}	Young's Modulus of composite perpendicular to the fiber direction	GPa
G	Shear Modulus	GPa
G _a	Shear modulus of adhesive	GPa
G _C	Fracture energy release rate	N/m
G _f	Shear Modulus of fibre	GPa
G _m	Shear Modulus of matrix	GPa
G _{LT}	Shear Modulus of composite in L-T plane	GPa
G ₁₂	Shear Modulus of composite in 1-2 plane	GPa
G ₁₃	Shear Modulus of composite in 1-3 plane	GPa
G ₂₃	Shear Modulus of composite in 2-3 plane	GPa
G _{IC}	Mode I fracture energy release rate	N/m
G _{IIC}	Mode II fracture energy release rate	N/m
G _{IIIC}	Mode III fracture energy release rate	N/m
K _{nn}	Elastic tensile stiffness for mode I	N/m ³

Nomenclature

K_{ss}	Elastic shear stiffness for mode II	N/m ³
K_{tt}	Elastic shear stiffness for mode III	N/m ³
L_e	Length of the cohesive element	mm
L_{cz}	Length of the cohesive zone	mm
N_e	Number of elements in cohesive zone	--
P	Standard force	N
S	Shear strength in xy- plane	MPa
S_{11}	Tensile stress	MPa
S_{22}	Peel / transverse stress	MPa
S_{12}	Shear stress	MPa
t_a	Thicknes of adhesive	mm
V_f	Volume fraction of fibre	%
V_m	Volume fraction of matrix	%
X	Longitudinal strength	MPa
Y	Transverse strength	MPa
σ_o	Peak normal strength (Mode I)	MPa
σ_{22}	Transverse stresses	MPa
τ_o	Peak shear strength (Mode II)	MPa
τ_{12}	Shear stress in 1-2 plane	MPa
ν	Poisson's ratio	--
ν_{LT}	Poisson's ratio in L-T plane	--
ν_{12}	Poisson's ratio in 1-2 plane	--
ν_{13}	Poisson's ratio in 1-3 plane	--
ν_{23}	Poisson's ratio in 2-3 plane	--
ρ_f	Density of fibre	g/cm ³
ρ_m	Density of matrix	g/cm ³
ε	Strain	--
θ	Transformation angle	Degrees
δ	Displacement of the cross-head of the testing machine	mm

Abbreviation

BS	British Standard
BK	Benzeggagh-Kenane damage evolution criterion
CBT	Corrected Beam Theory
CBBM	Compliance Based Beam Method
CFRP	Carbon Fibre Reinforced Polymer
CZM	Cohesive Zone Model
D	Damage variable
DCB	Double Cantilever Beam
DLS	Double Lap Shear
ECM	Experimental Compliance Method
ENF	End Notched Fluxure
FEA	Finite Element Analysis
FRP	Fibre Reinforced Polymer
FPZ	Fracture Process Zone
GFRP	Glass Fibre Reinforced Polymer
LEFM	Linear Elastic Fracture Mechanics
LHS	Left Hand Side of the quarter model (end of the joint overlap)
PTFE	Polytetrafluoroethylene
RHS	Right Hand Side of the quarter model (centre of the full joint)
SBT	Simple Beam Theory
SDEG	Scalar Stiffness Degradation
TAST	Thick Adherend Shear Test
UD	Unidirectional
UTS	Ultimate Tensile Strength
VCCT	Virtual Crack Closure Technique

Chapter 1

1 Introduction

1.1 Motivation and scope

Hybrid joints, like metal/polymer composite structures, have great potential for application in a large number of engineering sectors. These material systems are opening up new possibilities for advanced applications such as marine, aircraft and automobile application, as well as load-bearing structural parts, continuous long fibre polymer matrix composite laminates; therefore these are going to be highlighted in this thesis. The high specific stiffness and physic-chemical resistance of polymer composites are combined with the traditional strength of metals in these advantageous combinations. The joints can be produced by mechanical fasteners or by means of adhesive bonding [1]. Fasteners such as bolted joints introduce considerable stress concentration which often requires the thickness of adherends to be increased, compromising weight saving. Adhesive bonding is a material joining process in which an adhesive, placed between the adherend surfaces, solidifies to produce an adhesive bond. Adhesive bonding is the most suitable method of joining, and joint structural efficiency can be should be maximised at minimum weight [2, 3]. The reasons why adhesive bonding are so desirable compared to other joining methods have been given by Vinson, Adams and others [4, 5].

- Often, thinner gauge materials can be used with attendant weight and cost savings.
- Number of production parts can be reduced.
- Manufacturing procedures like milling, machining, forming, and riveting can be reduced or eliminated.
- Adhesive bonds can potentially provide a high strength-to-weight ratio with three times the shearing force of riveted joints.
- Improved aerodynamic surfaces and visual appearance.
- Excellent electrical and thermal insulation properties.
- Superior fatigue resistance at moderate loading conditions.

- Often, the adhesive is sufficiently flexible to allow for variations in the coefficients of thermal expansion when joining dissimilar materials.
- Adhesive joints can distribute the load over a larger area, and take advantage of the ductile response of the adhesive to reduce peak stresses.
- Large area bonds can be made with a minimum work force without special skills.
- Damping characteristics and noise reduction are superior to riveted assemblies.
- Reduction of corrosion, due to absence of fasteners, and the additional benefit of the adhesive acting as a sealant within a joint.
- Elimination of welding and drilling processes where joining is required in explosion-proof environments, e.g. steel repair on offshore oil installations.

It can be seen that there are many advantages to using adhesive bonding compared to mechanical fasteners, but it is, however, difficult to analyse, design, and optimise adhesive bonded joints.

Carbon Fibre Reinforced Polymer (CFRP) materials are increasingly being used for structural retrofitting or repair of steel members in recent years [6, 7]. Adhesively bonded joints have become more important, since the CFRP strips can be conveniently and efficiently joined to the steel elements by using structural adhesives. CFRP has shown some unique advantages above other construction materials, such as excellent resistance to corrosion and environmental degradation, high longitudinal strength, high fatigue endurance and reduced weight. These features have made the CFRP adequate for reinforcing structures that are being affected by degradation.

Cross-ply laminates are composed of unidirectional layers (with parallel aligned fibres). The direction of the layers alternate in mutually perpendicular directions, such as 0/90/0/90..., where the angle given is relative to the load direction. When a cross-ply laminate of, for example, carbon/epoxy is loaded in tension along the longitudinal direction, it often exhibits several distinguishing modes of deterioration such as transverse matrix cracks, delamination and debonding of fibres preceding final fracture under loading. Matrix cracking is the first stage of damage, and although it is not catastrophic in nature, its presence can influence the overall mechanical behaviour of the structure [8, 9]. The existence and multiplication of matrix cracks can degrade the life of the structure by introducing other more severe damage, such as delamination and fibre breakage [9, 10].

The stress analysis of adhesive joints is primarily based on two approaches: the strength of materials approach and the linear elastic fracture mechanics (LEFM) approach. The former approach generally utilises a maximum stress or maximum strain as a failure criterion. Failure is assumed to occur when the maximum stress or strain at the end of the bonded overlap reaches a critical value. The LEFM approach assumes that flaws are present in materials but that they are very small and uniformly distributed. The strength of materials approach is more complicated than it seems for several reasons. One complexity arises in the determination of local stresses in the adhesive joint.

In addition, stresses typically occur from the application of loads on a system; however, deformation of adherends with respect to the adhesive and stress concentrations in the joint can also produce large local stresses. Another reason for complications is that each joint geometry or design can produce different types of stresses and in different locations. Adhesive materials, as well as all polymers, inherently contain flaws such as porosity voids or micro cracks. The realisation that these voids actually govern the performance of the material has led to the application of linear elastic fracture mechanics in the study of adhesive joints. The LEFM approach was used by Fernlund and Spelt [11, 12] and Papini and Spelt [13], who employed an energy-based fracture mechanics criterion to predict failure of elastic adhesive joints which contain a substantial plastic zone, occurring ahead of the macroscopic crack tip of the adhesive layer. However, when the adherends deform plastically, the application of the LEFM is inappropriate, because the plastic deformation of the adherends will, in general, affect the crack tip stress field, and thus the fracture process occurring in the adhesive layer. Although it has been well recognised that the influences of adherend plasticity are significant [14, 15], analytical tools are far from being established.

Tvergaard and Hutchinson [16, 17, 18, 19] made great progress in developing a cohesive zone modelling (CZM) approach to analyse the interfacial failure of bi-material systems. The CZM is characterized by the traction-separation relation that describes the fracture process occurring ahead of the crack tip. It was shown that this modelling approach is a promising tool for analysing interfacial failure in the presence of extensive plasticity in the surrounding materials, which is similar to the case of plastically deforming adhesive joints. A detailed review of the strength of materials approach, the fracture mechanics approach and the cohesive zone modelling approach will be given in Chapter 2

1.2 Aims and objectives

The aim of this thesis is to evaluate and assess failure and behaviour of long double lap shear (DLS) joints, based on thick adherend carbon fibre reinforced polymer (CFRP) materials and steel in ambient conditions. The study is based on experimental and numerical programmes. The experimental programme is based on a mechanical testing method, which compared with the numerical method, both use strength of material and cohesive zone modelling (CZM) approaches. The main goals of this work are:

- To conduct mechanical testing and assess failure of various DLS joints using a standard fabrication method and materials
- To determine strength and fracture materials properties using standard materials testing methods.
- Perform the more tests according to testing standards to obtain the strain energy release rate for pure mode I and pure mode II.
- To conduct numerical modelling including modelling the adhesive-adherend interface and composite matrix layers using the principles of CZM.
- To validate the developed methodologies and test apparatus by comparing the experimental results with CZM numerical models.
- To analyse how interfaces with different properties affect the response of steel/carbon composite double lap shear joints under tensile loading.
- To understand how load transfer and failure occur along the adhesive layer and epoxy resin layers in CFRP composite under tensile loading condition.
- To perform a damage initiation and propagation analysis in the DLS joint using cohesive elements containing the intrinsic CZM.
- To obtain stress distributions, damage initiation and propagation.
- To predict and assess the structural failure of the joint, including delamination of the composite.
- To determine the effects of the design parameters of adherend thickness, overlap length and fabric orientation on the joint's failure.
- To compare the prediction of joint failure, using CZM approach with strength limit approach.

1.3 Outline of the thesis

The structure of the thesis is as follows:

Chapter 2: Literature review - Review on bonded joints covering lap joint theories, adhesive modelling, experimental/numerical modelling. The main parameters effect on the adhesive bonding design and the failure mechanisms are explained. The background research about hybrid joints is considered. Finally, a discussion of strength of materials approach and cohesive zone modelling are used for failure prediction.

Chapter 3: Experimental work (material properties) – Explains the experimental procedures on various materials used in this research to obtain essential mechanical properties. Rule of mixtures equation and experimental testing are used. Also, this chapter focuses on experiments issued from fracture mechanics, dedicated to characterisation of the damage and fracture behaviour of adhesive and resin. The double cantilever beam (DCB) test is used to measure the fracture resistance of adhesive and resin joints under mode I (tensile), and ENF test is used to measure the mode II (in plane shear) conditions. The method used is British Standard (BS 7991:2001).

Chapter 4: Experimental investigations of DLS joint - Considers the experimental fabrication and testing of the DLS joints with different overlap, outer adherend thickness and orientation angle. The preparation of the specimen, the test procedure and the instrumentation is described. Additionally, the experimental results, including load-displacement curves and failure surface for each different type of hybrid joint, are presented. Finally, the strain gauges attached to the composite laminate and steel adherends at the specified position are illustrated, and load strain curves are presented. A high speed camera was also used in an attempt to locate where failure initiates in the DLS joint.

Chapter 5: Numerical simulation of DLS joint based on strength of material approach - This chapter presents the geometry and configuration of the double lap shear (DLS) joint, meshing methodology and mesh convergence. This chapter attempts to identify the critical stress locations that occur in a steel/CFRP hybrid.

Chapter 6: Numerical investigation of pure mode I and mode II - This chapter presents a finite element modelling with cohesive elements of the tests of fracture mechanics already discussed in chapter 3, and a comparison between the results of the modelling and those obtained from the experimental tests. The tests considered in this chapter for modelling are

the DCB test (mode I) and the ENF test (mode II). The analysis was carried out with the commercial finite element software ABAQUS 6.9-1.

A two-parameter bilinear cohesive law was used in the study to define the interfacial behaviour under both mode I and mode II loadings. A stress-based quadratic criterion was used. The inverse technique was used to identify the cohesive parameter values by prediction of load-displacement curve matching with the experimental measurement. The convergence study on mesh density and the convergence study on the cohesive element viscosity for both model I and II was studied. The numerical simulation and the results of DCB and ENF models are under discussion.

Chapter 7: Numerical analysis of DLS joint based on cohesive zone model - This chapter presents the geometry of 2D DLS joint model, mesh type, cohesive zone model parameters in ABAQUS, and the simulation and results for different types of joint geometry. FEA results were compared with experiments and numerical analysis.

Chapter 8: Discussion, conclusion and future work - Provides overall discussion on the experimental results, numerical modelling and their failure modes. This chapter explains the FEA results of both strength of the material model and cohesive zone model, and compares them with experimental results. Also discussed is the prediction failure of DLS joints. Finally, this section concludes with an overview of this thesis, followed by proposals for future work.

Chapter 2

2 Literature review

2.1 Introduction

Fibre reinforced polymer (FRP) composites are finding increased usage in structural applications, in particular for aerospace, marine, construction and automotive purposes. One of the critical issues in these applications is the associated damage and failure mechanisms of FRP laminate composite/structures bonded joints under tensile loading.

In this chapter there is background information on composite materials, adhesive joint design and application of adhesive joints and carbon fibre reinforced polymer (CFRP) in some fields. The main parameter effects on adhesive bonding design and the failure mechanisms of composite joints are explained. Finally, a discussion of strength of materials approach and cohesive zone modelling are used for failure prediction, and the background research about double lap shear (DLS) joint is considered. In addition, the chapter reviews some studies regarding the application of numerical simulation technique used for steel/CFRP joints.

2.2 Composite materials

This section gives explanations for the general characteristics of the composite materials. The composite materials can be defined as materials, obtained from the combination of two or more materials, whose properties are different from their individual components [20]. These materials consist of two or more physically and/or chemically distinct, suitably arranged or distributed phases, with an interface separating them. Composite materials have two phases, which are continuous, known as the matrix, and non-continuous, known as the reinforcement. The dimensions and shapes of reinforcement constituents are very important in determining the mechanical properties of the composite. Also, the different fibre orientation and stacking sequences have many effects on the structural response and failure mechanisms of the composite.

2.2.1 Matrices

Most composite materials use a polymeric matrix in their construction. These matrices can be divided into two categories, which are thermosetting resins and thermoplastic resins, depending on reaction to heat. The two main thermosetting resins used commercially are epoxy-based and polyester. Other thermosetting resins include vinyl-ester, silicone and phenolic. The matrix material plays an important role in the overall function of the composite and must be able to satisfy a number of somewhat conflicting demands regarding strength, toughness, moisture and environmental resistance, elevated temperature properties, and cost [21]. Their main role is to bond the reinforcement fibre together, keeping them aligned and protecting them from damage. Alignment is crucial to prevent the creation of complex loading systems within the material. A common problem experienced with polymeric matrices is the shrinkage associated with them when undergoing curing [22]. Shrinkage during curing and thermal contraction during cooling introduces residual stresses within the material, and hence will have a detrimental effect on the FRP's mechanical properties.

Epoxy resins are widely used for a variety of applications, such as some of the most effective engineering adhesives and water resistant coatings. Epoxies are formed by condensation of epichlorohydrin and polyhydroxy compounds. Epoxy resins have higher strength and adhesion to fibres than polyester. This however comes at a higher cost relative to polyesters, especially in processing. Resins are normally based a two part resin consisting of an epoxide polymer mixed with a hardening agent, and are cured by a chemical reaction between the two, usually under elevated temperature conditions.

Polyester resins are the most widely used of all resin systems in FRP materials. Polyesters are formed by a condensation reaction between a glycol and an unsaturated dibasic acid. Their effectiveness follows from their moderate cost. In general the resins have good performance in a marine environment, ease of use within hand lay-up or spray-up fabrication processes [23]. The chemical reaction itself generates exothermic heat which, although helping to cure the resin, can damage it if the resin is too thick, by producing voids. Also, this resin suffers from high shrinkage during curing, which will have a detrimental effect on the strength of the finished laminate.

Typical mechanical properties of some commercially available resins are found in Table 2.1, which shows the superiority of epoxy over polyester in terms of mechanical properties and adhesion (shrinkage). The selection of matrix material type depends on the mechanical and chemical properties.

Table 2.1: Comparison of resin properties [23, 24]

Material	Young's Modulus (GPa)	Poisson's Ratio	Tensile strength (MPa)	Failure strain (%)	Heat distortion temp (°C)	Relative cost	Shrinkage (%)
Polyester	3.6	0.36	60	2.5	95	1	4-7
Vinyl ester	3.4	-	83	5	110	1.8	6-10
Epoxy	3	0.37	85	5	110	2.3	3-4
Phenolic	3	-	50	2	120	0.8	8-10

2.2.2 Fibres

Fibres are a type of filler which are added to the matrix to improve its qualities. While matrices are generally ductile and have good fracture toughness, fibres provide stiffness and resistance to both creep and wear. They can either be short, continuous or woven within the matrix material, and aligned in a variety of different ways. The short, discontinuous fibres exist as chopped strands and can either be aligned in a particular direction or randomly dispersed, whereas the continuous fibres will have a distinct orientation. Chopped fibre composites will lower values of strength and stiffness compared to composites with continuous fibre reinforcement.

The fibre orientation is a vital component of the fibre material strength as they are much stronger when loaded longitudinally than transversely. The fibre alignment has a significant effect on the failure load of a joint and its associated mode of failure. Many applications will impose a combination of different stresses and load directions upon the structure, which is of particular importance when considering the anisotropic nature of composite fibre reinforcement. A way of countering this would be to lay up layers of varying orientation to obtain quasi isotropy within the composite material.

Carbon fibres have good strength-to weight and stiffness-to-weight ratios which has encouraged their widespread use within the aerospace industry, and also in some applications of sporting goods. This high strength and stiffness, combined with low density and an intermediate cost, have made their use second only to glass fibres [21]. Different manufacturing processes allow for variety in the properties of the carbon fibres. Intermediate-modulus and high-strength fibres are usually made using the synthetic resin polyacrylonitrile (PAN) as the raw material. The PAN is heated and stretched to achieve proper alignment and to remove any non-carbon material. Fibres with a higher modulus can

be manufactured at a reduced cost using petroleum pitch, but those produced in this manner have much lower strength and so are not suitable in structural capacities.

2.2.3 Fibre Orientation

Having inspected the common constituents of a composite material, details will now be given of the various possible arrangements of these parts within the material, see Figure 2.1. As mentioned before, the fibres used for reinforcement can be arranged within the matrix material as randomly dispersed chopped strands, woven into a cloth or in unidirectional layers. The latter configuration will be used within this investigation and described in further detail.

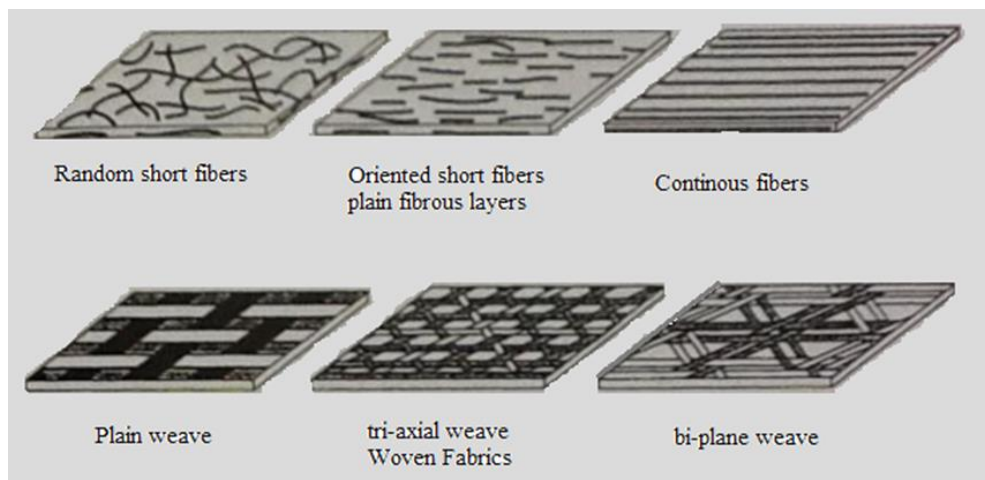


Figure 2.1: Fibre arrangement patterns in the layer of a fibre-reinforced composite [25]

2.2.4 Unidirectional Lamina

Unidirectional lamina (ply) consist of long continuous fibres all orientated parallel to one another and bound together by the matrix. For analysis they can be idealised to be arranged in a uniform manner as can be seen in Figure 2.2. In reality, most unidirectional lamina contain many voids which have detrimental effects on the mechanical properties of the composite. As mentioned above, unidirectional laminas have very good tensile strength in the direction of the fibres, however their transverse strength is significantly lower. For this and other reasons, unidirectional laminas are used to build up laminates. Here, the unidirectional layers are bonded together with the fibre directions of each layer, typically

orientated in different directions, to give different strengths and stiffness of the laminate in different directions.

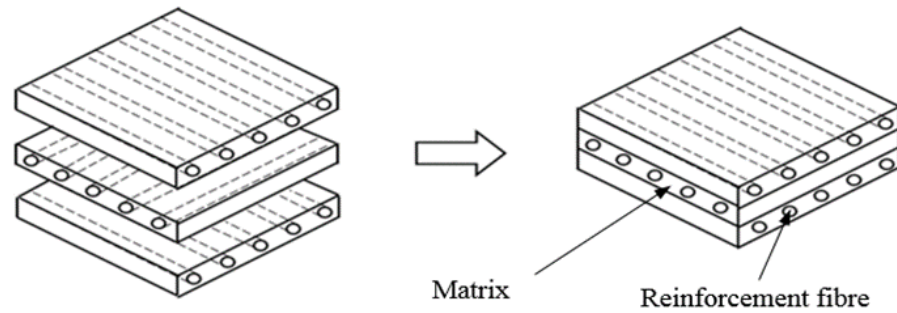


Figure 2.2: Unidirectional lamina lay-up to produce cross ply laminates

2.2.5 Cross ply Laminate

Carbon fibres cross ply composite laminates are formed by combining individual layers (lamina) into a multi layered structure. Continuous fibre composites combine unidirectional lamina (fibres aligned) into a structure with different layers in a laminate, generally having the fibres oriented in different directions. Figure 2.3 shows the carbon fibres cross ply composite prepared by vacuum infusion processing of monolayers with rich resin regions between the individual layers.

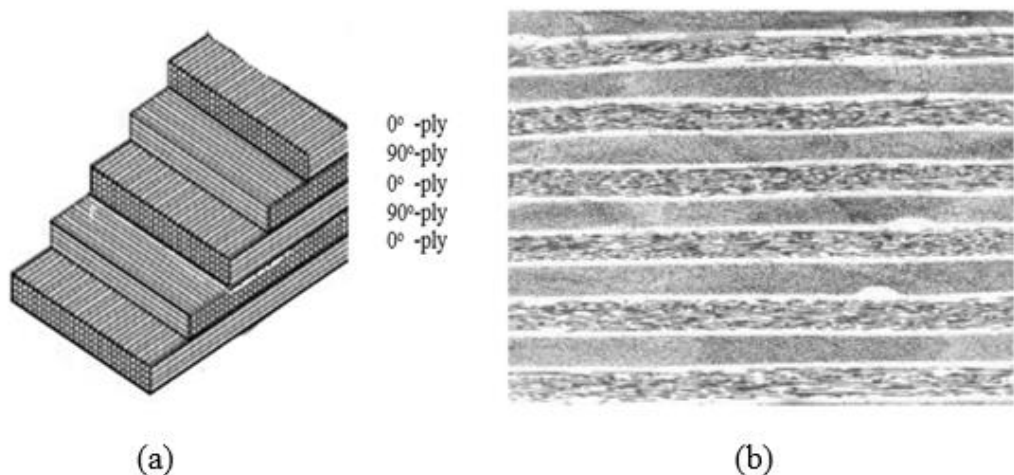


Figure 2.3: Illustration of a) the lay-up of a 5 layer cross ply laminate and b) optical micrograph of layer cross ply laminate [26]

2.3 Carbon fibre reinforced polymers

Carbon fibre reinforced polymer (CFRP) can be defined as a composite material consisting of carbon fibres, which provide strength, stiffness, and load carrying capacity, and a polymer matrix [27]. During the past few decades the aerospace, marine and automobile industries have witnessed expanded use of advanced composite materials. More recently, the construction industry has started to use composites as strengthening materials [28]. While the strengthening and rehabilitation of concrete structures by CFRP composites have attracted considerable interest [29], the first application of bonding CFRP material to metallic structure was in mechanical engineering applications [30].

The mechanical properties of CFRP composites depend on the type and orientation (transverse or longitudinal direction) of carbon fibre, percentage of resin material and curing conditions. Some researchers have focused on the effect of the adhesive materials because of the fact that the success of this technique depends mainly on the ability of the adhesive material to keep transferring the load between the adherends, e.g. CFRP composite laminates. This transferring is affected by many factors, such as surface preparation, bonded length, type of adhesive material, and thicknesses of adhesive and laminate.

CFRP laminates have been successfully used to repair damaged aluminium and steel aircraft structures [31, 32]. Bonding of composite laminates has also been shown to have many advantages for marine structures [33, 34]. Bonding techniques are critical to the success of attaching CFRP to steel members. To provide a strong bond between the CFRP composite and a steel member, the steel surface needs to be prepared by using an abrasive disk or sand blasting to remove rust and paint, and then cleaned by acetone to obtain a rough and clean surface [35]. At the same time, the surface of CFRP laminate can be treated by light grade P120C sandpaper to clean the bond area, and then acetone used to clean the bonding surfaces.

2.4 Moulding processes

Continuous fibre materials are available in a number of different forms, with the specific form utilised depending on the manufacturing process. The majority of composite laminates using infusion technology use epoxy resin or polyester in this process. Prepreg technology is currently exclusively epoxy based. A simplistic overview of the fundamentals of specific manufacturing techniques is presented in the following sections.

2.4.1 Infusion moulding

The general principal of infusion technology is to draw a resin into the reinforcing fibres and fabrics using a vacuum. The vacuum reduces the pressure at one end of the fabric stack allowing atmospheric pressure to force the resin through the stack. The speed and distance with which you can infuse a fabric stack will be dependent on the viscosity of the resin and the pressure gradient acting on the infused resin.

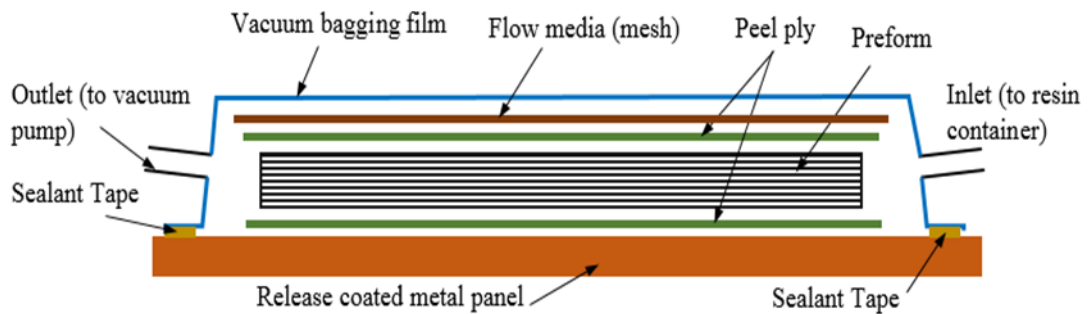


Figure 2.4: Vacuum infusion moulding showing the vacuum bag, sealant, outlet to vacuum pump, inlet to resin supply and the preform surrounded by peel ply

As shown in the vacuum bagging illustration Figure 2.4, the metal panel was coated by a mould release agent before stacking the peel ply, preform, flow media and vacuum bagging film on top of it. The vacuum bag with inlet and exit was set up and sealed with circuitous and occlusive mastic tape and vacuum bagging film.

2.4.2 Autoclave moulding

This section will briefly describe the manufacturing process used when building laminates. The individual lamina themselves usually come in “prepreg” form. Prepregs are a partially cured mixture of fibre and resin which are lined with a removable paper and wound onto spools. These prepregs come in either unidirectional tape or as woven cloth which, once partially cured, must be refrigerated to prevent further curing. Because the individual fibres are relatively straight, the use of unidirectional prepreg provides a method, along with filament winding, of achieving finished products with good mechanical properties [21].

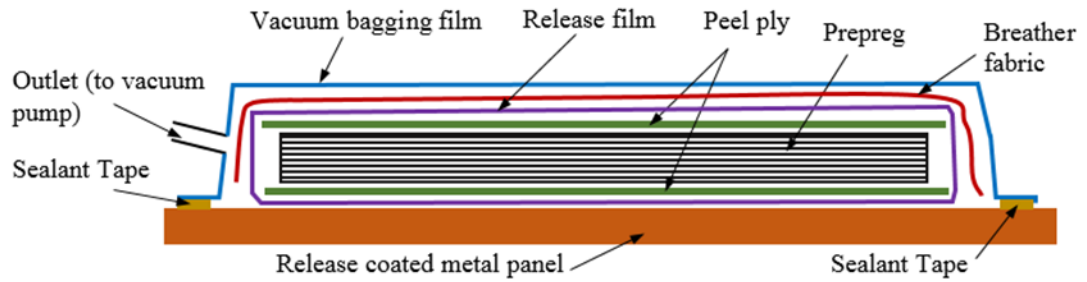


Figure 2.5: Prepreg moulding showing the vacuum bag, sealant, outlet to vacuum pump and the preform surrounded by peel ply

The curing routine for the prepreg panels' autoclave moulding was much easier than for Vacuum infusion. The prepreg panel was bagged by peel ply and release film on both sides, as shown in Figure 2.5. A breather fabric was placed on the top of this package in order to provide venting for gas in the vacuum bag. A full vacuum was applied before placement in the autoclave. To ensure a good bond between the laminas, the sequence of stacked plies are cured in a vacuum under pressure and at elevated temperatures, in an autoclave. Prior to the part being placed in the autoclave, it is placed inside a vacuum bag and the air is expelled. The purpose of this is to consolidate the lay-up, and draw out any gasses given off during the curing process.

2.5 Adhesive bonding

Adhesive bonding is desirable in many circumstances, because it eliminates the stress concentration factors associated with mechanical means of joining. Introducing holes into a structure, in order to accept mechanical fasteners, significantly reduces the strength of the composite, and therefore composite materials are prime candidates for adhesive bonding. In this section the adhesion and properties of adhesives, such as wetting and surface preparation, are all discussed.

2.5.1 Adhesion

Adhesion occurs when the adhesive interlocks the parts by an interlocking action around the surface roughness of the parts [36], as shown in Figure 2.6. The mechanism of adhesion is not fully understood, and several theories have been proposed. The main mechanisms has

been proposed by Kinloch [37] through absorption theory. This states that the parts are initially joined together by intermolecular contact. This intermolecular contact is achieved through molecular forces on the surface of adhesive and adherend. Kinloch [38] also found that mechanical interlocking and surface irregularities are the main source of adhesion. Bikerman [39] suggests that the mechanical inter-locking between the bonded surfaces was sufficient to have a strong interface. Voyutskii [40] proposed that the adhesive particles dispersion established adhesion across the interface. Deryaguin [41] suggests that the electrical charge layer at the interface formed adhesion. Staverman [42] pointed out that the adherend surface forces, due to chemical composition at the interface, followed adhesion. Perhaps the most important factor that can determine the adhesive's strength is the ability of the material to be wetted. Wetting can simply be described as the contact angle between a fluid and a surface when they are brought into contact. If a surface is said to have high surface energy, then a drop of liquid will be seen to spread over the surface, or wet the surface effectively. On the other hand, if the surface energy is low, then the droplet will remain as a droplet on the surface. Therefore, in order to achieve effective wetting, there needs to be strong attraction between the adhesive molecules and the substrate surface [43].

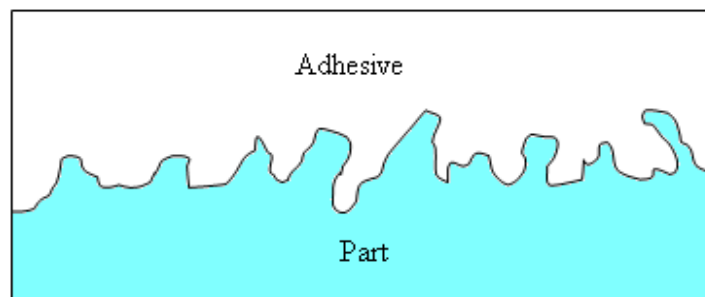


Figure 2.6: Mechanical Inter-locking [37]

Several authors [44, 45] have noticed the wetting behaviour and proposed different hypotheses, which differentiate the wetting features between smooth and rough surfaces. The degree of wetting can be measured by the contact angle in which the adhesive drop is plunged on the adherend surface, with the assumption that the adhesive drop should not interact with the surface. The size of adhesive drop is in tens of micro litres, measured by a goniometer. Such measurements are based on direction i.e. receding and advancing contact angles. The contact angle hysteresis is obtained under receding and advancing contact angle

conditions. Surface roughness and molecular changes in the adherend surface with the interaction of the adhesive are the possible reasons for contact angle hysteresis [44].

2.5.2 Surface preparation

Surface preparation plays an important role in a joint's strength and durability. For the development of a strong bond joint, intermolecular contact at the interface is very important. Moreover, thorough surface preparation is also imperative if an acceptable joint strength is to be achieved. Any sort of contaminant can ingress into the adhesive and have an adverse effect on the overall strength of the joint. However, no amount of preparation will ever be completely free a surface of contamination; even if the material surface has been newly machined, there may still be a surface film present due to metal oxides, carbon dioxide or water vapour [43].

To ensure full utilisation of the applied CFRP material, surface preparation of the steel must be undertaken to enhance the formation of chemical bonds between the adherend and the adhesive. This requires a chemically active surface that is free from contaminants. Most surface treatment involves cleaning, followed by removal of weak layers and then re-cleaning [46, 47]. Degreasing is a necessary first step in preparing most metals to remove oils and other potential contaminates. Brushing, ultrasonic or vapour degreasing systems are claimed to be most efficient in removing this surface contamination, especially when sufficient amounts of solvent are used (Hashim [34]). Contamination may then be removed with the excess solvent, rather than simply red posited on the surface as the solvent evaporates.

As stated previously, the surface needs to be such that high wettability can occur by initiating high surface energies on the surface. This cannot occur on smooth surfaces, and so the surface of joints often needs to be prepared in order to maximize surface energy and ensure thorough wetting. Some of the methods often used are: mechanical abrasion, sandblasting, acidic etching and solvent degreasing, but some methods are restricted to composite material.

The most effective means of achieving a high-energy steel surface is by grit blasting. Hollaway and Cadei, [6]. Baker [48] found that for composite joints, those that were grit blasted had higher peel strengths than those that were hand abraded. Shahid et al. [49] revealed that the surface roughness produced by grid blasting improved the strength of

cleavage joints. Harris et al. [50] also suggests that grit blasting along with degreasing or solvent will achieve good strength in dry conditions.

All methods change the chemical composition of the surface as reported by Pocius [51]. Boone et al. [52] reported that whichever method is chosen, all result in changes in surface tension, surface roughness and surface chemistry, which in turn affect the bond strength. It has been proven that roughening the surfaces prior to adhesion actually enhances the joint strength, and the effect of this is that any loose contaminant particles are removed from the surface. This enhances mechanical interlocking with the adhesive [52]. Baker [48] proposed improved joint strength when the argon ion etching technique is used for surface cleanliness after grit blast. Wingfield [53] and Brockmann [54] pointed out that the joint bond strength is directly related to proper surface preparation of the parts to be joined.

Sandblasting is unsuitable to prepare a composite surface prior to bonding. This is due to the fact that the extremely harsh abrasion caused by sandblasting would have actually damaged the fibres, and therefore the reinforcing nature of the composite material. Ultimately, this would have reduced the mechanical properties of the composite.

Parker [55] suggests that in composite adherends, the initial bond strength is directly related to the surface preparation to remove all surface contaminations. Guha et al. [56] conclude that acrylic and urethane adhesives give better strength with only a wipe of the surface. Also epoxy adhesives give good strength with abrasion or flaming the joining surface.

Wingfield [53] suggests various surface preparation methods for composites, which are as follows:

“Dry clean rag wipe: good to remove surface dust only.

Solvent wipe: solvent wipe is better than dry cleaning, but still oil /grease exists on the surface after the solvent wipe.

Abrasion with emery paper: ideal for GFRP composites.

Grit blasting: good for epoxy resin composites.

Flame, laser, plasma: good for low surface energy thermoplastic.”

2.6 CFRP and adhesive bonding applications

CFRP offers high specific stiffness and strength in comparison with materials such as steel and aluminium. CFRP parts are currently used in aero-structures and assembled by mechanical fasteners. The first applications of hybrid (composite/metal) joints are met in the

aerospace structures, with the use of composite patch repairs of aluminium structures [57]. This type of design implies weight penalties emanating from the need to deal with the stress concentrations developed around the bolts. Moreover, bolts and rivets damage the continuous reinforcing fibres and, consequently, can greatly affect the overall load-carrying capacity of the structure [58].

Adhesive bonding of aerospace components is a fabrication technique which has increased markedly in popularity during the last two decades. While adhesives have been used in a number of repair and maintenance operations they have yet to make a great impact.

Military applications initiated the use of adhesively bonded advanced composites, and aircraft such as the F-18 and the F-22, which employed significant amounts of bonded polymer matrix composite laminates at wing skins and control surfaces [59]. Similar applications may be found on many types of commercial aircraft, whose economic operation benefits considerably from the reduced weight offered by the bonded composite assemblies (e.g. AIRBUS A380) Figure 2.7, where around 42% of the joints are based on adhesive bonding structure [60]. Another example of the extensive use of CFRP is in Figure 2.8, which shows a fuselage section of the A350 with skin panels, doublers, joints and stringers entirely made of carbon fibre composites.

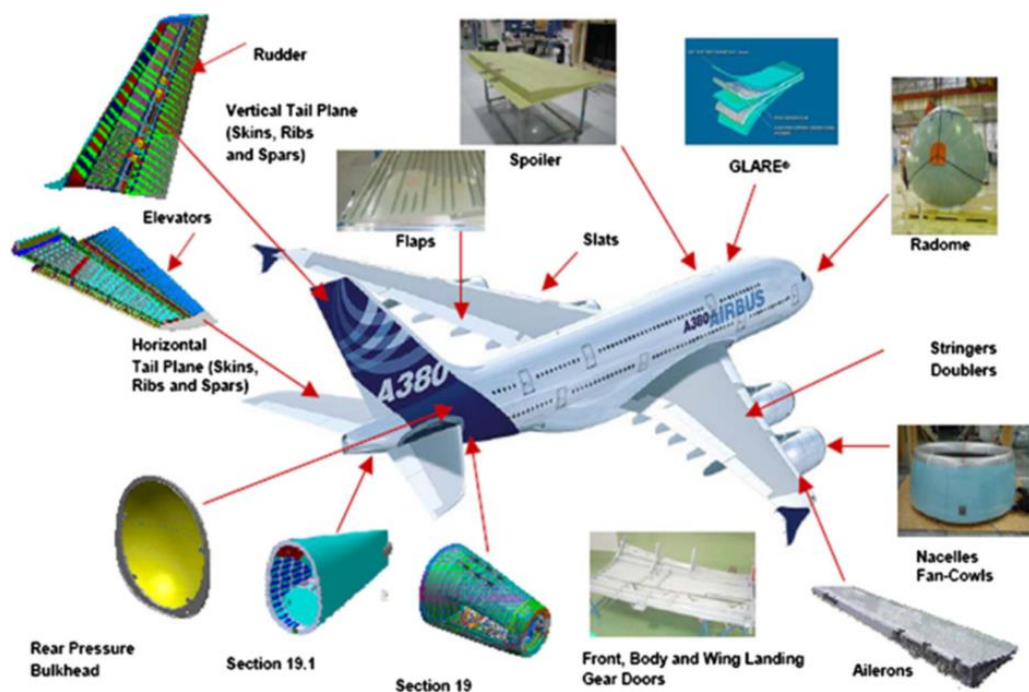


Figure 2.7: Adhesive bonding applications at the new AIRBUS A380 [60]

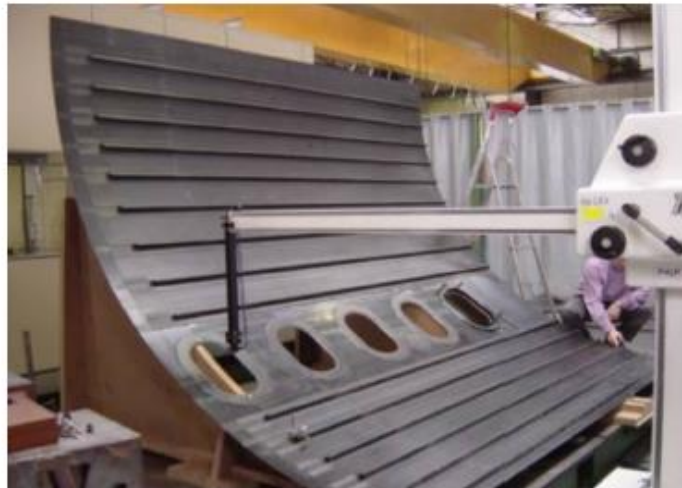


Figure 2.8: A fuselage section of the A350

Composite and adhesive bonding has been adopted by the marine industry since the 1980s. The construction of composite superstructures has been increasing in the use of composite materials for naval superstructures [61]. The French navy have implemented such a superstructure on their La Fayette class frigate in the form of a helicopter hangar [62, 63]. It has been a field of research by several scientists since then, with the design of adhesive joints in marine structures (deck-to-hull joints) gaining the greatest focus. Specific structural parts of a ship, such as superstructures, bulkheads, masts or even the entire deck, may be replaced by composite materials [61, 64, 65, 66], properly designed and adhesively bonded either to composite or metal parts. The study of composite hybrid joints has been extended to applications in the marine industries [62, 63, 61, 67]. Figure 2.9 presents a modern large-scale application where a composite deck is adhesively bonded to a steel hull.

Additionally, modern adhesive bonding technologies offer many techniques for repairing defected structural elements. By using an adhesively bonded patch, the repair is much easier and quicker to carry out. The design of each repair is a very promising technique in marine applications, where carbon, glass or combined fabric patches are either directly laminated, or cured composite patches are adhesively bonded on the cracked or corroded area of metallic parts, for example, the fuel tank, water tank, or hull of an oil tank.

This technology is advantageous in the marine industry [67, 68] since the hot work of welding is avoided, thus reducing the risk of a fire. Also, if a composite material is used for

the patching of steel, then the materials used are easy to transport and handle, with no need of heavy lifting machinery.



Figure 2.9: Composite deck adhesively bonded to steel hull [69]

Adhesives are used in the construction industry in repair and strengthening of existing structures and new built structures. During the 1950's and 1960's an enormous amount of new constructions were built and, as these structures age, many faults have become evident. The repair substrate may be ordinary concrete or polymer concrete, with or without reinforcement. If increased structural capacity is needed then external plate bonding can be an alternative.



Figure 2.10: CFRP used to strengthen bridges [70]

During the 1970s and up to the end of the 1990s, steel plate bonding was not unusual; however in the last decade, the use of advanced composites for external strengthening has

become quite common (a photo of a bridge strengthened this way is shown in Figure 2.10 [71]). Also a great number of models for debonding have been presented [72, 73].



Figure 2.11: World's largest carbon composite bridge in Paris (left) and Composite bridge on UK motorway (right) [70]

At the 2007 JEC-fair in Paris (the largest European exhibition on composite materials), the world's largest carbon composite bridge was shown. The carbon composite bridge is 24.5 meters long and 5 meters wide and weighs only 12 metric tonnes. This makes the bridge about 30 times lighter than a comparable concrete bridge (Figure 2.11).

Gradually, bridges are also being introduced on highways, where load-carrying capacity is much larger. A fibre-reinforced polymer bridge was constructed over the M6 motorway in the UK, carrying 40 tonnes which is the standard for road bridges on the highway network. The bridge uses a glass fibre composite deck on steel girders, placed on reinforced concrete substructures (Figure 2.11).



Figure 2.12: External strengthening of concrete structures [70]

Finally, composites are an attractive solution for repair of damaged concrete structures. Carbon fibre-reinforced strips are glued on the exterior surface of the structure and help in taking up the loads of the structure (Figure 2.12).

2.7 Adhesive joint design

Many early bonded joint and repair designs were based on their joint strengths and optimal overlap lengths determined from lap shear tests. With the analysis of adhesive bonds within certain limits of overlap length and adherend thickness, bonded joints can be designed so that the load capacity of the bond is greater than the unnotched strength of the adherends material [71].

2.7.1 Effects of adherend thickness

Figure 2.13 shows a series of typical bonded joint configurations. Adhesive joints in general are characterised by high stress concentrations in the adhesive layer. These originate, in the case of peel stresses, because of unequal axial straining of the adherends, because of eccentricity in the load path. Considerable ductility is associated with shear response of typical adhesives, which is beneficial in minimising the effect of shear stress joint strength. Response to peel stresses tends to be much more brittle than that to shear stresses, and the reduction of peel stresses is desirable for achieving good joint performance.

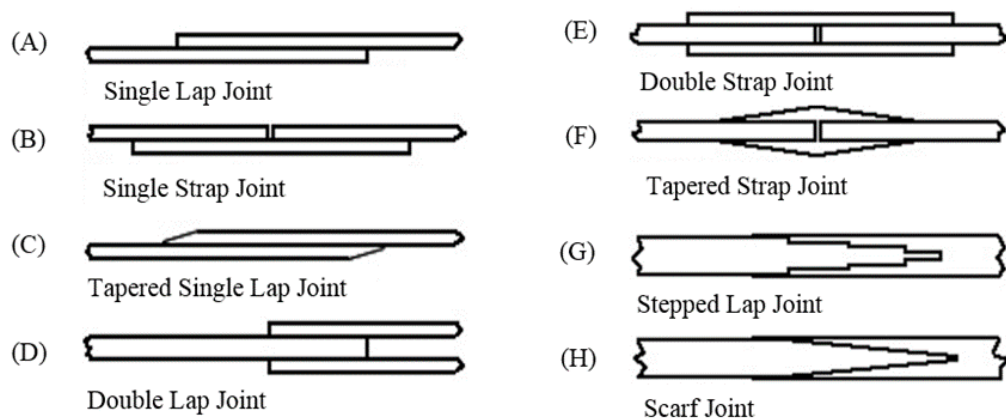


Figure 2.13: Different joint geometry of adhesive joints [72]

From the standpoint of joint reliability, it is vital to avoid letting the adhesive layer be the weak link in the joint; this means that, whenever possible, the joint should be designed to

ensure that the adherends fail before the bond layer. This is because failure in the adhesive is resin dominated, and thus subject to effects of voids and other defects, such as thickness variations, environmental effects, deficiencies in surface preparation and other factors that are not always adequately controlled.

This is a significant challenge, since the adhesives are inherently much weaker than the composite or metallic elements being joined. However, the objective can be accomplished by recognising the limitations of the joint geometry being considered, and placing appropriate restrictions on the thickness dimensions of the joint for the geometry. Figure 2.14, which has been used by Hart-Smith [74] to illustrate this point, shows a progression of joint types, which represent increasing strength capability from the lowest to the highest in the figure.

When the adherends are relatively thin, the results from stress analyses show that for all of the joint types in Figure 2.14, the stresses in the bond will be small enough to guarantee that the adherends will reach their load capacity before failure can occur in the bond. As the adherend thicknesses increase, the bond stresses become relatively large until a point is reached at which bond failure occurs at a lower load than that for which the adherends fail.

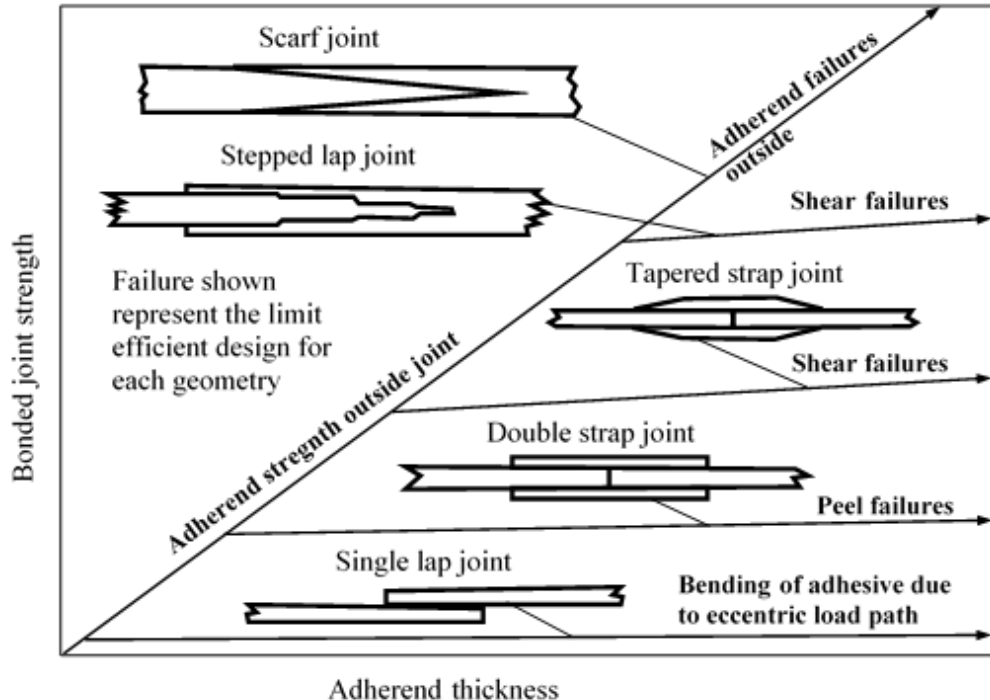


Figure 2.14: Joint geometry effects [74]

This leads to the general principle that for a given joint type, the adherend thicknesses should be restricted to an appropriate range relative to the bond layer thickness. As a result, each of the joint types in Figure 2.13 and Figure 2.14 corresponds to a specific range of adherend thicknesses, and therefore of load capacity. As the need for greater load ability increases, it is necessary to change the joint configuration to one of higher efficiency, rather than increasing the adherend thickness indefinitely.

2.7.2 Joint geometry effects

Single and double joints with uniformly thick adherends (Figure 2.13: Joints A, B, D and E) are the least efficient joint type, and are suitable primarily for thin structures. Single lap joints are the least capable, since the eccentricity of this type of geometry creates important bending of the adherends that magnifies the peel stress. Peel stresses are also present in the case of symmetric double lap strap joints, and become a limiting factor on joint performance when the adherends are relatively thick.

Tapering of the adherends (Figure 2.13: Joints C, and F) can be used to reduce peel stresses in areas of the joint where the peel stresses are tensile, which is the cause of primary concern. No tapering is needed at ends of the overlap where the adherends butt together, because the transverse normal stresses at that location is compressive and small. For double strap joints under compressive loading, there is no concern with peel stresses at either location, since the transverse extensional stresses that do develop in the adhesive are compressive in nature rather than tensile; indeed, where the gap occurs, the inner adherends bear directly on each other, and no stress concentrations are present for the compression loading case.

For joints between adherends of identical stiffness, the scarf joint (Figure 2.13: Joint H) is in theory the most capable, having the possibility of complete elimination of stress focus. In practice, scarf joints may be less durable, because of a tendency toward creep failure associated with a uniform distribution of shear stress along the length of the joint, unless care is taken to avoid letting the adhesive become stressed into the non-linear range. In theory, any attractive load capacity can be achieved in the scarf joint by making the joint long enough and thick enough. However, scarf joints tend to be used only for repairs of very thin structures.

Step lap joints (Figure 2.13: Joint G) represent a practical solution to the challenge of bonding thick adherends. These types of joint provide manufacturing by taking advantage

of the layered structure of composite laminates. In addition, high loads can be transferred if a sufficient number of short steps and small increase in each step are used.

2.7.3 Behaviour of composite adherends

Polymer matrix composite adherends are affected much more by interlaminar shear and tensile stresses than are metals; as a result there is an important need to account for such effects in stress analyses of joints. Transverse shear and thickness of the adherends have an effect similar to the bond layer thickness. In addition, the adherend matrix is often weaker than the adhesive in shear and transverse tension. As a result, the limiting element in the joint may be the interlaminar shear and transverse tensile strengths of the adherend rather than the bond strength.

The effect of the stacking sequence of the laminates making up the adherends in composite joints is important. For example, 90° layers placed adjacent to the bond layer theoretically act largely as additional thicknesses of bond material, leading to lower peak stresses, while 0° layers next to the bond layer give stiffer adherend response, with higher stress peaks. In practice it has been observed that 90° layers next to the bond layer tend to critically fail the joint, because of transverse cracking which extends through those layers.

2.7.4 Influence of fibre architecture on joint strength

The fibre architecture (including tow size and fibre length) interaction with the fibre orientation was interesting, as this demonstrated that the choice of tow size and fibre length only become significant if the loading of the adhesive joint was away from the principal fibre direction. The laminate lay-up or fibre architecture has a great impact on the bonded composite joint strength and failure modes. The mechanical properties of many composite materials are strongly dependent on fibre architecture and orientation, fibre volume fraction and matrix properties [75]. The problem with having varying orientations in the composite laminate is that stress concentrations that can arise from having differing local stiffness between the layers, that can cause premature failure of adhesive joints manufactured using a composite laminate. Mortensen [76] studied the effect of changing the stacking sequence of the plies in a laminate numerically. The findings demonstrated that the transverse normal stresses within the adhesive layer increased by up to 58% at the overlap ends when the stacking sequences were changed from 0° to 45° . The shear stresses also increased by up to

39% when the stacking sequences were changed. This highlights the importance of having a 0° surface layer, as this limits the deformation in the top layer of the composite laminate, which in turn reduces the stresses imparted into the adhesive layer.

Taib et al. [58] studied the effect of fibre orientation on the joint strength of single lap-joints using two different fibre orientations. Using $[0^\circ, 90^\circ]_s$ and $[\pm 45^\circ]_s$ composite laminates, the failure loads were 29% higher for those laminates using a $[0^\circ, 90^\circ]_s$ stacking sequence. The failure modes also changed with the fibre orientation, from a cohesive failure initiating in the spew fillet for the 0° surface fibre orientation to an inter-laminar failure for those specimens with a 45° surface fibre orientation. The elongation to failure was higher for the 45° specimens, as the fibre orientation allowed for more deformation of the substrate, despite the failure load being lower [58].

Lee et al. [75] presented the experimental investigation of pultruded GFRP decks under static load. Two types of fabric architecture were used, one fabric architecture with a $[45^\circ, 90^\circ, -45^\circ]$ and the other with a $[0^\circ, 90^\circ]$ fibre orientation. The general purpose finite element package ABAQUS was used for the verification of experimental results. It was found that the behaviour of all specimens showed linearly elastic and brittle fracture. They concluded from the experimental results that $[45^\circ, 90^\circ, -45^\circ]$ deck exhibits higher stiffness and strength than $[0^\circ, 90^\circ]$ specimen.

Meneghetti [77] modified the near surface layers of a composite material to change the adhesive/substrate interface. The static and dynamic properties of the joints were then analysed. The authors manufactured 2 different types of substrate, one substrate with a $[+45^\circ, 0^\circ, 0^\circ]$ near surface fibre orientation, and the other with a $[+45^\circ, +45^\circ, 0^\circ]$ fibre orientation. The presence of the extra 0° layer changed the failure mechanism of the samples when tested. In the $[+45^\circ, 0^\circ, 0^\circ]$ samples, simultaneous damage occurred in both the bond and within the substrate. For the $[+45^\circ, +45^\circ, 0^\circ]$ samples, the failure occurred entirely within the substrate itself.

de Goeij [78] observed that when composite joints were subject to cyclic loading, the fatigue life of specimens was larger when the surface fibre orientation was 0° compared to $\pm 45^\circ$ surface laminates, which still outperformed those with a 90° configuration. The failure modes were also similar to those observed by Taib et al. [58], with the 0° surface laminates failing at the interface or in the adhesive, whilst for the $\pm 45^\circ$ orientations, the failures occurred either in the surface ply or between the $\pm 45^\circ$ layers as inter-laminar failures [78].

When investigating the effect fibre orientation has on the bond strength of a fibre, reinforced composite multiple researchers have found that lay-up patterns with larger effective moduli carry greater loads [79, 80, 78, 77, 81].

2.8 Previous work on hybrid connections

Many experimental works and theoretical studies address the bonding of CFRP composite on steel members, each dealing with a different parameter to discover more advantages of the material and its suitability for steel structures.

Mertz and Gillespie [82] investigated the advantages of using advanced materials in the rehabilitation of deteriorated steel bridges. In their small-scale tests, they retrofitted eight 1.52 m long W8×10 steel beams with a yield strength of 250 MPa using five different retrofitting schemes. They reported an average 60% increase in strength for carbon-retrofitted specimens. They also concluded that in order to avoid the possibility of galvanic corrosion, an electrically insulating layer of composite, such as GFRP, could be placed between CFRP and steel.

A number of researchers have studied the effect of overlap length of CFRP strips bonded to steel structures. Miller et al. [83] determined where force transfer occurs within the bond of CFRP to steel from tension tests, performed with steel plates reinforced on each side with CFRP laminate strips. Test results and an analytical model, validated by strain gauges on one sample specimen, and indicated that 98% of the force transfer occurs within 100 mm of the end of the CFRP strips. With similar materials, Lam et al. [84] concluded that increasing the overlap bond length from 100 mm to 300 mm for a series of steel/CFRP double lap shear joints did not significantly increase the bond strength of the joint. This was due to the presence of significant bond stress concentrations near the end of the CFRP and steel materials. Increasing the bond length did however increase the maximum ductility of the joints.

Fawzia et al. [85] examined different bond lengths of normal modulus CFRP to find an effective bond length by testing CFRP/steel double strap joints. The effective bond length of CFRP is a certain value “beyond which no significant increase in load carrying capacity will occur”. This study shows the test results for different bond lengths, and shows the plotting of ultimate load capacity verses the bond length. According to the results, the

effective bond length is 75 mm on each side of the joint, which means 75 mm on notch right side and 75 mm on notch left side.

Lenwari et al. [86] studied analysis predictions of development length by testing seven steel beams strengthened with conventional modulus CFRP laminate strips using three different lengths. The different strip lengths considered were 500 mm, 650 mm and 1200 mm. Both of the shorter lengths failed by debonding at the same applied moment, while the 1200mm length failed by rupture of the CFRP strip. Measured strains at a distance of approximately 100 mm from the end of the CFRP were required to achieve conformance with the predicted strains obtained from an elastic-plastic section analysis. The measured 100 mm length was also required to conform to the predicted adhesive shear stresses obtained from a stress-based analysis, which uses differential equilibrium and compatibility to predict the shear stresses in the adhesive layer. For the stress-based analysis, this 100 mm length was found to be independent of the length of the CFRP.

Liu et al. [87] report a study of the direct tension fatigue behaviour of bonded CFRP sheets used to create “strap joints” between two steel plates. This study reported an apparent fatigue limit of 40% of the ultimate static strength of the strap joint specimens. Below this limit, specimen failure and steel-CFRP bond behaviour were not affected by the applied fatigue loads.

Schnerch [88] conducted an extensive research program into the performance of CFRP in strengthening steel monopoles and steel-concrete composite beams. A major component of this program was testing a series of epoxies to determine the optimal one for CFRP to steel bonding. An optimal one was selected through an elimination process by which the development length of the CFRP to steel was reduced with each test until the shortest length with CFRP rupture was determined. The tests were performed with CFRP bonded to the tensile flange of a Super Light Beam (SLB) 100x4.8 and tested under four-point bending. In this study, development length was defined as the length of bonded CFRP in the varying moment region.

Roy et al. [89] have reported that a unidirectional laminate has more ultimate strength than cross-ply laminates in their examination of double lap shear joint. The effect of laminate stacking sequence on crack initiation was studied by employing a strain gauge on the specimen. The failure was within the laminate itself, well before the adhesive showed any

sign of cohesive or interfacial failure; very few specimens were tested for this strength prediction.

Hashim et al. [90] proposed design guidelines for the structural integrity of composite pipe-work systems. They tested adhesively bonded taper/taper connections (GRE) and a double lap shear joint (steel) under a monotonic loading of 0.5 mm/min in an Instron universal testing machine. Two failures, adhesive layer and failure in composite adherend just outside the edge of the joint, were reported. von Mises criterion was used for numerical validation. However, the assumption made here is that the behaviour of double-lap shear joints might realistically simulate pipe joints of larger diameters.

Altus [91] has analysed the double lap joint three dimensionally to observe the singularities. He pointed out that a 3D singularity exists at the corner point of the double lap specimen for the multi-material cases, which was not found in the 2D case. The shear energy, which represents the tendency for yielding, is observed at the 3D corner. Both the plane stress and plane strain solutions give higher bounds for the critical values, by which the need for 3D analysis is emphasised.

McGeorge [92] used a fracture mechanics approach to develop a new model to predict the fracture load of bonding overlap joints. To understand the mechanical behaviour of bonded overlap joints and the effects of short and long overlap, McGeorge was able to derive simple formula for elastic energy in the adherends and adhesive, as well as for inelastic energy in the bondline. These formula could be derived to obtain the energy release rate G occurring at the most loaded end of the bondline for unbalanced single butt strap joint with long overlap.

Wright et al. [67] investigated a fibre-reinforced composite–steel connection for transverse ship bulkheads. These joints were tested in tension, compression and lateral bending. They found that a suitable connection could be made, and that symmetric rather than asymmetric joints provide better strength characteristics.

Boyd et al. [63] performed the experimental and numerical investigation of a similar hybrid joint, based on the design for the hangar-to-weather deck connections on La Fayette class frigates. They characterised the fatigue life of the hybrid joint and assessed the residual strength of the joint under in-plane and out-of-plane loading. They developed a stress reduction model to account for the nonlinear behaviour of the joint after their initial failure.

2.9 Analytical solutions of adhesive joints

Before finite element analysis was widely available to researchers, stress distributions in the adhesive layer in bonded joints were analytically investigated. An analytical method is important to study critical parameters, and thus closed form solutions, in the preliminary design stage. Therefore, considerable efforts have been devoted to the development of theoretical and analytical methods for studying adhesively bonded joints. One of the most common adhesive joints that can be found in practice is the single lap shear joint [5]. In this analysis, the adhesive is considered to deform only in shear, and the adherends to be rigid. The adhesive shear stress (τ) is constant over the overlap length, and is given by $\tau = P/bl$, where P is the applied load, b is the joint width and l is the overlap length. The value of the shear stress can be interpreted as the average shear stress acting on the adhesive layer.

For a single lap joint in tension, Volkersen [93] derived a simple solution considering only shear stress in the adhesive layer and tensile load in the adherends. His shear-lag combined these elastic deflections with the shear deformation of the adhesive, and predicted that the shear stress should peak towards the ends of the adherends, as shown in Figure 2.15. In the middle of the joint, the shear stress will be a minimum. The tensile stress in the upper adherent is maximum at A and decreases to zero at B, so the strain must progressively reduce from A to B. The reduction of the strain in the adherends along the overlap and the adhesive/adherent interface cause a non-uniform shear strain and stress distribution in the adhesive layer.

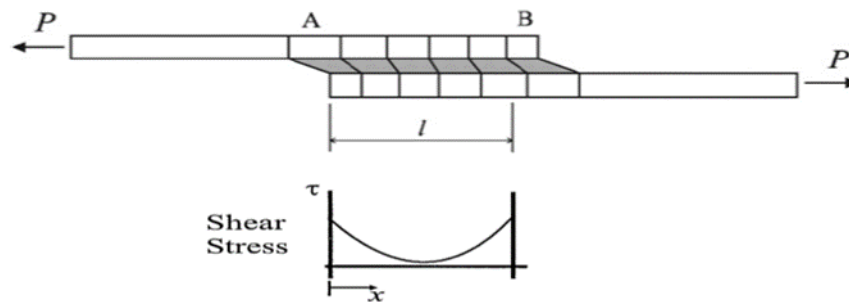


Figure 2.15: Deformations in single lap shear joints with elastic adherends [94]

De Bruyne [95] adapted Volkersen's single lap theory for double lap joints. De Bruyne modelled the adherends as bars which are allowed to deform in the longitudinal direction, uniformly through the thickness of the adherends. The adhesive layer was considered to be

a shear spring carrying only the shear stresses needed to transfer the longitudinal forces from the inner to the outer adherends.

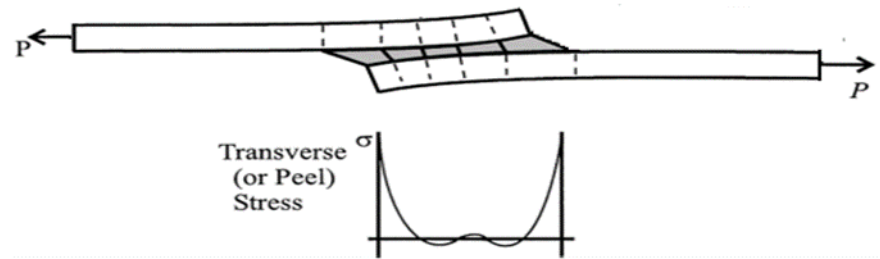


Figure 2.16: Deformations in single lap joints predicted with Goland and Reissner's model [94]

Goland and Reissner [94] made a significant contribution by taking into account the adherend bending moment and adhesive peeling effects, as well as adherends large deflection. Figure 2.16 illustrates the joint deformation they predicted under tensile loading. It can be clearly seen that the peel stresses peak at the ends of the overlap. This work has been widely used and evaluated experimentally and numerically by many investigators.

Hart-Smith [96] proposed an improved model which removes the lumped overlap (assumed by Goland and Reissner analysis) restriction, by treating the adherends as beams on an elastic foundation, and providing stress solutions for linear elastic and elastic plastic adhesives. Hart-Smith has also applied his theory on composite laminated adherents, validating his results with respective numerical and experimental studies. There is no doubt that the earlier work done by Volkersen [93] and Goland and Reissner [94] was a major step forward in the stress analysis of adhesively bonded joints. But, according to da Silva et al. [97] their work has several limitations: they do not account for variations of the adhesive stresses through the thickness direction, especially the interface which are important when failure occurs close to the interface. The authors also support that the peak shear stress occurs at the ends of the overlap, which violates the stress-free condition, as presented in Figure 2.17. Analyses that ignore the stress free condition overestimate the stress at the ends of the overlap, and tend to give conservative failure load predictions. Crocombe and Adams adopted Goland and Reissner's formulation [98]. Ojalvo and Eidinoff used a more complete strain/displacement equation for the adhesive layer to investigate the influence of adhesive thickness on stress distribution [99].

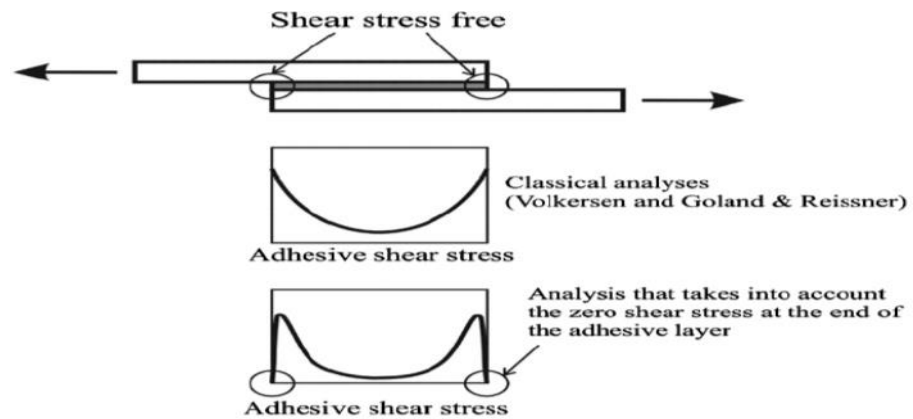


Figure 2.17: Adhesive shear stress distribution when the stress free condition at the ends of the overlap is verified [97]

Tsai et al. [100], improved the theoretical solutions of Volkersen and De Bruyne and Goland and Reissner's for double lap and single lap adhesive joints, respectively. This study is based on the assumption of linear shear stress distributions through the thickness of the adherends. Additionally, other researchers have made contributions to theoretical analysis for adhesively bonded joints incorporating composite or steel adherends [100, 101, 102, 103, 104].

Zou et al. [101] presented an analytical tool for joint design. This tool is based on classical laminated plate theory, in conjunction with an adhesive interface constitutive model for balanced composite joints subjected to in-plane and out-of-plane loads. According to the authors, this promising tool can be easily extended to the application of various types of joints.

Luo and Tong [105] presented closed-form solutions that predict accurate edge moment and adhesive stresses for an isotropic single lap joint. Their study is also based on the use of Euler beam theory. However, their analysis of adhesive joints can be highly complex if composite adherends are used, the adhesive deforms plastically, or if there is an adhesive fillet.

In these cases, several differential equations of high complexity might be obtained for the non-linear and non-homogeneous. For these cases, numerical methods are more adequate.

2.10 Numerical solutions of adhesive joints

Finite Element Analysis (FEA) is the most common technique used in adhesively bonded joints for stress analysis. One of the first applications for the use of FEA was to assess the influence of the spew fillet. Joint rotation and adherends and adhesive plasticity are other aspects where it is easier to use FEA. Adams et al. were among the first to have used FEA for analysis of adhesive joint stresses (Adams and Peppiatt [106], Crocombe and Adams [98], Adams and Harris [107], Adams et al. [108] and Adams and Davies [109]). The meshing of the FEA model is an important factor to obtain accurate results for the analysis. In FEA modelling there are methods to reduce the simulation time, such as submodelling, mesh refinement and symmetry boundary conditions.

2.10.1 Strength of materials approach

In the strength of materials approach, the maximum values of stress, strain or strain energy, predicted by the FEA, are usually used in the failure criteria, and are compared with the corresponding material allowable values. Initially, the maximum principal stresses were proposed for very brittle materials whose failure mode is at right angles to the direction of maximum principal stress. Establishing the failure modes in lap joints bonded with brittle adhesives, Adams et al. [5] extensively used this criterion with success to predict joint strength. However, because of the singularity of stresses at re-entrant corners of joints, the stresses depend on the mesh size used and how close to the singular points the stresses are taken. Although the criterion is sensitive to the mesh size used, the physical insight into the failure process is very clear, as the maximum principal stress is the most responsible for the failure of joints bonded with brittle adhesives.

von Mises proposed a yield criterion, which states that a material yields under multi-axial stresses when its distortion energy reaches a critical value. This criterion was used by Ikegami et al. [110] to study the strength of scarf joints between glass fibre composites and metals. Hashim et al. [90] also used the von Mises criteria, at a prescribed distance from the point of singularity to predict joint strength, and to deduce scaling effect in pipes. It should be noted that this criterion is more applicable to material yielding than strength.

Shear stresses have been extensively used to predict lap joint strength, especially in closed-form analyses, considering a limiting maximum shear stress equal to the bulk adhesive shear

strength. These are also described here for a complete description of the continuum mechanics approach.

John et al. [111] used shear stresses with a critical distance to predict the strength of double lap joints. Lee and Lee [112] also used the maximum shear stress in tubular joints. da Silva et al. [113] showed that for single lap joints, this criterion is only valid for brittle adhesives and short overlaps. This approach ignores the normal stresses existing in lap joints.

When ductile adhesives are used, criteria based on stresses are not appropriate, because joints can still endure large loads after adhesive yielding. For ductile adhesives, Adams and Harris [107] used the maximum principal strain as failure criteria for predicting the joint strength. This criterion can also predict the failure mode. da Silva et al. [113, 114] have shown, for single lap joints, that the maximum shear strain criterion is very accurate for ductile adhesives. Crocombe [115] studied the failure of cracked and un-cracked specimens under various modes of loading, and used a critical peel stress at a distance from the singularity with some success. A critical damage zone has been suggested as an alternative criterion. Clark and McGregor [116] proposed that cohesive failure could be predicted when the maximum principal stress over a finite length exceeds the adhesive's allowable tensile stress. However, it was found for the latter criterion, the critical distance at which it should be applied varied with different modes of loading, because of the change in the plastic zone size. No general criterion for a given adhesive was presented. As most of them are dependent on parameters such as adhesive thickness, overlap length and adherend thickness, no general criterion of failure is available within these methods.

The strain energy is the area under the stress-strain curve. Therefore, both stress and strain criteria can be related to strain energy. However, it should be noted that criteria based on strain energy take account of all the stress and strain components. As a result, they are more suitable as a failure criterion than either stresses or strains alone.

2.10.2 Damage mechanics approach

Generally fracture mechanics is suitable for showing separation due to the separation of two parts of the continuum, and is related to a crack which has been initiated and has known locations in the continuum. When the location of crack initiation and its propagation direction are unknown, fracture mechanics cannot be applied, as determining the crack propagation from which cracking initiates is required. Damage mechanics is suitable to predict the location of this critical flaw [117].

The damage mechanics approach permits the simulation of step by step damage and fracture at a pre-defined crack path, or arbitrarily within a finite region, up to complete structural failure [118]. However, this approach is still under development, regarding more accurate modelling techniques, simple parameter determination methods, increase of toughness and elimination of convergence issues [119], and it is also under heavy operation in commercial FEA software packages such as ABAQUS [120]. The techniques for damage modelling are limited to a zero volume line or surface, allowing the simulation of an interface failure between materials, e.g. between the adhesive bond and the adherend [121], the interlaminar failure of stacked composites [122] or the interface between solid phases of materials [123]. Also, the damage is modelled over a finite region, within solid finite elements of structures to simulate a bulk failure [124] or along an adhesive bond to model a cohesive fracture of the adhesive bond [125].

2.10.2.1 Cohesive zone model

The cohesive zone model (CZM) regards fracture as a gradual phenomenon in which separation takes place across an extended crack tip, or cohesive zone and is resisted by cohesive tractions [17]. Thus, cohesive zone elements do not represent any physical material, but describe the cohesive forces which occur when material elements (such as adhesive) are being pulled apart. Therefore cohesive zone elements are placed between the adherends, and the implementation and calibrations of the models is mainly via FEA. The main asset of this approach is that it mixes the stress-based approach used to model the elastic range with the energy fracture approach used to model the degradation of the adhesive properties.

An alternative method to linear elastic fracture mechanics (LEFM) exists in the form of CZM technique, which was first formulated by Dugdale and Barenblatt (1960 & 1962 respectively) [126, 127]. This approach works by collating tractions (T) and displacement jumps (Δ) across cohesive surfaces on a crack line into which the fracture process has been combined. This relation works with the increase in separation across relative surfaces, meaning an increase in traction before a maximum traction is obtained (peak cohesive strength, σ_0), which is then followed by a softening curve describing the post-peak behaviour that eventually vanishes, allowing for traction-free crack surfaces to be created [128]. The process of using CZM originates from the 1960's; however, with the advances in modern FEA software, this technique is gaining momentum in terms of applicability and use in the field of progressive damage mechanics. An important aspect to the successful

implementation of a CZM involves the determination of the traction-separation relation used. This incorporates fracture parameters such as the fracture strength, σ_0 , and the relevant fracture energy which is specific to the mode of loading. Due to the complexities faced in trying to obtain accurate values for the respective peak strength and fracture energy, many workers in this field have opted to compare these fracture parameters with idealised numerical simulations in order to achieve a best fit (Blackman et al [129], Liljedhal et al [119] and Alfano [128]). The most common traction-separation relations that have been developed are the bilinear model, the exponential model and the trapezoidal model [128, 130] as shown in Figure 2.18.

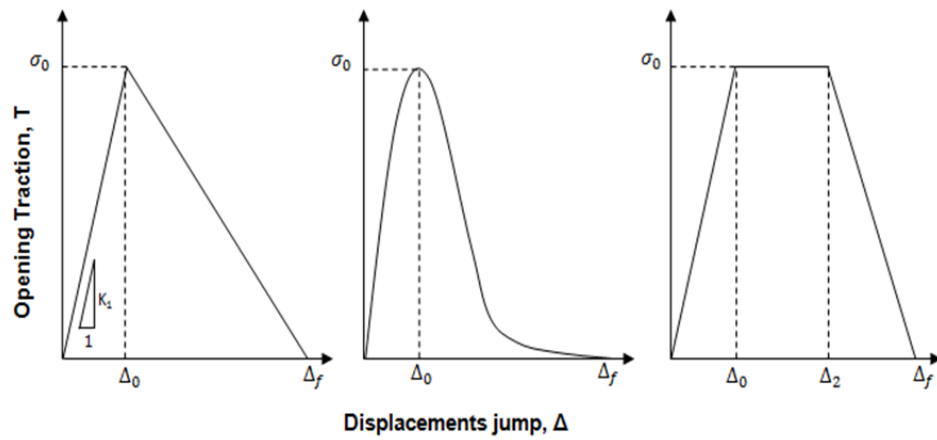


Figure 2.18: Schematic of bilinear, exponential and trapezoidal CZM [128]

Where σ_0 represents the peak stress of the traction-separation relation, which has been argued to be of the same order as the tensile yield stress of the material used for the mode I loading case, which is something which will be analysed later in this report, when considering the mode I loading of the double cantilever beam (DCB) specimen [119]. The subsequent critical displacement jump at the peak stress is shown as Δ_0 , with the resultant failure point seen as Δ_f (for the trapezoidal relation an extra displacement point, Δ_2 , is added at the end point of an additional plateau in the softening region, which aims to capture the softening behaviour in more detail in order to represent the ductility of the material more adequately).

In FEA, the cohesive zone model is represented by cohesive elements to connect the two surfaces of materials. Normally this connection is achieved by boundary constraint or sharing common nodes. In the simulation, cohesive elements hold the surfaces together until

the stress value at any cohesive element reaches the critical value to initiate the crack, and then complete the failure.

The cohesive zone model is a great tool to simulate the initial crack and crack propagation along the interface between materials. Researchers determine cohesive zone parameters in several ways. In the beginning, researchers assumed the values of parameters depending on which value could make the best results compared with the test results. Later, Yang et al. determined these parameters via DCB or end notch flexure (ENF) experiments, but needed to compare their results with tests of bulk materials [121]. This typical approach was also applied by Andersson and Stigh [131]. Liljedahl et al. used the cohesive zone for their mixed-mode flexure (MMF) simulation via determination of the initial traction stress from the test curve of load-displacement, then determining the fracture energy by correlation of the predicted failure load with the experimental failure load [119].

In this work, the sensitivity of the bilinear CZM parameters are tested for an adhesive joint consisting of a DCB specimen in order to monitor crack initiation and propagation using the British Standard (BS 7991:2001) [132]. Also, an end notched flexure (ENF) test was used to determine the parameters of mode II. These help to find the model parameters before implementing them into the double lap shear joint model.

2.10.2.2 Determination of cohesive zone parameters

Finite element analyses that include CZM techniques offer a powerful means to account for the largely nonlinear fracture behaviour of modern adhesively bonded joints, but the CZM parameters require careful calibrations by experimental data and respective validation in order to accurately simulate the failure process. Despite this fact, standardised methods for the definition of the critical stresses are not yet available. In recent years, many works have been published regarding the definition of the CZM parameters (G_{IC} , σ_0 and G_{IIC} , τ_0 in Mode I and II, respectively) and a few data reduction techniques are currently available (e.g. the property determination technique, the direct method and the inverse method) that enclose varying degrees of complexity and expected accuracy of the results.

By the direct method, the complete CZM law and the respective shape for a given material strip or interface can be precisely estimated by differentiation of the $G-\Delta$ curve [131]. The most commonly used experimental set-ups in order to measure Mode I and Mode II cohesive laws are the DCB and the ENF test, respectively, as shown in Figure 2.19. Ji et al. [133] measured the Mode I cohesive laws of a bonded DCB joint, trying to provide data for the

parameter calibrations in numerical models, and also to investigate the relation between adhesive thickness and interface toughness. The same authors [134] have conducted experiments for measuring the Mode II cohesive laws by testing bonded ENF specimens. In both cases LOCTITE Hysol 9460 was utilised as the adhesive material system.

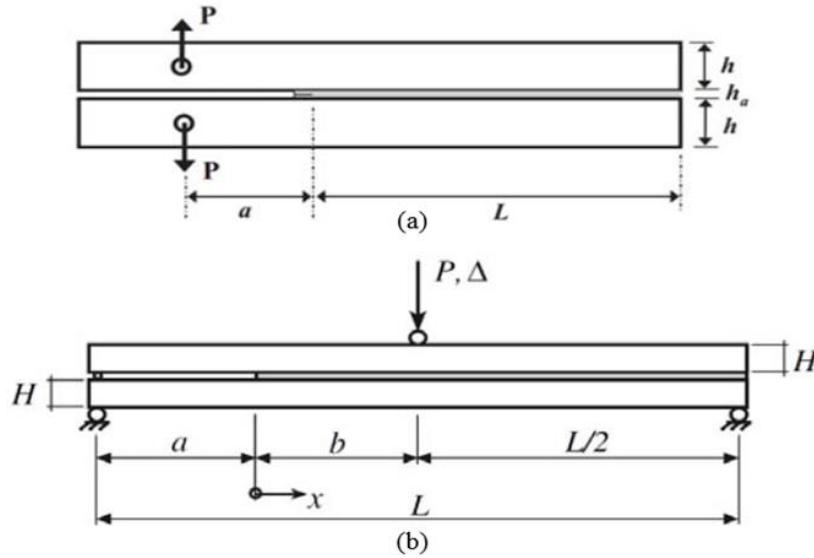


Figure 2.19: Double Cantilever Beam (a) and End Notch Flexure (b) specimens for measurement of the pure Mode I and II cohesive laws

Andersson et al. [131] used a direct method to determine the continuum CZM parameters in Mode I of a ductile adhesive bond of Dow Betamate® XWI044-3 in a DCB test configuration, after approximation of the $G-\Delta$ data to a series of exponential functions to reduce errors in the measured data. In the work of Carlberger et al. [135], the continuum CZM laws of a thin bond of a ductile adhesive (Dow Betamate® XWI044-3) were determined in tension and shear using the DCB and ENF test configurations, respectively. The values of G_{IC} and G_{IIC} were derived by a J-integral formulation to accurately capture the large plastic straining effects present at the crack tip of the ductile adhesive [136].

For the measurement of mixed mode cohesive laws, different experimental set-ups have been used. Efforts have been made to find a test set-up that will allow testing under the full range of mode-mixed, which means from pure Mode I to pure Mode II, with just one type of specimen geometry. One of the most used experiment set-ups is the Mixed Mode Bending (MMB), shown in Figure 2.20, providing an easy variation of the mode ratio by just altering the lever length of the loading lever [137]. The MMB test can be considered as a

superposition of the DCB and the ENF tests, used for the fracture characterisation of pure Mode I and pure Mode II, respectively.

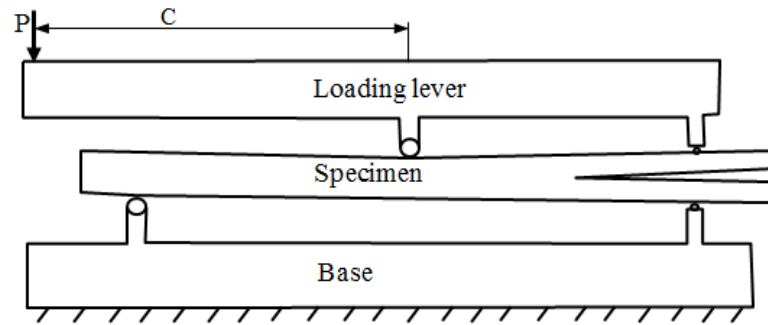


Figure 2.20: Mixed Mode Bending specimen [137]

Apart from the MMB specimen, other configurations have also been used. A promising one was presented in Choupani [138], where the author used modified Arcan specimens. This test set-up consisted of various combinations of adhesive, composite and metallic adherents with a special loading fixture, in which by altering the loading angle, a full range mode mixity loading was achieved. Choupani [138] was able to obtain Mode I, Mode II and mixed mode fracture data, and perform numerical analyses of the experiments, and almost any combination of Mode I and Mode II loading, to be tested with the same test specimen configuration. His main goal was to determine the stress intensity factors K_{IC} and K_{IIC} and then derive formulas for the derivation of energy release rates G_{IC} and G_{IIC} . Figure 2.21 shows the experiment set-up with modified Arcan test.

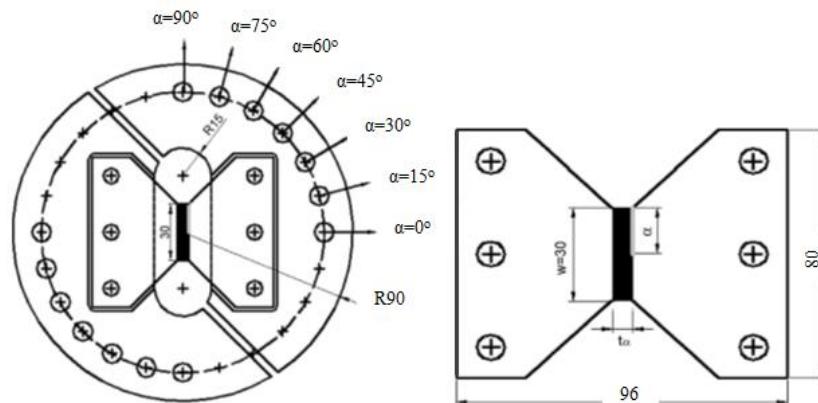


Figure 2.21: Modified Arcan test specimen and loading fixture [138]

By the inverse method, using an iterative curve fitting procedure between experimental data and the FEA predictions, considering a precise description of the experimental geometry and approximate cohesive laws, can be established based on the typical behaviour of the material to be simulated [139]. The inverse characterisation of adhesive bonds should be applied individually for each tested specimen to account for slight geometric variations between specimens [140]. By this technique, the value of G_{IC} or G_{IIC} - which corresponds to the steady-state value of G_I or G_{II} during crack propagation in the respective R-curve built from the fracture characterisation test data - is input in the FE model. To define the other parameters of CZM law, approximate bulk values can be used for the cohesive strength in tension and shear σ_o and τ_o respectively for the initiation of the trial and error iterative process [140, 141]. Tuning of the cohesive parameters is performed by a few numerical iterations until an accurate prediction of the experimental data is achieved. Examples of reliable experimental data for the iterative fitting procedure are the crack opening profile [142], and more commonly, the P- Δ curve [143].

2.11 Comparing cohesive zone model with strength of material approach

On the strength prediction of adhesive joints, two different methods of analyses were developed over the years: the strength of materials and fracture mechanics-based methods. The strength of materials approach is based on the evaluation of allowable stresses [144, 145] or strains [146], by theoretical formulations or numerical analysis, especially in FEA. The joint strength can be predicted by comparing the equivalent stresses or strains at the critical regions, obtained by stress or strain-based criteria, with the properties of the structure constituents. These criteria are highly mesh dependent, as stress singularities are present at the end of the overlap region due to the sharp corners [147, 148, 149].

As for fracture mechanics, using LEFM, an inherent flaw is required for the calculation of the stress intensity factor or strain energy release rate [150, 151, 152]. However, LEFM can only be used with the assumed presence of an initial crack concurrent with a relatively small size of the non-linear zone at crack tip, compared to the overall dimensions of the specimens.

The limitations of the reported approaches are surpassed by CZM, combining elements of strength and fracture approaches to derive the fracture loads [152, 153] .

The main advantage of CZM is related to their ability to simulate crack initiation and propagation damage without the requirement of an initial flaw, unlike classical fracture mechanics approaches.

An important feature of CZM is that they can be easily incorporated in conventional FEA software to model the fracture behaviour in various materials, including adhesively bonded joints [133, 154]. CZM is based on the assumption that one or multiple fracture interfaces/regions can be artificially introduced in structures, in which damage growth is allowed by the introduction of a possible discontinuity in the displacement field. To date, CZM has been successfully applied to model fracture for a wide class of materials, e.g. metals, concrete, polymers, ceramics, composites [124, 143, 155, 156], and its range of applications continue to expand.

2.12 Failure mechanisms of composite adhesive joint

The major failure types are shown in Figure 2.22. Specifically, cohesive failure is obtained if a crack propagates in the bulk polymers which represent the adhesive, and as such, is evident when adhesive remains on the surfaces of both the adherends after the debonding.

The crack may propagate in the centre of the layer or near an interface. In the last case, the failure can be said to be ‘cohesive near the interface’. Most quality control standards consider a good adhesive bond to be cohesive [60].

The failure is adhesive or interfacial when debonding occurs between the adhesive and the adherend in most cases, the occurrence of interfacial fracture for a given adhesive going along with lower fracture toughness. Other types of fracture include the mixed type, which occurs if the crack propagates at some spots in a cohesive, and in others in an interfacial manner, the alternating crack path type which occurs if the crack jumps from one interface to the other.

There are several reasons which contribute to the escape of the crack out of the adhesive and lead to cohesive/interfacial failure. The most common is reduced bonding quality, usually caused by insufficient treatment of the adherends’ surface, or by physio-chemical incompatibilities between the composite and the adhesive. In addition, the higher through – thickness tensile strength of the laminate, compared with that of the adhesive laminate, compared with that of the adhesive/laminate interface, is also a possible reason for moving the failure location outside the adhesive [157].

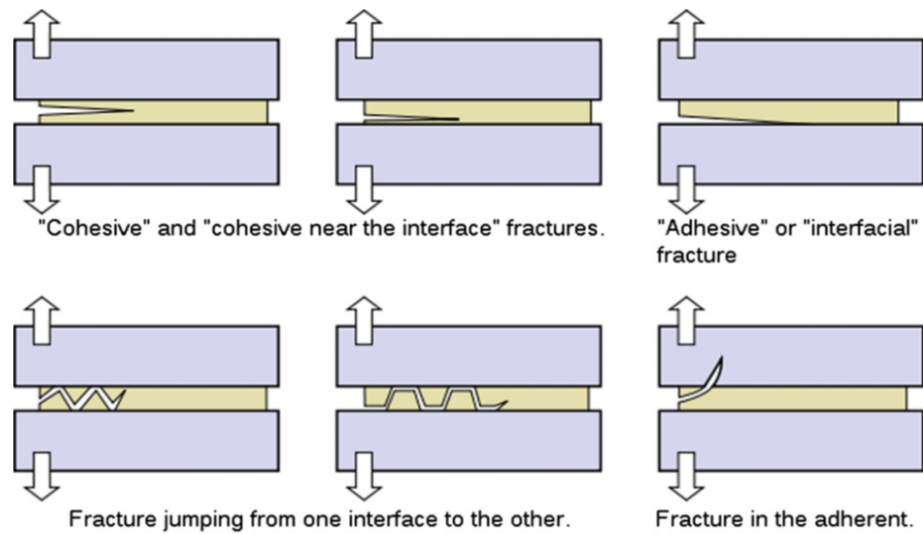


Figure 2.22: Major fracture types [60]

The failure in adherends is dependent on a variety of factors. This is where the adherend used fails before the adhesive layer. Generally this is caused by using materials that have less strength than the adhesive bond. When a composite is used in an adhesive joint, composite laminates are subjected to different types of failure. The fracture process is quite complex and involves intralaminar damage mechanisms, such as matrix cracking or fibre fracture, and interlaminar damage, which is delamination.

Zhao and Zhang [158] explained the possible failure modes associated with bonding of FRP composite to a steel system subjected to a tensile force. These failure modes are shown in Figure 2.23 and can include:

- (a) Interfacial debonding between the steel and adhesive layer,
- (b) Failure of the adhesive layer,
- (c) Interfacial debonding between CFRP and the adhesive layer,
- (d) Delaminating of CFRP composites,
- (e) Rupture failure of CFRP composites,
- (f) Yielding of steel members.

Failure mode type (b) is a common failure which is usually associated with a low quality adhesive layer. Failure mode type (d) can happen when there is a separation of carbon fibres from the resin matrix of CFRP, which means low elastic modulus CFRP composite, while failure mode type (f) rarely happens because there is usually a sufficient thickness of the

steel member. So, elastic modulus of CFRP, elastic modulus of steel, and the quality of adhesive material can all affect the failure mode of this technique.

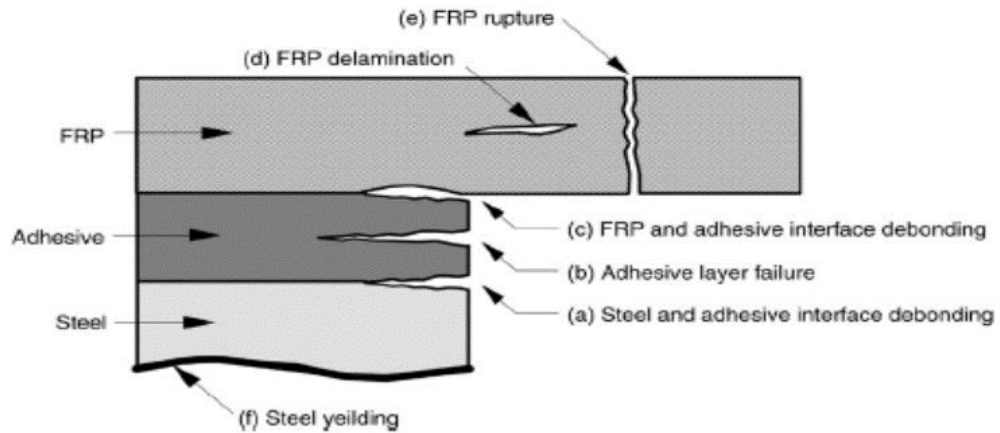


Figure 2.23: Possible failure modes in a CFRP bonded to steel system [158]

The study of delamination is usually approached by the analysis of its two components: the onset of delamination and its propagation when already started. Analysis of the first point is based on study of the interaction of the interlaminar stresses, whereas, in prediction of the propagation, fracture mechanic approaches are usually considered, in order to avoid problems due to the singularity of the stresses in the tip of the crack.

2.13 Delamination failure of composite

Delamination failure is generally accepted as the most common mode when failure occurs in the laminated composite adherend. Experimental tests and theoretical analyses have been carried out for a wide range of composite laminated structures, including glass reinforced polyester, glass reinforced epoxy, carbon reinforced epoxy, etc. Standard tests, such as lap shear and double lap shear tests, are used to identify the strength of simple joints in composite materials, and are well documented [65].

The remaining dominant characteristic of adhesive-bonded joints is the peel stress, developed in association with the shear stresses. Like the shear stresses, these peak at the ends of the joint. While this phenomenon has long been known for single-lap joints, it is only recently that its impact on inducing laminate failures in thick double-lap joints has been recognised. The low interlaminar tension strength of composite laminates limits the thickness of the adherends which can be bonded together efficiently by lap joints. The

interlaminar splits apart locally due to peel stresses, thereby destroying the shear transfer capacity between the inner and outer plies. This overloads the outer filaments, which break in tension, and the failure progresses as portrayed [73] in Figure 2.24.

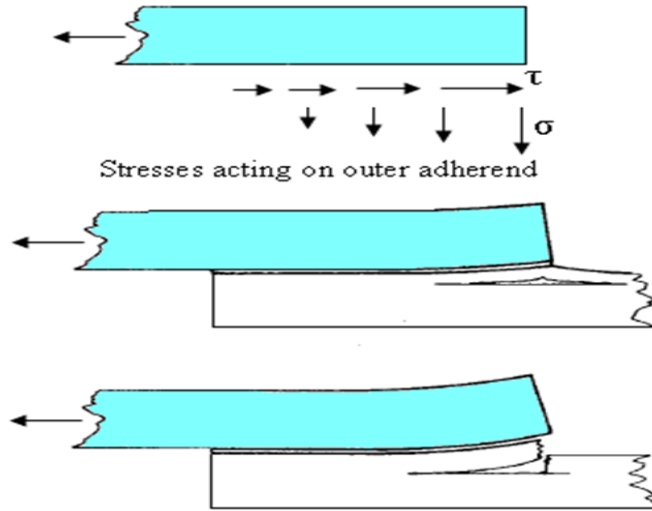


Figure 2.24: Stages of delamination failure [73]

Understanding of failure mechanisms and behaviour in composite bonded joints is important for accurate and reliable failure prediction. Failure prediction requires complete understanding of failure initiation, growth and modes. Finite element analysis (FEA) with a suitable failure criterion can be used for predicting the failure initiation of laminate composite structures. Different failure criteria have been reported for joints and are active in the literature, e.g. Maximum Stress or Strain criteria, Tsai-Hill, Tsai-Wu and the Hashin failure criteria etc. (see Appendix E).

In 1967, Hayashi proposed the first analytical model to compute the interlaminar shear stresses [159]. Then, much research has been devoted to this problem, and focused on the calculation of edge effect stress field and the development of failure criteria [160]. Basically, there are two distinct approaches to predict the delamination onset in laminated composites, one related to mechanics of materials, and the other related to fracture mechanics. The mechanics of materials approach is based on local three-dimensional stress analysis in conjunction with stress-based failure criteria [161, 162]. The development of analytical and numerical solution techniques to calculation of interlaminar stresses at free edges has made stress analysis more convenient. However, because of a weak interlaminar stress singularity at free edges, an average stress approach, similar to [163] for the strength of notched

composites, must be adopted by averaging interlaminar stress components over a characteristic length from the free edges. Usually, the characteristic length is viewed as a material constant, even though it seems to be dependent on the laminate's configurations [164]. Moreover this approach suffers from the difficulties in measuring the interlaminar strength components.

The fracture mechanics technique is based on the assumption that delamination is modelled as an edge crack, and thus either stresses the intensity factor or strain energy release rate, which can be determined by the classical elasticity approach to be compared with their critical values [165]. Due to the difficulties in computing the interlaminar stress intensity factor, the strain energy release rate approach is more popular. The advantage of the strain energy release rate approach is that there have been convenient test methods to reliably measure the critical values for all the three interlaminar fracture modes, and no critical length is required to characterise interlaminar stress concentrations. This approach can also be extended to predict delamination growth, because the strain energy release rate remains nearly constant during delamination propagation [166, 167]. For instance, laminated composites can further carry loads beyond the free edge delamination onset which is caused by the interlaminar normal stress component [168], while a disintegration failure of laminated composites takes place immediately after delamination onset which is caused by the interlaminar shear stresses [169]. Also, experimental results indicate that matrix transverse cracks subsequently occur after delamination onset, and are followed by the simultaneous growth of transverse cracks and delamination areas [170]. Delamination growth depends on the mixed-mode strain energy release rates G_I , G_{II} and G_{III} governed by the stress state at the crack tip. Under static loading conditions, the generation of new surface area at initiation could be evaluated by some failure criteria in terms of three distinct fracture modes of strain energy release rates and their corresponding critical values [171, 172, 173, 174]

2.14 Summary of the literature review

Hybrid assembly combines the structural and architectural features of components made from different materials. In hybrid assembly, various materials may work independently or act together homogeneously, but are always better than a single material. The advanced materials, such as carbon fibre reinforced polymer (CFRP) composite laminates are being

used in aerospace, marine and automotive components. These materials are providing opportunities to reduce component weight and connections between components. Previous research on systems consisting of FRP bonded to steel indicates that the adhesive bond is the most important design concern. Because of the high strength and rigidity of steel, CFRP may be more effective in strengthening steel structures compared with other FRP materials, due to its higher strength and rigidity.

Having reviewed the literature relating to adhesive bonding for composite materials, there is a lack of available resources pertaining to adhesive joining of CFRP/steel. With the development of these materials for use in structural applications, an understanding of their bonded behaviour is necessary. The double lap shear joint (DLS) was used in the investigation, as there is an established understanding of the expected behaviour of the hybrid joints with regard to metallic and composite adherends. However, understanding of the performance of hybrid joints in structural engineering applications is important to the successful design of adhesive connection. This will be addressed through test evaluation of static performance under tensile loads. The joint assessment cannot be completed without the detailed understanding of the fracture mechanics used to measure the mechanical properties of the adhesive joints. The stress analysis of adhesive joints further enhances the full understanding of how the joints behave when subjected to a different loading conditions, and where the failure is likely to be initiated, due to various stress distributions.

The mechanical method used consists of performing a test that describes the damage initiation, and another energy parameter to describe the damage propagation. This damage initiation and damage propagation is called the traction separation law. The tests that are used in this work to identify the traction-separation laws of the adhesive used are the DCB and ENF test. Once the traction-separation laws have been obtained, it is possible to simulate and predict the behaviour of adhesively bonded specimens.

Mechanical strength modelling may be based on strength of materials, fracture mechanics or continuum damage mechanics failure criteria. A number of studies of joint strength prediction, based on various methods of modelling, have been presented in the literature.

In the literature, most workers highlight variations of joint strength with overlap length, adherend thickness and surface preparation before bonding. In addition to this, the layup and stacking sequence of adherends and other parameters are studied in many different ways,

but further research is needed to improve joint design and increase the strength of the adhesively bonded joints.

The analysis and design of adhesively bonded joints is not complete. However, for the effects of design parameters on the joints' failure, very few models can predict failure and damage evaluation.

The numerical methods are based on 2D models, using strength-limit and cohesive zone modelling methods, taking into consideration the composite properties of the plies and the resin layers separating them. Although these approaches have been used in some areas of engineering applications, especially automotive structures, the current research is more relevant to thick-adherend hybrid connections, where the scale and behaviour are markedly different from standard bonded constructions. Large structures can benefit greatly from the reliability and computing economy associated with cohesive zone modelling stress analysis.

Chapter 3

3 Experimental work (Material properties)

3.1 Introduction

This chapter introduces the materials and joints studied in this thesis. The main experimental techniques and loading spectra used will also be discussed. These analytical and experimental procedures on materials were used in this work to obtain essential mechanical properties. The main materials used in this research are carbon fibre reinforced (CFRP) composite, epoxy adhesive Araldite 2015 and mild steel. The main constituent materials used in the fabrication of CFRP laminates are based on carbon fibre and epoxy resin. Since a composite material is not isotropic, it is impossible to predict exact properties, as there are too many variables. The rule of mixtures Tsai and Hahn relationships are used to determine the material properties. In this chapter two types of experimental tests are used. The adhesive properties are based on previous work at Glasgow University [175] in addition to a standard steel butt joint and thick adherend shear test. The main focus of the experiments in this chapter is related to fracture mechanics, and dedicated to the characterisation of the damage and fracture behaviour of adhesives (Araldite 2015) and the matrix epoxy resin (Araldite LY3505/XB3405).

3.2 Composite material properties

Carbon fibre can be classified into different categories based on modulus, strength and final heat treatment temperature. The selection of any polymer system will be a function of the design criteria including operating environment, cost, fibre type and manufacturing method. The main constituent material used in the fabrication of CFRP composite is based on carbon fibre as a reinforcement and epoxy resin as a binder.

Cross ply carbon fibre/epoxy composite laminate was used as the material in this work, joined adhesively with mild steel. The cross ply composite laminates were produced and

supplied by the Norwegian Defence Research Establishment (FFI), Norway. These were produced by infusion molding of lightly stitched UD high strength carbon fibre mats/plies and epoxy resin.

3.2.1 Resin system - Epoxy resin LY3505/Hardener XB3405

Epoxy resin LY3505 with hardener XB3405, manufactured by Huntsman Advanced Materials [176], was used for the coupon manufacture. The manufacturer's recommended resin / hardener ratio is 100:35 (see Appendix A). The reaction between these two components, classified as an amine/epoxy reaction, enables the resin system formulation to be adjusted to give a wide range of properties. The properties of this system are presented in Table 3.1, using a fast hardener (XB3405) type. The choice of hardener determines the final mechanical properties of the mix, as shown in Table 3.1, as it was not a requirement to optimise the mechanical properties of the parts.

Table 3.1: Properties for LY3505 epoxy with hardener XB3405 [176]

Matrix systems	LY3505/XB3405
Mix ratio by weight	100:35
Gel time at 60°C, (min)	18-26
Tg (glass transition temperature), (°C)	87-92
Tensile modulus, E_m (GPa)	3.5-3.9
Poisson's ratio, ν_m	0.35
Tensile strength, Y_{mT} (MPa)	80-90
Ultimate elongation, ϵ_{mT} (%)	5.0-6.2
Density at 25°C, (g/cm ³)	0.95-1.2

3.2.2 Fibre properties

Cross ply carbon fibre/epoxy composite laminate was chosen as the material to be studied in this work, joined adhesively with mild steel. The mechanical properties of the carbon fibre have been obtained from the relevant manufacturers and literature data [177], as provided in Table 3.2. The modelled fibre properties contribute to the mechanical properties of the composite in the fibre direction only. Therefore, the mechanical properties of the modelled matrix include contributions from the resin and fibre in the remaining transverse directions. Classical laminate analysis has been used to obtain the required transverse ply properties, but first requires the fibre volume fraction to be a known quantity. In this work, the rule of

mixtures is used to calculate the composite properties based on the volume fraction of carbon fibre and resin, which are 60% and 40% respectively.

Table 3.2: Properties of single carbon fibre [177]

Fibre type	High Strength
Longitudinal modulus, E_{f1} (GPa)	230
Transverse modulus, E_{f2} (GPa)	15
In-plane shear modulus, G_{f12} (GPa)	15
Major Poisson's ratio, ν_{f12}	0.2
Transverse shear modulus, G_{f23}	7
Longitudinal tensile strength, X_{fT} (MPa)	2500

3.2.3 Unidirectional composite material coordinates

Unidirectional fibres are the simplest arrangement of fibres to analyse. The basic element of a unidirectional composite is a thin sheet (ply). They provide maximum properties in the fibre direction, but minimum properties in the transverse direction. By convention, the principal axes of the ply are labelled '1, 2, and 3'. This is used to denote the fact that ply may be aligned differently from the Cartesian axes x, y, z . Material axes are defined as follows:

- Longitudinal direction (1) – parallel to fibres
- Transverse direction (2) – perpendicular to fibres in plane
- Through thickness direction (3) – out of plane

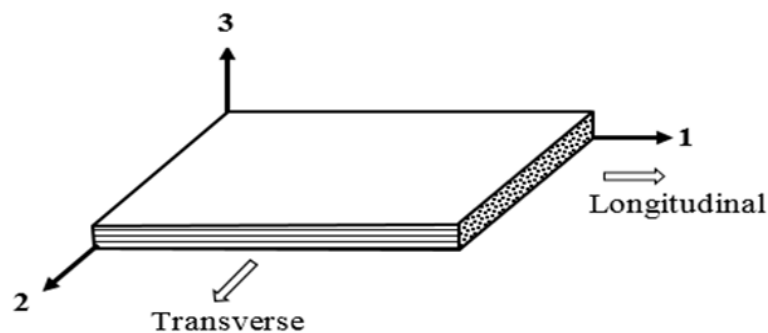


Figure 3.1: Composite ply coordinate system

3.2.4 Rules of mixture

Rules of Mixtures are mathematical expressions which give some property of the composite in terms of the properties, quantity and arrangement of its constituents. It is one of the ways to estimate composite material, by summarising the properties of the individual constituents based on their contribution to the overall material volume. In the case of a continuous fibre-reinforced composite layer, a fibre volume fraction V_f and a matrix volume fraction V_m , must satisfy.

$$V_f + V_m = 1 \quad (3.1)$$

The values for the volume fractions of the components can be used to make estimations on the longitudinal and transverse Young's modulus, Poisson's ratio and shear modulus of the corresponding composite. The procedures to make these calculations are given below.

The longitudinal elastic modulus E_l of the composite lamina can be calculated from the Young's moduli of the constituents E_{f1} and E_m , using the rule of mixtures as follows:

$$E_l = E_{f1}V_f + E_mV_m \quad (3.2)$$

The Poisson's ratio (ν_{12}) of an unidirectional reinforced composite can be calculated by the following formula:

$$\nu_{12} = \nu_f V_f + \nu_m V_m \quad (3.3)$$

Where:

E_{f1} is the longitudinal modulus of elasticity for the fibres

E_m is the modulus of elasticity for the matrix (resin)

V_f is the volume fraction of the fibres

V_m is the volume fraction of the matrix (resin)

Tsai and Hahn stress that a partitioning parameter [178] is used for better value estimation in transverse directions. The transversal modulus of elasticity E_2 can be calculated using the following equation:

$$E_2 = E_m \frac{V_f + \eta_y V_m}{\eta_y V_m + V_f E_m / E_{f2}} \quad (3.4)$$

E_{f2} is the transverse modulus of elasticity for the fibres.

Shear modulus G_{12} and G_{23} can be calculated using the following expressions:

$$G_{12} = G_m \frac{V_f + \eta_s V_m}{\eta_s V_m + V_f G_m / G_{f12}} \quad (3.5)$$

$$G_{23} = G_m \frac{V_f + \eta_G V_m}{\eta_G V_m + V_f G_m / G_{f23}} \quad (3.6)$$

Where:

- Volume fraction of matrix

$$V_m = 1 - V_f \quad (3.7)$$

- Shear modulus of matrix.

$$G_m = E_m / 2(1 + \nu_m) \quad (3.8)$$

Stress partitioning parameters η_y , η_s , and η_G are the additional parameters in the rule of mixtures to measure the accurate transverse properties of laminate introduced by Tsai and Hahn [178]. η_y , η_s and η_G are calculated through the relation:

$$\eta_y = 0.5(1 + E_m / E_{f2}) \quad (3.9)$$

$$\eta_s = \frac{3 - 4\nu_m + G_m / G_{f12}}{4(1 - \nu_m)} \quad (3.10)$$

$$\eta_G = \frac{3 - 4\nu_m + G_m / G_{f23}}{4(1 - \nu_m)} \quad (3.11)$$

Tsai and Hahn used the assumption of transversely isotropic material for calculating the other transverse properties like $E_2 = E_3$, $\nu_{13} = \nu_{12}$, $G_{12} = G_{13}$, and G_{23} , ν_{23} is given by the relation.

$$G_{23} = E_2 / 2(1 + \nu_{23}) \quad (3.12)$$

$$\nu_{23} = E_2 / (2G_{23}) - 1 \quad (3.13)$$

The CFRP lamina properties using the rule of mixtures, Tsai and Hahn, and transversely isotropic materials assumption, as mentioned above, are tabulated in Table 3.3. The values in this table are calculated from equations (3.1-3.13) by using the materials properties in Table 3.1 and Table 3.2.

Table 3.3: Material properties of CFRP laminate

Property		CFRP laminate
Young's modulus (GPa)	E_{11}	139.4
	$E_{22}=E_{33}$	7.66
Shear modulus (GPa)	$G_{12}=G_{13}$	3.68
	G_{23}	2.94
Poisson's ratio	$\nu_{12}=\nu_{13}$	0.26
	ν_{23}	0.304

3.3 Adhesive properties

In this section, selection of the adhesive and its properties used in finite element analysis are all discussed. Clearly, the use of proper adhesive has many advantages to offer, such as it allows excellent joint strength, assemblies of similar and dissimilar adherend, and they can often result in cost reduction [43]. There is no 'universal' adhesive that will bond every substrate together, and so the choice of adhesive is always involved.

3.3.1 Adhesive selection

Araldite 2015, a two parts epoxy paste adhesive, was chosen for adhesive bonding in this research. In general, the epoxy based adhesives offer strong bond strength and exhibit good stability. The two part epoxy adhesives are good candidates for the bonding of composites rather than single part adhesives. The choice of Araldite 2015 was based on the following key properties:

- Ideal for bonding FRP (fibre reinforced polymers) to itself and many other dissimilar adherends.
- Excellent adhesion to metals and thermoset composites.
- It is thixotropic and non-sagging up to 10 mm thickness.
- High shear and peel strength which are particularly important given the nature of the types of tests performed it has low shrinkage properties.
- It can either be cured at room temperature or at elevated temperature.
- Araldite 2015 exhibits good gap filling properties.

Araldite 2015 is stored in a refrigerator controlled at the low temperature of 5°C. The recommended temperature set by the manufacturer is 2-8°C. Shelf life established by the

manufacturer at this temperature is 2 years, and should be replaced within 6 months after being used, prior to the expiry date. The adhesive preparation work requires more care, especially before applying. The adhesive needs to be placed at room temperature for at least 30 min. This process is essential to promote effective adherend surface wetting. Araldite 2015 exhibits good gap filling properties, so the first thin coat of adhesive was applied by a knife- coating procedure, and the following coats by a normal smooth pressure. Bonding pressure on the joint was applied by using specially designed bonding jigs.

3.3.2 Tensile testing of adhesive butt-joint specimens

In order to verify the bulk adhesive results using the steel butt joint, British Standards were used (BS 5250-C3) [179]. The butt joint specimen consists of two steel adherends bonded together at end faces using adhesive. Each butt joint specimen was fabricated and tested (Figure 3.2).

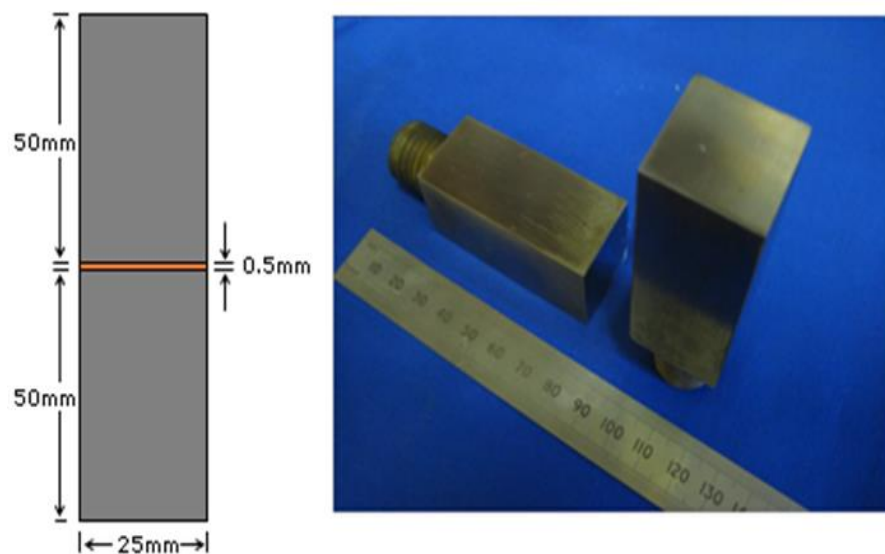


Figure 3.2: Steel butt joint

These were bonded with Araldite 2015 adhesive with 0.5 mm bondline thickness. These were tested under monotonic tensile loading, with a Zwick/Roell tensile testing machine at a constant cross head speed of 0.5 mm/min at ambient temperature. Specimen 2 and specimen 3 have comparable and better strength than specimen 1, as shown in the stress-strain curve of Araldite 2015 (Figure 3.3). Araldite 2015 tensile strength using butt joint gave 35 MPa, much closer to the claim by the supplier (30 MPa). The specimens were tested to failure and the best specimen results were selected. The main reason for this is voids, and

the specimen being defect free. Specimen 1 data was rejected as after testing voids were seen in the adhesive layer. Consequently, the manufacture of joints requires careful control and minimisation of void contents.

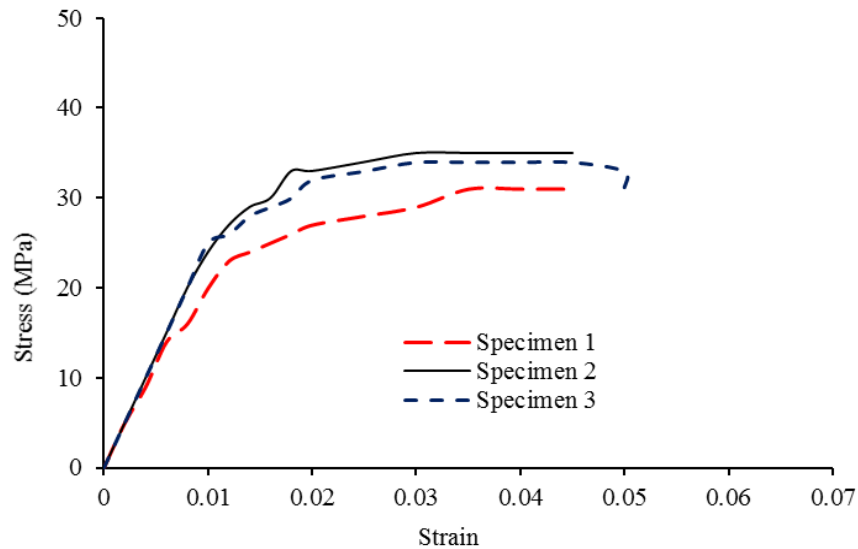


Figure 3.3: Stress strain curves from steel butt joint

3.3.3 Extrapolation of data

Since the adhesive displays both the plastic and elastic regions, these properties had to be included in the finite element analysis.

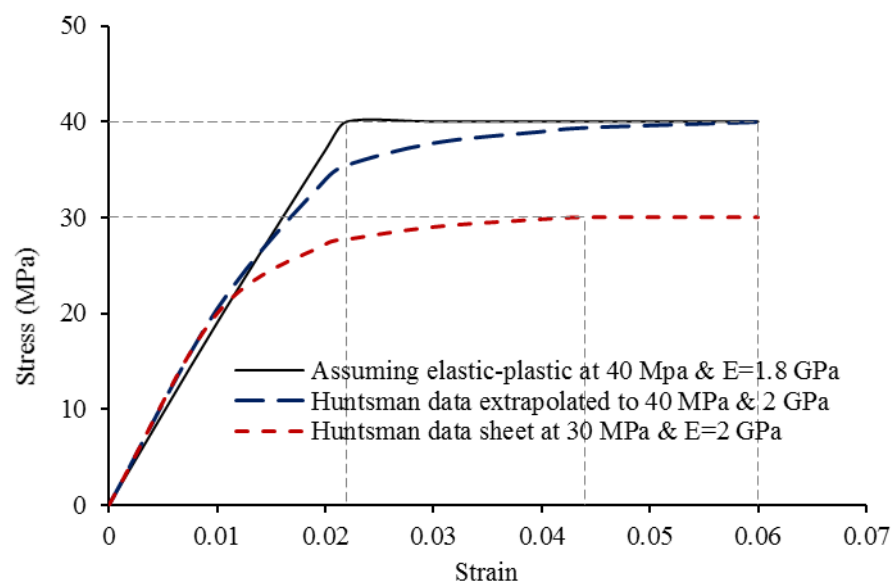


Figure 3.4: Stress-strain curves for Araldite 2015 [175]

Therefore it is necessary to produce elasto-plastic data, based on available test and manufacturer data and relevant engineering assumptions. The stress-strain curve for Araldite 2015, the small dashed line is the true stress-strain curve from the Huntsman technical data sheet (Appendix B) for the stress-strain curve.

In order to calculate the strain at the adhesive failure load, the true curve is extrapolated to 40 MPa. This is the large-dash line. The extrapolated true stress-strain curve is then converted to an elastic-plastic stress strain curve: the continuous line (Figure 3.4 and Table 3.4).

- At 30 MPa, strain is 0.044 (Appendix B -data sheet).
- Properties assuming perfect elastic / perfect plastic at 40 MPa & 1.8 GPa

$$E = \frac{\sigma}{\varepsilon} \quad (3.14)$$

$$\varepsilon = \frac{\sigma}{E} = \frac{40}{1.8 \times 10^3} = 0.022$$

$$\frac{\varepsilon}{40} = \frac{0.044}{30}$$

$$\varepsilon = 0.044 \times \frac{40}{30} = 0.06$$

For the elastic plastic model, the adhesive fails at a stress of 40 MPa. The adhesive is in the elastic region between a strain of 0 and 0.022. After 0.022, the adhesive is in the plastic region, until 0.06, where it fails. Plastic properties are tabulated in Table 3.4. The adhesive elastic properties are quite comparable to the HUNTSMAN Adhesive data sheet, as shown in Appendix B.

Table 3.4: Plastic properties of Araldite 2015

Yield stress (MPa)	Plastic strain
39.999999	0
40.000000	0.022
40.000001	0.044
40.000002	0.060

3.3.4 Thick adherend shear test (TAST)

The thick adherend shear test is a lap shear specimen with high thickness of the steel adherends chosen to determine shear strength. It is prepared in accordance with the standard NF-EN 14869-2 and ISO 11003-2 represented in Figure 3.5. The specimen has an overall length of 155 mm, a width of 25 mm and an overlap length of 5 mm. The adherend thickness is 6 mm and the bondline thickness is typically 0.2 mm.

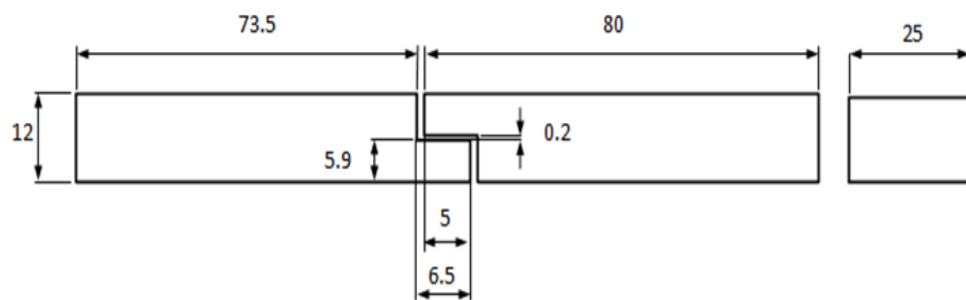


Figure 3.5: Geometry and dimensions (in mm) of the thick adherend shear test

The high thicknesses of the steel adherends make them very stiff, and their shape avoids bending during the load history. This reduces the peel stress in the adhesive joint as well as plastic deformations in the adherends. Preparing a TAST specimen requires perfect control of the geometry of adherends, as well as the application and curing process of the adhesive. Indeed, steel adherends must be milled to ensure a gap of 0.2 mm corresponding to the adhesive thickness. Adhesive must be applied carefully to avoid spew fillets around the small overlap area. In addition, the bonding must be carried without any aligning defect. Finally, the adhesive curing process must also be controlled, since the warming of adherends influences the curing time of the adhesive (1 hour at 80°C). The cured assembly is then ready for testing, as represented in Figure 3.6.



Figure 3.6: Thick adherend shear test specimen

These were tested under monotonic tensile loading with a Zwick/Roell tensile testing machine at a constant cross head speed of 0.5 mm/min at ambient temperature. The load-

displacement curves from the lap shear test and a picture of the specimen at failure are shown in Figure 3.7 and Figure 3.8 respectively.

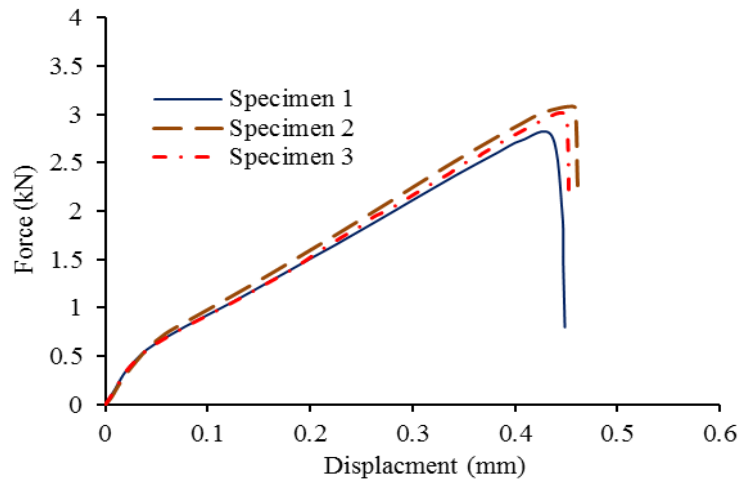


Figure 3.7: Load-displacement curves of the TAST specimen bonded with Araldite 215

The shear stress τ is obtained by:

$$\tau = \frac{F}{bl} \quad (3.15)$$

Where F is the measured force, b is the specimen width and l is the bonded overlap length. The average shear stress computed according to equation (3.15) from three specimens 1, 2 and 3 as shown in the force-displacement curves of Araldite 215 (Figure 3.7). The average shear stress for Araldite 215 adhesive using TAST specimen gave 24 MPa.

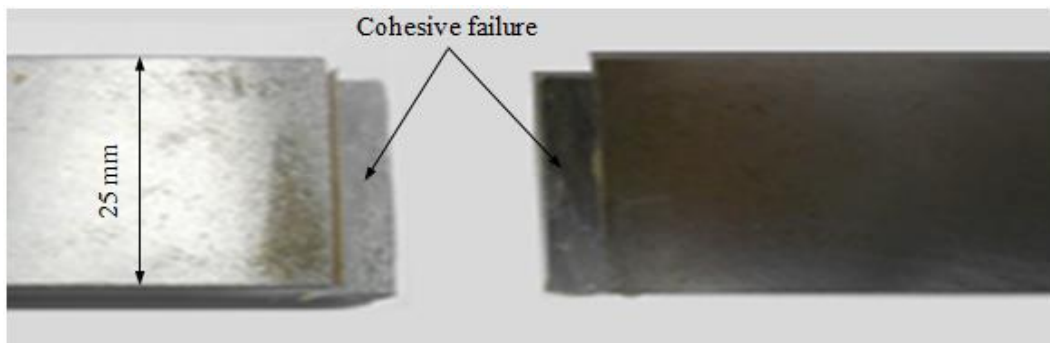


Figure 3.8: Failure of TAST specimen

3.4 Damage and fracture experiments

The following sections focus on experiments issuing from fracture mechanics, and are dedicated to characterisation of the damage and fracture behaviour of adhesive and resin. These tests enables measurement of the fracture resistance of adhesive joints under mode I (tensile) and mode II (in plane shear) conditions, as shown in Figure 3.9. The other mode of fracture is mode III (out of plane shear), which is neglected compared to the two other modes, and generally not studied.

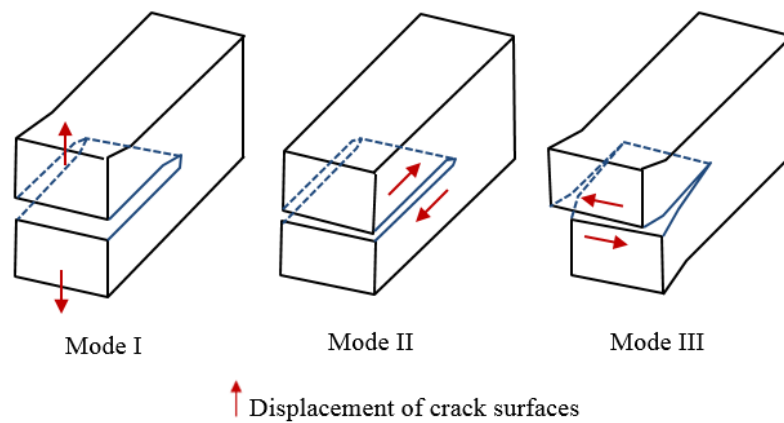


Figure 3.9: Fracture modes

The fracture energy of a particular adhesive experimental method (known as G_{IC} and G_{IIC} for mode I & II respectively) may also be referred to as the critical strain energy release rate or fracture toughness, and hence is a material property of the adhesive [180]. The double cantilever beam (DCB) specimen, as shown in Figure 3.10, is dedicated to the characterisation of the adhesive under mode I loading of fracture, whereas the end notched flexure (ENF) specimen is dedicated to the study of mode II as shown in Figure 3.23.

3.4.1 Double cantilever beam experiments

The double cantilever beam (DCB) test is widely used as an experiment to test the strength of adhesive joints. The method used is based upon the British Standard (BS 7991:2001) [132], in which linear elastic fracture mechanics (LEFM) are used for the determination of the fracture resistance of structural adhesive joints under an applied mode I opening load. The adhesive fracture energy G_{IC} can be calculated in order to produce a resistance to fracture curve (R-curve) i.e. a plot of the magnitude of adhesive fracture energy G_{IC} versus

crack length [132]. Figure 3.10, the basis of the DCB test, is to place two mild steel substrates under a cleavage load to initiate and propagate a crack through the adhesive layer adjoining both substrates, with this adhesive layer being the same thickness as desired for latter purposes in evaluating the DLS joint.

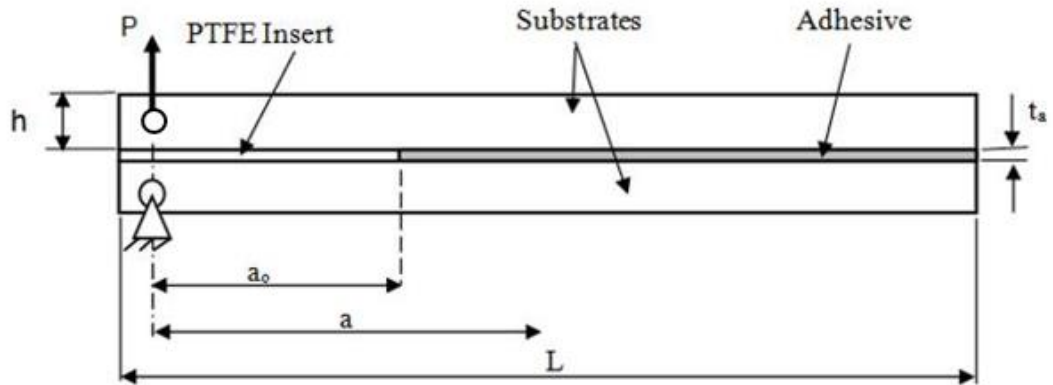


Figure 3.10: Illustration of DCB specimen

Where:

$a_0 = 70$ mm, $L = 200$ mm, $h = 20$ mm, $t_a = 0.2$ mm, and the width = 25 mm. The values of a is parameter measured throughout the test (i.e. crack length measurements).

3.4.1.1 Specimen Preparation

In order to prepare the specimens for use with Araldite 2015 and with resin LY3505/XB3405, one must prepare the surface of each substrate to ensure that the bond achieves suitable strength and durability, as these parameters should be kept to a minimum in order to allow the DCB test to be minimally affected in a negative manner. The grit-blasting allows the surface topography to be roughened in order to increase the mechanical adhesion properties [181]. The use of Acetone to clean the surface will help to reduce the presence of any debris such as grease, chemical contaminates or metal particles from the grit-blasting process. As can be seen from Figure 3.11 a PTFE sheet was used to control the thickness of the adhesive. The adhesive being used is Araldite 2015, in Figure 3.11c before applying a primary layer, followed by a secondary layer of adhesive using a spatula. Once the adhesive had been fully applied, the specimen was then placed into a containment jig, which was used to clamp the substrates together as seen in Figure 3.11d. Figure 3.12 shows the bonding surfaces of the adherends cleaned with acetone and the resin LY3505/XB3405. Thin Polytetrafluoroethylene (PTFE) sheeting was applied to one of the steel adherends to achieve the correct bonding thickness along the DCB specimen.

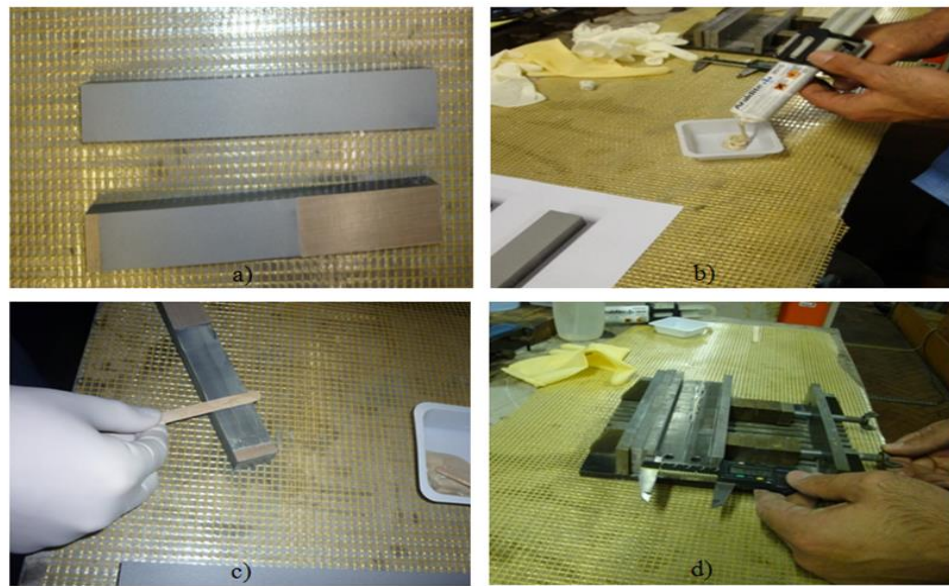


Figure 3.11: DCB Specimen preparation and bonding in jig

The resin and hardener were mixed together, according to the mix ratio defined in Figure 3.12, and degassed to remove air. This step was performed to remove any gaseous components entrapped in the resin, which could lead to void formation within the specimen affecting its mechanical properties.



Figure 3.12: Steel adherends with PTFE sheet and the resin LY3505/XB3405

Afendi et al. [182] have recommended 15 min degassing, followed by 1 hour at atmospheric pressure, in order to let the bubbles diffuse to the surface. After a mix time, the resin was applied to bond the steel adherends as a DCB specimen, and then placed into a containment jig, which was used to clamp the adherends together, as seen in Figure 3.11d.

The specimen was cured in the oven for 1 hour at 80°C. To reduce the possibility of any thermal shock or residual stresses accumulating within the adhesive layer, the entire assembly was left in the oven to slowly cool to room temperature.

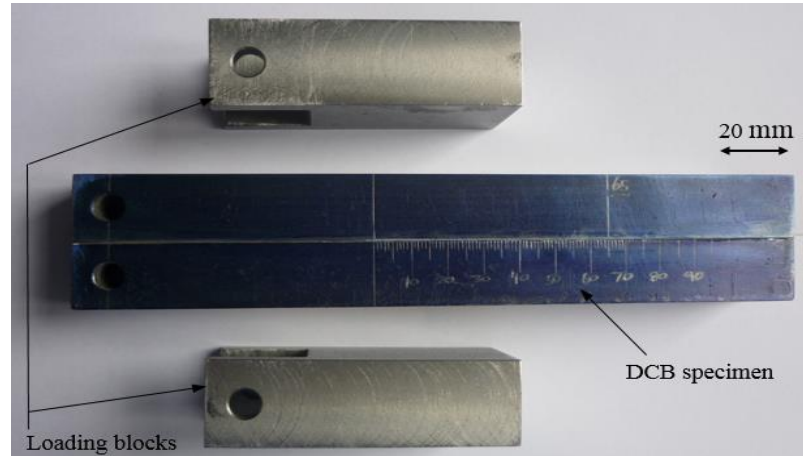


Figure 3.13: DCB specimen and loading blocks

As stated in BS 7991:2001, the specimen was accurately measured using a micrometer before and after bonding, to find the variation in bondline thickness across the length of the specimen [132]. The front surfaces of the upper and lower mild steel substrates were stained with correction fluid (suitable for use with mild steel) and then finely marked using a microscope and a metallic scribe. As seen in Figure 3.13, markings have been made every 1 mm up to 65 mm in total along the edge of the specimen, in order to aid with crack growth monitoring. The crack length should be measured along the edge of the specimen to an accuracy of at least ± 0.5 mm, done via a travelling microscope in this instance, as shown in Figure 3.14.

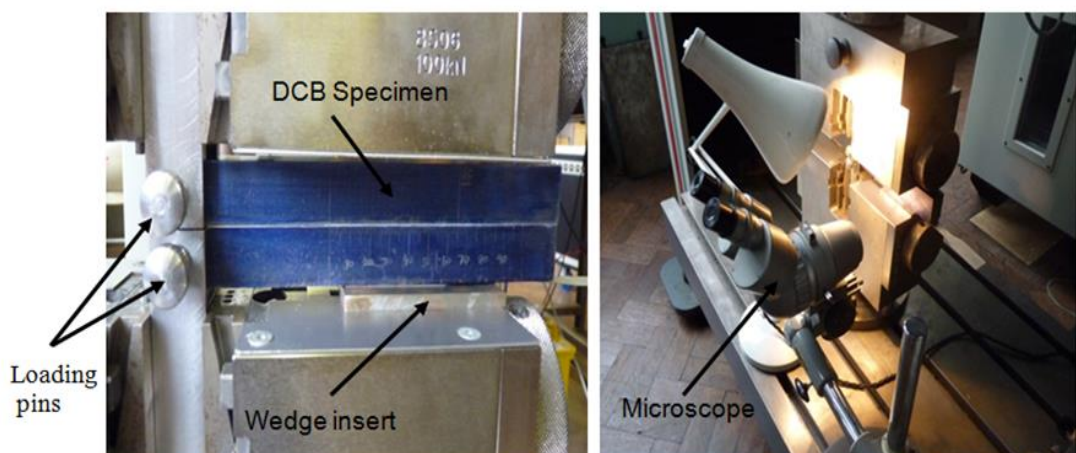


Figure 3.14: Experimental setup using a travelling microscope

3.4.1.2 Test results of DCB specimen bonded with adhesive 2015

The testing was performed using a Zwick/Roell universal tensile testing machine with a 250 kN load cell and wedge grips. The loading rate was 0.5 mm/min, and the tests were performed at room temperature.

For testing in this work, four specimens were conducted in order to initially analyse the accuracy of these methods with the laboratory equipment available, and to illustrate the inherent difficulties associated with this testing protocol. In Figure 3.15 shows the load-displacement curves for four DCB specimens tests.

As is evident from the fracture surface profiles of the DCB test results shown in Figure 3.16, the fracture surface consists of cohesive failure within the adhesive, as matching patterns of adhesive still remain on both substrates. This proof of cohesive failure within the adhesive is important, as it confirms that the actual fracture process occurs within the adhesive and, as such, the fracture toughness deduced from this test is characteristic of the adhesive being evaluated, as opposed to fracture occurring at the adhesive-substrate interface, or if the fracture was both cohesive and adhesive [183].

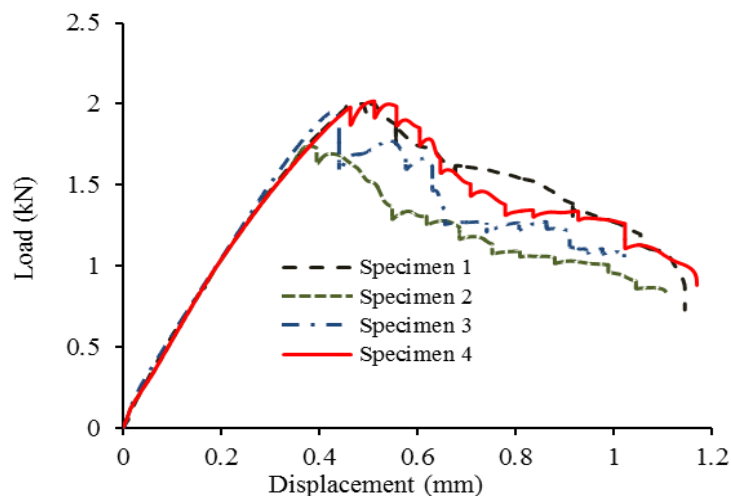


Figure 3.15: Load-displacement curves of DCB specimen bonded with Adhesive 2015

A feature that became apparent when tracking the crack propagation using the travelling microscope involved the actual crack evolving in a manner where the tip appeared to jump from one interface to another as it propagated along the specimen. This phenomenon may be attributed to the crack tip (or crack front) being diverted in its direction of propagation by the rubber inclusions within the epoxy adhesive that act as a toughening mechanism [184].

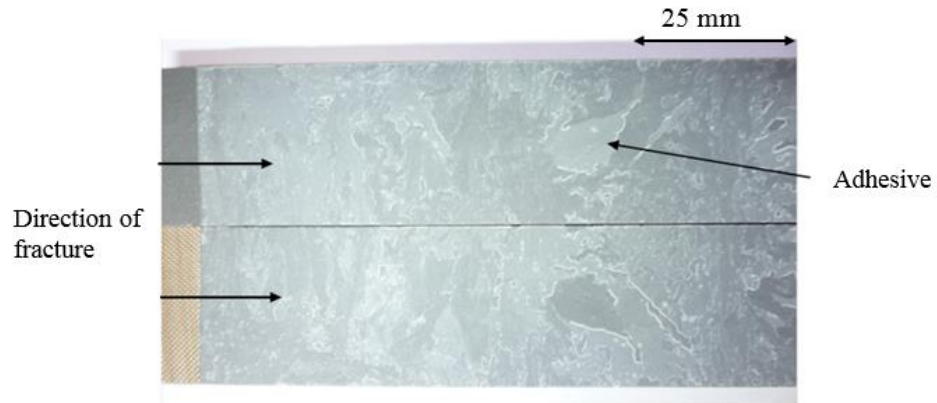


Figure 3.16: Failure surfaces from DCB test

3.4.1.3 Test results of DCB specimen bonded with resin LY3505/XB3405

The same geometry of the DCB specimen in Figure 3.10 was used in measuring the experimental values of G_{IC} . The testing was performed using a Zwick/Roell universal tensile testing machine with a 250 kN load cell and wedge grips. The loading rate was 0.1 mm/min, and the tests were performed at room temperature. Three tests were used to measure the experimental values of G_{IC} from the DCB tests. Figure 3.17 shows the load-displacement curves for three DCB specimens test. The fracture surface of a DCB specimen with resin LY3505/XB3405 is shown in Figure 3.18 . It is clear that the fracture is cohesive in failure and the resin is remained in both adherends.

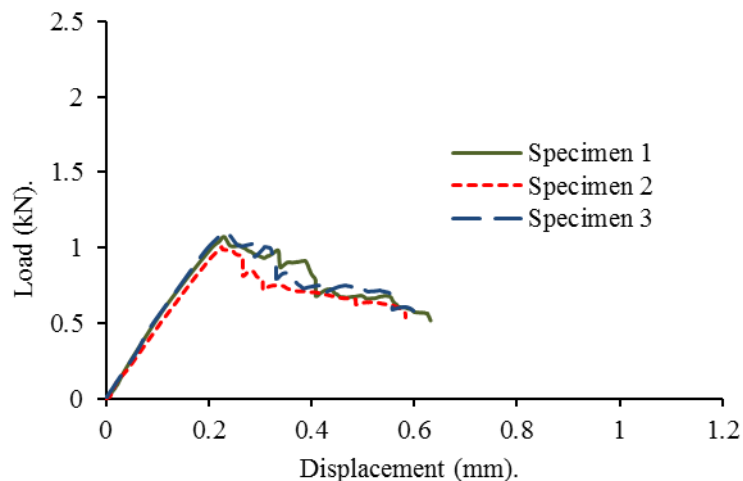


Figure 3.17: Load-displacement curves of DCB specimen bonded with Resin LY3505/XB3405

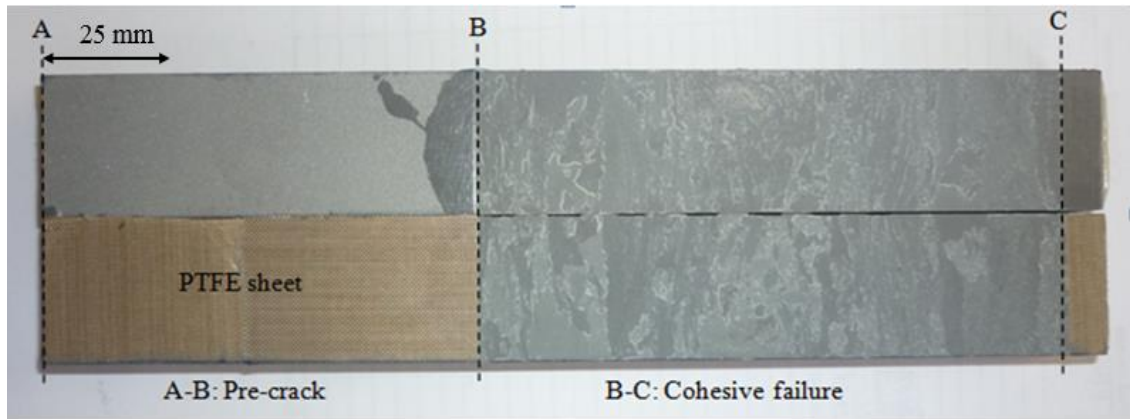


Figure 3.18: Failure surfaces of DCB test with resin LY3505/XB3405

3.4.1.4 Mode I Fracture Energy of Adhesive 2015, G_{IC}

The following methods used to ascertain the magnitude of G_{IC} from the DCB tests all require the need for simultaneous measurements of the load, displacement and relative crack propagation, in order to be utilised.

There are three methods that will be presented for obtaining the value of G_{IC} from the DCB test are:

- 1- Simple Beam Theory (SBT)
- 2- Corrected Beam Theory (CBT)
- 3- Experimental Compliance Method (or Berry's Method)

(1): Simple Beam Theory

The value of adhesive fracture energy G_{IC} may be found from:

$$G_{IC} = \frac{P^2}{2B} \cdot \frac{dC}{da} \quad (3.16)$$

Where C is the compliance and is given by (displacement/load). For relatively thin adhesive layers it has been illustrated from SBT that dC/da may be shown as:

$$\frac{dC}{da} = \frac{8}{E_s B} \left(\frac{3a^2}{h^3} + \frac{1}{h} \right) \quad (3.17)$$

With E_s representing the flexural modulus of the mild steel substrate used, hence combining the above equations we can deduce G_{IC} from:

$$G_{IC} = \frac{4P^2}{E_s B^2} \left(\frac{3a^2}{h^3} + \frac{1}{h} \right) \quad (3.18)$$

Where P is the load applied, B is the width of the substrates, a is the crack length and h is the thickness of the substrates.

(2): Corrected Beam Theory

The SBT theory shown above takes into account the deflections of the beam due to bending and shear, but does not account for the effects of beam root rotation [150]. Root rotation affects both the compliance of the beam and the subsequent values of G_{IC} . Also, as stated in BS 7991:2001, the SBT expression for the compliance of a perfectly built-in DCB will in fact underestimate the compliance of the beam, as the beam is not actually perfectly built for this test. In order to remedy this effect, we can treat the beam as having a slightly longer crack length than that which is actually measured, i.e. $(a + |\Delta|)$. The term $|\Delta|$ may be found by plotting the cube root of the compliance ($C^{1/3}$), as shown in Figure 3.19. By extrapolating a linear fit through the data we can deduce the value of Δ as the negative x-axis intercept value.

Therefore in order to find the value of G_{IC} from CBT we can use:

$$G_{IC} = \frac{3P\delta}{2B(a + |\Delta|)} \quad (3.19)$$

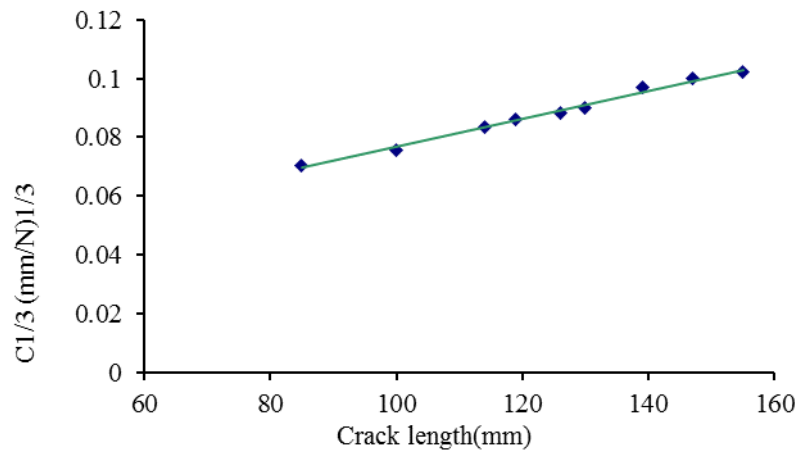


Figure 3.19: Linear regression data used for CBT method

(3): Experimental Compliance Method (or Berry's Method)

Another method used to calculate the value of G_{IC} from this test involves plotting the logarithm of the compliance (C) versus the logarithm of the crack length (a), as shown in Figure 3.20. The slope of this plot, n , can then be used to obtain G_{IC} using:

$$G_{IC} = \frac{nP\delta}{2Ba} \quad (3.20)$$

Where: P the load, δ the displacement, a the crack growth and B the width of the specimen. The experiments consisted of using adhesive thickness $t_a = 0.2$ mm. In Figure 3.21 the values of the fracture energy obtained from the limited number of measurement points are illustrated. The curve shown in Figure 3.21 represents the fracture energy obtained from the third test of the DCB experiment. As can be seen, the ECM and CBT methods provide consistent results, but the SBT method produces a fracture energy that is much lower than the others. This is because the SBT method assumes a perfect specimen, which is not the case, so the values produced from the ECM and CBT methods are much more accurate.

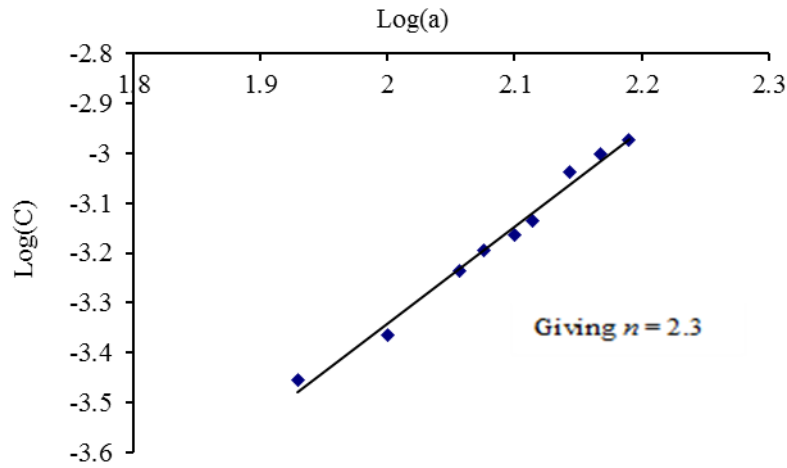


Figure 3.20: Linear regression data used for ECM method

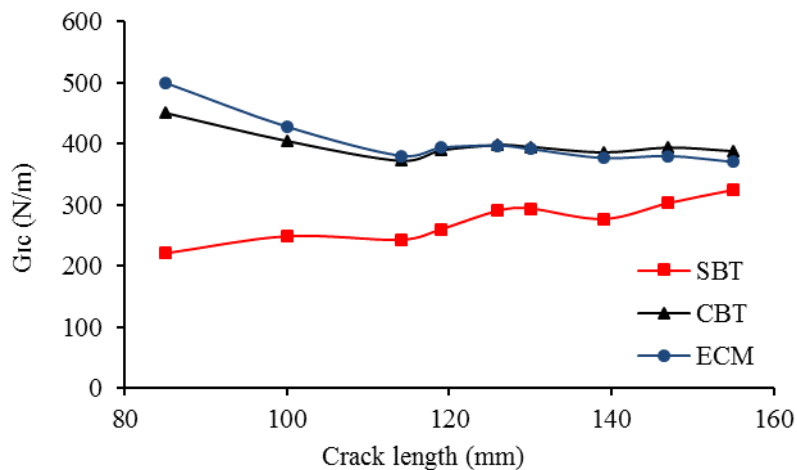


Figure 3.21: R-Curve for adhesive 2015 using SBT, CBT and ECM

The extracted values from the experiments are summarised in Table 3.5. The values of the fracture energy obtained from the tests are between minimum and maximum range; the final values will be found later with the use of the numerical analysis.

Table 3.5: Results of the DCB experiments of Adhesive 2015

Test No.	G_{IC} (N/m)
Specimen 1	353-502
Specimen 2	338-475
Specimen 3	340-480
Specimen 4	363-498

3.4.1.5 Mode I Fracture Energy of Resin LY3505/XB3405, G_{IC}

The British Standard 7991:2001 [132] was used, repeating the same methods in section 3.4.1.4 to measure the magnitude of G_{IC} of the epoxy resin LY3505/XB3405.

The curve shown in Figure 3.22 represents the fracture energy obtained from test 1 of the DCB experiment. The curves of the ECM and CBT methods provide consistent results, but the SBT method produces a fracture energy that is lower than the others. So the values obtained from the ECM and CBT methods are more accurate.

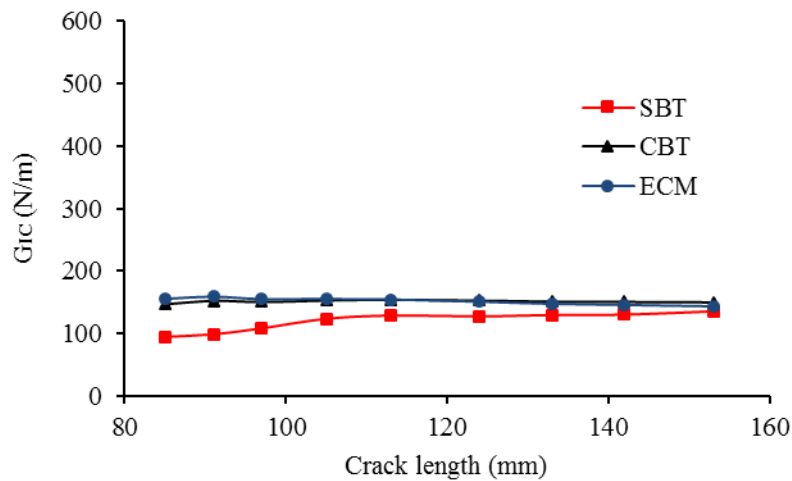


Figure 3.22: R-Curve for Resin LY3505/XB3405 using SBT, CBT and ECM

The experiments' values of fracture energy G_{IC} for epoxy resin LY3505/XB3405 are summarised in Table 3.6. The values of the fracture energy obtained from the three tests are between minimum and maximum range; the final value will be found later with the use of the numerical analysis.

Table 3.6: Results of the DCB experiments of resin LY3505/XB3405

Test No.	G_{IC} (N/m)
Specimen 1	141-165
Specimen 2	135-160
Specimen 3	144-161

3.4.2 The end notched flexure specimen (ENF)

In this section, the end notched flexure (ENF) specimen for determining mode II is introduced. In the ENF test, the specimen is simply supported at the ends and a load applied in the middle of the specimen Figure 3.23. This specimen was used by e. g. Carlsson et al. (1986) and Chai (1988) to study both brittle and ductile adhesive layers [185, 186]. In the ENF specimen, stress distribution in the adhesive layer is essentially pure shear, except at the loading point, where some compressive stresses appear. The specimen geometry is represented in Figure 3.23. The steel was used for the substrates where the adherend thickness H is 16 mm, the width B is 32 mm, and the length between the supports $2L$ is 1000 mm. The geometry of the ENF specimen must satisfy some conditions. Indeed, as reported in Leffler (2005) [187], the ENF specimen is conditionally stable, and estimates based on beam theory with elastic beams and rigid adhesive layer show that the initial crack length must be at least equal to 350 mm.

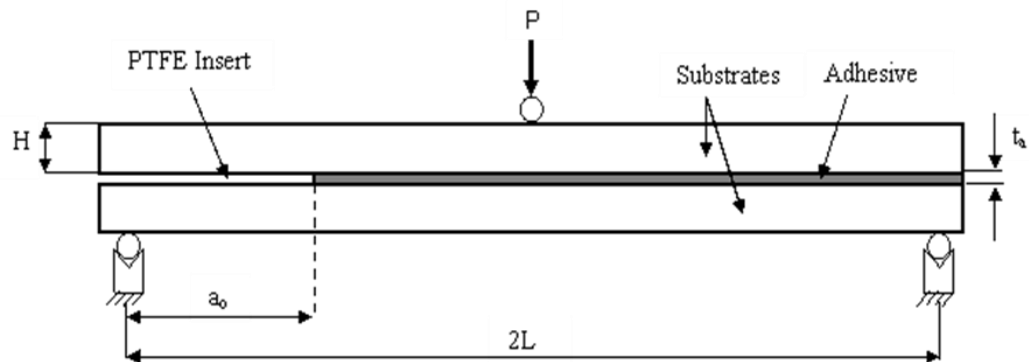


Figure 3.23: Illustration of ENF specimen

Where:

$a_0 = 350$ mm, $L = 500$ mm, $H = 16$ mm, $t_a = 0.2$ mm, and the width = 32 mm

3.4.2.1 Specimen preparation

The bonding surfaces of the adherends were sand papered and degreased with acetone. Good alignment of the two adherends was secured with the use of a fixture. To achieve correct adhesive thickness along the entire specimen, steel wire with a diameter of 0.2 mm was adhesively bonded to one of the adherends. A Polytetrafluoroethylene (PTFE) sheet was inserted between the two steel adherends to make a mid-plane pre-crack, which lead to the 350mm total initial crack at one end of the specimen.

This ensures the thickness of the adhesive layer, and also minimises friction between the adherends during the experiment. Once the adhesive had been fully applied, the specimen was then placed into a containment jig, and clips were used to add pressure to both surfaces of specimens after bonding, as seen in Figure 3.24. To ensure good adhesion between the adhesive and the adherends, a small compressive force was applied to the specimens during the curing; the specimen was then cured for 1 hour at 80°C. After curing, the specimens were left in the oven to slowly cool to room temperature to avoid serious inner stress. When the joint had cooled, it was removed from the jig, and any excess adhesive was removed from the joint with the use of a scraper, which leaves a smooth level adhesive layer, as seen in Figure 3.25.

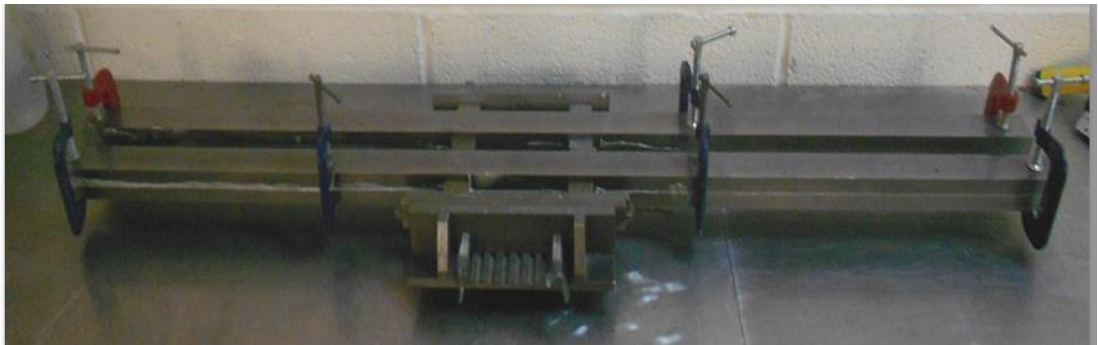


Figure 3.24: The ENF specimen preparation and bonding in jig



Figure 3.25: ENF specimen

3.4.2.2 Test processing of ENF specimen

The testing was performed using a Zwick/Roell universal tensile testing machine with a 250 kN load cell and upper wedge grip. The cross head velocity rate was 0.5 mm/min and the tests were performed at room temperature. The specimens were placed over a test fixture consisting of two supporting semi cylinders. A third semi cylinder connected to the load cell of a tensile machine was used to bend the sample at its mid-point. Figure 3.26 shows a photograph of the ENF test. The span between the two supports was 1000 mm, and the initial crack length was 350 mm. The force and relative displacement between the centre loading point and the supports can be recorded through the actuator displacement of the machine, as the specimens were deformed.

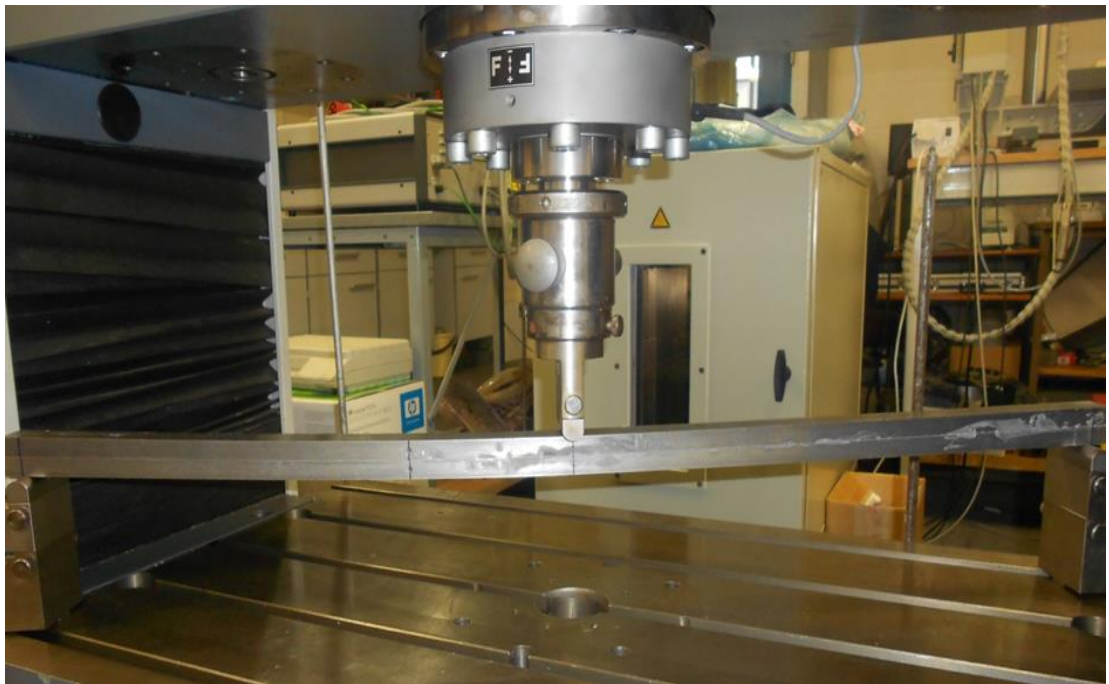


Figure 3.26: Photograph of ENF test setup

3.4.2.3 Test results of ENF specimen bonded with adhesive 2015

For testing in this work, four specimens were conducted in order to initially analyse the accuracy of these methods with the laboratory equipment available, and to illustrate the inherent difficulties associated with this testing protocol.

Figure 3.27 shows the load-displacement curves for ENF specimen tests. A typical fracture surface is displayed in Figure 3.28. The fracture pattern was classified as partly adhesive and partly cohesive.

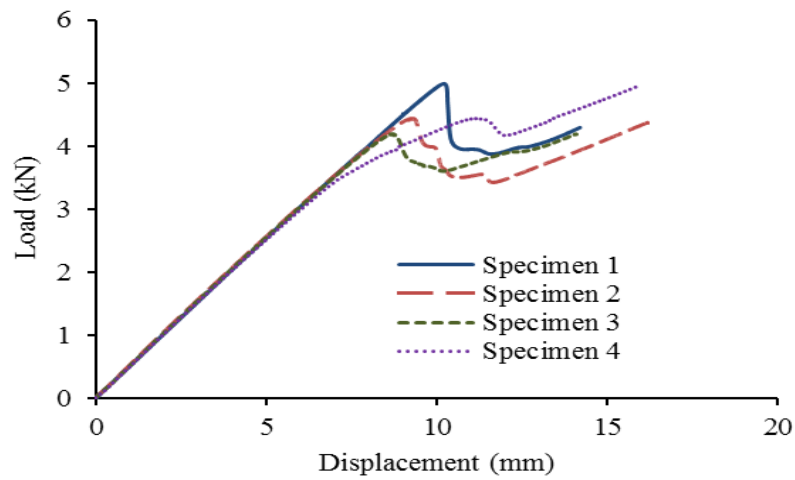


Figure 3.27: Load-displacement curves of ENF specimen bonded with Adhesive 2015

As is evident from the fracture surface profiles of the ENF test results shown in Figure 3.28, the fracture surface consists of cohesive failure within the adhesive, as matching patterns of adhesive still remain on both substrates. It is clear that the fracture is still a cohesive domain failure. This proof of cohesive failure within the adhesive is important, as it confirms that the actual fracture process occurs within the adhesive and, as such, the fracture toughness deduced from this test is characteristic of the adhesive being evaluated, as opposed to fracture occurring at the adhesive-substrate interface, or if the fracture was both cohesive and adhesive [4].

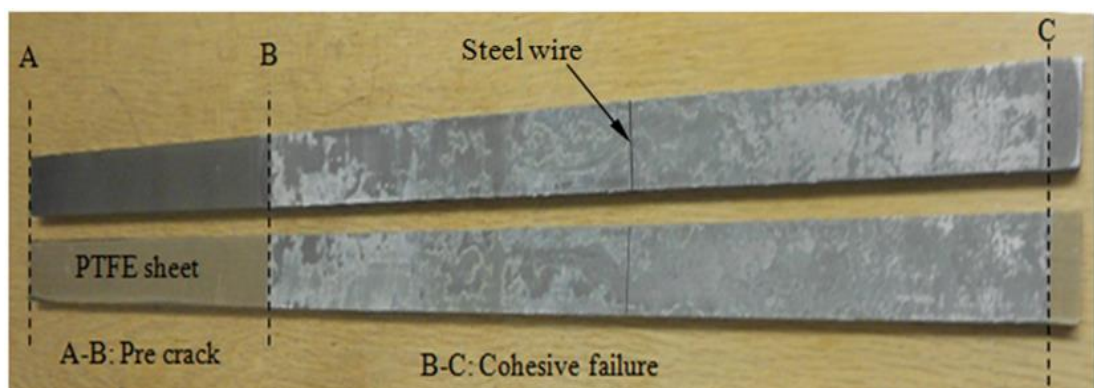


Figure 3.28: Failure surfaces of ENF test

3.4.2.4 Test results of ENF specimen bonded with resin LY3505/XB3405

The same geometry and dimensions of ENF specimens in Figure 3.23 were used to measure the experimental values of G_{IIC} . The testing was performed using a Zwick/Roell universal tensile testing machine with a 250 kN load cell and wedge grips. Three tests were used to measure the experimental values of G_{IIC} from the ENF tests. The tests were performed at room temperature. In Figure 3.29 is shown the load-displacement curves for specimens test. The fracture surface of ENF specimen with resin Ly3505/XB3405 is shown in Figure 3.30.

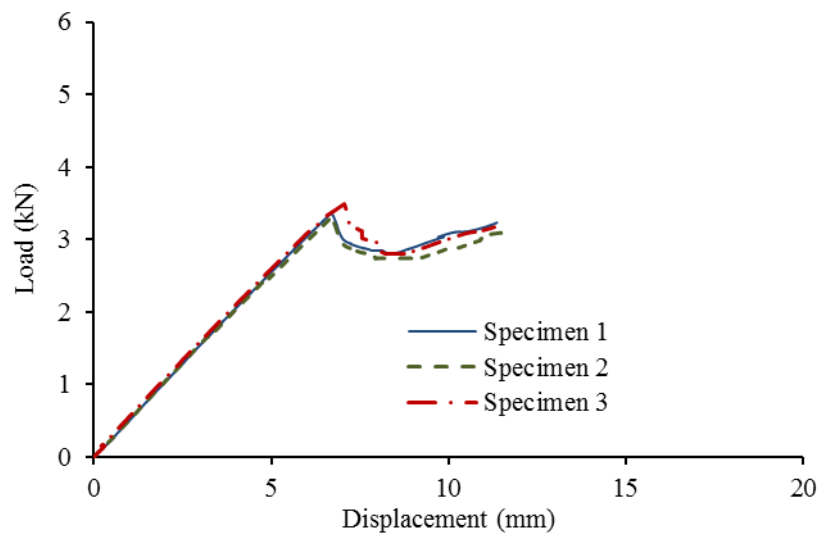


Figure 3.29: Load-displacement curves of ENF specimen bonded with Resin LY3505/XB3405

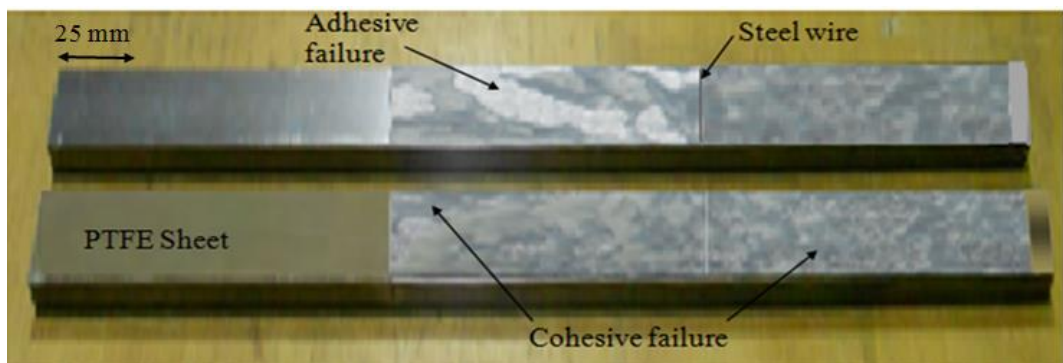


Figure 3.30: Failure surfaces of ENF test with resin LY3505/XB3405

3.4.2.5 Data analysis

According to linear elastic fracture mechanics,

$$G_c = \frac{P^2}{2B} \frac{dC}{da} \quad (3.21)$$

Where the C is the compliance defined by $C = \Delta / P$, B is the joint width and P is the load for crack growth. Using the beam theory and the above equation,

$$G_{IIC} = \frac{9P^2 a_e^2}{16B^2 EH^3} \quad (3.22)$$

Where, G_{IIC} is the fracture toughness of mode II. Also the toughness in mode II can be determined by the partial derivative of the compliance with crack length by analytical equation, and fits the experimental data completely to the crack length. However, experimental measurement of the crack length is very difficult, and at the crack tip - the fracture process zone (FPZ) - damage of the material occurs by plasticity. An equivalent crack length (a_e) that takes the FPZ into account should be used. De Moura and Morais [188] proposed a method that does not require crack length measurement, and that takes into account the FPZ, they called the compliance based beam method (CBBM).

$$C = \frac{3a^3 + 2L^3}{12EI} + \frac{3L}{10GBH} \quad (3.23)$$

The modulus E refers to the adherends. The compliance of adhesive depends on the thickness, and can affect the compliance of the specimen. So, the flexural modulus can be estimated considering the initial of crack length a_0 and compliance C_0

$$E_f = \frac{3a_0^3 + 2L^3}{12I} \left(C_0 - \frac{3L}{10GBH} \right)^{-1} \quad (3.24)$$

An equivalent crack length (a_e) is the sum of crack length a and the correction (Δa_{FPZ})

$$C = \frac{3(a + \Delta a_{FPZ})^3 + 2L^3}{12E_f I} + \frac{3L}{10GBH} \quad (3.25)$$

Combining the equations (3.24) and (3.25), the equivalent crack length can be obtained as,

$$a_e = a + \Delta a_{FPZ} = \left[\frac{C_{corr}}{C_{0corr}} a_0^3 + \frac{2}{3} \left(\frac{C_{corr}}{C_{0corr}} - 1 \right) L^3 \right]^{1/3} \quad (3.26)$$

Where:

$$C_{corr} = C - \frac{3L}{10GBH} ; \quad C_{0corr} = C_0 - \frac{3L}{10GBH}$$

Put the value of a_e in equation (3.23)

$$G_{IIC} = \frac{9P^2}{16B^2E_fH^3} \left[\frac{C_{corr}}{C_{0corr}} a_0^3 + \frac{2}{3} \left(\frac{C_{corr}}{C_{0corr}} - 1 \right) L^3 \right]^{2/3} \quad (3.27)$$

This method does not require crack length monitoring during growth.

The extracted values from the experiments are summarised in Table 3.7. The values of the fracture energy obtained from the tests are between minimum and maximum range; the final values will be found later with the use of numerical analysis.

Table 3.7: Results of the ENF experiments of Adhesive 2015 and resin LY3505/XB3405

Test No.	Adhesive 2015 G_{IIC} (N/m)	Resin LY3505/XB3405 G_{IIC} (N/m)
Specimen 1	3750-4345	1187-1410
Specimen 2	3600-4225	1292-1406
Specimen 3	3605-4215	1305-1418
Specimen 4	3652-4335	-

3.5 Comments

Section 3.4 presented the tests of fracture mechanics carried out for one of aims of this thesis. They were a mode I test, DCB, and a mode II test, ENF.

The specimens were manufactured from steel as adherends and two types of bonding materials, adhesive (Araldite 2015) and epoxy resin (LY3505/XB3405), the consolidation happening under a hot press. All the manufacturing processes of the specimens have shown positive characteristics of repeatability.

From each of these two tests, the force versus displacement curve has been obtained. Moreover, the tests for mode I and mode II were used for calculation of the interlaminar fracture toughness for the relevant mode of delamination. The experimental tests showed accordance with the typical results of these tests. They can therefore be considered a good starting point for the comparison with finite element modelling with cohesive elements discussed in Chapter 6.

Chapter 4

4 Experimental investigations of DLS joint

4.1 Introduction

This section will describe the bonding characteristics of structural adhesives. However, lap shear joints are the most common form to be investigated, and perhaps the easiest to prepare. In this work, the Double Lap Shear (DLS) joint was chosen to study adhesive behaviour, because this geometry minimises bending moments. Tensile testing experiments have been undertaken on two steel members in the same plane joined to CFRP plates, in which two CFRP plates are bonded to the steel plates, one each side.

Strains were measured to provide information on the longitudinal profiles over a chosen bond length on both the steel and CFRP adherends, and on the load transfer mechanism across the two adherends. The overall extensions of the joints were also measured. The average thickness of the adhesive was 0.2 mm for all joints. In general, at least three nominally identical specimens were tested for each case.

Several failure mechanisms were observed, which were generally a mixture of cohesive failure within the adhesive, adhesive failure at the bondline with either the steel or CFRP adherend, and composite delamination.

4.2 DLS joint preparation

This section will give details of the bonding procedure used during the preparation of test specimens. It is important maintain the same conditions when constructing the joints to enable an accurate comparison of strength. The adhesive thickness is kept the same for all joints using a wire insert method. Care is also taken during alignment of the adherends to ensure symmetrical joints are produced. The geometry of the DLS test specimen is shown in Figure 4.1. This is made up of two thick mild steel inner adherends and two CFRP straps at

the outer adherend. The width of the specimens was 25mm and the length of joint overlaps (OL = 25, 50, 75, 100 and 125 mm).

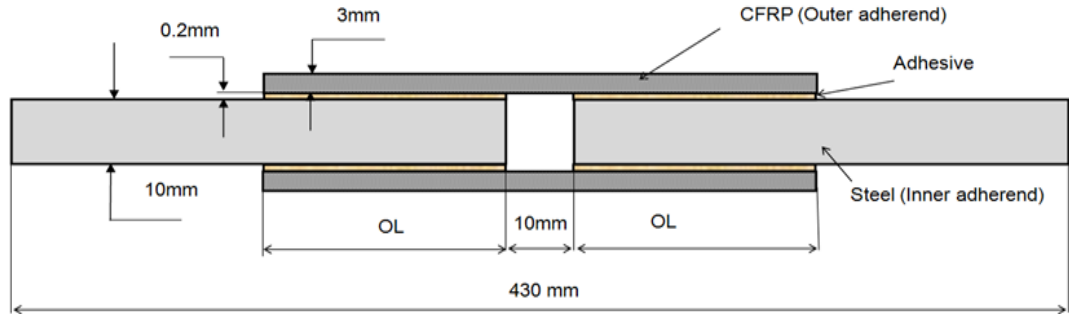


Figure 4.1: DLS Joint (Steel/CFRP)

4.2.1 Surface preparation

The bonding surfaces of all the mild steel inner adherends were grit blasted using a jet air suction blast cleaning machine to improve the effectiveness of the adhesive bond [51]. The grit blasted was chilled iron grit, G24 (0.6-1.0 mm) particle sizes. The grit blasting machine and the steel surfaces can be seen before and after treatment in Figure 4.2. The ends to be positioned in the centre of the joint then had pre-cut PTFE sheets applied to them in order to prevent bonding of these surfaces. This ensured that the joint was subjected only to shear loading during testing. The composite adherends could not be prepared in this way due to the possibility of damaging the fibres.

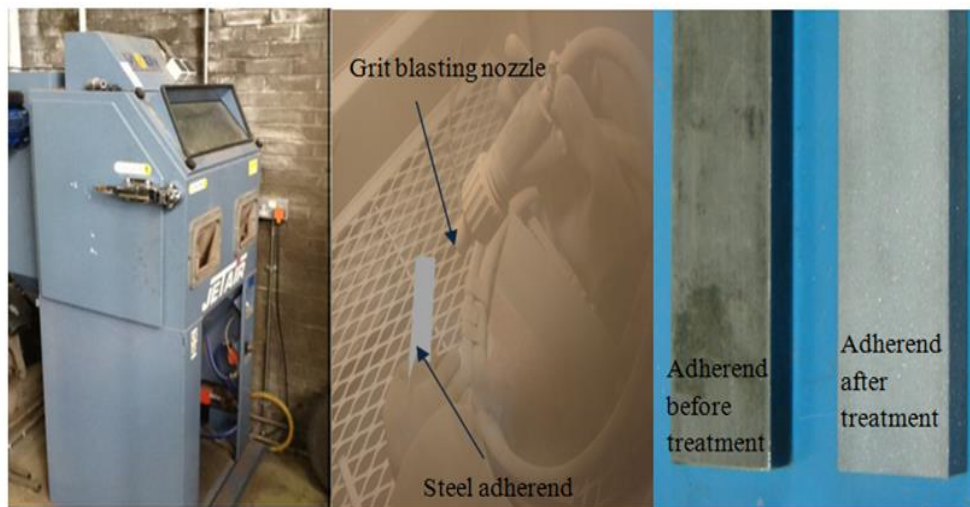


Figure 4.2: Grit blasting used to treat steel adherends

Light grade P120C silicone carbide paper was used for the composite adherends to clean the bond area and eliminate unevenness in the bonding surfaces. To maintain consistency, 10 strokes were performed along the length of the strap, and another 10 strokes across the breadth. After abrading the mild steel and composite adherends, it was necessary to clean all of the bonding surfaces to remove any potential bond contaminants. This was achieved using the commercially available organic solvent, acetone. The cleaning agent was applied using a polyethylene wash bottle and wiped from the surface using paper towels Figure 4.3 . When cleaning was complete, reference points were marked on the adherends to aid alignment when positioning the specimens in the bonding jig.

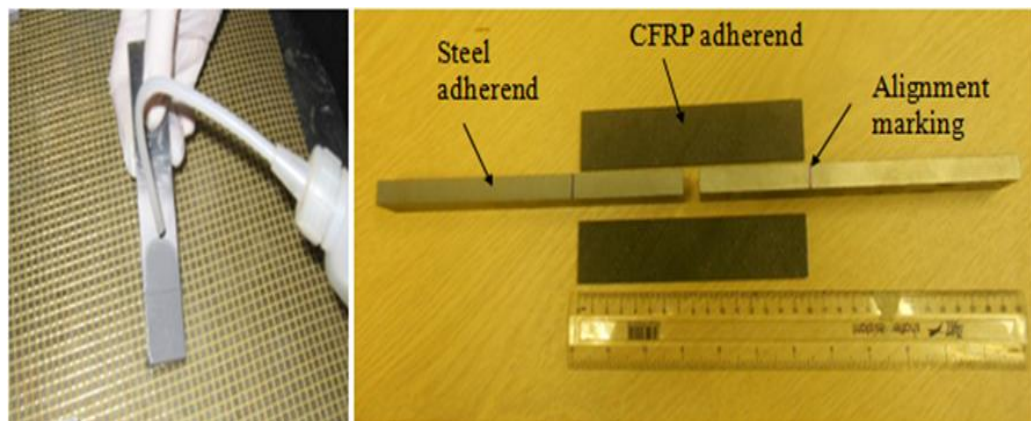


Figure 4.3: Acetone used to clean the adherends surfaces of DLS joint before bonding

4.2.2 Adhesive application

The epoxy adhesive used in the bonding process was Araldite 2015. The two-part adhesive was mixed using an Araldite application gun with a mixer nozzle and putting the mixed adhesive into a clean plastic tray; see Figure 4.4. After mixing the adhesive, the following steps were followed: firstly, a thin layer of adhesive was applied to the surface of adherents using a spatula, shown in Figure 4.4b.

The process was repeated, but more quantities of adhesive were applied to the surface bonded area than was required. This was done to prevent air entrapment, which would lead to void development within the adhesive. When pressure was applied by the jig, the adhesive flowed outward from the centre, forcing the air out of the joint. Most of this excess adhesive was removed using the wooden stick, with the rest being removed after curing using a file. The adhesive thickness was controlled by four 0.2 mm steel wires inserted vertically into the joint and withdrawn at the end of clamping.

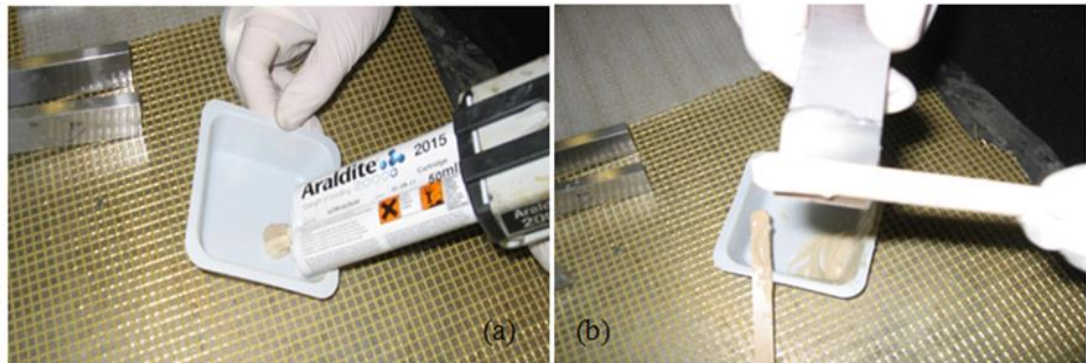


Figure 4.4: Picture of applying adhesive to adherends

4.2.3 Clamping

The specimens were placed in the jig and separated with steel bars, see Figure 4.5. The jig was then tightened by hand to apply equal pressure along the bond, to produce a constant adhesive thickness within the joint with the help of the wire insert. As the jig was tightened, corrections for slippage were performed to maintain alignment of the joint components. This was aided by the reference points previously marked on the components.



Figure 4.5: Two test specimens clamped in the jig, ready for curing

4.2.4 Curing

The adhesive needs to be heated to cure, in order to gain a strong durable bond, so the specimens - including the jig - were placed in a standard laboratory oven and heated at a constant temperature of 80°C for one hour Figure 4.6 . After that time, the oven was switched off and the door opened, and the contents were left to cool gradually over 24 hours. This process of slowly cooling the joints reduces the presence of residual stresses forming in the joint and ensures the cure is completed. When the joint had cooled, it was removed from the jig and any excess adhesive removed from the joint with the use of a scraper, which leaves a smooth level adhesive layer.



Figure 4.6: Laboratory oven used to cure the adhesive joints

4.3 DLS joints testing procedure

The DLS joint geometry and dimensions are represented in Figure 4.7. The joint was made up of two mild steel inner adherends and two outer adherends made from the CFRP materials. The width of all specimens was 25 mm, adhesive thickness, $t_a=0.2$ mm and the thickness of inner adherends is 10 mm. The overall length remained constant i.e. 430 mm varies overlaps were used. Two different values of outer adherend thickness, namely 3 mm and 6 mm for 12 layers and 24 layers respectively, and five values of overlap length OL (25, 50, 75, 100 and 125 mm) were evaluated, see Figure 4.8.

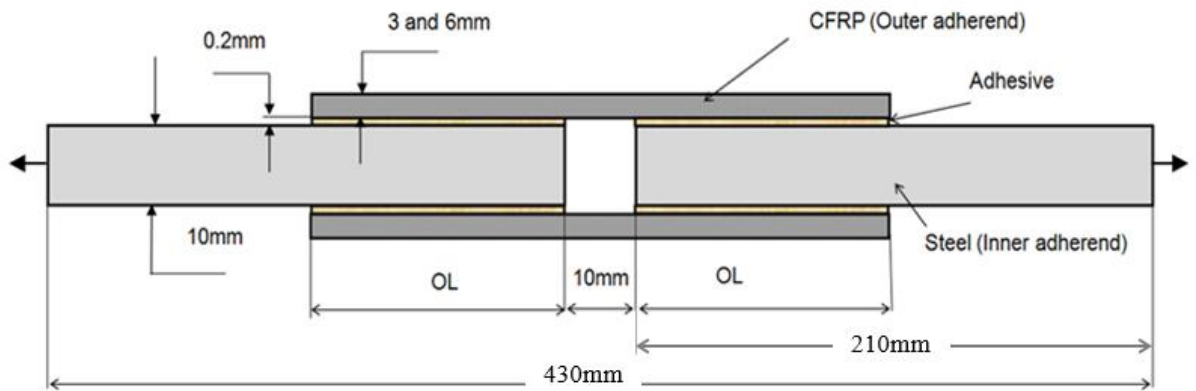


Figure 4.7: DLS Joint geometry and dimensions

Also, various ply orientations for the composite were used, including $[0^\circ, 90^\circ]$, $[+45^\circ, -45^\circ]$ and $[90^\circ, 0^\circ]$. For example, the first ply of the $[0^\circ, 90^\circ]$ lay-up had the UD fibers orientated at 0° relative to the direction of the applied load. The type and details of the specimens used for tensile testing are presented in Table 4.1. The designations for the CFRP adherend are used to describe the types of the specimens. This also indicates the orientation of the UD fibre and total laminate thickness.

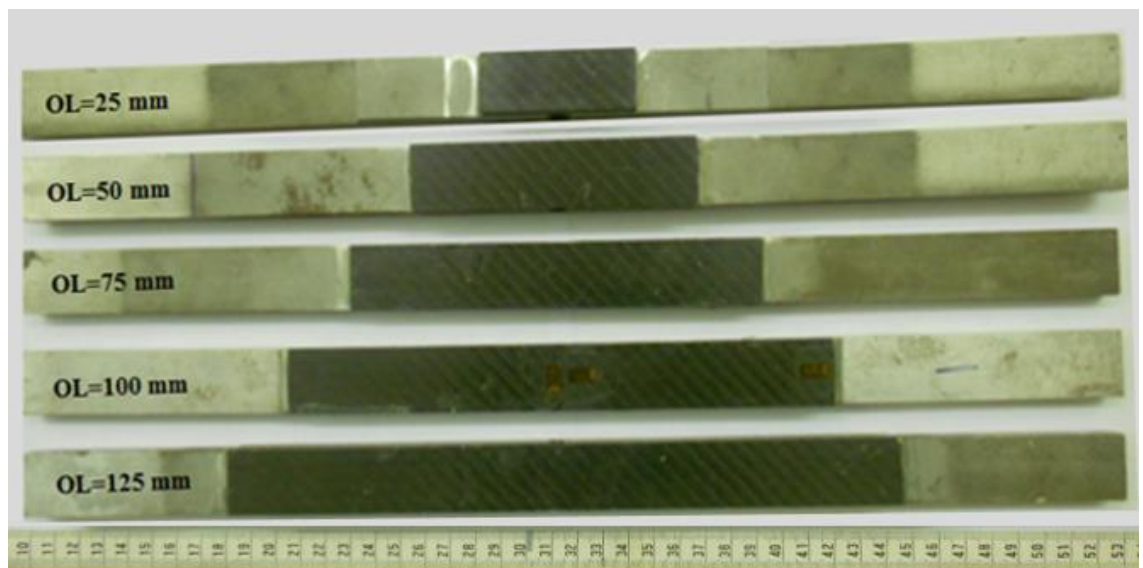


Figure 4.8: Bonded specimens showing $[0^\circ, 90^\circ]_6$ specimens with various overlap lengths

Table 4.1: Type and number of specimens

Specimen type	Overlap length (mm)	CFRP adherend thickness (mm)	Number of specimens
[0°,90°] ₆	25	3	5
	50	3	6
	75	3	6
	100	3	5*
	125	3	4**
[90°,0°] ₆	25	3	6
	50	3	6
	75	3	6
	100	3	4*
	125	3	3**
[+45°/-45°] ₆	25	3	5
	50	3	5
	75	3	5
	100	3	4*
[90°,0°] ₁₂	25	6	4*
	50	6	3**

* One of these was discarded due to bonding defects.

** Limited number due to materials availability.

4.3.1 Tensile testing Set-up

The setup for the experiments can be seen in Figure 4.9. The testing used a Zwick/Roell 250 kN Universal testing machine which provided load and extension data for each test. Each specimen was gripped at 50 mm from the edge at both ends. The loading rate was 0.5 mm/min, and all tests were performed at room temperature. The load and displacement values were recorded to give the failure load. The specimens were clamped at either end and then pulled apart until failure.

This process was completed for all different joints. The reasoning for this was to find the effects of increasing the joint overlap, changing the laminate direction and outer adherend thickness on the type of fracture, and the peak load of the joint. During the testing of DLS joints, the failure path of the specimens occurred in the form of an S-shape or U-shape, as shown in Figure 4.10a and b.

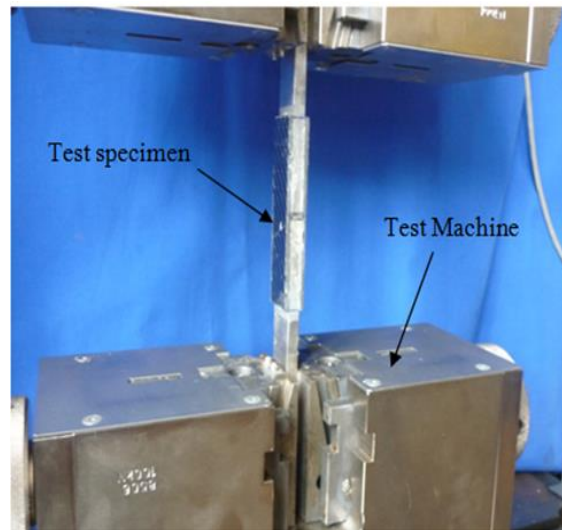


Figure 4.9: Tensile test of $[0^\circ, 90^\circ]_6$ specimen with 75 mm overlap length

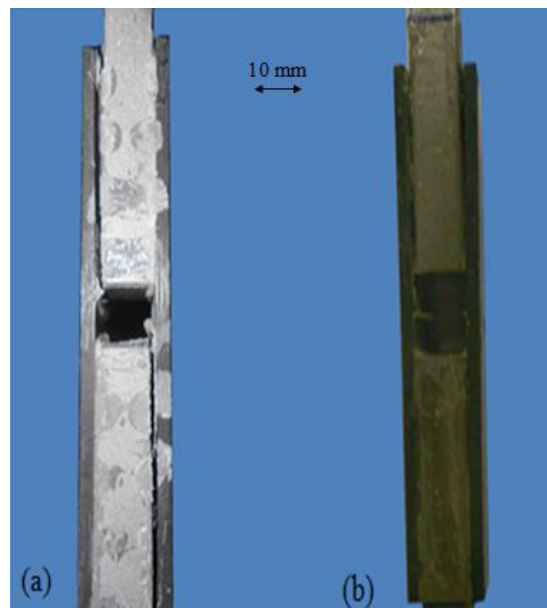


Figure 4.10: Failure shapes: a) S-shape, b) U-shape

4.3.2 Test Results

4.3.2.1 Effect of fibre orientation

As mentioned in the literature review section, assessed fibres are strongest when loaded along their length. Experiments were conducted to the effect of fibre direction was

considered in relation to the 75 mm overlap with 3 mm outer adherend thickness at different orientations. Figure 4.11 shows the test results for types $[0^\circ, 90^\circ]_6$, $[90^\circ, 0^\circ]_6$ and $[+45^\circ, -45^\circ]_6$ specimens, and indicate these are maximum values for respective test specimens.

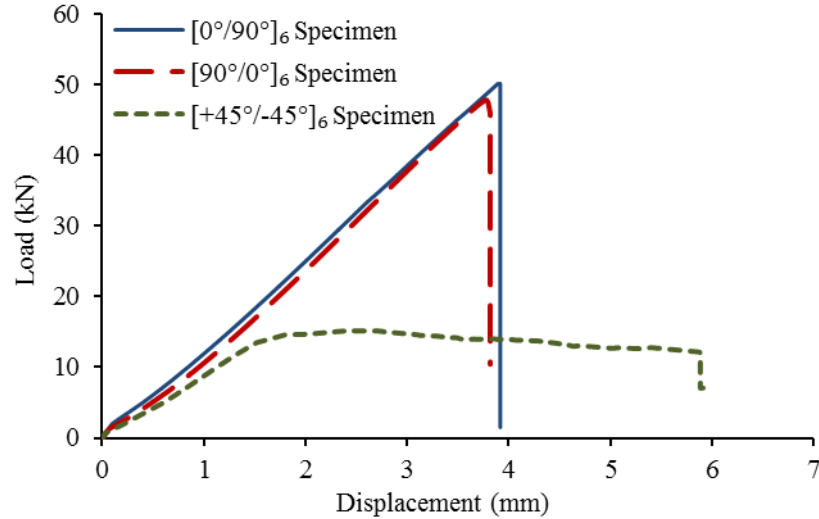


Figure 4.11: Load displacement curves for different orientation angle with 75 mm overlap length and 3 mm thickness of CFRP adherend

This shows that the failure load for $[0^\circ, 90^\circ]_6$ specimens produced 5% and 70% higher strength than the $[90^\circ, 0^\circ]_6$ and $[+45^\circ, -45^\circ]_6$ specimens, respectively.

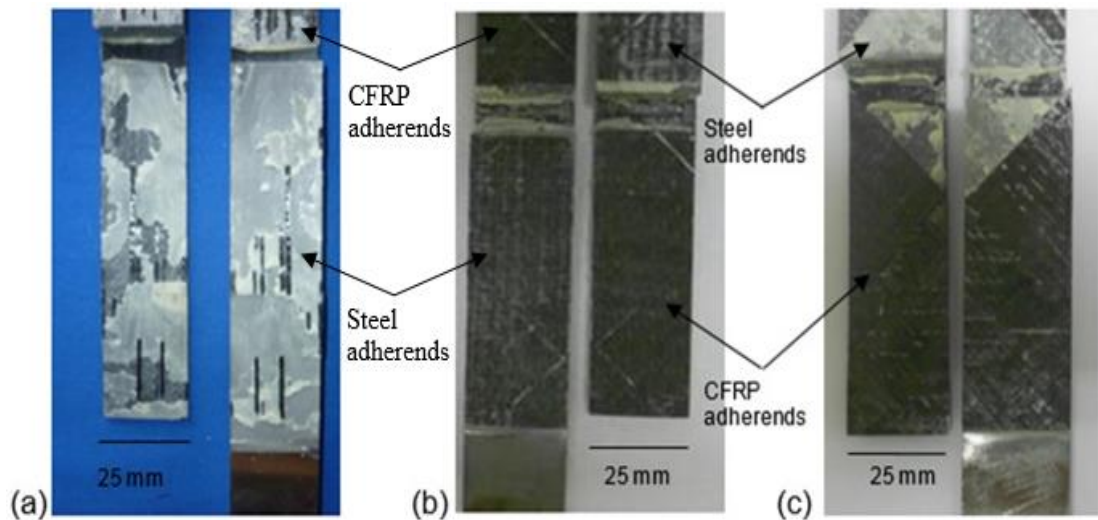


Figure 4.12: Experimental fracture surfaces for: (a) $[0^\circ, 90^\circ]_6$ specimen, (b) $[90^\circ, 0^\circ]_6$ specimen and (c) $[+45^\circ, -45^\circ]_6$ specimen

The failure surfaces of the specimens were inspected to speculate on where the crack may have been initiated. A large amount of adhesive can be seen on the steel adherend $[0^\circ, 90^\circ]_6$ specimen with fragments of the fractured composite, as shown in Figure 4.12a. This suggests that failure was initiated in the adhesive either by cohesive failure or lack of adhesion. The high failure load of the joint suggests cohesive failure, as failure by lack of adhesion usually occurs at low loads. From Figure 4.12b it can be seen that in the $[90^\circ, 0^\circ]_6$ specimen, the bond area of the steel is completely covered by layers of the composite laminate, which suggests that failure initiated within the CFRP adherend. This supports the argument that failure of the joint was within the carbon fiber laminate, and the likely cause is delamination in the composite material. For the $[+45^\circ, -45^\circ]$ specimen, the failure can also be characterised as delamination, as shown in Figure 4.12c. This could have started in the first or second ply due to in-plane shear and transverse stresses. As would be expected, the joint with $[+45^\circ, -45^\circ]_6$ specimen also fails at a much lower load than the $[0^\circ, 90^\circ]_6$ specimen. After initial failure, it continues to carry a substantial load as shown in Figure 4.11. This load-carrying capacity gradually decreases until final failure is reached. The failure occurs at a greater extension than both of the other configurations. This is demonstrated in Figure 4.11, which shows that extension of the $[+45^\circ, -45^\circ]_6$ specimen is approximately 2 mm greater than that of the $[0^\circ, 90^\circ]_6$ specimen. The failure load of this type fibre alignment is so low due to the fibres being delaminated in line with the direction of the applied load. This results in high shear stresses in the laminate.

Also, from Figure 4.12c it can be seen that the failure surface of the joint with $[+45^\circ, -45^\circ]_6$ specimen is similar to the $[90^\circ, 0^\circ]_6$ specimen, and shows a large amount of the composite covering the steel surface with a smaller portion of adhesive also visible. This suggests that failure initiation for this joint was also within the composite laminate.

4.3.2.2 Effect of overlap length

Tests were also conducted to determine what effect the overlap length of the composite adherend has on the strength of the joint. Specimen overlap lengths of 25, 50, 75, 100, and 125 mm based on $[0^\circ, 90^\circ]_6$ and $[90^\circ, 0^\circ]_6$ specimens were considered. The test results for these are shown in Figure 4.13 and Figure 4.14, demonstrating that increasing the length of the overlap bonding increases the load at which the joint will fail. As the length is increased, a greater extension of the joint before failure can also be seen.

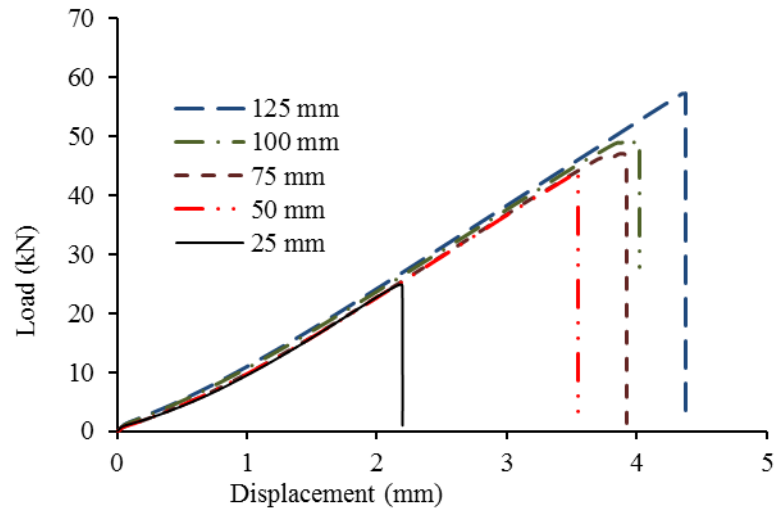


Figure 4.13: Load-displacement curves for $[0^\circ, 90^\circ]_6$ specimens at varying overlap lengths

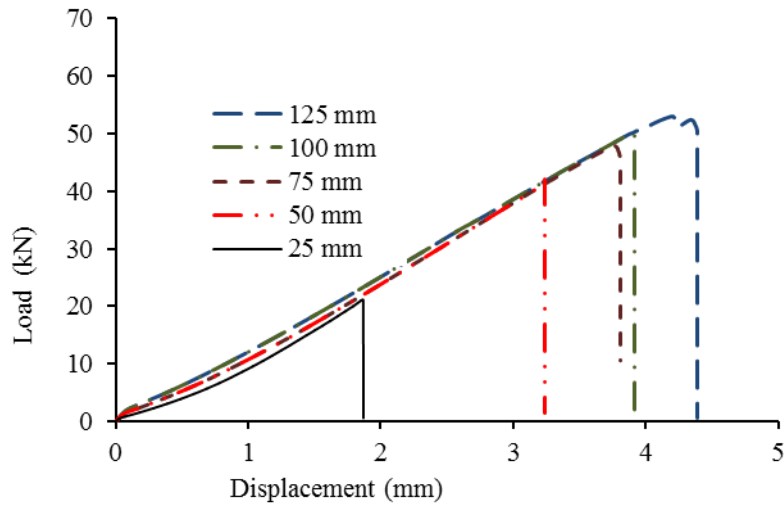


Figure 4.14: Load-displacement curves for $[90^\circ, 0^\circ]_6$ specimens at varying overlap lengths

However, studies into the effects of overlap length have shown that this trend is limited. For each type of joint there exists a plateau at which point the strength of the joint cannot be influenced by further lengthening of the CFRP adherend. Also, from Figure 4.15 can be seen that with shorter overlaps (25-50 mm), the load seems to be proportional to overlap length. For longer overlaps, the failure load tends to reach a plateau independent of overlap lengths.

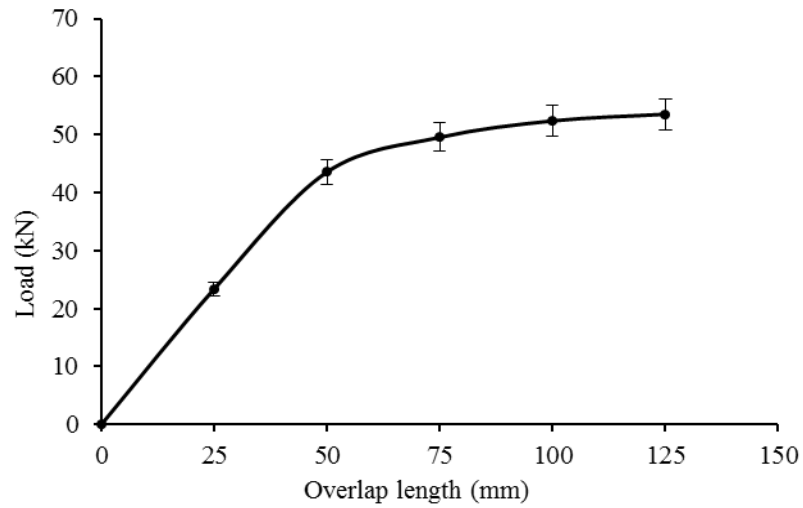


Figure 4.15: Influence of the overlap length on the failure load for $[0^\circ, 90^\circ]_6$ specimens

4.3.2.3 Effect of CFRP adherend thickness

Tests were also conducted to determine the effect of the thickness of the CFRP laminate adherend on the strength of the DLS joint. The joints were based on $[90^\circ, 0^\circ]_6$, and $[90^\circ, 0^\circ]_{12}$ specimens were used. The overlap length for both cases was 50 mm.

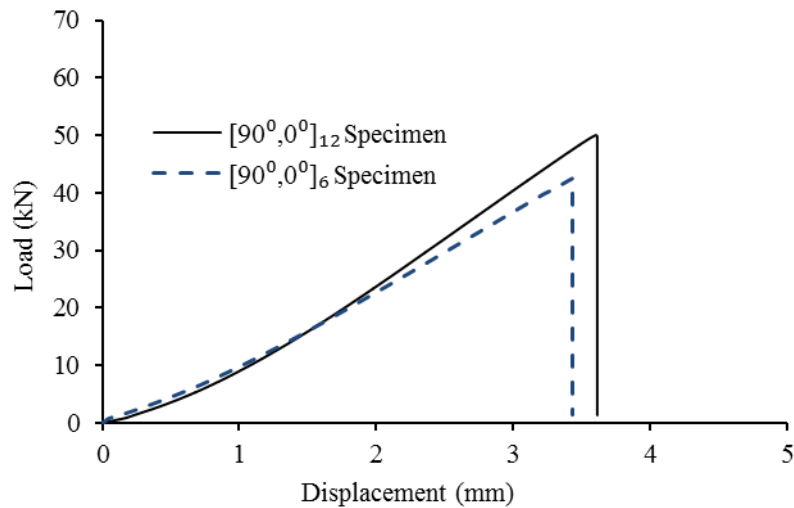


Figure 4.16: Load-displacement curves for specimens with different outer adherend thickness

The experimental results show that the $[90^\circ, 0^\circ]_{12}$ specimen has 15% higher strength than the $[90^\circ, 0^\circ]_6$ specimen, as can be seen in Figure 4.16. In this case the failure for both specimens

took place at top ply, possibly initiated by transverse cracks in the ply next to the resin layer. Figure 4.17 shows the failure surfaces.

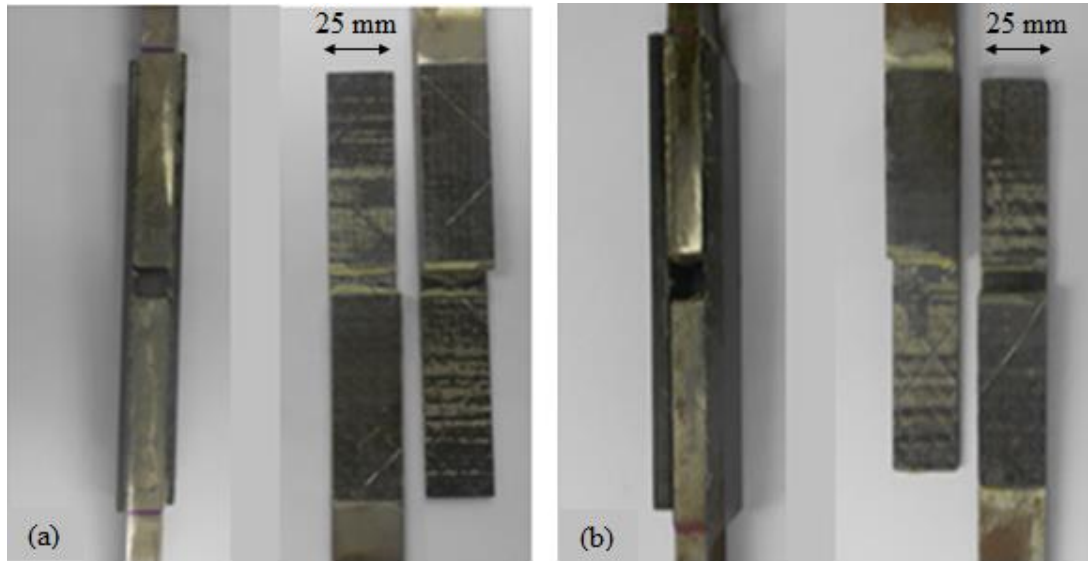


Figure 4.17: Failure surfaces for: a) $[90^\circ, 0^\circ]_6$ specimen, b) $[90^\circ, 0^\circ]_{12}$ specimen

4.4 Testing of DLS joint using the strain gauges

The double lap shear joint specimens were instrumented with foil type electrical resistance strain gauges at several points of interest. Gauges were attached to the CFRP laminate and steel adherends. Gauge numbering and the location of each gauge are illustrated in Figure 4.18.

A high speed camera was also used in an attempt to locate where failure initiates in the DLS joint. The strain gauges were used in the $[0^\circ, 90^\circ]_6$ specimen test study for assessing strain variation in the adherends (CFRP and steel) by means of monitoring the longitudinal strains at several points of interest. In addition, the strain gauges provided high sensitivity and detailed measurements of surface deformation, which can provide an information on the interaction between adherends and the adhesive layer, and yield the strain distributions in the adherends and adhesive. The DLS joint specimen was instrumented with uniaxial strain gages from Vishay (CEA-06-250UN-120) having a gauge length of 8 mm, which are capable of measurements up to 5% deformation. The manufacture data sheet is presented in Appendix C. It is important that the surface of adherend is clean and the gauge is perfectly bonded to the adherend. Therefore, the preparation procedure consisted of abrading the surface with fine emery paper and cleaning with acetone. Vishay M-Bond AE-10 Epoxy

strain gauge adhesive was used to bond the strain gauge to the adherend at the specified position. The manufacturer data sheet of the strain gauge adhesive is given in Appendix D. The locations of strain gauges on the specimen are shown in Figure 4.18. All data was automatically recorded by an Orion data logger data acquisition system shown in Figure 4.19. Typical load strain curves are presented in Figure 4.20.

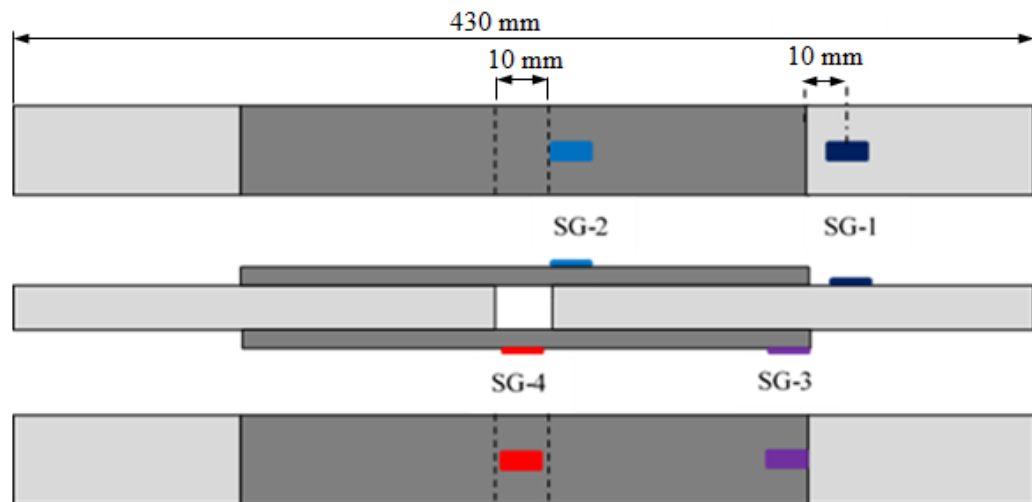


Figure 4.18: The location of strain gauges on $[0^\circ, 90^\circ]_6$ specimen with 75 mm overlap length

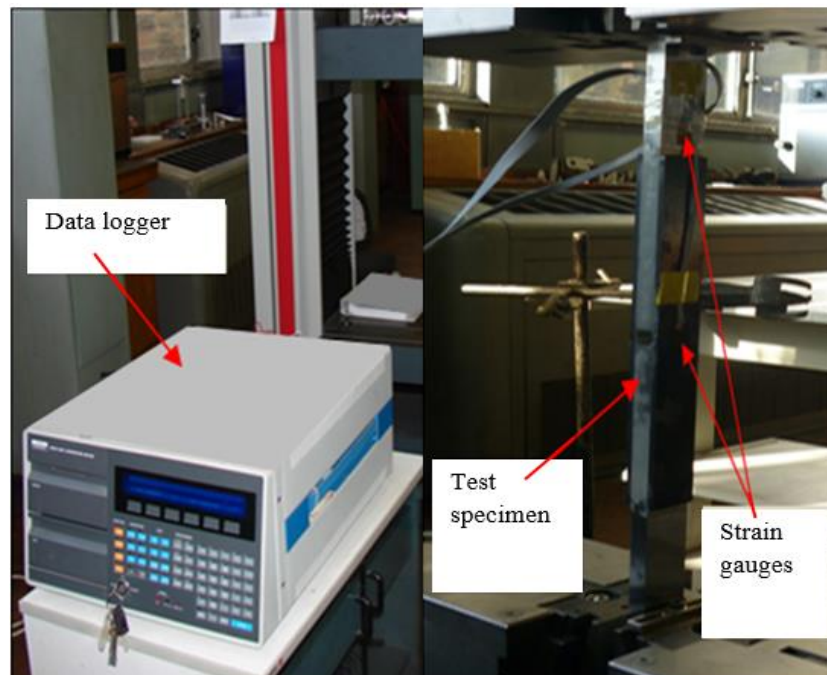


Figure 4.19: Strain gauges positions and test set up

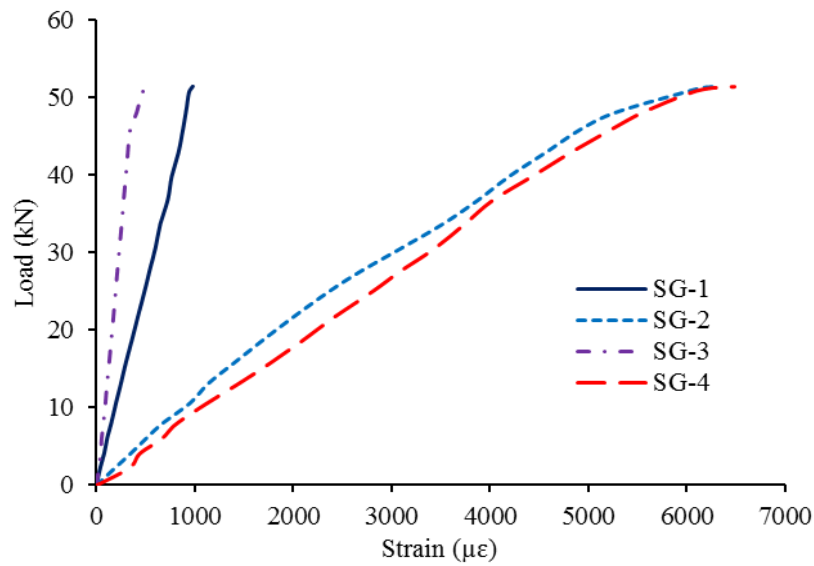


Figure 4.20: Typical curves of load vs. strain measurement for $[0^\circ, 90^\circ]_6$ specimen with 75 mm overlap length as experimentally registered on adherends. (Figure 4.18)

Figure 4.20 shows the experimentally measured load-strains for double lap shear joint specimen. It shows a linear response up to the failure load. The strains at the measurement locations follow a linear shape, which denotes that they remain within the linear elastic region of either the CFRP or the steel substrates.

The maximum strains in the CFRP have reached about 6480 $\mu\epsilon$ as given by gauge SG-4 attached to the CFRP adherend at the centre of the joint. From this Figure it can be seen that the strain value reached about 6254 $\mu\epsilon$ as given by gauge SG-2, and that all perverse strains take only positive values.

4.5 Testing of DLS joint using high speed camera

The setup for the experiments can be seen in Figure 4.21. A specimen can be seen gripped in the Zwick/Roell Z250 Universal testing machine, which provided force and extension data for each of the tests. Each specimen was gripped at 50 mm from the edge at both ends, and the test was conducted at a rate of 0.5 mm/min. A high speed camera was also used in an attempt to locate where failure initiates in the joint. This was a Photron FASTCAM – Ultima APX by Nikon which comes with its own software to adjust the camera's image settings and monitor the recorded data. When the shutter is open the camera is constantly recording, and there are various options to decide which data to retrieve.

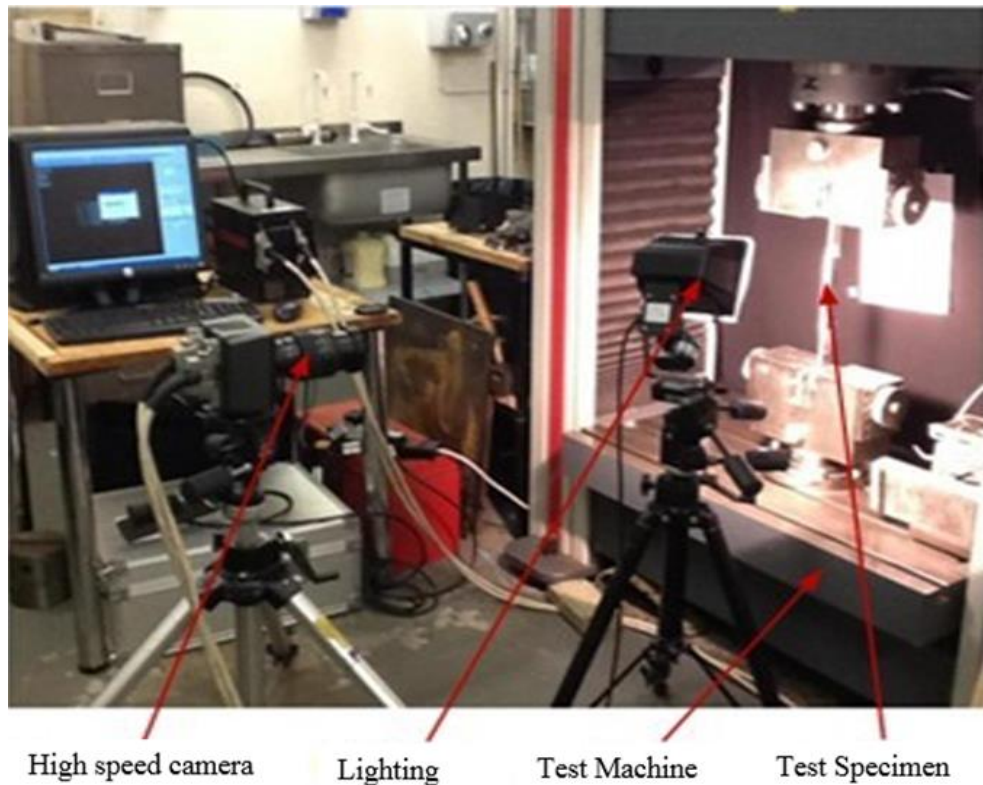


Figure 4.21: Setup for experimental investigation

The End Trigger capture option was used, which means that the record button must be clicked immediately after joint failure, and a set amount of time prior to this moment is saved to allow for editing. The higher frame rates used for this experiment allowed for about 4 seconds of video to be recorded. Due to the lack of colour in the image and the black background of the testing machine, white paper had to be pinned behind the test specimen in order for the composite material to stand out in the image.

The failure process of the $[+45^\circ, -45^\circ]$ specimen was relatively slow compared with the other two configurations. As such, the crack could be seen initiating at the centre of the joint and propagating outwards towards the end of the overlap. This was impossible for the $[0^\circ, 90^\circ]$ and $[90^\circ, 0^\circ]$ specimens which failed abruptly. The high speed camera was necessary to identify the location of failure initiation for these joints. As for the $[+45^\circ, -45^\circ]$ specimen, failure also initiated at the centre for both of these joints. Even at the highest frame rate used in this investigation, the failure process still occurs very quickly. The clearest videos were recorded with the camera set at 12500 frames per second. Setting the rate at lower levels made it impossible to identify where the crack initiates. Any higher and the resolution is

reduced to the point where the video is unclear. The software used with the camera allows settings such as brightness and contrast to be altered once the camera placement and zoom settings have been finalised. The failure of a $[90^\circ, 0^\circ]$ specimen with a 125 mm overlap length can be seen in a series of frames in the Figure 4.22. The images clearly show the crack initiating at the centre of the joint and propagating outwards towards the end of the overlap.

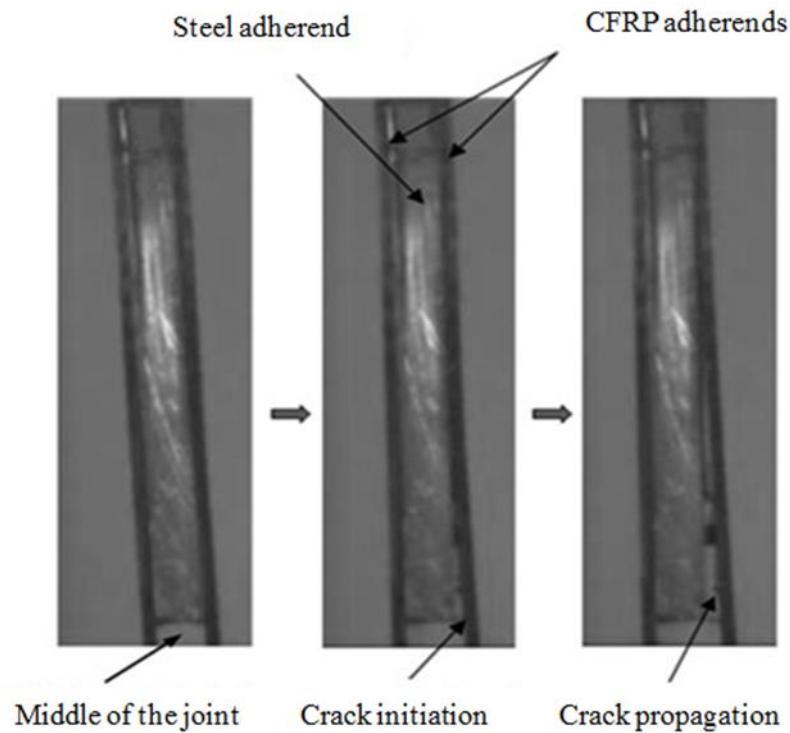


Figure 4.22: Failure initiation and growth in the DLS joint

Chapter 5

5 Numerical analysis of DLS joint based on strength of material approach

5.1 Introduction

Numerical modelling of the adhesive joints was carried out using the finite element method. Finite element analysis is a powerful tool used in the industry mainly to simulate stresses and strains in any structural part, given the material properties and loading configuration. The effectiveness of finite element methods for modelling adhesive joints has been demonstrated in recent years [189, 190, 191, 192, 193]. This chapter details numerical models of the double lap shear joint created and analysed during this study. A commercially available finite element code, ABAQUS, was used for the numerical analysis. The geometry and meshing of the two dimensional (2D) model was carried out using Abaqus/CAE.

5.2 Geometry and boundary conditions

The geometry and configuration of the double lap shear (DLS) joint used in this research is shown in Figure 4.1, and the nomenclature used with reference to DLS joint geometry is given in Figure 5.1.

In order to optimise the computational cost of the analysis, symmetry in the joint geometry and loading was employed. The joint can be simplified to one quarter of the specimen, thus making the model easier to create, and reducing the complexity of the FEA simulation and the computational time. The loading and boundary conditions are shown in Figure 5.1.

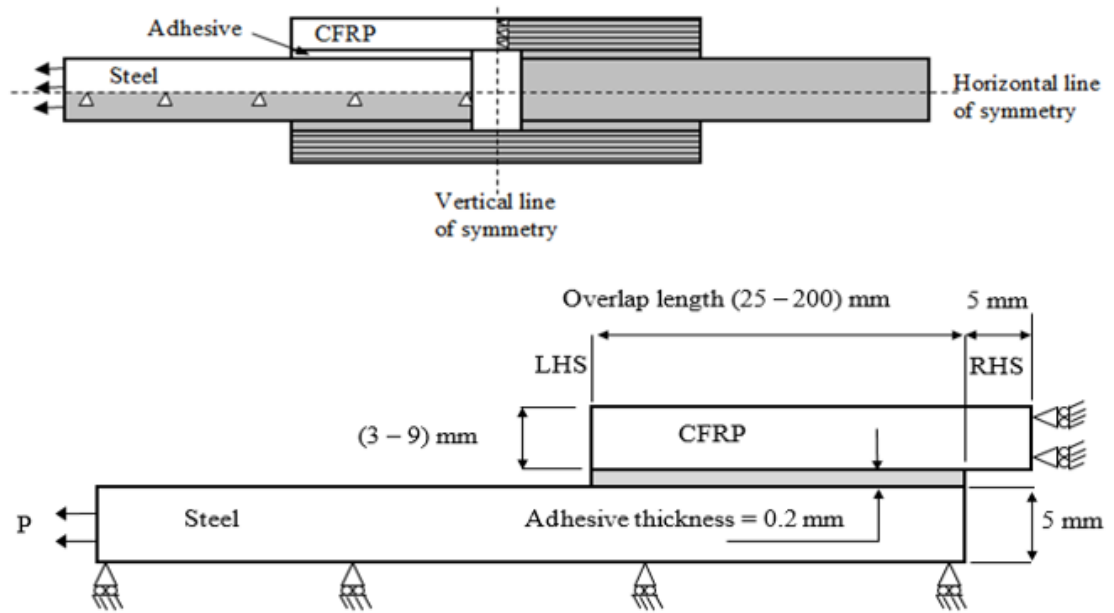


Figure 5.1: Loading and boundary conditions of the DLS joint

5.3 Meshing Methodology

Meshing along the DLS joint is challenging, owing to the presence of a very thin adhesive layer, compared to the overall dimensions of the joint. The presence of a corner at the ends of the overlap further complicates the meshing requirements. There are numerical singularities of stresses at re-entrant corners of the DLS joints, the stresses depending on the mesh size used, and how close to the singular points the stresses are taken.

The methodology considered in meshing the DLS joint is to use dissimilar meshes in the adhesive layer and adherends, and to join them using tie constraints. Tie constraints allow for translational and rotational motion, as well as all other active degrees of freedom, equal for nodes on both sides of the tie constraint. Therefore a coarse mesh may be used in the adherends and a fine mesh may be used in the adhesive layer. In this analysis, an attempt was made to model the CFRP laminate at its constituent level i.e. the resin layer and the unidirectional (UD) laminates.

To gain a greater insight into the CFRP composite, a Normasky microscope was used, which provided an excellent view of the layers in the composite. Figure 5.2a shows an image taken from the Normasky microscope. From this image we can see that the composite consists of fibre layers and very thin layers of epoxy based matrix between those fibre layers. The

average thickness of the layers was found to be 0.2 mm for the fibre layers and 0.05 mm for the epoxy matrix. Using these values, a 2D representation of the CFRP was created, as shown in Figure 5.2b.

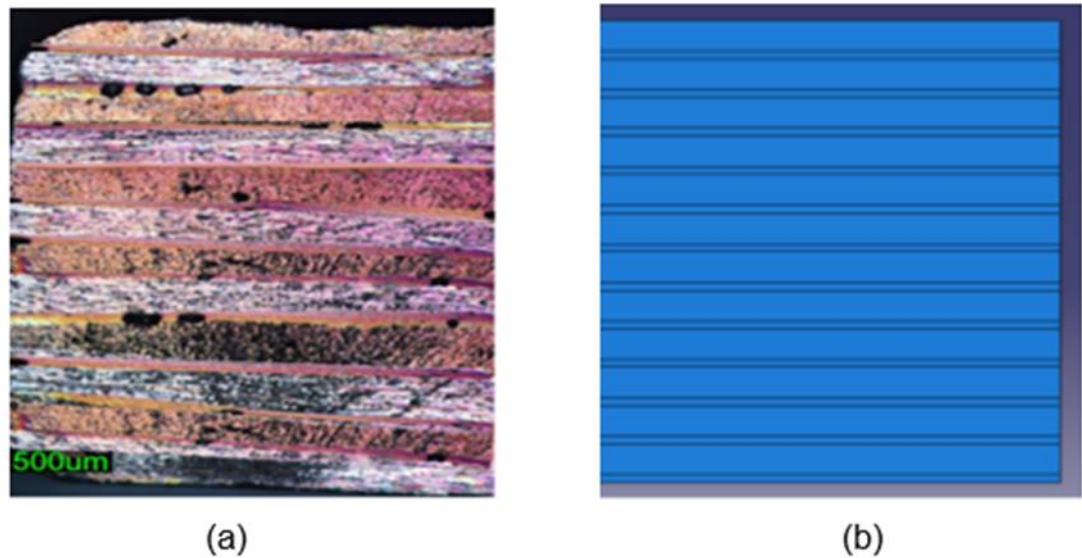


Figure 5.2: Image of $[0^\circ, 90^\circ]_6$ CFRP laminate (a) using Normasky microscope, (b) modelled in Abaqus

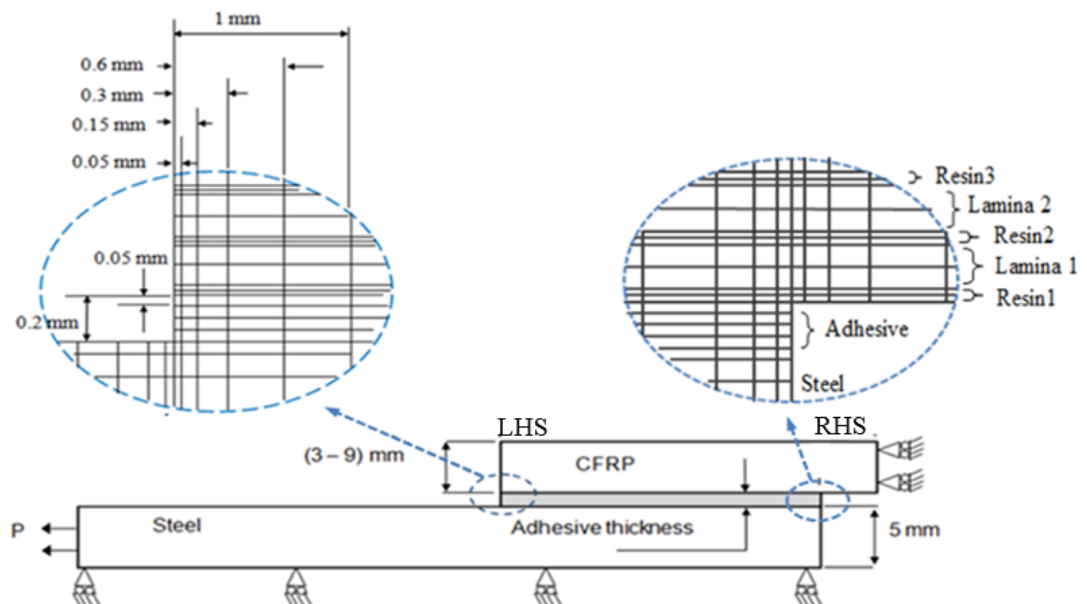


Figure 5.3: Finite element mesh of the DLS joint

Each ply was modelled to represent the fibre oriented in different direction. The epoxy matrix was modelled with its isotropic, elastic properties. The steel and adhesives were assigned elastic-plastic properties. A number of meshing methods are available in ABAQUS and the geometry was meshed based on its shape, as shown in Figure 5.3. The 2D model was used taking into consideration the non-linear material and geometry factors, using the plane-strain quadratic elements and rectangular 8-noded elements, CPE8R (reduced integration). The coarse mesh was far from the overlap region that was the area of interest during the analysis. The adherends were meshed with multiple elements through thickness to capture their bending behaviour accurately.

5.4 Material properties

Composite laminates are formed by combining individual layers (lamina) into a multi-layered structure. A laminate is a bonded stack of lamina with various orientations of principal material directions in the laminate, as in Figure 5.4. The layers of a laminate are usually bonded together by the same matrix material that is used in individual lamina.

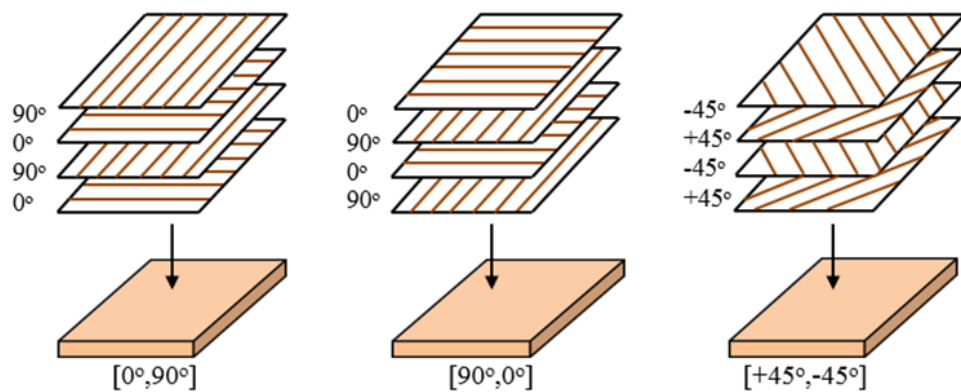


Figure 5.4: Schematic illustrations of laminates with various layup sequences

The mechanical behaviours of fibre reinforced composite materials are highly dependent on the direction of loading. For instance, considering a unidirectional laminate, the elastic modulus parallel to the fibre direction, E_{LL} , (referred to as the longitudinal direction) is significantly different from the elastic modulus perpendicular to the fibre direction, E_{TT} , (referred to as the transverse direction).

The L and T directions are referred to as the material axes. In this case, the L-axis is defined to be parallel to the fibres (0°), and the T-axis is defined to be perpendicular to the fibres (90°) see Figure 5.5a. If the plate is loaded parallel to the fibres, the modulus of elasticity E_{11} approaches that of the fibres. If the plate is loaded perpendicular to the fibres in the T-axis or 90° direction, the modulus E_{22} is much lower. However, if the load is applied at an acute angle θ to the fibre direction, see Figure 5.5b, the elastic response along the loading axis (1 and 2 directions) can be calculated by the transformation rules [194, 20] from the properties measured along the materials axes (L and T) where;

$$E_{11} = E_{LL} \left[\cos^4 \theta + \frac{E_{LL}}{E_{TT}} \sin^4 \theta + \frac{1}{4} \left(\frac{E_{LL}}{G_{LT}} - 2\nu_{LT} \right) \sin^2 2\theta \right]^{-1} \quad (5.1)$$

$$E_{22} = E_{LL} \left[\sin^4 \theta + \frac{E_{LL}}{E_{TT}} \cos^4 \theta + \frac{1}{4} \left(\frac{E_{LL}}{G_{LT}} - 2\nu_{LT} \right) \sin^2 2\theta \right]^{-1} \quad (5.2)$$

Note that in equations (5.1) and (5.2) the material parameters needed include transformation angle (θ), in-plane shear modulus (G_{LT}), in-plane Poisson's ratio (ν_{LT}) and the longitudinal and transverse elastic moduli (E_{LL} and E_{TT}). For unidirectional composites, in-plane shear modulus follows the “Rule of Mixtures” and can be determined from the constituent matrix and fibre properties (see Table 3.3).

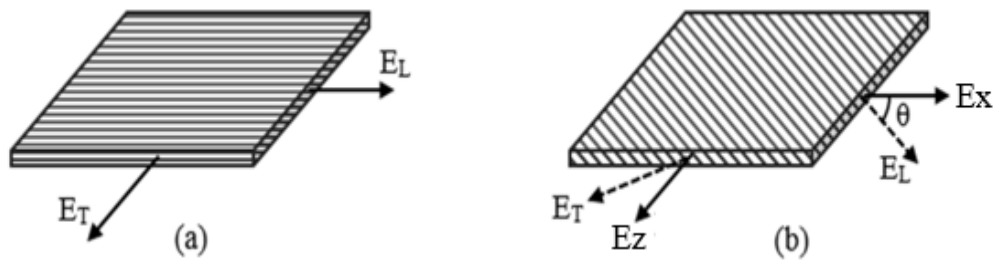


Figure 5.5: Illustration of shear strain produced by tensile loading of a fibre composite

The transformation of (ν_{LT}) and (G_{LT}) along the material axes into (ν_{12}) and (G_{12}) along the loading axes is given by:

$$\nu_{12} = \frac{E_{11}}{E_{LL}} \left[\nu_{LT} - \frac{1}{4} \left(1 + 2\nu_{LT} + \frac{E_{LL}}{E_{TT}} - \frac{E_{LL}}{G_{LT}} \right) \sin^2 2\theta \right] \quad (5.3)$$

$$G_{12} = \left[2 \left(\frac{2}{E_{LL}} + \frac{2}{E_{TT}} - \frac{1}{G_{LT}} + \frac{4\nu_{LT}}{E_{LL}} \right) \cos^2 \theta \sin^2 \theta + \frac{1}{G_{LT}} (\sin^4 \theta + \cos^4 \theta) \right]^{-1} \quad (5.4)$$

The material properties assigned to each part are given in Table 5.1. This includes data from manufacturers, mechanical testing and calculation methods.

Table 5.1: Material properties of carbon-epoxy composite, adhesives and mild steel,

Property		Carbon fibre lamina			Adhesive Araldite 2015	Epoxy resin matrix LY3505/XB3405	Mild Steel
		0° layer	90° layer	±45° layer			
Young's modulus (GPa)	E ₁₁	139.4 ¹	7.66 ¹	9.85 ¹	1.8 ¹	3.5 ²	210 ²
	E ₂₂	7.66 ¹	139.4 ¹	9.85 ¹	-	-	-
	E ₃₃	7.66 ¹	7.66 ¹	7.66 ¹	-	-	-
Shear modulus (GPa)	G ₁₂	3.68 ¹	3.68 ¹	7.07 ¹	0.662 ¹	1.296 ¹	80.7 ¹
	G ₁₃	3.68 ¹	2.94 ¹	2.94 ¹	-	-	-
	G ₂₃	2.94 ¹	3.68 ¹	2.94 ¹	-	-	-
Poisson's ratio	ν ₁₂	0.26 ¹	0.014 ¹	0.34 ¹	0.36 ²	0.35 ²	0.3 ²
	ν ₁₃	0.26 ¹	0.304 ¹	0.304 ¹	-	-	-
	ν ₂₃	0.304 ¹	0.26 ¹	0.304 ¹	-	-	-
Tensile strength (MPa)		1400 ²	-	-	40 ³	85 ²	450 ²
Transverse strength (MPa)		86 ²	-	-	-	-	-
Shear strength (MPa)		137 ²			24 ³	51 ²	270 ²

Note: 1- Calculation data, 2- Manufacture data, and 3- Test data.

The maximum tensile strength of the adhesive is known to be 40 MPa. Using the maximum tensile strength and Young's modulus of the material, the strain at which yielding occurs was calculated, and used to allow for plastic deformation in the model (see Table 5.2).

Table 5.2: Properties of Araldite 2015 in the plastic region

Yield stress (MPa)	Plastic strain
39.999	0.000
40.000	0.022
40.001	0.044
40.002	0.060

5.5 Mesh convergence

A mesh convergence study was carried out with three different finite element meshes, as shown in Figure 5.6, Figure 5.7 and Figure 5.8. Therefore, the problem is considered to be two dimensional. The meshes were generated using eight-node quadrilateral 2D plane strain solid element (type CPE8R). Four elements were used through thickness of the adhesive, two for the resin layer and two for the carbon fibre layer. Three different mesh types were used to model the double lap joints and subjected to the same level of tensile loads.

The maximum principal stress, shear stress and peel stress at the middle of the adhesive layer for 2D meshes are plotted in Figure 5.9, Figure 5.10 and Figure 5.11 respectively. The stress distribution by the three meshes were very similar in the middle of the overlap, with the differences seen in the region of the overlap edges. The results of Mesh 2 and Mesh 3 were in good agreement and Mesh 3 was selected for use in further analysis, as it was computationally less expensive.

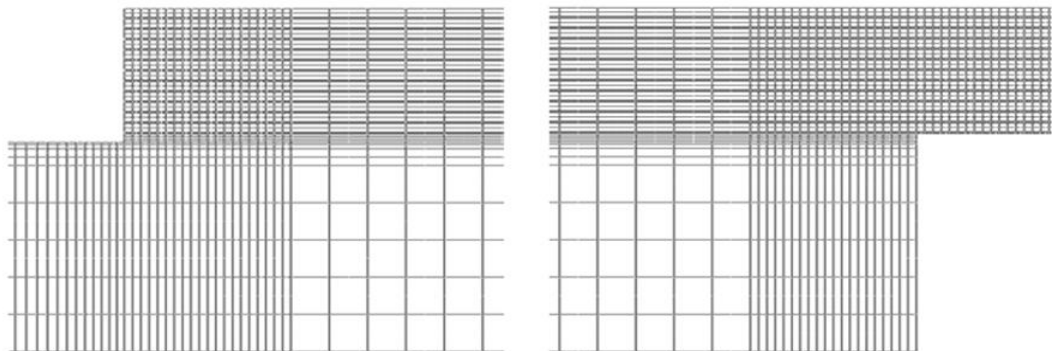


Figure 5.6: Mesh distribution in regions LHS and RHS for the $[0^\circ, 90^\circ]_6$ model, element ratio 0.5 (mesh 1)

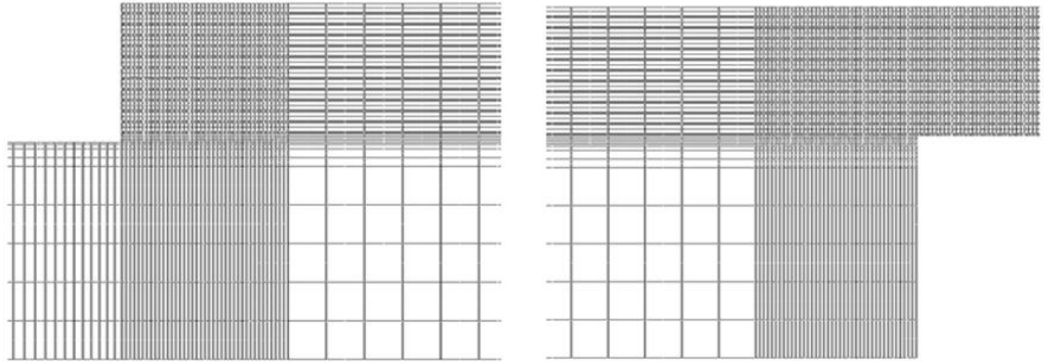


Figure 5.7: Mesh distribution in regions LHS and RHS for the $[0^\circ, 90^\circ]_6$ model, element ratio 1(mesh 2)

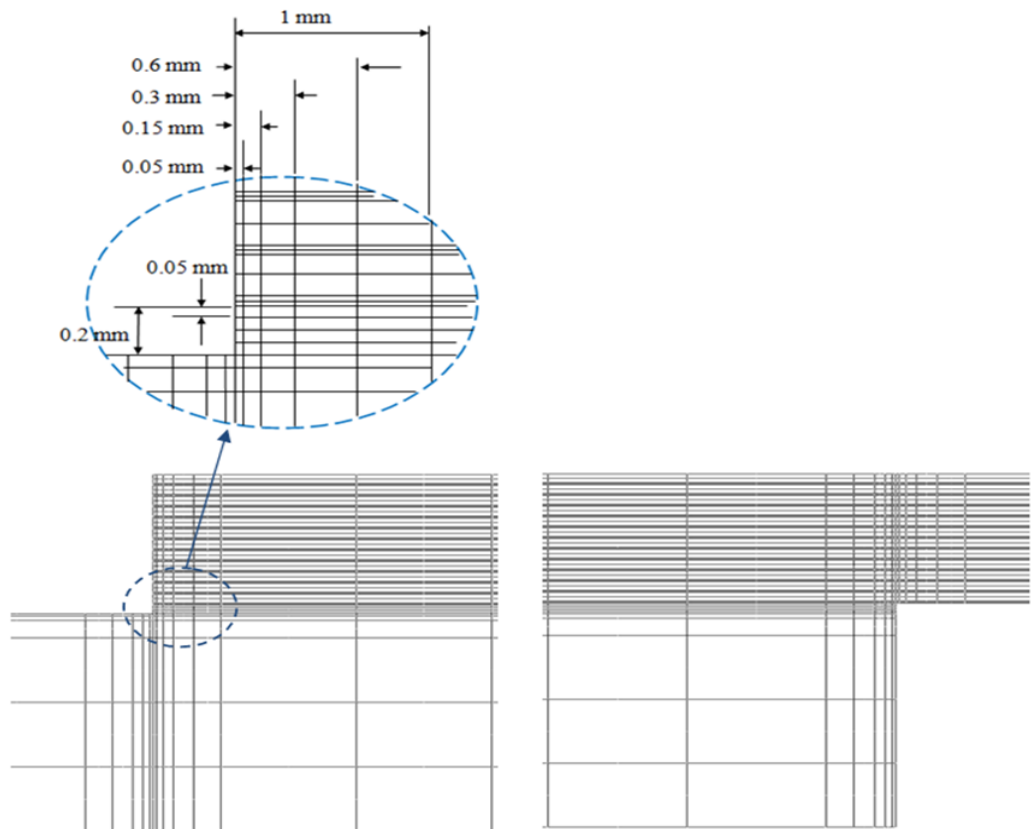


Figure 5.8: Mesh distribution in regions LHS and RHS for the $[0^\circ, 90^\circ]_6$ model (mesh 3)

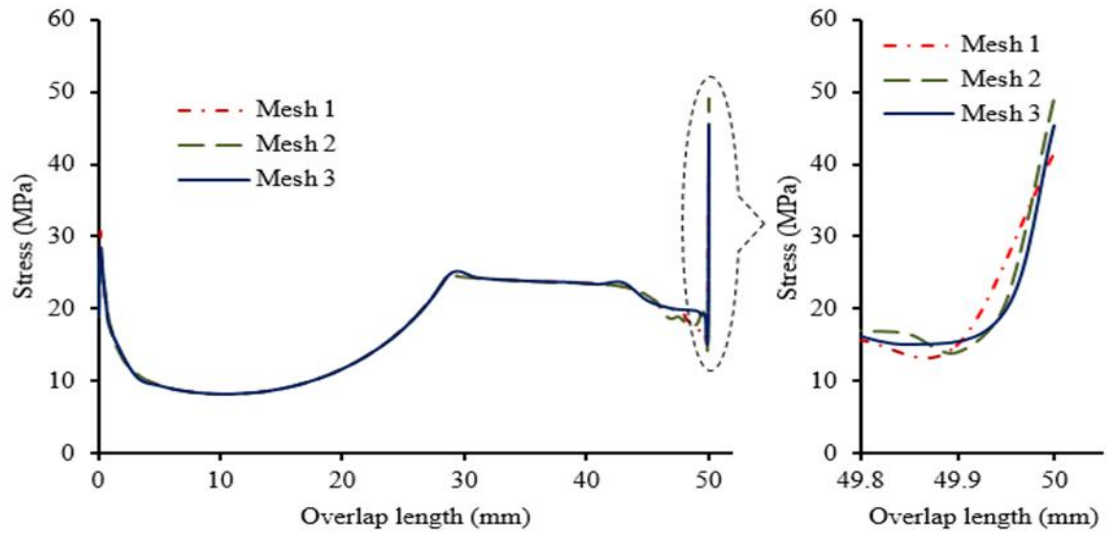


Figure 5.9: Maximum principal stress distributions along the centre of adhesive layer for $[0^\circ, 90^\circ]_6$ model with 50 mm overlap at different meshes.

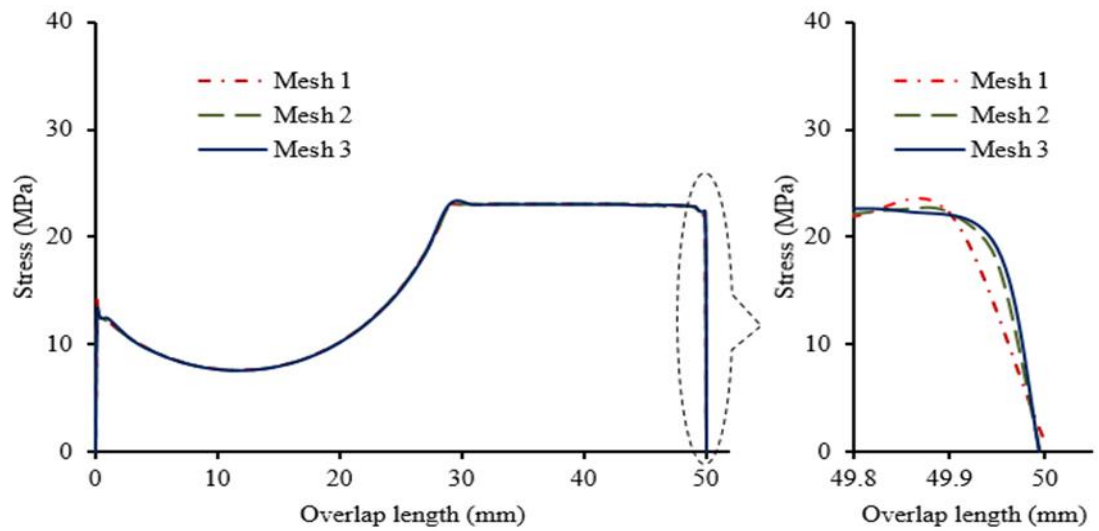


Figure 5.10: Shear stress distributions along the centre of adhesive layer for $[0^\circ, 90^\circ]_6$ model with 50 mm overlap at different meshes.

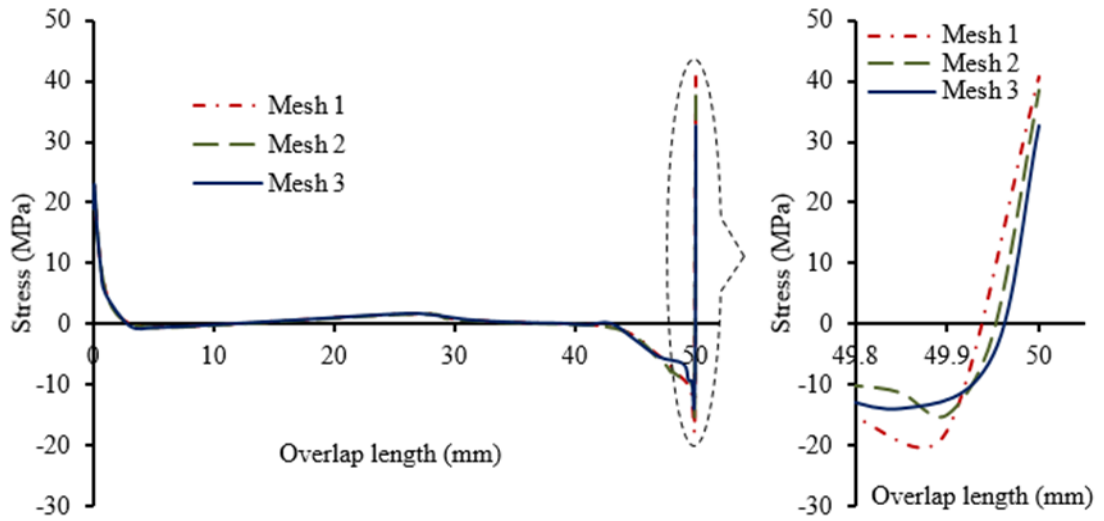


Figure 5.11: Peel stress distributions along the centre of adhesive layer for $[0^\circ, 90^\circ]_6$ model with 50 mm overlap at different meshes.

5.6 Stress distributions

The mechanical properties of various materials were based on the values in Table 5.1. As mentioned before, in this analysis an attempt was made to model the laminate as its constituent parts i.e. resin and UD plies. Each ply was modelled to represent the 0° and 90° directions. For the $(+45^\circ/-45^\circ)$ joint, the ply was modelled with different fibre angles $+45^\circ$ and -45° considered for analysis. The mesh size was adjusted in all models for a similar element size at the overlap edges. This is to ensure that the comparative stresses are measured at the same locations. The stress magnitudes for the adhesive and resin matrix were subsequently evaluated at a prescribed distance from the free surface of the inner adherend. The node at the free edge of the adhesive was ignored, due to spurious effects at this point as a result of the stress tip singularity [195]. In addition, failure also took into consideration the spread of principal stresses at a level higher than maximum tensile stress over a finite zone at the joint edge, in accordance with Clarke and McGregor's approach [196]. Singularity issues at the interface of the adhesive and laminate were dealt with according to the third-node stress consideration proposed by Gleich et al [197]. In this region the critical stresses in adhesive and composites are taken into consideration to assess joint failure.

5.6.1 Effect of stacking sequence

$[0^\circ, 90^\circ]_6$, $[90^\circ, 0^\circ]_6$ and $[+45^\circ, -45^\circ]_6$ models with 75 mm overlap were used to study the effect of orientations on stress distribution in each model. The mechanisms of failure of these models with different orientations are presented in Figure 5.12, which shows the contours of maximum principal stresses for these joints. As mentioned before, the maximum stresses occur at the centre of the joint (RHS-Figure 5.3). The maximum principal stress distribution along the upper interface of the adhesive layer is shown in Figure 5.13, with the peak stresses for the three cases at the RHS of the joint. In addition, Table 5.3 summarises the adhesive stresses which were taken at the middle of the adhesive and its interfaces with the adherends. The table highlights the stress values that exceed the relevant failure strength.

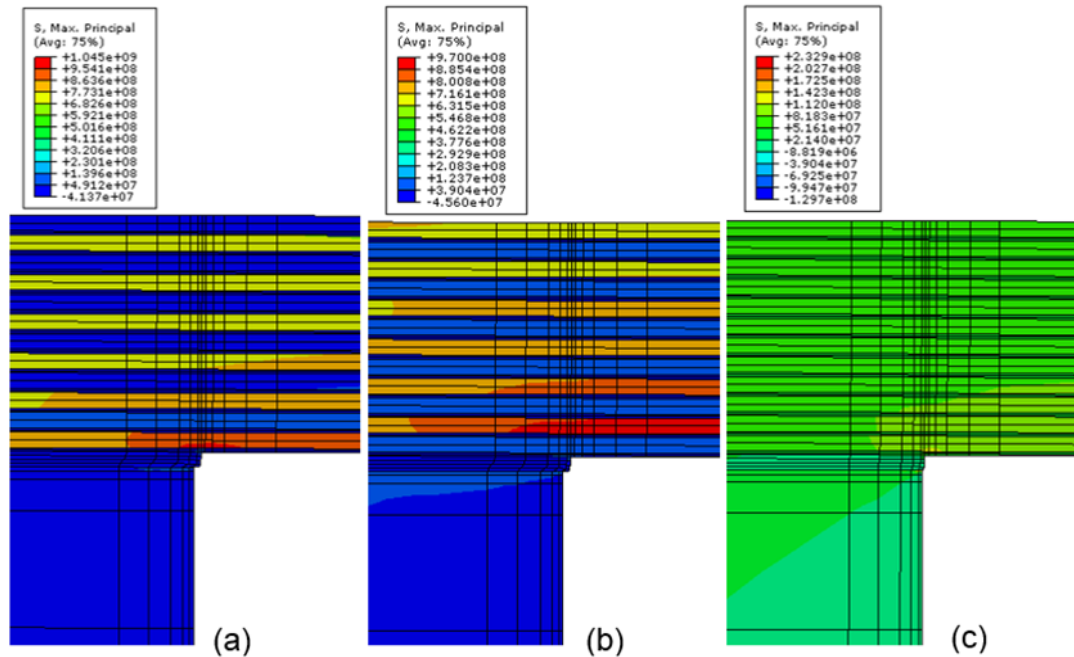


Figure 5.12: Contours of maximum principal stress in the CFRP for different models with 75 mm overlap: (a) $[0^\circ, 90^\circ]_6$, (b) $[90^\circ, 0^\circ]_6$ and (c) $[+45^\circ, -45^\circ]_6$ at failure loads (50 kN, 47.5 kN and 17 kN) respectively

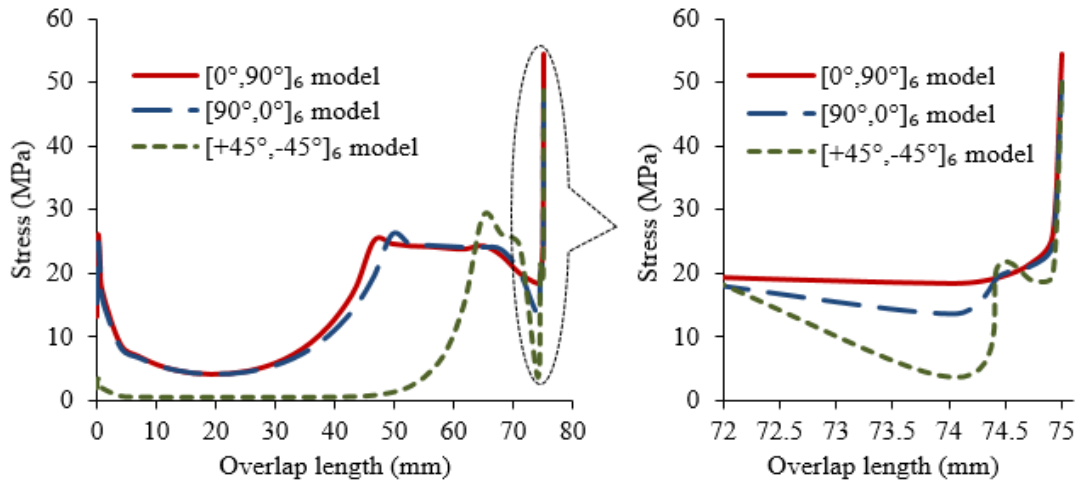


Figure 5.13: Maximum principal stress distribution along the upper of adhesive layer for various models with 75 mm overlap at failure loads

Figure 5.14-5.16 show the variation of the longitudinal (S_{11}), transverse (S_{22}) and shear (S_{12}) stresses in the composite, at failure loads (from experiments). The stresses were taken at the middle of the top ply of laminates. All peak stresses are below the strength values for the composite given in Table 5.1. However, the longitudinal direct stress (S_{11}) for the $[90^\circ, 0^\circ]_6$ model (Figure 5.15) is close to the ultimate transverse strength of the laminate, and hence there is a possibility of adherend failure in this case, as indicated earlier in Figure 4.12b (Section 4.3.2.1). This transverse crack in the 90° ply may have extended to the resin-rich interface between it and the 0° ply. Leading to delamination. Transverse cracking may also be initiated from defects in the matrix.

In addition, Table 5.4 shows the maximum stress values in the composite, including the matrix resin at the RHS of the three models. The maximum tensile strength of the resin is 85 MPa. As can be seen from the table, the resin tensile stress (S_{11}) exceeds this for the $[+45^\circ, -45^\circ]_6$ model. Also, the tensile stress (S_{11}) of the top ply, which is 165 MPa, can cause delamination failure either in shear or transverse stresses, or both. The maximum principal and tensile stress (S_{11}) in the composite is 911 MPa for the $[90^\circ, 0^\circ]_6$ model, which is very close to ultimate tensile strength of the UD laminate. However, the values at the end of the table indicate that the shear (S_{12}) and peel (S_{22}) stresses in the matrix resin for the $[90^\circ, 0^\circ]_6$ model are twice those for the $[0^\circ, 90^\circ]_6$ model. However, being well below the respective strength values of the matrix resin, these are unlikely to initiate failure.

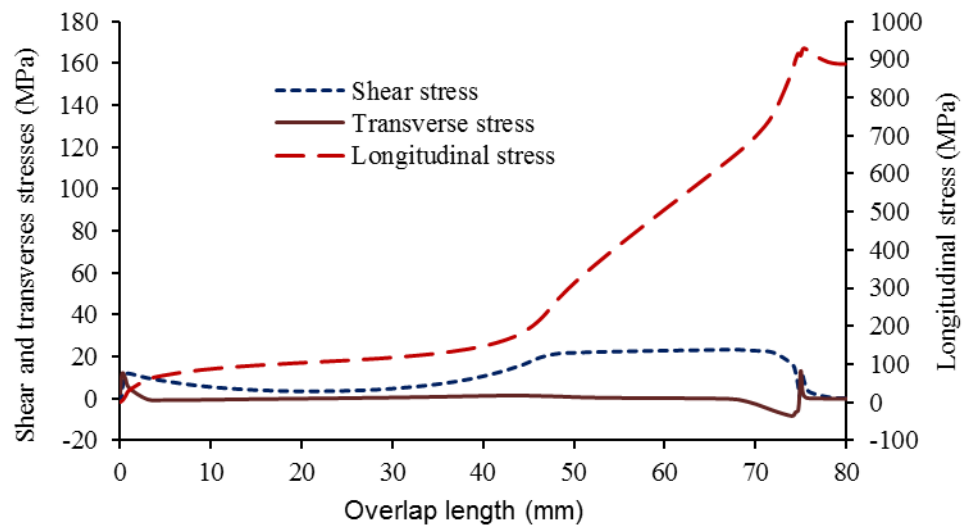


Figure 5.14: Stresses distribution along the centerline of the ply next to the bondline for $[0^\circ, 90^\circ]_6$ model at failure load (50 kN)

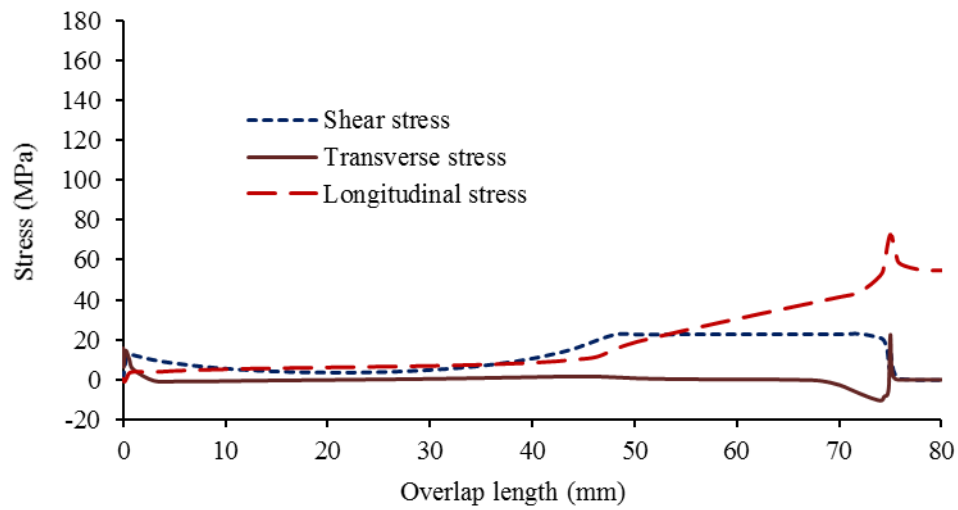


Figure 5.15: Stresses distribution along the centerline of the ply next to the bondline for $[90^\circ, 0^\circ]_6$ model at failure load (47.5 kN)

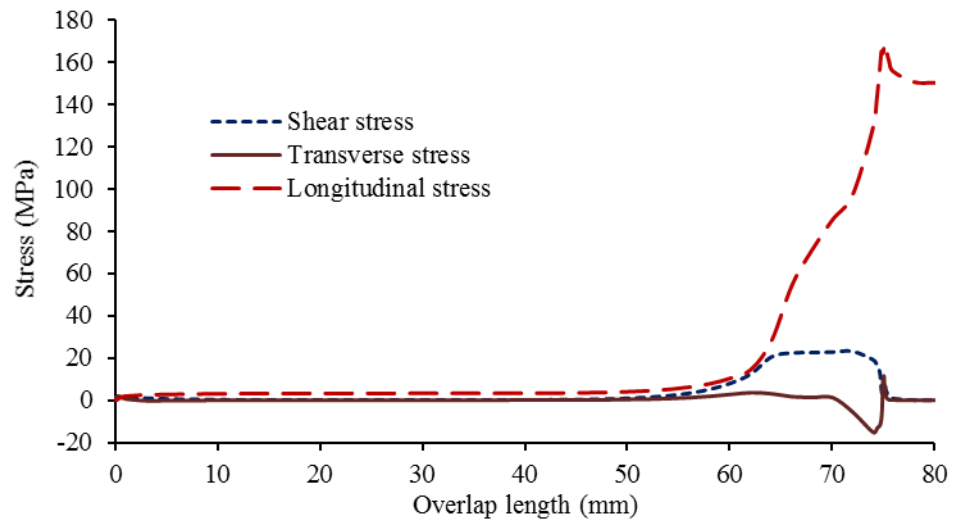


Figure 5.16: Stresses distribution along the centerline of the ply next to the bondline for $[+45^\circ, -45^\circ]_6$ model at failure load (17 kN)

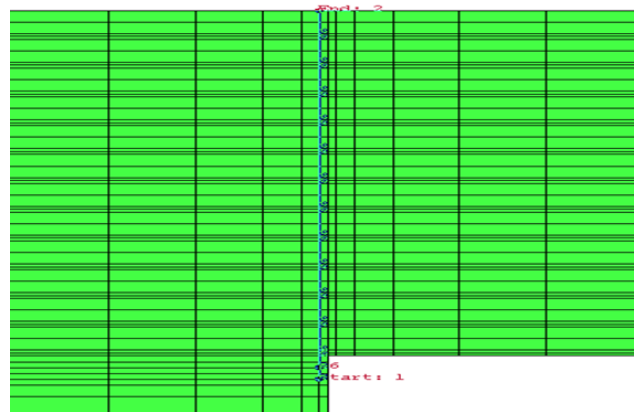


Figure 5.17: Data path through the thickness of the adhesive and CFRP laminate (at RHS)

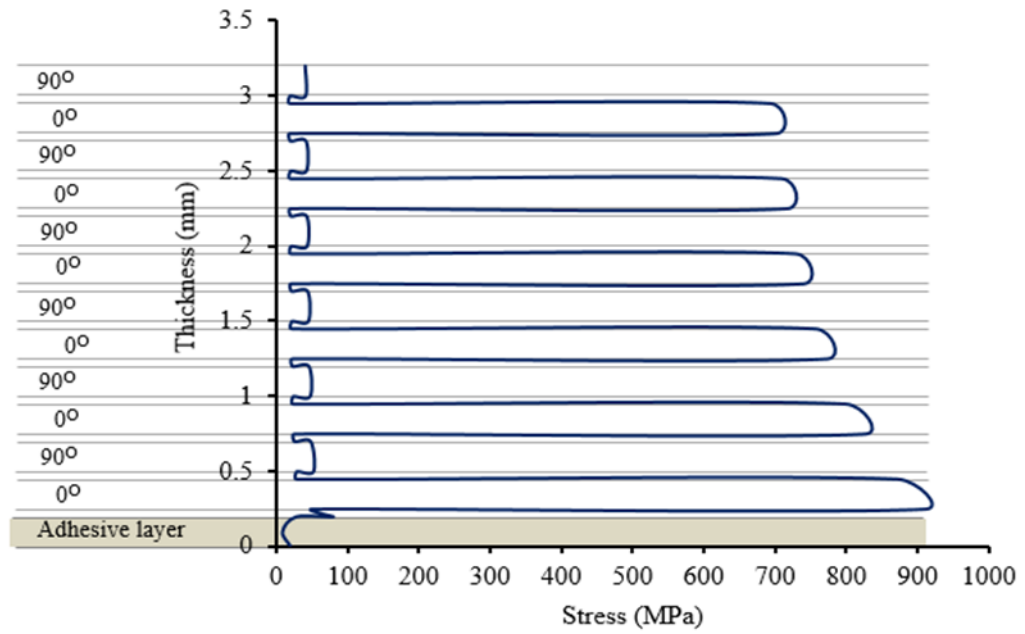
A further data path was created through the thickness of the composite laminate near the centre of the DLS joint in order to show stress distribution through the various layers Figure 5.17.

Table 5.3: Stress results through the adhesive layer at failure loads (Figure 5.12), the numbers in bold indicate maximum critical stresses.

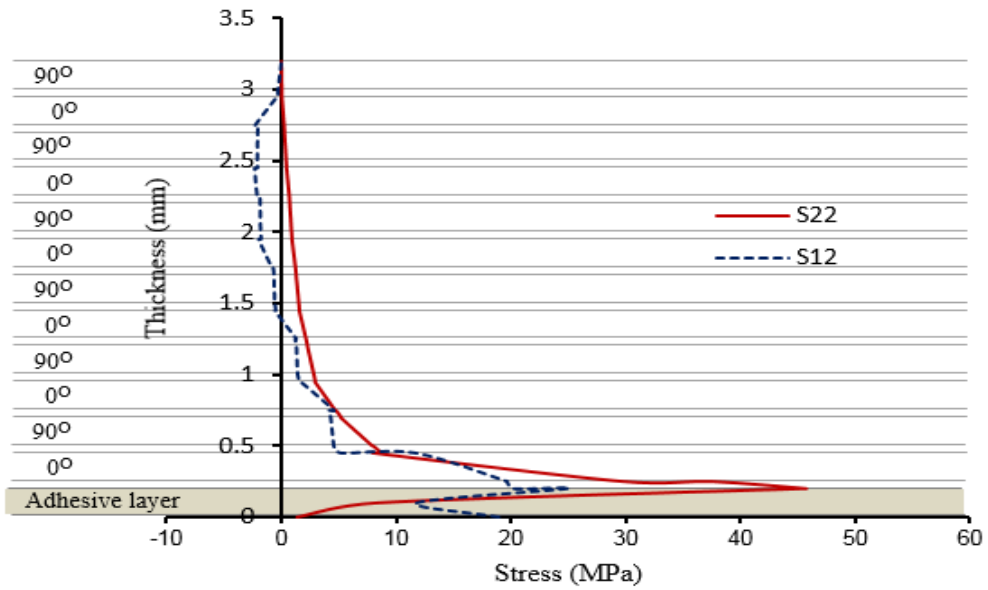
	Stress (MPa)	Data path	[0°,90°] ₆ model		[90°,0°] ₆ model		[+45°,-45°] ₆ model	
			LHS	RHS	LHS	RHS	LHS	RHS
Adhesive layer	Max Principal	Upper	13.3	54.5	15.2	49.8	2.05	50.2
		Middle	25.6	20.4	25.6	17.1	3.74	16.7
		Lower	40.1	13.9	37.5	17.3	5.07	17.1
	Max S11	Upper	29.4	28.8	3.3	28.1	0.05	33.8
		Middle	0.56	-3.34	0.05	-4.76	0.06	-1.52
		Lower	10.5	-14.1	10.9	-76.3	2.14	-62.1
	Max S12	Upper	3.52	14.8	1.81	16.4	0.26	19.1
		Middle	8.57	11.8	7.24	10.1	0.79	10.1
		Lower	17.6	24.5	15.9	24.2	2.1	24.1
	Max S22	Upper	12.1	45.3	15.1	35.9	2.01	22.1
		Middle	22.7	8.3	23.5	24.4	3.4	-3.22
		Lower	29.3	-62.9	27.8	-72.8	3.56	-72.2

Table 5.4: Stress results through the laminate and resin layers from numerical analysis at failure load (Figure 5.12), the numbers in bold indicate maximum critical stresses.

	Stress (MPa)	Data path	[0°,90°] ₆ model		[90°,0°] ₆ model		[+45°,-45°] ₆ model	
			LHS	RHS	LHS	RHS	LHS	RHS
Composite	Max Principal	First resin	25.7	65.3	25.7	70.6	3.47	92.5
		First lamina	17.1	911	19.8	74.3	2.54	165
		Second resin	12.6	30.2	18.3	38.8	2.1	62.1
	Max S11	First resin	8.6	50.1	10.2	58.4	1.56	85.6
		First lamina	6.45	911	2.5	71.6	0.4	165
		Second resin	5.2	28	6.04	34.7	0.82	61.5
	Max S12	First resin	13.8	20.1	11.7	19.1	1.6	18.7
		First lamina	7.06	11.7	1.2	13	1.2	9.5
		Second resin	4.3	5.12	8.6	10.3	0.83	5.8
	Max S22	First resin	14.6	37.9	16.8	39.5	2.1	40
		First lamina	12.2	11.5	1.4	12.1	1.9	11.4
		Second resin	9.9	7.72	12.3	14.6	1.57	7.6

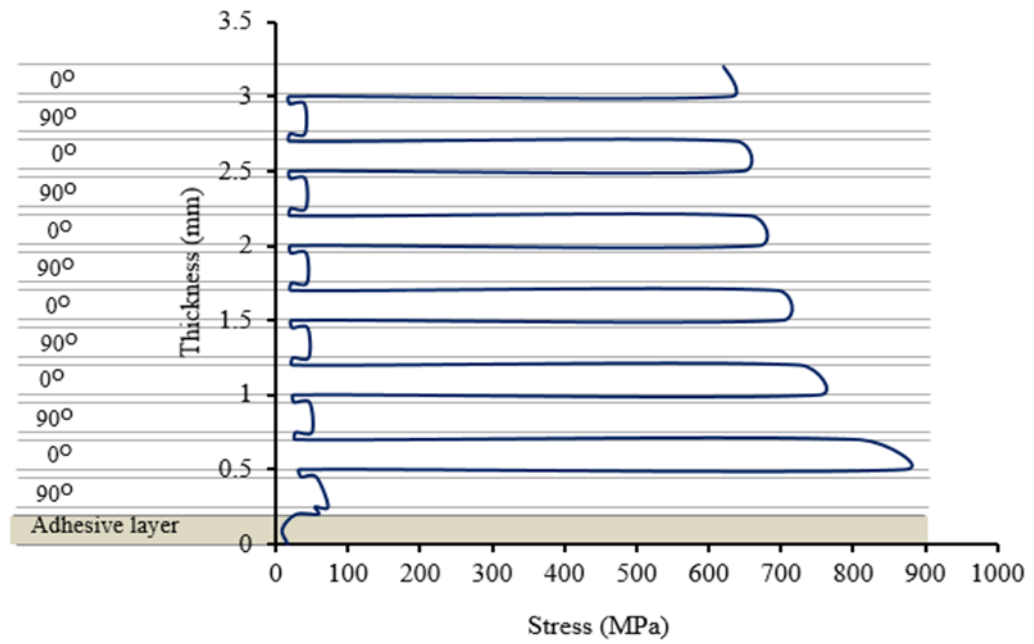


(a)

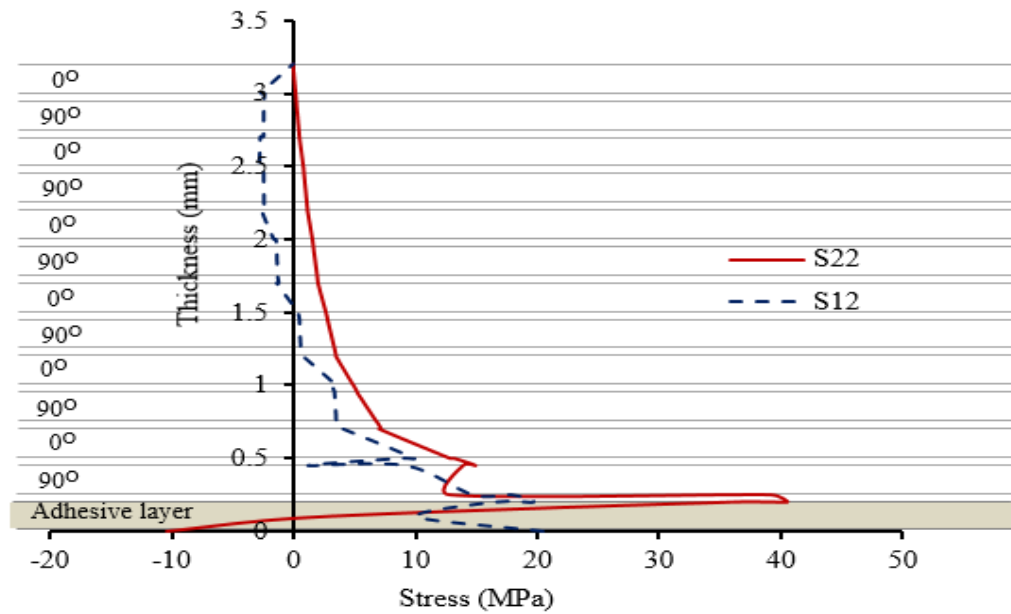


(b)

Figure 5.18: Stress distributions through the thickness of adhesive and CFRP laminate of $[0^\circ, 90^\circ]_6$ model; (a) Tensile stress (S_{11}), (b) Peel stress (S_{22}) and Shear stress (S_{12}) at data path (Figure 5.17)

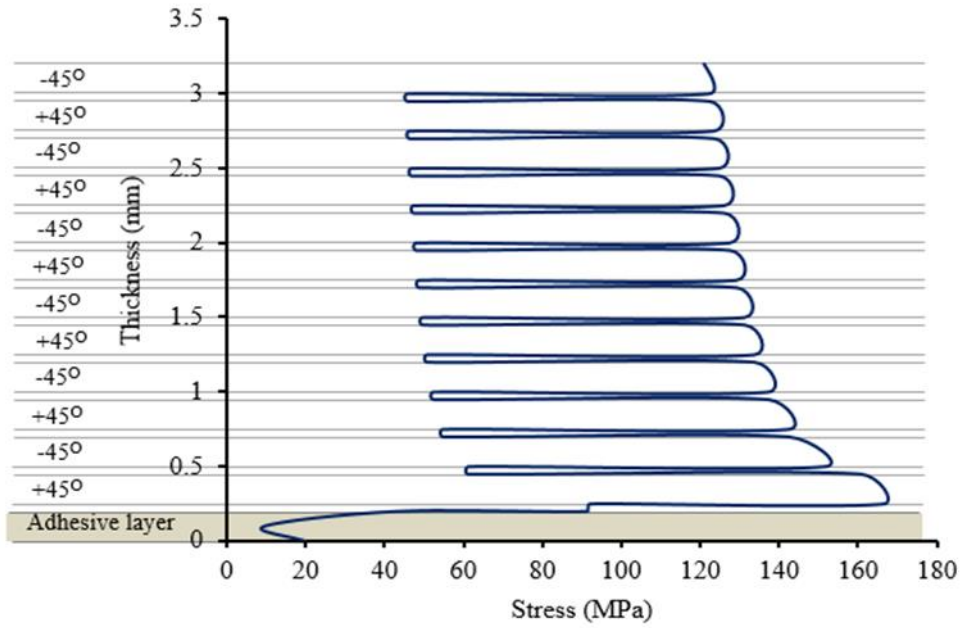


(a)

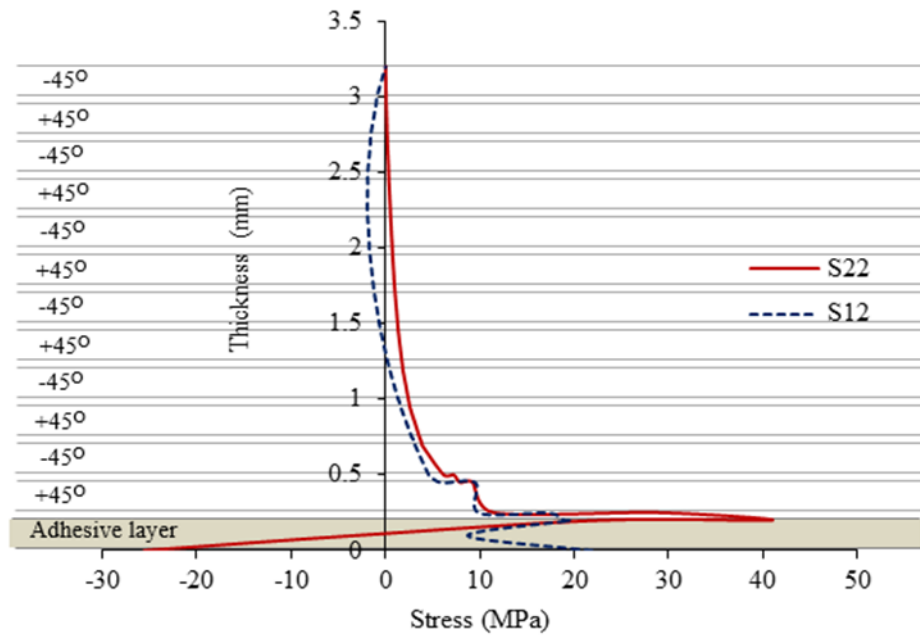


(b)

Figure 5.19: Stress distributions through the thickness of adhesive and CFRP laminate of $[90^{\circ}, 0^{\circ}]_6$ model; (a) Tensile stress (S11), (b) Peel stress (S22) and Shear stress (S12) at data path (Figure 5.17)



(a)



(b)

Figure 5.20: Stress distributions through the thickness of adhesive and CFRP laminate of $[+45^\circ, -45^\circ]_6$ model; (a) Tensile stress (S11), (b) Peel stress (S22) and Shear stress (S12) at data path (Figure 5.17)

Different DLS joints subjected to failure tensile loading, tensile (S11), peel (S22) and shear (S12) stresses distribution, through the thickness of adhesive and the CFRP laminate with different stacking sequences $[0^\circ, 90^\circ]_6$, $[90^\circ, 0^\circ]_6$, and $[+45^\circ, -45^\circ]_6$ models, are given in Figure 5.18- 5.20. The curves demonstrate the values obtained at the interfaces between each layer of the composite laminate. These curves show that the ply stacking sequences appear to have considerable influence on the stress distribution between layers of the composite laminate. In general, for the three models with different ply stacking sequences, it can be seen that the tensile stress results clearly show a step-wise distribution of stresses, due to discontinuities in material properties between plies. Important results obtained from these curves can be outlined as follows:

- In all models, stress concentration decreases from the first layer to the last one.
- When tensile stress (S11) distributions in load direction are examined, it can be seen that stress concentration is higher at 0° layers, see Figure 5.18a, and 5.19a.
- When peel stress (S22) distributions, which are important for the failure of the joint, are examined, it can be detected that in $[0^\circ, 90^\circ]_6$ model stress is higher at the upper interface of the adhesive layer in (RHS) compared to the lower interface, see Figure 5.18b. On the other hand, for $[90^\circ, 0^\circ]_6$, and $[+45^\circ, -45^\circ]_6$ models the stresses are lower than those occurring at the $[0^\circ, 90^\circ]_6$ model, see Figure 5.19b and Figure 5.19b. This directly changes the mode of failure occurring in the joint.
- In the adhesive layer of the $[0^\circ, 90^\circ]_6$ model, shear stress (S12) value near the centre of the joint (RHS) is higher than that of other models, see Figure 5.18b, and 5.19b.

5.6.2 Effect of overlap length

One of the important parameters that influence the joint strength is the overlap length. The $[0^\circ, 90^\circ]_6$ models with various overlap lengths (25-200 mm) were used to study the effect of bonded length on stress distributions along the adhesive layer. An adhesive thickness of 0.2 mm was used in each model. Every model analysed used identical boundary conditions, and the failure loads obtained from experimental tests were used to validate the finite element models. The same standard mesh was used in each model, as can be seen in Figure 5.3.

The shear stress results in the adhesive at failure loads with respect to various overlap length are shown in Figure 5.21. The shear stress distribution along the upper interface of the adhesive for all models is high at the RHS near the centre of the joint. The adhesive reaches plasticity for all joints which display similar zones of plasticity in shear. The size of the

plastic zone may be taken as a measure to predict joint failure, which will be discussed in Chapter 8.

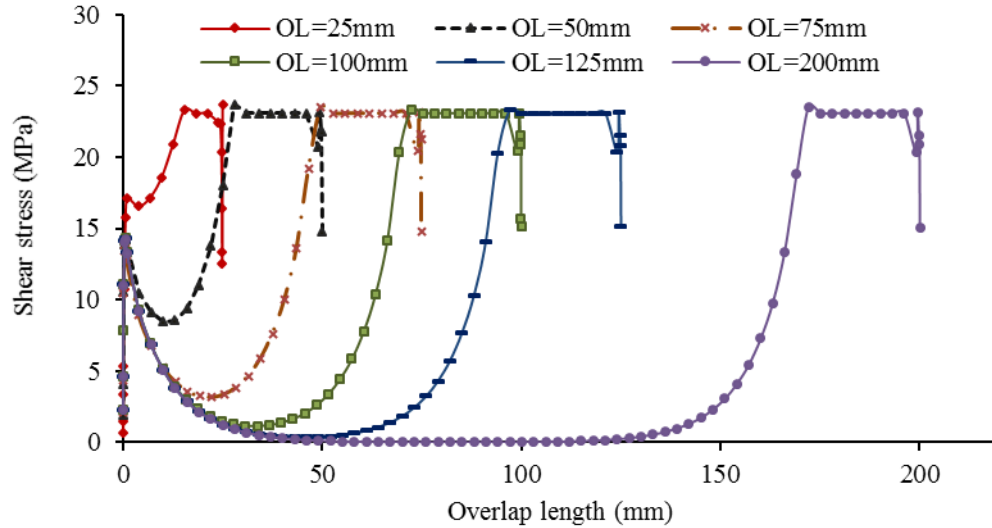


Figure 5.21: Shear stress distributions along the upper of adhesive layer for different values of overlap length for $[0^\circ, 90^\circ]_6$ models at failure loads

5.6.3 Effect of outer adherend thickness

In this section the $[0^\circ, 90^\circ]_6$, $[0^\circ, 90^\circ]_{12}$ and $[0^\circ, 90^\circ]_{18}$ models with different laminate thicknesses are examined i.e. 3 mm, 6 mm and 9 mm respectively. The overlap is 75 mm. The same standard mesh was used in each model, as can be seen in Figure 5.3, with the additional thickness of the outer adherend doubling the number of layers for other models (12, 24 and 36 layers). Every model analysed used identical boundary and loading conditions. Loading of each model was 50 kN, applied at the steel adherend as a tensile load. Table 5.5 presents the results of the stress distribution at the upper, middle and lower interfaces of the adhesive. The table contains the peak stresses at the RHS and LHS of the different models. It can be seen that increasing the thickness of CFRP composite laminate has a significant effect on the distribution of stress. The greatest stress is no longer in the upper adhesive layer at the RHS near to the joint centre. The stress occurs in the lower adhesive interface towards the end of the overlap.

The maximum principal stress at the upper RHS has decreased dramatically. The same can be seen for the peel stresses through the adhesive at the RHS, with the greatest decrease shown in the upper interface at the centre of the joint. The middle and upper regions at the

LHS of the adhesive are above this threshold for the thicker composite adherend, when previously they were below. The maximum peel stresses at these locations are also shown to have increased (highlighted in bold numbers).

Table 5.5: Stress results through the adhesive layer at a load of 50 kN, the numbers in bold indicate maximum critical stresses.

	Stress (MPa)	Data Path	CFRP [0°,90°] ₆		CFRP [0°,90°] ₁₂		CFRP [0°,90°] ₁₈	
			LHS	RHS	LHS	RHS	LHS	RHS
Adhesive layer	Max Principal	Upper	13.3	54.3	19.1	31.7	23.6	25.3
		Middle	25.6	20.4	31.4	15.6	34.1	12.3
		Lower	40.1	14	52.1	32	53.9	34.1
	Max S12	Upper	3.5	14.8	16.5	21.7	18.5	20.2
		Middle	8.6	11.8	16.5	23	17.7	23.7
		Lower	17.6	24.5	22.2	22.6	23.5	22.3
	Max S22	Upper	12.1	45.3	18.7	18.7	23.5	11.3
		Middle	22.7	8.3	28.5	-7.3	31.8	-11.8
		Lower	29.3	15	41.1	9.2	42.5	8.5

Data paths were created along the same node path as before to enable an accurate comparison. The path at the upper interface of the adhesive layer was used to plot the stresses distribution for three models.

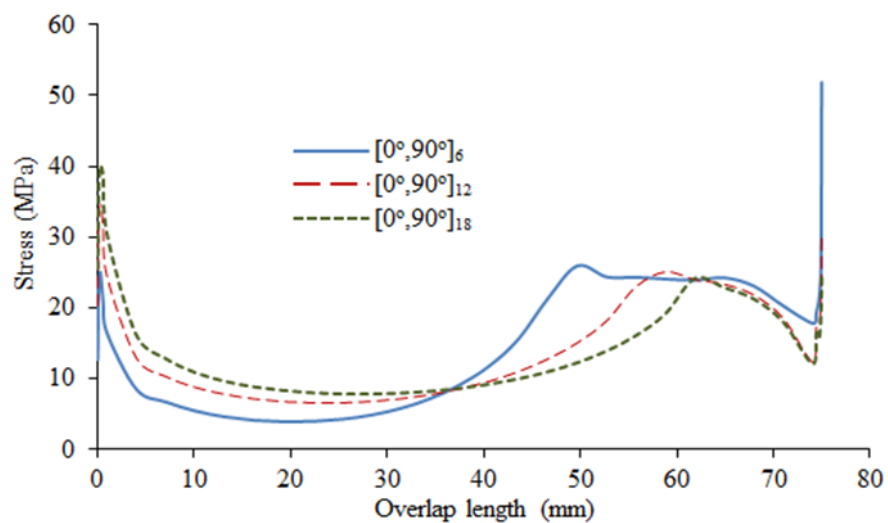


Figure 5.22: Maximum principal stresses distribution along the upper adhesive layer for different outer adherend thickness

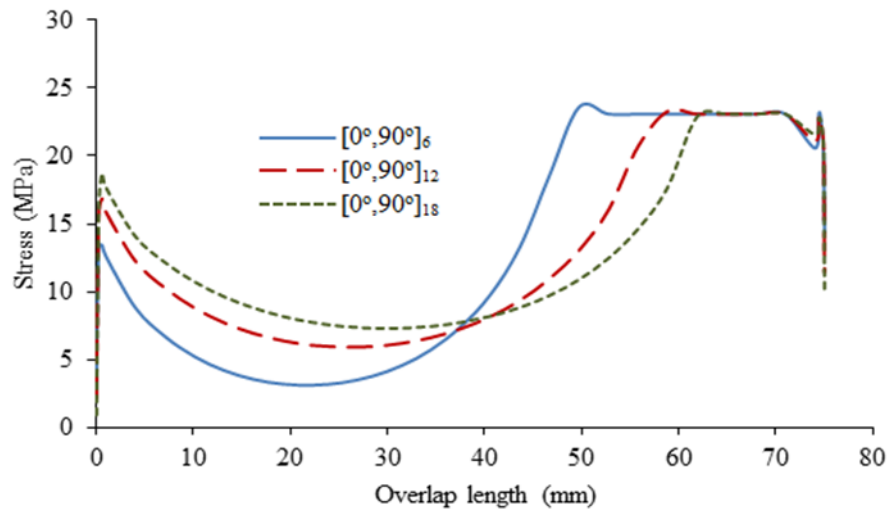


Figure 5.23: Shear stresses distribution along the upper adhesive layer for different outer adherend thickness

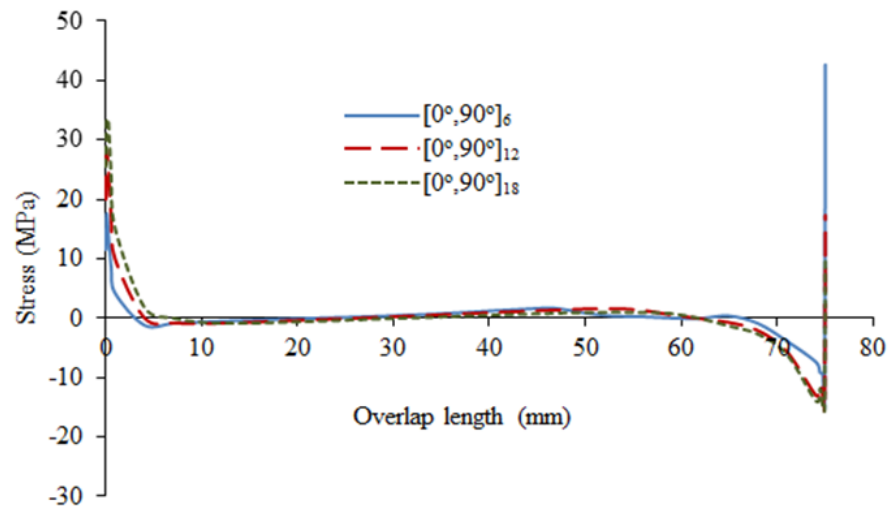


Figure 5.24: Peel stresses distribution along the upper adhesive layer for different outer adherend thickness

It can be observed from Figure 5.22 - 5.24 that with increase in the outer adherend thickness, reductions in the values of maximum principle stress, shear stress and peel stress towards the centre of the joint RHS take place. Also, as the thickness increases, the maximum stresses at the end of the joint overlap are seen to increase. As for the maximum principal stress and the peak peel stress, a high increase of approximately 52% at the left hand side of the upper adhesive interface can be seen. One conclusion from these results is that the maximum stress

within the adhesive moves location, from the joint centre RHS to the end of the joint overlap LHS, as the stiffness of the outer adherend increases.

5.7 Summary

The methods employed in the development of the finite element models were discussed in this chapter. The model geometry for 2D models was selected based on their symmetry in joint geometry and the loading. The boundary conditions were based on tensile loading of the joints. A continuous mesh was used to discretise the geometry, where smaller elements were used in the adhesive layer and relatively larger elements used in the adherends. 2D models were based on a plane strain formulation, which provided good results. The sizes of 2D meshes were finalised after a mesh convergence study, and the mesh with the least number of elements was selected after the convergence in stresses was achieved.

In this study DLS joints with composite laminate with different orientation angles were subjected to tensile loading, and their mechanical behaviours were investigated numerically. Accordingly, the following conclusions might be drawn:

- The numerical analyses gave a good indication of the likely areas where failure would initiate when compared with the specimens tested experimentally.
- The fibre orientation and ply stacking sequence had a significant effect on the stress distribution.
- The adhesive plastic shear zone at failure remains about 30 mm in length when increasing the overlap length of the DLS joint.
- Increasing the thickness of the outer adherend significantly reduces the stress at the centre of the joint (RHS), particularly in the upper adhesive interface. However, increased thickness is seen in this layer at the left hand side towards the end of the overlap in the upper adhesive interfaces.

Chapter 6

6 Numerical investigation of pure mode I and II

6.1 Introduction

This chapter uses experimental results introduced in Chapter 3 to identify the sets of material parameters required for FEA simulation of the confined structural adhesive. Numerical accuracy is ensured by modelling the adhesive layer using several solid continuum elements in the thickness. Such a mesh is not valid for large models since it is extremely time consuming. Consequently, computational efficiency is addressed using specific interface elements that run very fast. The FEA model was used in correlation with the experimental data, in order to obtain the material parameters values for the cohesive zone for the DLS joint numerical model. These include fracture energy, interface strength and cohesive zone length. The formulation of the cohesive finite elements is based on the cohesive zone model (CZM) approach. The CZM approach [126, 198] is one of the most commonly used tools for the investigation of interfacial fracture.

The tests considered in this chapter for the modelling are the following:

Double Cantilever Beam (DCB) test for mode I.

End Notched Flexure (ENF) test for mode II.

The modelling has been done with the finite element code ABAQUS 6.9-1. For each model, the first step was a comparison between the loads versus displacement curve obtained from the modelling, with the equivalent curve obtained experimentally.

Finally, the influence of interface cohesive parameters for the two models has been evaluated.

6.2 Cohesive zone model concept

The CZM offers an alternative method to linear elastic fracture mechanics for the simulation of damage evolution in materials. The cohesive zone model comprises of two parts that are

separated by a material discontinuity. The CZM concept is useful to visualise the domain Ω shown in Figure 6.1. A material discontinuity, Γ_c , has been defined as an interface bounding the regions Ω_1 and Ω_2 respectively. This interface surface is an internal surface in the domain, and hence represents a cohesive surface that has not yet been separated. Prescribed tractions, f_i against the surface domain Γ_f , with the prescribed displacements on the boundary are denoted as Γ_u . If the body forces are neglected, the stress field can thus be related to the external loading and to the closing traction, T , in the material discontinuity. In the simplest formulation of CZM, the whole body volume remains elastic while the nonlinearity is embedded in the cohesive model, which dictates the boundary conditions along the crack line, Γ_c . The peak stress on the traction-separation relation is considered to be the cohesive strength, σ_o , of the material, while the area under the curve for the traction-separation relation is also equal to the critical fracture energy of the material [128, 199]. The fracture energy of an adhesive layer involves the intrinsic fracture energy (G_0) needed for breaking the intrinsic bonding forces, and a viscos-elastic and/or plastic energy terms (ψ) that accounts for the energy dissipation in the surrounding adhesive layer [128, 200]. The plastic energy usually represents the main sources of energy absorption in a ductile adhesive such as Araldite 2015, and, as a result, the adhesive fracture energy is often characterised as; [200].

$$G_c = G_0 + \psi \quad (6.1)$$

The traction on the discontinuity rises until the peak stress is reached, at which point a crack begins to form between the two parts. As separation between the two parts increases, traction at the surfaces decreases, following a specific relation until the traction free surfaces are created. At this point the crack has been fully developed [128]. Figure 6.1 visually describes the fracture processes in a CZM (from right to left in the figure); (1) the material initially assumes linear elastic behaviour, (2) the peak stress is reached at the crack tip, and at this point the crack begins to develop, (3) the two parts separate further and traction at the surfaces decreases, following a specific traction separation relation until the traction reaches zero, and (4) when the traction reaches zero, the parts have been separated and the crack has fully developed.

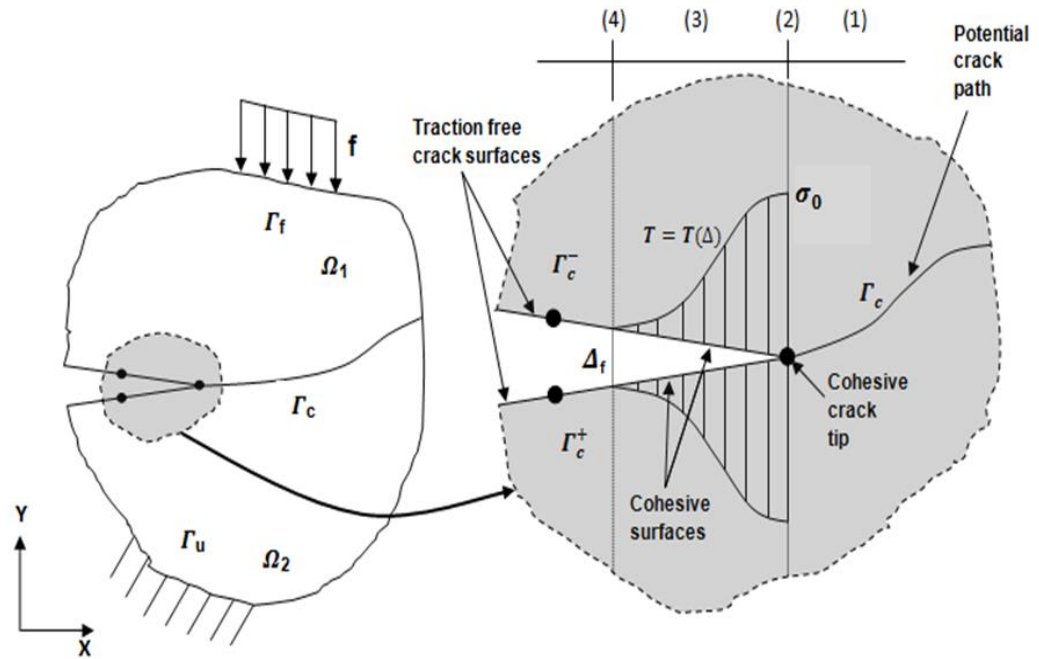


Figure 6.1: Illustration of cohesive zone model concept [128], at first a linear elastic material response prevails (1), as the load increases the crack initiates ($T=\sigma_0$) (2) and then, governed by the nonlinear cohesive law, it evolves from initiation to complete failure (3) with the appearance of new traction free crack surfaces ($\Delta=\Delta_f$) (4).

The use of cohesive elements in a numerical model allows crack onset and propagation to be modelled without the need for pre-defining an initial flaw as in LEFM. The crack evolution is being governed by the softening relationship adopted, which defines the stresses and relative displacements between crack faces. A negative aspect with respect to implementing a CZM through cohesive elements involves knowledge of the expected plane of damage, as the cohesive elements need to be aligned along this route, which can often be difficult to know beforehand [199].

In the cases of DCB and ENF experiments, two steel adherends are joined by an adhesive layer. As the steel adherends have much higher strengths than the adhesive, it is clear that the crack will form in the adhesive layer. However, in the composite DLS joints, it is unclear as to where the joint will fail. It could fail in the adhesive or the composite layers, and therefore the crack path must be investigated before creating the model.

CZM elements are not assigned any specific material properties and, as such, do not represent any particular material. Instead, the properties that are needed during the analysis are the required energy to cause fracture propagation, and normal stress in the adhesive layer.

By implementing this data, the FEA software ABAQUS is able to determine the amount of energy needed to cause failure and the development of fracture level.

6.3 Numerical modelling using cohesive elements

The ABAQUS FEA software used for the investigation uses three types of cohesive models.

- 1- Traction Separation model
- 2- Continuum model
- 3- Gasket model

The traction-separation description of the interface is most commonly used for the modelling of bonded interfaces using composite materials. It uses the main assumption that the intermediate glue material is very thin, and can be typically assumed as having zero-thickness, therefore allowing the possible illustration of interface; ‘debonding’ for example. With this method, the macroscopic material properties are not utilised in a direct manner, instead the fracture energy required to create new surfaces must be known a priori. The cohesive elements can model the initial loading, the initiation of damage and the propagation of damage which ultimately evolves to complete failure, without the need for an initial crack used with LEFM. If non-zero thickness cohesive elements are used with this constitutive response [128], the initial stiffness value is dependent on the actual thickness of the cohesive layer.

As stated above, the traction-separation constitutive model requires description of the actual interface properties involved in a simulation, and is best suited to negligibly thin adhesive layers or zero-thickness layers. In Abaqus Standard however, the methods available for zero-thickness mesh generation in 2D are severely limited without the use of a custom user defined element (UEL). For initial modelling using cohesive elements in the DCB model and ENF model, it was considered sufficient to regard the 0.2 mm thickness of adhesive. The initial model, which encompasses the entire thickness with one layer of cohesive elements using the traction-separation response will be presented, taking the adhesive stiffness directly into account via the elastic moduli and thickness of the layer. The reasoning behind being able to use the traction-separation model with a 0.2 mm adhesive layer evolves from the fact that it is a small geometric dimension in relation to the other parts of the model geometry. As a result, the adhesive layer will behave differently compared to a bulk

specimen of the adhesive, due to the influence of the much stiffer inner and outer substrates in the DLS joint directly affecting the actual macroscopic properties of the adhesive.

If the adhesive is applied correctly, then the fracture should be of the so-called ‘cohesive’ type and propagate mainly within the adhesive. Therefore, it is acceptable to put just one layer of interface element of 0.2 mm thickness through the adhesive layer. When using cohesive elements with this method, a coarse indication of the damage distribution within the adhesive layer will be found, and for more accurate information i.e. discovering if the failure is in the vicinity of the interfaces or through the centre of the adhesive, more accurate modelling methods are required. This ability is, however, severely hindered if we wanted to model the adhesive with two very thin rows of cohesive elements above and below the adhesive layer (say 0.05 mm thick). This model needs knowledge of the respective fracture energy and cohesive strength of this specific thickness, as the cohesive elements require the properties of the adhesive at this thickness, in order to attempt to simulate damage occurring in the vicinity of the interface. The elements used in this analysis are 4-node plane strain quadrilateral CPE4R and cohesive COH2D4 elements. The COH2D4 element is basically two surfaces which are separated by a relevant thickness; this thickness is normally zero to model two joined parts, but in this case it is 0.2 mm to model the adhesive layer [128].

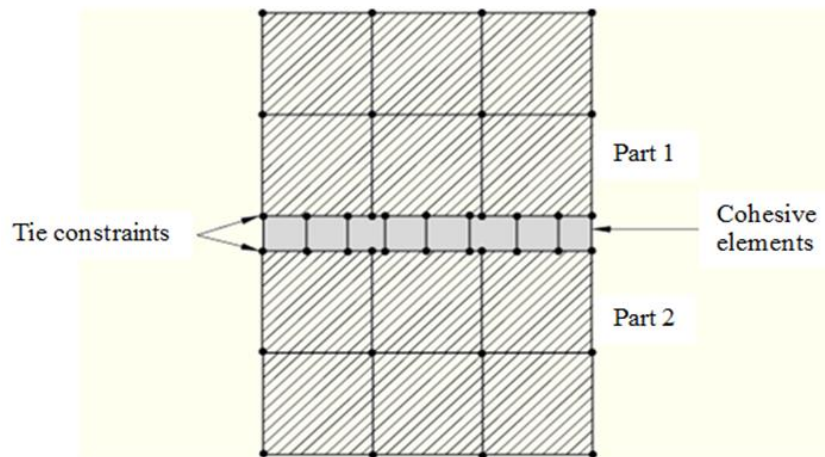


Figure 6.2: Independent meshes with tie constraints [201]

When placing cohesive elements into the initial model geometry using the intrinsic approach, it is advisable to use independent mesh regions for the cohesive and bulk elements respectively. This is due to the fact that the cohesive zone needs to be sufficiently represented

by elements small enough to clearly capture the tractions in this zone; this zone can be considered to be small, hence suitably small cohesive elements are needed. However, to allow the fast computational and effectiveness traits associated with the use of cohesive elements, there is no need to match the mesh regions and use equally small bulk elements in the metallic adherends. In order to implement independent mesh regions, we therefore utilise a surface-based tie constraint in the numerical modelling, as depicted in Figure 6.2.

6.3.1 Traction separation relations

When using the traction separation method, there are three relations analysed in the literature.

1. Bilinear
2. Trapezoidal
3. Exponential

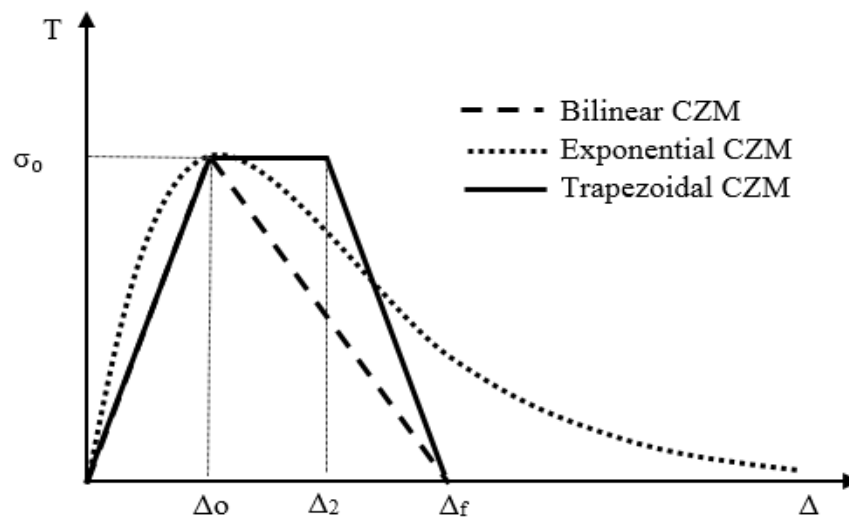


Figure 6.3: Diagram of the three most commonly used relations [128]

All three relations shown in Figure 6.3 initially behave the same, in that the stress increases as displacement increases, until the cohesive strength is reached, at which point the traction decreases with the increase in displacement, and follows a particular softening curve, dependant on the relation used.

1. The bilinear relation - here the stress increases as the displacement increases linearly, until the cohesive strength is reached, at which point the traction decreases, following a linear path until zero traction is reached.
2. The trapezoidal relation uses linear relations similar to the bilinear , except that once the cohesive strength is reached, the traction is held at a constant level until a second displacement is reached, at which point the traction decreases, following a linear path until zero traction is reached.
3. The exponential relation follows the same pattern as the bilinear relation, except that an exponential curve is used for the increase and decrease of the tractions. Once the tractions return to zero, the element has completely failed, and so the crack has fully developed in that particular part of the surface.

The bilinear relation will be used to model the traction-separation relation in this investigation. For the traction-separation constitutive response in the numerical modelling in the form of the bilinear relation, we must first ascertain the relevant cohesive parameters for mixed-mode loading in the DLS joint. This includes seven separate entities, and will be presented in the following sections:

- Two elastic stiffness parameters K_{nn} and K_{ss} .
- Two strength parameters σ_0 and τ_0 .
- Two fracture energy parameters G_{IC} and G_{IIC}
- One mixed-mode parameter η .

6.3.1.1 Linear elastic response

The traction-separation law formulation in ABAQUS assumes an initial linear elastic behaviour, followed by initiation and subsequent evolution of damage, where the stiffness of the element is degraded according to a specific damage evolution law. The cohesive elements in ABAQUS exist in 2D and 3D versions, but only 2D analyses are conducted in this work. Elasticity is defined by an elastic constitutive matrix relating stresses and strains across the interface [120].

$$\sigma = K\varepsilon \quad , \quad K = \begin{bmatrix} k_{nn} & k_{ns} \\ k_{sn} & k_{ss} \end{bmatrix} \quad (6.2)$$

The stiffness of the cohesive zone contributes a considerable effect to the functionality of the analysis. The stiffness terms K_{ns} and K_{sn} are assumed to be zero, and the stiffness terms

K_{nn} and K_{ss} are a function of the Young's/ shear moduli and thickness of the adhesive or the rich resin. The stiffness can be calculated by these equations:

$$K_{nn} = \frac{E}{t_a}, \quad K_{ss} = \frac{G}{t_a} \quad (6.3)$$

Where G is the shear modulus and is found from:

$$G = \frac{E}{2(1+\nu)}$$

6.3.1.2 Damage initiation criterion

The damage initiation criterion is generally stress-based or strain-based, and damage initiates when the maximum stress or strain value is reached.

Under pure mode I and pure mode II loading, the onset of damage can be determined simply by comparing the traction components with their respective critical values.

Under mixed-mode loading, damage onset and the corresponding softening behaviour may occur before any of the traction components involved reach their respective critical values in pure modes loading. The quadratic nominal stress criterion equation 6.4 signifies that the damage is assumed to initiate when either of the normal or shear components of the traction σ or τ exceeds the respective critical values (σ_0 or τ_0).

$$\left(\frac{\langle \sigma \rangle}{\sigma_0} \right)^2 + \left(\frac{\tau}{\tau_0} \right)^2 = 1 \quad (6.4)$$

The quantity within the Macaulay bracket $\langle \rangle$ is put to zero when negative, signifying that a pure compressive deformation does not contribute to damage [202].

6.3.1.3 Damage evolution

Damage propagation is studied in terms of energy release rate and the fracture toughness. In order to accurately predict the mode-mix of the epoxy under loading [202], the Benzeggagh Kenane (BK) criterion is used.

$$G_{IC} + (G_{IIC} - G_{IC}) \left(\frac{G_{II}}{G_I + G_{II}} \right)^\eta = G_c \quad (6.5)$$

Where G_I and G_{II} are the energies released by the traction due to their respective separation in normal and shear direction respectively, and G_{IC} and G_{IIC} are the critical energy release

rates in modes I and II , and η in the BK criteria can be regarded as a kind of material properties [121]

Damage evolution describes the rate at which a material's stiffness is degraded once the corresponding initiation criteria is reached. Figure 6.4 shows the bilinear traction separation law. For linear softening, ABAQUS uses an evolution of the damage variable (D) that reduces to:

$$D = \frac{\Delta_f (\Delta^{\max} - \Delta_0)}{\Delta^{\max} (\Delta_f - \Delta_0)} \quad (6.6)$$

Where:

Δ^{\max} - The effective displacement maximum value in the loading history

Δ_0 - Critical displacement jump of CZM at the peak stress.

Δ_f - Displacement at failure.

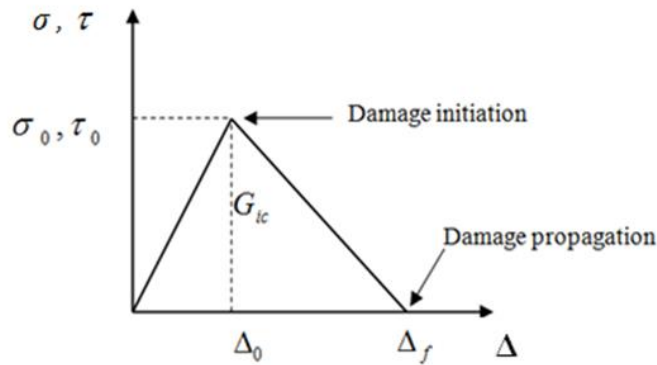


Figure 6.4: Bilinear traction-separation law

A scalar damage variable D represents the overall damage in the material. Therefore, these parameters can be shown in the numerical simulations in terms of output variables showing the 'Status' of the cohesive element i.e. if the status of an element is 1.0 then the element is fully active, and if it is 0 the element is not yet active. The overall value of the variable D defining the value of scalar stiffness degradation (SDEG) can be determined [120]. If the value of D is known during the full time of an FEA simulation, then a complete description of the damage history can be illustrated [203].

6.3.2 Characteristic of the models

This section describes the characteristics of finite element models presented in this chapter. In each model, the adherends of the specimen and the cohesive layer are each modelled with particular characteristics. The adherends of the specimen (mild steel) were modelled with two-dimensional elements with four nodes (CPE4R). The elastic parameters for these elements are shown in Table 6.1.

Table 6.1: Young's modulus (E) and Poisson's ratio (ν) used for the CPE4R elements

Material	E (GPa)	ν
Mild steel	210	0.3

For the modelling of cohesive layer, four-node, two-dimensional cohesive elements (COH2D4) are used. These elements follow the constitutive law that has already been described in Section 6.3.1, and the parameters required for describing the cohesive law are shown in Table 6.2.

Table 6.2: Young's modulus (E), shear modulus (G), normal cohesive strength (σ_0), shear cohesive strength (τ_0), normal fracture energy (G_{IC}) and shear fracture energy (G_{IIC}) used for the COH2D4 cohesive elements

Material	E (MPa)	G (MPa)	σ_0 (MPa)	τ_0 (MPa)	G_{IC} (N/m)	G_{IIC} (N/m)
Araldite 2015	1800	662	40	24	400	4000
Resin LY3505/XB3405	3500	1296	85	50	150	1300

Some of these quantities are determined experimentally, while the other elastic parameters are assumed from the literature.

The interface stiffness is the elastic modulus of the adhesive or epoxy resin per unit thickness, and is therefore given by dividing the elastic modulus of the adhesive or resin by the thickness of the cohesive layer. The values of the elastic modulus E and the shear modulus G of the adhesive and the resin are shown in Table 6.2, and the interface thickness is $t_a = 0.2$ mm.

The interface stiffness K_{nn} for the mode I is given by the equation (6.3);

For adhesive (Araldite 2015); $K_{nn} = \frac{E}{t_a} = \frac{1800 * 10^6}{0.2 * 10^{-3}} = 9 * 10^{12} N / m^3$

For resin (LY3505/XB3405); $K_{nn} = \frac{E}{t_a} = \frac{3500 * 10^6}{0.2 * 10^{-3}} = 17.5 * 10^{12} N / m^3$

The interface stiffness K_{ss} for the mode II is given by the equation (6.3);

For adhesive (Araldite 2015); $K_{ss} = \frac{G}{t_a} = \frac{662 * 10^6}{0.2 * 10^{-3}} = 3.3 * 10^{12} N / m^3$

For resin (LY3505/XB3405); $K_{ss} = \frac{G}{t_a} = \frac{1296 * 10^6}{0.2 * 10^{-3}} = 6.5 * 10^{12} N / m^3$

All the analyses are nonlinear and under displacement control.

6.4 Numerical simulation of the DCB specimen

A DCB model was used according to the geometrical description given in Figure 6.5. The FEA model was used in correlation with the experimental data, in order to obtain the material parameters values for the cohesive zone for the DLS joint numerical model. For analysis of the DCB specimen, we began by incorporating a solitary row of cohesive elements through the entire thickness of the adhesive (Araldite 2015) layer or resin (LY3505/XB3405) layer, with the intrinsic properties of the adhesive and the resin contained therein by means of the bilinear CZM. The testing equipment used in the laboratory consisted of a grip attached to the upper adherend, and a vertical tensile force was applied, whilst the lower adherend was held fixed. Hence a reaction force was generated equal and opposite to the tensile force in magnitude and direction. we have replicated this test by fixing the lower adherend. Figure 6.5 shows the 2D model where the adhesive is modelled as a row of cohesive elements. The fracture processes are assumed to occur within the adhesive. The adherends (mild steel) were modelled using bulk continuum elements i.e. 4-noded linear plane strain reduced integration continuum elements (CPE4R). The adhesive layer was modelled with a single row of 4-node cohesive elements (COH2D4) [201].

Numerical analysis of the DCB model began with a study on the effect of varying the normal cohesive strength of the bilinear CZM used through means of tailoring this model with experimental data. A sensitivity study was then performed on this mode I fracture parameter, also in order to gain a suitable best fit to the experimental data, which was then followed by searching for an optimal cohesive element length. Subsequent analysis of the effects of

varying all other relevant parameters involved was carried out, thus monitoring the load-displacement curve in each case as a reference.

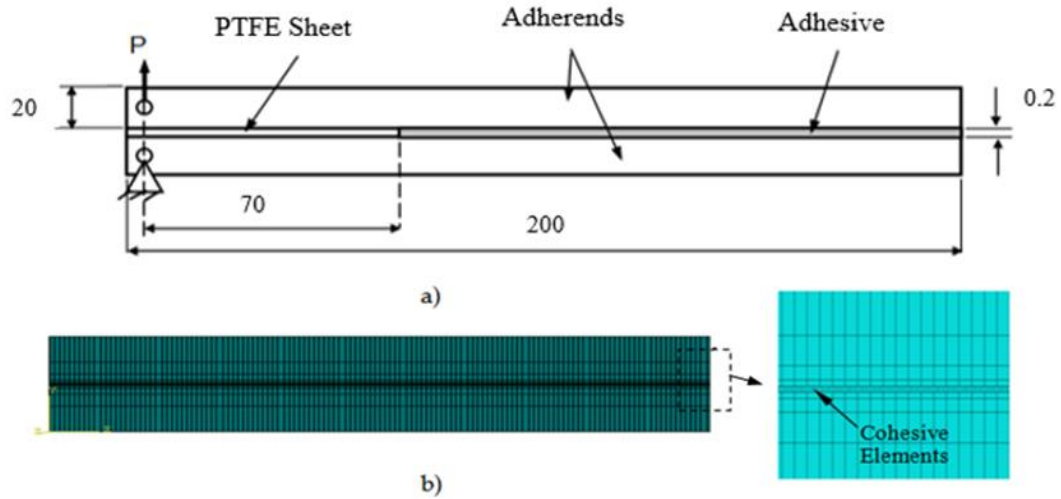


Figure 6.5: a) Geometry and dimensions (in mm) of the DCB model and boundary conditions, b) DCB mesh used with single row of cohesive elements to represent the adhesive thickness

6.4.1 Deducing the normal cohesive strength for bilinear CZM

The method used in this study to obtain the normal cohesive strength of the bilinear CZM model involves an inverse identification method consisting of iteratively adjusting numerical load-displacement plots in order to obtain a match with the experimental data. This was mainly due to the methodology adopted to experimentally obtain the fracture parameters from the DCB specimen, as no stress-elongation expression was derived from using the British Standard (BS 7991:2001). This was due to BS providing a clear and step by step guide to follow in the testing stage, which was not available for the other methods, and it is simpler to conduct than other more complex methods of measuring the fracture energy G_{IC} [150]. The tailoring of the CZM was based on the DCB test being the simplest test to conduct to extract G_{IC} , but it provides a unique solution, and hence, other methods may be employed to gain a wider picture of the fracture parameters of Araldite 2015 and epoxy resin LY3505/XB3405, which will be discussed later in discussion of this topic [119]. It has been found that by iteratively adjusting the cohesive strength to gain a data fit, the resultant maximum tripping traction should be of the order of the maximum tensile yield stress of the bulk adhesive, which for Araldite 2015 is 40 MPa. In order to add a degree of accuracy to the iterative data fit procedure, it is sensible to use an extremely small cohesive element size.

Initially in this report, a cohesive element of 0.01 mm in length (along the direction of interface layer) was adopted in order to capture the size of the cohesive zone accurately, as the size isn't fully known at this stage, and will change with a variation in tripping traction entered into the bilinear CZM iterative model. This element will not be smaller than 0.01 mm from preliminary calculations, as it is recommended to have at least 3 cohesive elements in the cohesive zone in order to fully capture the tractions present [128]. An effect of lowering the estimate of cohesive strength is to increase the length of the respective cohesive zone in the model [204].

The meshes used for all of the sensitivity analyses have a finer discretisation of elements in the cohesive zone compared to the surrounding bulk elements. This is deemed to improve accuracy without comprising results, while allowing for fast computations to be achieved [201]. As mentioned earlier, by using surface-based tie constraints, the cohesive layer can be modelled with a much finer discretisation than the surrounding bulk elements, as the cohesive elements are effectively tied to the surface of the adherend throughout the analysis [201].

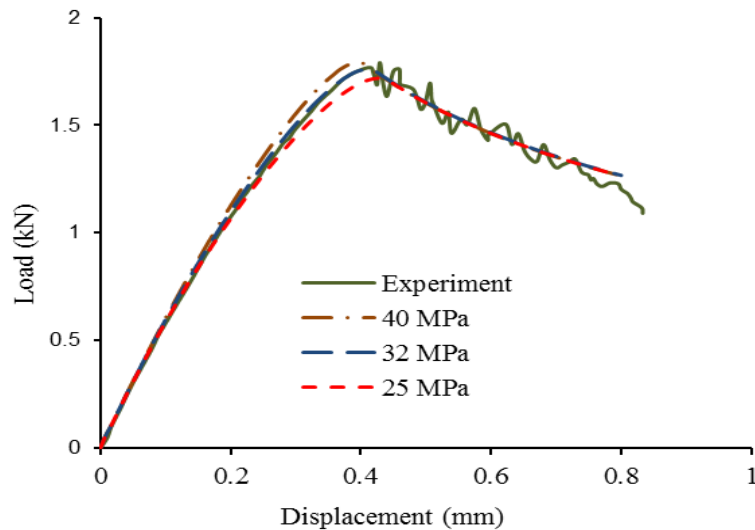


Figure 6.6: Study on effect of varying normal strength of Araldite 2015

The experimental load-displacement curve that has been used for comparative purposes throughout this section is from the mode I pre-crack initiation stage. It gives an indication of the peak force reached, but ends soon after the loading was removed once the pre-crack was initialised, thus allowing for sensitivity studies to be conducted in comparison to the peak force observed in this plot from the 0.2 mm DCB experimental test. Figure 6.6 depicts

the effects of varying the cohesive normal strength whilst holding the fracture energy constant (at $G_{IC} = 410 \text{ N/m}$). As can be seen, this has the effect of increasing the peak load with an increase in the cohesive strength value input to the model. However the global energy (area under curve) differs only slightly. As the cohesive strength is altered, the stiffness degrades with respect to the experimental plot as the peak load is reached, with lowering the cohesive strength entered lowering the stiffness, and vice versa for an increase in evaluated cohesive strength. By modelling the DCB with the lower substrate fixed to evaluate the reaction force in the upper substrate, this is referred to as the force on all P- δ curves in this section. The work presented here has only focussed on the use of the bilinear CZM relation, as from the literature the use of the exponential CZM relation is ill-suited for the ductile adhesive Araldite 2015 [130], and the trapezoidal relation requires the need for user-defined softening behaviour entered in a tabular form of displacements. However, this method alone requires an in-depth analysis of the displacement parameters, and then needs to be implemented via a custom scripting in Abaqus [130].

The same geometry and dimensions of the DCB specimen was used as a numerical model to investigate the fracture parameters for resin LY3505/XB3405. The study is based on a 2D plane strain mesh used to model adherends and resin layer. Figure 6.7 shows the load-displacement curves of the simulation and the experimental results for the DCB model with the effect of cohesive strength.

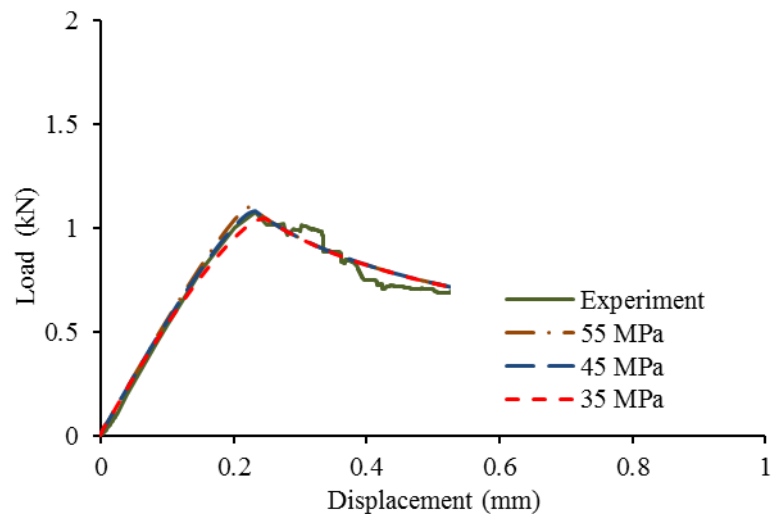


Figure 6.7: Study on effect of varying normal strength of Resin LY3505/XB3405

6.4.2 Varying mode I fracture energy, G_{IC} using bilinear CZM

Figure 6.8 illustrates the effects of varying the mode I fracture energy whilst keeping the cohesive strength fixed at 32 MPa (as obtained from the previous study analysing this parameter). The range of fracture energies tested was chosen to match the spectrum of fracture energies obtained from the ECM and CBT tests found experimentally (as these are considered most accurate) [132], with additional simulations above and below this limit for extra clarity. From Figure 6.8 it can be seen that when the cohesive strength is held constant, the fracture energy increases the area under the curve and the peak load increases, all relative to an increase in the fracture energy magnitude evaluated. The stiffness response of the slope is also constant with respect to variations in the fracture energy. It was also shown that the optimal fracture energy was around $G_{IC} = 410$ N/m.

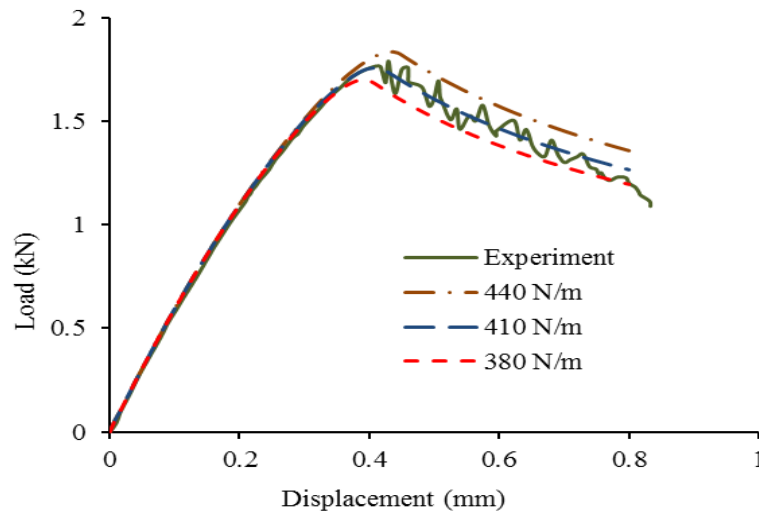


Figure 6.8: Study on the effect of the varying mode I fracture energy of Araldite 2015

The same dimensions of DCB geometry and the resin LY3505/XB3405 were used as interface of numerical model to investigate the cohesive strength parameters for resin LY3505/XB3405. The study is based on a 2D plane strain mesh used to model adherends and resin layer.

Figure 6.9 shows the load-displacement curves of the simulation and the experimental results for the DCB model with the effect of fracture energy. It was also shown that the optimal fracture energy of resin was around $G_{IC} = 155$ N/m.

The data fits achieved in Figure 6.6 to Figure 6.9 are the result of iteratively adjusting the cohesive strength and fracture energy of the bilinear CZM until an acceptable match with

the experimental plot was achieved. The cohesive parameters used are those that give rise to the minimum deviation between the experimental and numerical simulations, as summarised in Table 6.3.

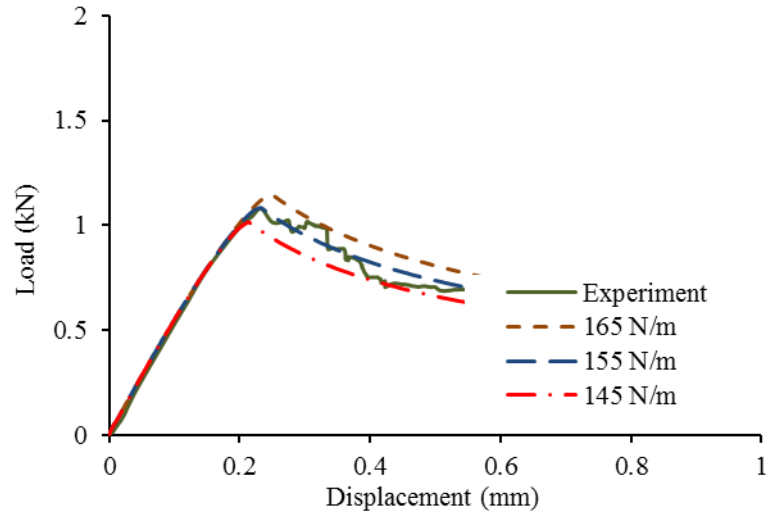


Figure 6.9: Study on effect of the varying mode I fracture energy of Resin LY3505/XB3405

Table 6.3: Cohesive parameters deduced from data fitting for mode I

Material	G_{IC} (N/m)	σ (MPa)
Araldite 2015	410	32
Resin LY3505/XB3405	155	45

6.5 Numerical simulation of the ENF specimen

For the analysis, the ENF Model was designed according to the geometrical description given in Figure 6.10. The specimen was modelled with two-dimensional, plane strain elements using ABAQUS software. The adherends (mild steel) were modelled using 4-noded linear plane strain reduced integration continuum (CPE4R) elements. The adhesive layer was meshed with interface elements as a row of cohesive elements (COH2D4) through the entire thickness of the adhesive layer, with the intrinsic properties of the adhesive contained therein by means of the bilinear CZM.

In order to have a smooth response, avoiding numerical fluctuation and investigating convergence, the element size needs to be very small. However, if the fine mesh is used in the whole model, huge computer resources are needed, as well as being time consuming. To

avoid this problem, an alternative meshing was created which would have a concentrated fine mesh along the crack path, and the rest of the model could have coarse meshing. The von Mises stress distribution and the damage propagation are shown in Figure 6.11 and Figure 6.12 respectively.

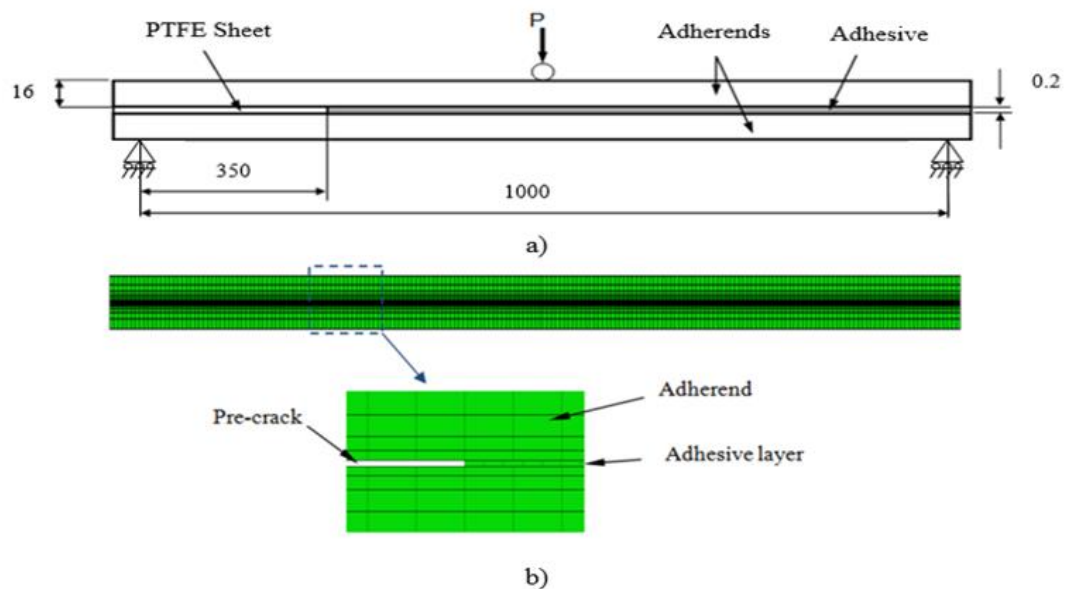


Figure 6.10: a) Geometry and dimensions (in mm) of the ENF model and boundary conditions, b) ENF mesh used with single row of cohesive elements to represent the adhesive thickness

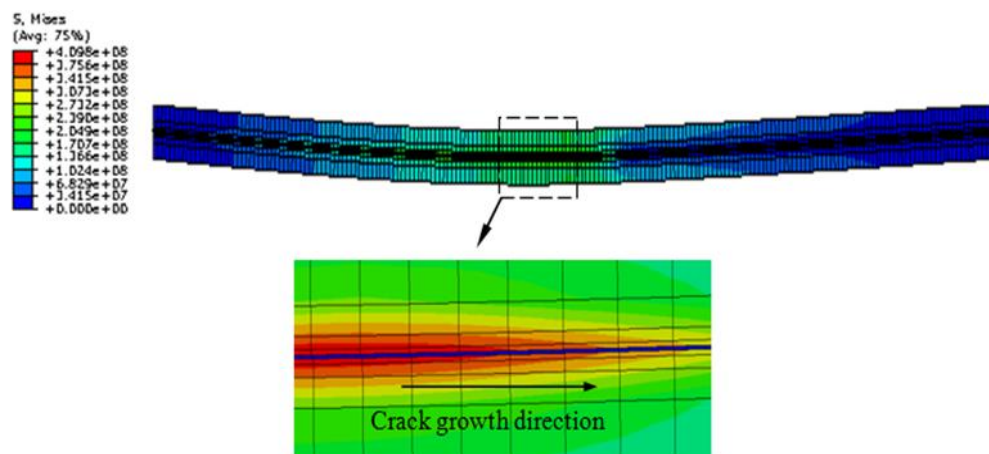


Figure 6.11: Deformed 2D model of ENF mesh after crack propagation in the adhesive

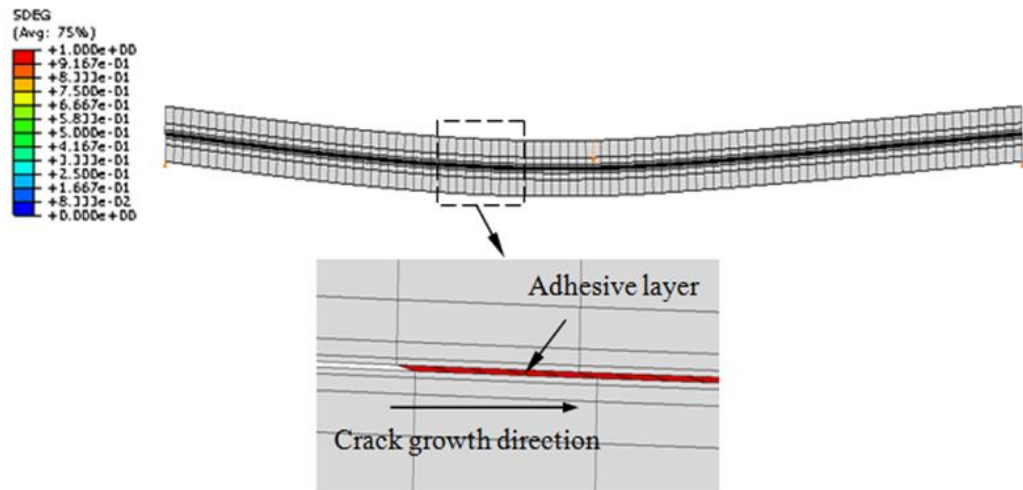


Figure 6.12: Cohesive failure in the adhesive for ENF model using the bilinear CZM

Numerical analysis of the ENF model begins with a study of the effect of cohesive strength on the response of the structure in crack propagation in a specimen with constant cohesive toughness. The bilinear CZM is used for tailoring this model with the experimental data. A sensitivity study is then performed on this mode II fracture parameter, also in order to gain a suitable best fit to the experimental data. This was followed by searching for an optimal cohesive element length, and subsequently analysing the effects of varying all other relevant parameters involved, thus monitoring the load-displacement curve in each case as a reference.

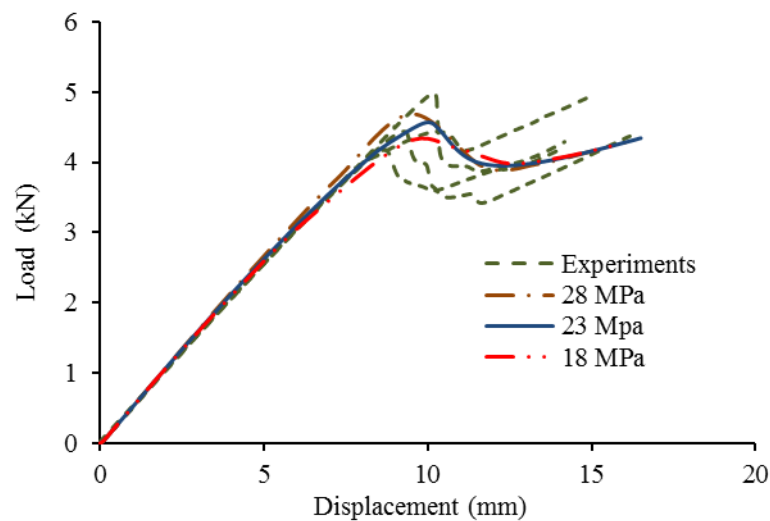


Figure 6.13: Influence of the cohesive strength on the response of ENF numerical results of Araldite 2015

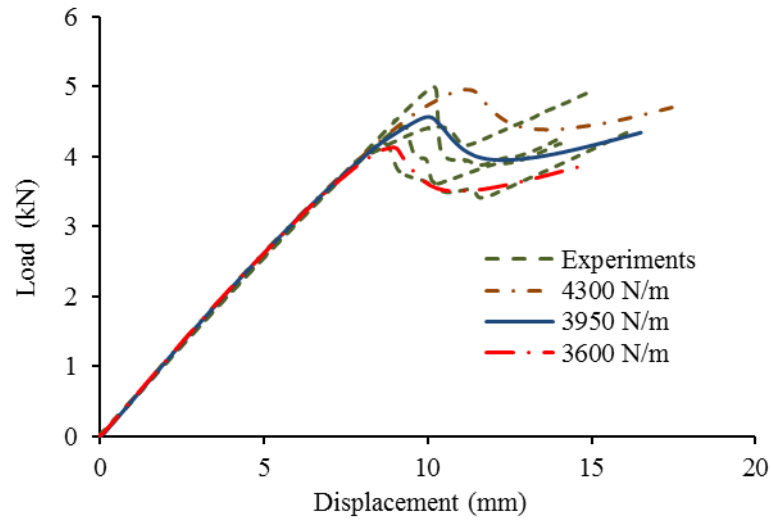


Figure 6.14: Influence of the fracture energy on the response of ENF numerical results of Araldite 2015

In Figure 6.13 and Figure 6.14, the 2D mesh with 2mm long interface elements provides a good fit between the experimental results and the results of the simulation. Good agreement between the experimental results and the result of simulation is seen in crack propagation, i.e. near the point of maximum force. Thereafter a difference between the curves is seen, and this disagreement could be justified by taking that into consideration according to the experimental curves.

The same ENF specimen was used to investigate the fracture parameters for resin LY3505/XB3405. The study was based on a 2D with 4-node plane strain quadrilateral CPE4R and cohesive COH2D4 elements used to model adherends and resin layer respectively. Figure 6.15 and Figure 6.16 show the load-displacement curves of the simulation, and the experimental results for the ENF models with the effect of cohesive strength and fracture energy respectively.

Based on the results, sensitivity analysis of the traction separation constitutive parameters on the numerical results was performed. Figure 6.13 and Figure 6.15 show that with increasing cohesive strength, the response of the structure become more linear in the first ascending part. In the softening part of the results, which is related to crack propagation before the half span of the beam length (length of ENF specimen), the cohesive shear stress at damage initiation τ_0 has a small influence only.

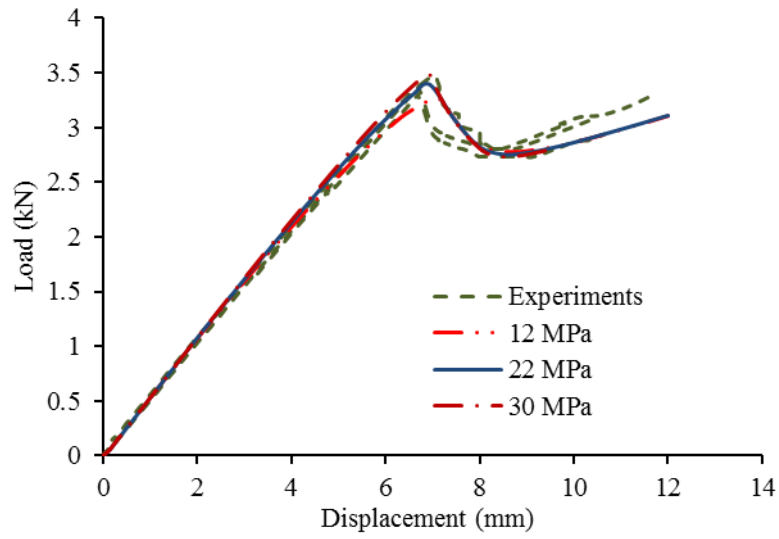


Figure 6.15: Influence of the cohesive strength on the response of ENF numerical results of resin LY3505/XB3405

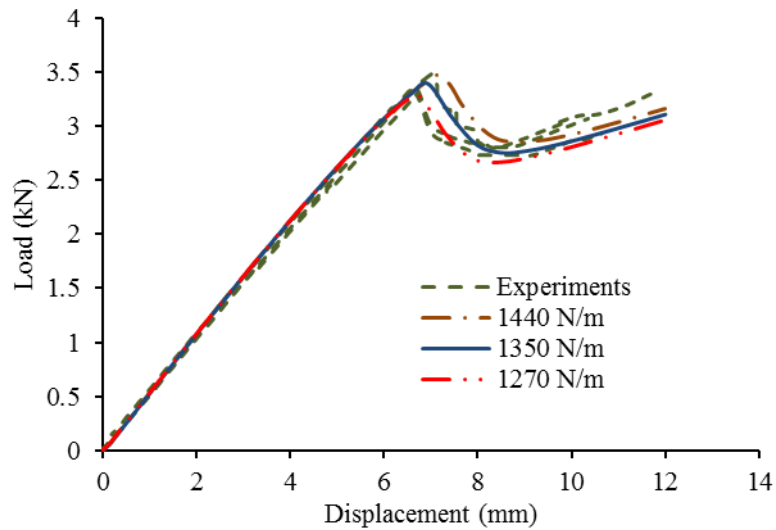


Figure 6.16: Influence of the fracture energy on the response of ENF numerical results of resin LY3505/XB3405

In Figure 6.14 and Figure 6.16 it can be seen that when the cohesive shear strength is held constant, the fracture energy increases the area under the curve and the peak load increases, all relative to an increase in the fracture energy magnitude evaluated. The stiffness response is also constant with respect to variations in the fracture energy. It was also shown that the average fracture energy of mode II for the adhesive 2015 and resin LY3505/XB3405 was

around 3950 N/m and 1350 N/m respectively. In addition we can see the effect of cohesive toughness in mode II, G_{II} has a large influence on the results.

The cohesive parameters used are those that give rise to minimum deviation between experimental and numerical simulations of mode II. In Table 6.4 a summary of each of the cohesive parameters of Araldite 2015 and resin LY3505/XB3405 used in this study is illustrated.

Table 6.4: Cohesive parameters used for traction-separation modelling using CZM

Material	G_{IIC} (N/m)	τ (MPa)
Araldite 2015	3950	23
Resin LY3505/XB3405	1350	22

6.6 Length of the cohesive zone

Another important factor in the numerical simulation of delamination is the length of the cohesive zone, L_{cz} . As opening or sliding displacement increases, elements in the cohesive zone gradually reach the maximum interfacial strength and the maximum stress rises up to the critical interfacial stress ahead of the crack tip. The length of the cohesive zone, L_{cz} , is defined as the distance from the crack tip to the point where the maximum cohesive traction is reached. Figure 6.17 describes the length of the cohesive zone.

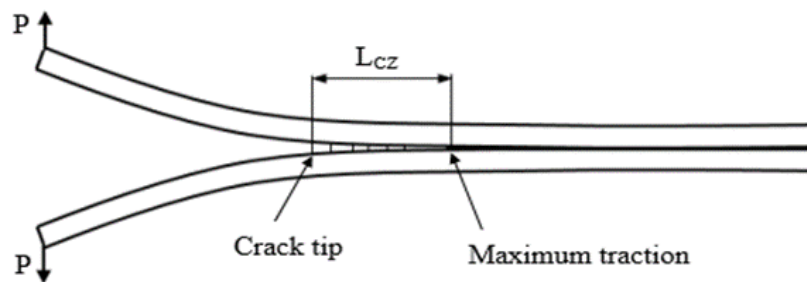


Figure 6.17: length of the cohesive zone

There are a number of different models that have been used in different literature, but the most commonly used models are Hillerborg's model and Rice's model. For Mode I and Mode II fracture, the cohesive lengths can be approximated by the following equation [205].

$$L_{CZ}^I = ME \frac{G_{IC}}{\sigma^2} \text{ and } L_{CZ}^{II} = ME \frac{G_{IIC}}{\tau^2} \quad (6.7)$$

Where E is the Young's modulus and M is a parameter that depends on the cohesive zone theory used to determine the cohesive zone length.

Different M values are given in Table 6.5.

Table 6.5: Different values of the parameter M in literature [205]

Proposed by:	M
Hui et al.	0.21
Irwin	0.31
Dugdale and Barenblatt	0.40
Rice and Flak et. al.	0.88
Hillerborg et al.	1.00

The length of the cohesive elements can be calculated from the following equations for Mode I and Mode II:

$$L_e = \frac{L_{CZ}^I}{N_e} \text{ and } L_e = \frac{L_{CZ}^{II}}{N_e} \quad (6.8)$$

Where N_e is the number of elements and L_e is the length of the cohesive element.

The cohesive zone length is directly related to the convergence issue that is the most crucial point for the CZM applications. Turon et al. [205] suggested that the minimum number of elements required for reaching converged solutions should be more than two. Therefore the resulting element length can be given as;

$$L_e \leq \frac{L_{CZ}^I}{3} \text{ and } L_e \leq \frac{L_{CZ}^{II}}{3} \quad (6.9)$$

From the inverse identification procedure, it is apparent that a cohesive strength of $\sigma = 32$ MPa and a mode I fracture energy of $G_{IC} = 410$ N/m returns the optimal solution in terms of correlating this model with the experimental DCB test. Using these values, we can therefore proceed to compute an estimate of the actual cohesive zone length in the numerical DCB model using equation (6.7).

$$L_{CZ}^I = M * 1.8 * 10^9 \left(\frac{410}{(32 * 10^6)^2} \right)$$

$$L_{CZ}^I = 0.15 \text{ mm ; minimum using } M = 0.21$$

$$L_{CZ}^I = 0.72 \text{ mm ; maximum using } M = 1$$

As mode I is the fracture mode: M is a parameter ranging from 0.21 to 1.0 [205]. For Araldite 2015, $E = 1.8$ GPa, and using the fracture energy and cohesive strength values for Mode I from Table 6.3, we can find the length of the fracture process zone in Mode I as; $0.15 \text{ mm} < L_{cz} < 0.72 \text{ mm}$ (by using $M = 0.21$ and 1.0 respectively). Many workers in this area have stipulated that in order to accurately characterise the cohesive zone (L_{cz}), one must use at least 3 cohesive elements along the fracture process zone [128, 205]. The parameter M is of some ambiguity, as this value is used to gain an estimate of the cohesive zone, derived from methods such as estimating L_{cz} as a function of crack growth velocity or estimating the size of the yield zone ahead of a mode I crack. It is common for M to equal unity, but this may add a degree of conservatism to the analysis. One method of investigating the length of the numerically predicted cohesive zone length is, for instance, by placing very fine (0.01 mm) cohesive elements along the length of the DCB bondline, then analysing the S_{22} (peel) stress ahead of the crack tip at the corresponding peak value of force (from the load-displacement plot found using 0.01 mm cohesive elements) [205].

A preliminary investigation into this procedure has been conducted and illustrated in Figure 6.5, allowing for an accurate estimation of the numerically predicted cohesive zone length to be found for the DCB geometry used in this work.

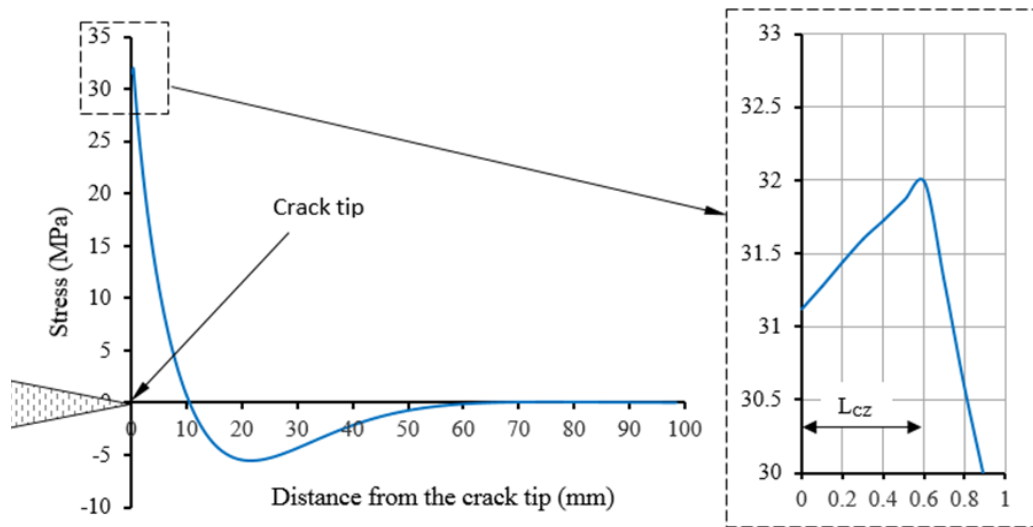


Figure 6.18: Illustration of S_{22} traction ahead of crack tip, with very fine mesh used to capture cohesive zone length

The S22 stress magnitudes obtained here are from the peak load (1640 N), and one can observe that the peak traction reached behind the crack tip will not exceed the cohesive strength set in the intrinsic bilinear CZM relation utilised here.

In order to obtain the accurate results, the tractions in the cohesive zone must be represented properly by the finite element spatial discretisation and as such this can be illustrated as:

$$N_e = \frac{L_{cz}}{L_e}$$

Where N_e is the number of cohesive elements in the cohesive zone.

In Figure 6.18 the peak normal stress occurs at 0.6 mm from the crack tip and so the cohesive zone length, L_{cz} is approximately 0.6 mm. Although this method is not precise, it does give a good estimate to the cohesive zone length. For an effective model, a value which is lower than this cohesive zone length must be used for the element size. A good model usually consists of 3 or 4 elements within the cohesive zone length. In the current study, cohesive element length, L_e is initially chosen to be 0.2 mm. By bisecting the element length in subsequently refined meshes along the crack path, L_e finally equals 0.05 mm in the most refined mesh of DCB model.

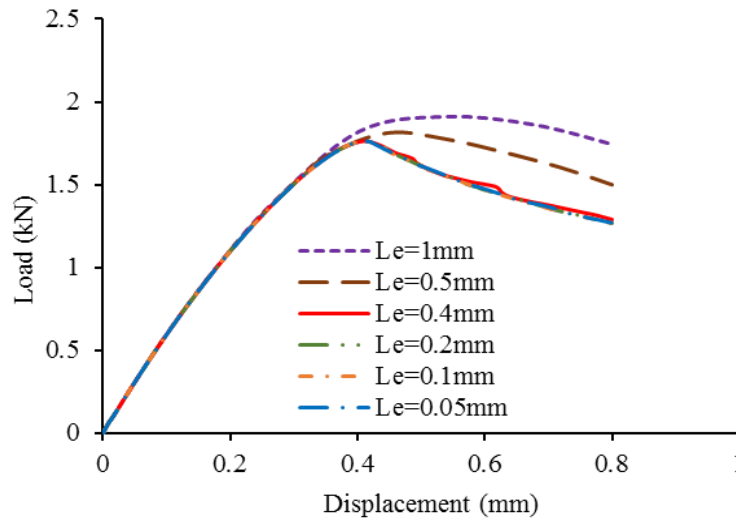


Figure 6.19: The effect of cohesive element length on the predicted load–displacement curve of DCB model

And the initially cohesive element length of ENF model was chosen to be 0.5 mm. Figure 6.19 shows a comparison of the simulation predictions of the load-displacement curves from meshes with $L_e = 1$ mm, 0.5 mm, 0.4 mm, 0.2 mm, 0.1 mm and 0.05 mm. It is

observed that the load-displacement curves corresponding to the meshes with $L_e = 0.2$ mm, 0.1 mm and 0.05 mm are almost the same. Based on this observation, simulation solutions with $L_e = 0.2$ mm or less are considered converged.

For ENF model, the Figure 6.20 shows a comparison of the simulation predictions of the load-displacement curves from meshes with $L_e = 1$ mm, 0.6 mm, 0.5 mm, 0.2 mm and 0.1 mm. It is observed that the load-displacement curves corresponding to the meshes with $L_e = 0.5$ mm, 0.2 mm and 0.1 mm are almost the same.

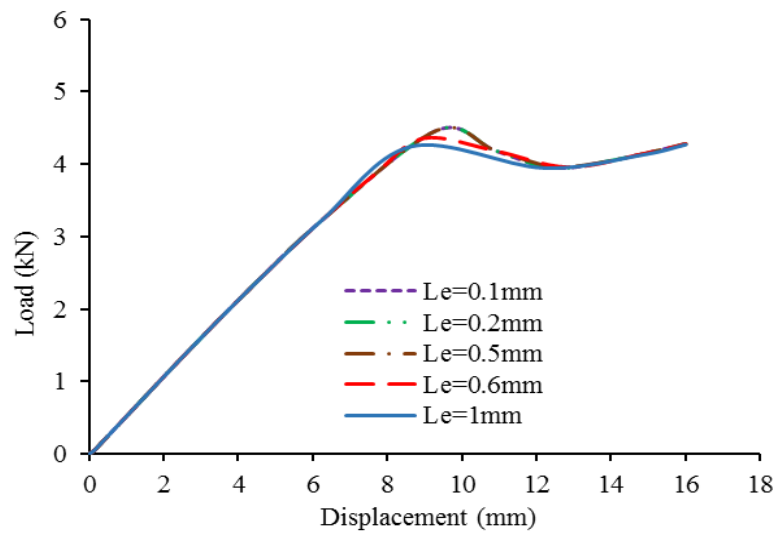


Figure 6.20: The effect of cohesive element length on the predicted load–displacement curve of ENF model

Based on this observation, simulation solutions with $L_e = 0.5$ mm or less are considered converged. Thus, the cohesive element length is fixed at 0.2 mm in the numerical simulations of mode I and mode II stable crack growths.

6.7 Viscous regularisation

Material models exhibiting softening behaviour and stiffness degradation often leads to severe convergence difficulties in finite element analysis. The implemented cohesive zone model is distinctive of material softening after the characteristic separation is reached and practical applications in Abaqus/Standard often come up with convergence problems.

A common technique to overcome some of these convergence difficulties is the use of viscous regularisation within the constitutive equations [206].

The regularisation process involves the use of a viscous damage variable, D_v , which is defined by the following evolution equation:

$$\dot{D}_v = \frac{1}{\mu}(D - D_v) = \frac{dD_v}{dt} \quad (6.10)$$

Where μ is the parameter of viscosity, representing the relaxation time of the viscous system and D is the damage variable evaluated in the current cohesive zone model.

A study has been conducted to estimate the effect of the numerical viscosity regularisation value used to force the convergence in highly non-linear analysis on the Abaqus cohesive elements. The numerical viscosity regularisation with connector elements in Abaqus/Standard is called through the program: (Mesh module: Mesh- Element Type: Viscosity = μ).

The study was carried on the DCB and ENF specimens tested to evaluate the cohesive properties of the adhesive (Araldite 2015) that has been analysed in this chapter. With a small value of the viscosity parameter, the viscous regularisation helps to improve the rate of convergence without compromising the results. In this study, the values of the viscosity (μ) of the cohesive elements are chosen from a set of small values starting from 10^{-3} and ending at 10^{-7} . Each subsequent viscosity value is one order of magnitude smaller than the previous one, and the load displacement response is predicted for each choice of the viscosity value. The predicted load-displacement curves are then compared to seek a convergence trend, thus the choice of the appropriate viscosity values. Figure 6.21 and Figure 6.22 shows the effect of the viscosity regularisation values on the predicted load-displacement curves of DCB and ENF models respectively. Figures show that the predicted load-displacement curves are dependent on the selection of the viscosity value, until the viscosity value becomes sufficiently small.

In particular, when the viscosity value changes from 10^{-5} to 10^{-6} and then to 10^{-7} , the simulation results tend to overlap with each other and become independent of the choice of the viscosity value; hence they can be considered to have converged.

It can be seen that when the value of $\mu=10^{-5}$ was used, this gave consistent convergence without affecting the predicted failure load. Therefore, in all models of the current work employing Abaqus Cohesive Elements, a viscosity regularisation factor larger than this value was never chosen.

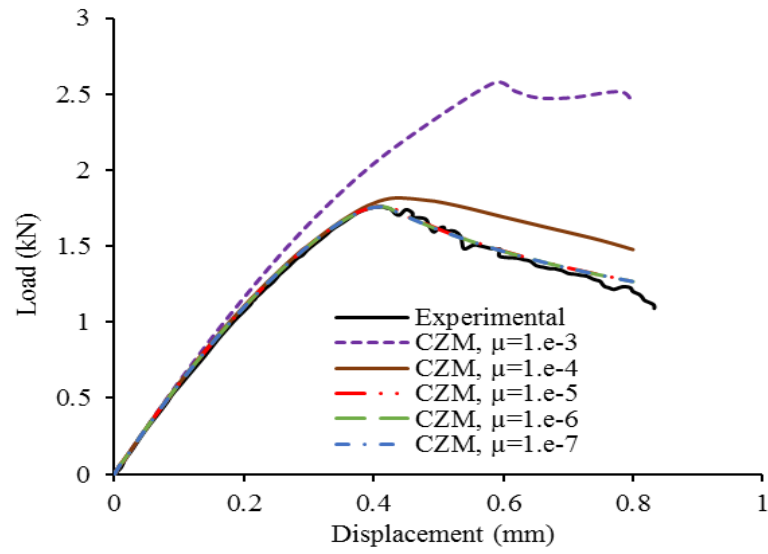


Figure 6.21: The effect of viscous regularisation factor on the predicted load–displacement curve of DCB model

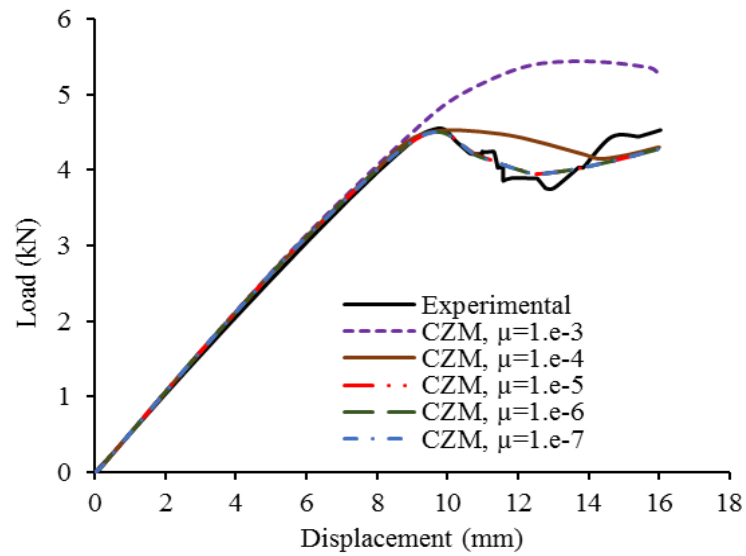


Figure 6.22: The effect of viscous regularisation factor on the predicted load–displacement curve of ENF model

6.8 Summary

In the numerical investigation of this work, the intrinsic modelling technique was initially conducted on the DCB and ENF models. This allowed for the adhesive Araldite 2015 and epoxy resin LY3505/XB3405 to be characterised by a tailored CZM, in the form of the bilinear relation.

In order to evaluate the adequacy of the several data reduction schemes to measure G_{IC} and G_{IIC} for DCB and ENF tests respectively, a numerical study was carried out including a bilinear cohesive damage model to simulate the behaviour of adhesive and epoxy resin. An inverse method was used to define the remaining cohesive parameters of the bilinear relation, fitting the numerical and experimental load-displacement curves. This was done by comparing the peak force of the experimental load-displacement plot with the numerical output of the DCB model and ENF model, until a minimum deviation between the two plots was observed.

The peak strength was obtained by using a very fine cohesive element length (0.01 mm) in order to accurately capture tractions in the cohesive zone of the numerical model. The procedure of tailoring the CZM implemented in this work serves as an illustration of how to deduce the relevant mode I and mode II fracture parameters using this commonly used technique. It was verified that the ECM and CBBM methods render the most accurate results, and are suitable methods to measure the fracture energy for mode I and mode II respectively. Comparing pure mode I fracture energy and pure mode II fracture energy which were obtained from the DCB test and ENF test, respectively, it is found that mode II fracture energy is much higher than mode I fracture energy. This implies that the fracture energy is strongly dependent on mode of failure.

Chapter 7

7 Numerical analysis of DLS joint based on cohesive zone model

7.1 Introduction

In order to obtain accurate predictions and cut the expense of repeated testing, 2D models with cohesive zone model (CZM) are presented in this chapter to predicate the failure load of double lap shear (DLS) joints. Progressive cohesive zone modelling will be used in the DLS joints simulations to detect damage initiation and growth. Since CZM plays a very important role in simulations, all parameters of CZM were determined via a series of numerical analysis and experimental results (see Chapters 3 and 6) and used in a 2D DLS joint. The finite element analysis program ABAQUS version 6.9-1 was used for numerical modelling. The effects of cohesive zone position on predicted failure load were studied. The numerical model allowed the simulation of damage initiation and propagation. The influences of the joint geometries are presented, including the effects of laminate thickness, orientation angle and overlap length.

7.2 Modelling parameters and details

7.2.1 Geometry and boundary conditions of model

The DLS joint is a more complex model than the DCB or ENF specimens discussed in chapter 6. This is because (1) there are two stress modes present in this joint, namely mode I and mode II and (2) the joint consists of a CFRP adherend, which means there are more ways for the joint to fail, and additional complications as the composite properties are orthotropic.

As in the case of the strength of material approach, only a quarter of the double lap shear joint was modelled due to its geometrical symmetry, thus making the model easier to create

and reducing the complexity of the FEA simulation and computational time. The geometry of the DLS model is shown in Figure 7.1, which shows a range of dimensions and boundary conditions.

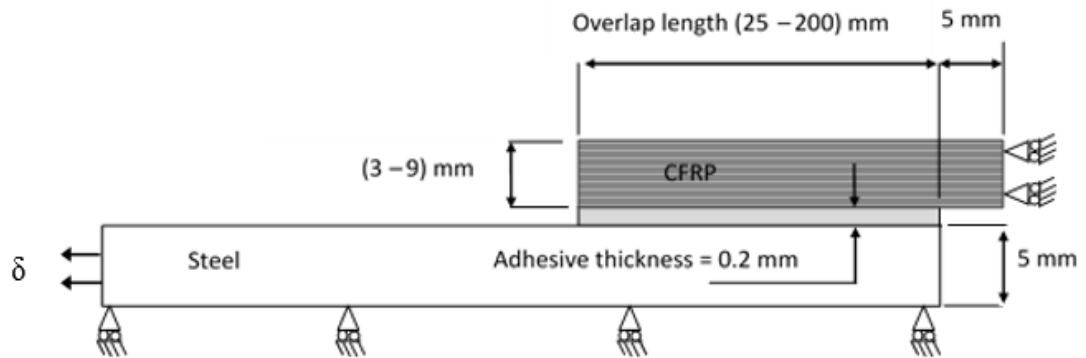


Figure 7.1: Geometry of DLS joint model and boundary conditions

It should be noted that the numerical models include outer adherend (CFRP) thicknesses of 3, 6 and 9 mm, and the inner adherend (steel) thickness is 10 mm. The thickness of adhesive was 0.2 mm. The models type/designation used for the numerical analysed in this chapter are presented in Table 7.1. All plies are identical (UD 0.25 mm thick), and their angles are taken with reference axis along the joint/model with the first angle at the bonding interface with outer adherend.

Table 7.1: Type of models

Model type	Overlap length (mm)	CFRP adherend thickness (mm)
$[0^\circ, 90^\circ]_6$	25 to 200	3
$[0^\circ, 90^\circ]_{12}$	75	6
$[0^\circ, 90^\circ]_{18}$	75	9
$[90^\circ, 0^\circ]_6$	75	3
$[+45^\circ/-45^\circ]_6$	75	3

7.2.2 Mesh of model

The finite element model shown in Figure 7.2 was developed in ABAQUS standard to predict the response of the DLS joint. The methodology considered in meshing the DLS joint is to use dissimilar meshes in the adhesive layer, steel adherend and the CFRP adherend to

join them using tie constraints, as shown previously in Section 5.3. Figure 5.2 shows the CFRP laminate consisting of fibre layers and very thin layers of epoxy based matrix between those fibre layers. In this analysis a 2D representation of the CFRP was created, as shown in Figure 7.2. Each ply was modelled to represent the fibre oriented in different directions. Four-node plane strain reduced integration continuum elements (CPE4R) were used for the steel adherend and the composite plies. The cohesive layer was modelled with a sweep mesh and four-node cohesive elements (COH2D4) with a bilinear traction separation response, to study progressive damage in the adhesive layer, and resin layers were modelled by a single row. There was only one element through thickness of the adhesive layer and of the rich resin zone between the two plies. The size of the cohesive element was 0.1x0.2 mm throughout the adhesive bond line, and 0.1x0.05 mm throughout the rich resin layers. The element size at the important points was determined by undertaking a mesh convergence study, and grew till 1 mm at the edges of the steel adherend. The 2D finite element mesh of DLS joint model is shown in Figure 7.2.

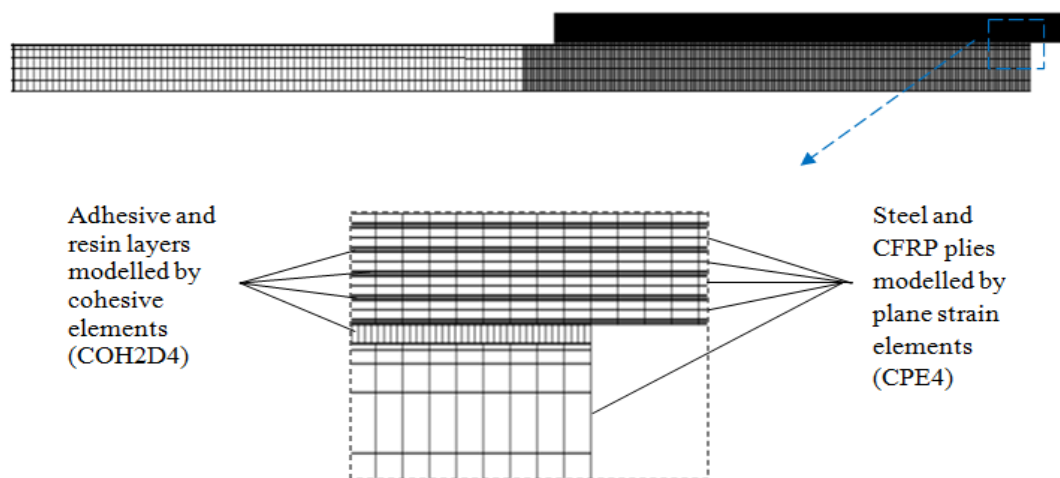


Figure 7.2: Finite element mesh of DLS joint

7.2.3 Material properties of model

The materials' properties considered for DLS joints were reported in Table 5.1, (see Section 5.4). This data was obtained from manufacturers, laboratory tests and calculation methods. To model the CFRP adherend, the properties of each layer were defined, as was use with

strength of materials analysis. The properties of the CZM parameters of adhesive and rich resin layers were determined in Chapter 6.

7.2.4 Cohesive zone model parameters

To simulate the specimens in ABAQUS the DLS joint using the CZM approach, thus cohesive elements were used. Using cohesive elements implies that the choice of material properties and section type is consistent with the type of cohesive element. The elastic behaviour was defined using the command elastic, type=Traction. The quadratic nominal stress (Quads) failure criterion for given peak value of quadratic nominal stress was selected for damage initiation in the cohesive elements. The damage initiation behaviour was defined using the command damage initiation, criterion=Quads Damage. After damage initiation completes, damage evolution determines how the stiffness degrades. The damage evolution was defined by command, type=Energy, mixed mode behaviour=BK, power=1. As no relevant experimental data was readily available for which parameter to use in the Benzeggagh and Kenane (BK) criterion [207], this value was kept at the default value of 1 used to govern the damage evolution of the model. Other parameters required for the FEA models were obtained using the open model for mode I loading and the shear model for mode II loading (see Chapter 6).

Elasticity is defined by an elastic constitutive matrix relating the current stresses and strains in tension and shear across the interface (subscripts n and s, respectively) [208].

$$\sigma = K\varepsilon \quad , \quad K = \begin{bmatrix} k_{nn} & k_{ns} \\ k_{sn} & k_{ss} \end{bmatrix} \quad (7.1)$$

Equation (7.1) has the quantities of nominal tractions in the normal and in the two local shear directions at the left side of the equation. The matrix is the elasticity in terms of traction and separations for cohesive elements. To simulate the tests, ABAQUS needs the input of elastic properties of the adhesive layer and the rich resin layer. These are found by taking the thickness of the layer directly into account with the relevant moduli (E or G), as shown previously in Section 5.4. Table 7.2 summarises the cohesive parameters used in this study; these include the stiffness values of the adhesive and the rich resin. The quadratic nominal stress criterion was considered for the initiation of damage. Table 7.3 summarises the parameters introduced in ABAQUS for damage initiation in the adhesive layer and resin

layer. Damage initiation for normal and shear modes were defined, based on the critical normal strength (σ_0) and shear strength (τ_0). The critical fracture energies required for pure mode failure are given by G_{IC} and G_{IIC} for normal and shear loading, respectively. The values introduced in ABAQUS for the simulation of damage propagation of the adhesive and resin are given in Table 7.4. As the model used 2-dimensional elements, the interface stiffness (K_{tt}), nominal stress second direction (τ_0) and shear mode fracture energy second direction (G_{IIIC}) are not required, and the values are equal K_{ss} , τ_0 and G_{IIC} respectively. It should be noted that all models use the same BK parameter of $\eta=1$. The parameter η does not change the simulation results significantly, while the initial failure stresses and fracture energies are the major factors to change the simulation results.

To improve the convergence rate of the iterative procedure, a viscous stabilisation scheme was implemented, as suggested by ABAQUS [201] for its cohesive element. In all the element types, the damage stabilisation cohesive was set as 10^{-5} to stabilise the process.

Table 7.2: Elastic properties of the adhesive and resin layers

Material	E or K_{nn} (N/m ³)	G_1 or K_{ss} (N/m ³)	G_2 or K_{tt} (N/m ³)
Araldite 2015	9.0E12	3.31E12	3.31E12
Resin LY3505/XB3405	70.0E12	25.9E12	25.9E12

Table 7.3: Damage initiation (Quads Damage)

Material	Nominal stress normal mode σ_0 (MPa)	Nominal stress first direction τ_0 (MPa)	Nominal stress second direction τ_0 (MPa)
Araldite 2015	32	23	23
Resin LY3505/XB3405	45	22	22

Table 7.4: Damage propagation (Damage Evolution)

Material	Normal mode fracture energy G_{IC} (N/m)	Shear mode fracture energy first direction G_{IIC} (N/m)	Shear mode fracture energy second direction G_{IIIC} (N/m)
Araldite 2015	410	3950	3950
Resin LY3505/XB3405	155	1350	1350

7.3 The effect of cohesive zone position

An important feature of CZM is that it can be easily incorporated in conventional FEA software to model the fracture behaviour in various materials, including adhesively bonded joints [133]. This technique consists of the establishment of traction–separation laws to model interfaces.

The CZM laws are established between paired nodes of cohesive elements, which can be used to connect superimposed nodes of elements representing different materials or different plies in composites, to simulate a zero thickness interface Figure 7.3a [209], or can be applied directly between two non-contacting materials to simulate a thin strip of finite thickness between them, e.g. to simulate an adhesive bond Figure 7.3b [210].

The $[0^\circ, 90^\circ]_6$ model with 75 mm overlap was studied to investigate the influence of two different failure models. These models chosen to study the CZM technique for the adhesive-cohesive model and cohesive model are illustrated in Figure 7.3. In both models the material properties of the steel and the CFRP were modelled as solid elements. The adhesive layer in Figure 7.3a was modelled as 2 layers of solid homogeneous material with a thin layer of cohesive elements in the middle. The adhesive layer in Figure 7.3b was modelled completely as cohesive elements.

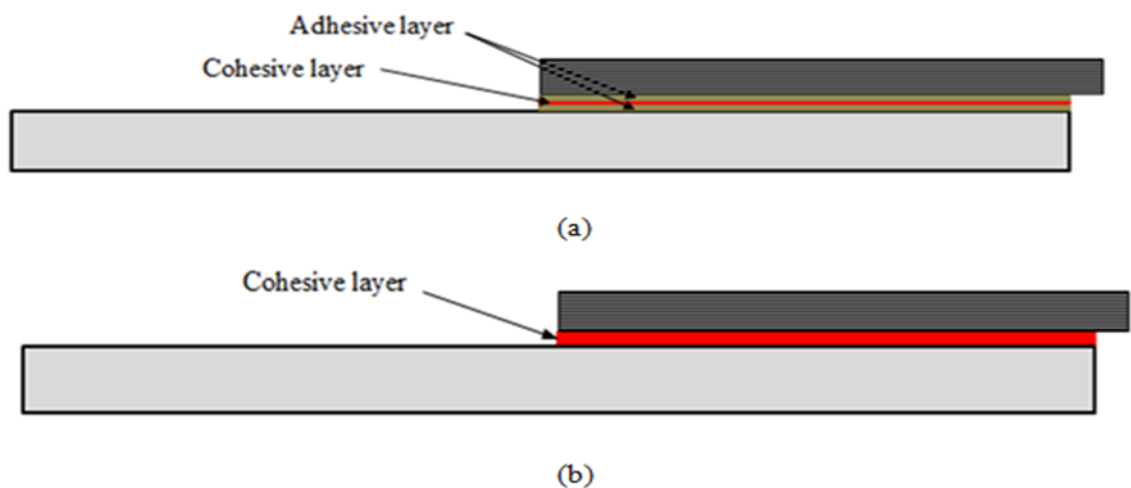


Figure 7.3: Cohesive elements to simulate failure paths in adhesive bond; (a) Adhesive-cohesive model and (b) cohesive model

In Figure 7.3a, the mesh size in the important points was 0.05×0.1 mm, but in Figure 7.3b there was only 1 element through the thickness of the adhesive layer. The overall mesh was 0.2 mm. The load–displacement behaviour is shown in Figure 7.4.

The Figure shows that two models have the same curves; the values of failure load have slight differences, which are that the adhesive-cohesive model converges to 52.2 kN while cohesive model converges to 50.08 kN. The relative error for this example is about 4%, which is very small. This comparison indicates that both models can be equivalent to each other. This conclusion is significantly useful to predict adhesive joints or other structures, since the failure path in practice is not clear and structures have very complicated geometry. The adhesive layer was modelled completely as cohesive elements to simulate the DLS joints in this work.

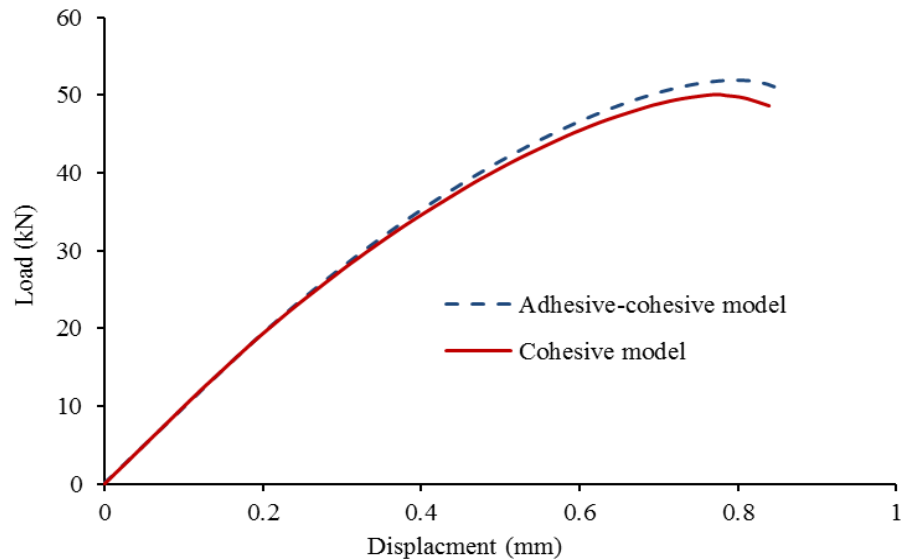


Figure 7.4: Comparison of Load-displacement curves of different failure models

7.4 Damage parameters sensitivity on DLS numerical results

Numerical results' sensitivity to damage constitutive parameters of the DLS joint loaded under tensile load are represented in Figure 7.5. Results appear to be insensitive to moderate changes in mode I parameters G_{IC} , σ_0 and K_{nn} . The sensitivity analysis shows that only the critical fracture energy parameter G_{IIC} and the stress damage initiation τ_0 significantly influences the numerical results of the DLS model. This can be explained by the way in which the mode I parameters have no influence, which is consistent with the fact that the adhesive layer here is mainly loaded under pure mode II.

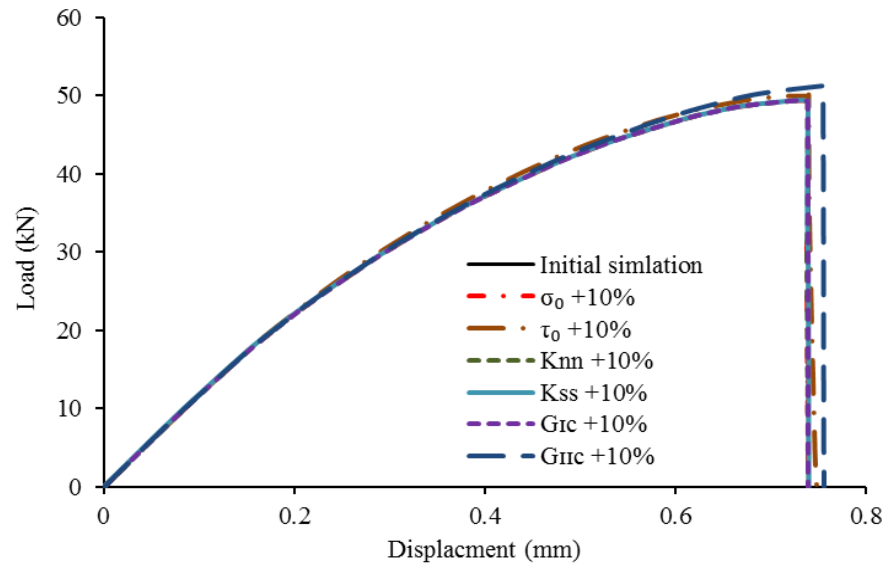


Figure 7.5: Numerical results sensitivity to 10% increase in constitutive damage parameters

7.5 Damage initiation and growth

Simulation of the DLS joint was performed considering symmetry conditions. However, this depends on the CZM parameters determined from the DCB and ENF specimens, which were presented in Tables 7.2, 7.3 and 7.4. The $[0^\circ, 90^\circ]_6$ model with overlap 75 mm was studied to investigate the location of the damage initiation and propagation. The failure predicted by the CZM was in the adhesive layer. The damage contour plots for the model at the beginning (50% of the failure load) and the end of the failure load are shown in Figure 7.6 and b.

Cohesive modelling has an advantage in showing failure initiation and propagation. The value of scalar stiffness degradation (SDEG) in the cohesive zone can be employed to show the joint failure history, and used to display the behavior of the interfacial element.

In Section 6.3.1, the damage variable (D) was defined in relation to the bilinear CZM model. A function that is available when using cohesive elements includes the ability to output the damage variable D, which is known as scalar stiffness degradation. The variable SDEG gives the value of the damage variable D for individual elements, a value of 0 indicates that damage has not initiated, and a value of 1 indicates that complete failure has taken place.

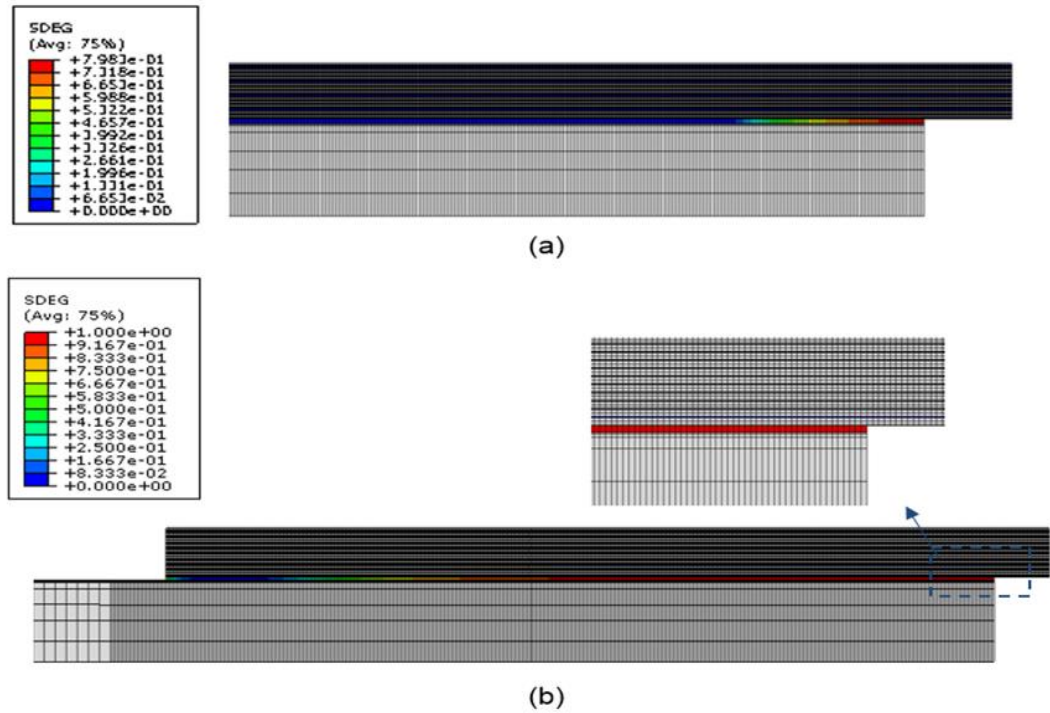


Figure 7.6: Contour, showing failure prediction of the $[0^\circ, 90^\circ]_6$ model: (a) damage initiation at the RHS (b) and propagation to the end of bond.

As illustrated in Figure 7.7, if the damage history throughout the time period is up to the failure load, it can plot the damage history along the adhesive bondline in various fractions of the failure load. This feature of being able to plot the damage history through the adhesive bondline allows an indication of which segment of the joint overlap failure initiates. This also explains how the failure evolves along the overlap, up until the failure load is reached. Therefore, it is useful to investigate the growth of the degradation variable related to the applied load.

Figure 7.7 shows the corresponding stiffness degradation, SDEG, for the whole joint (model) as a measure of damage propagation for the $[0^\circ, 90^\circ]_6$ model. As can be seen, when the load is applied, then full fracture occurs in the adhesive layer. By varying the load it can also be seen from the figure how the damage is initiated and propagated within the adhesive layer. This data shows that damage initiated at the RHS of the model, at the same point where the highest stress occurred in the strength of the material approach model. The failure initiation begins at the RHS of the adhesive layer at around 50% of the total failure load. The damage at the RHS begins to propagate, and at around 90% of the failure load, damage begins to

accumulate at the LHS. The respective damage at the centre and end of the overlap begins to grow, with a higher damage magnitude apparent at the RHS.

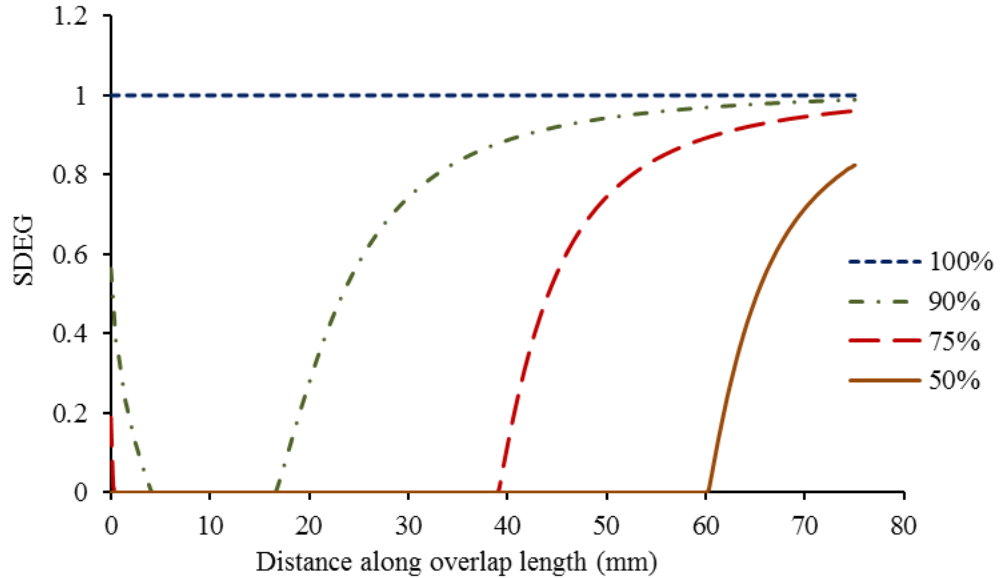


Figure 7.7: Stiffness degradation curves at various percentage of maximum failure load (50 kN) for the $[0^\circ, 90^\circ]_6$ model with 75 mm overlap length

7.6 Parametric studies

This parametric study focuses on investigating the effect of the geometric parameters to the behaviour and strength of the DLS joint. Geometric parameters include the fibre orientation angle of the laminates, the thickness of the CFRP adherend and the length of the overlap. The finite element model based on the CZM has been used for the parametric analysis.

7.6.1 Effect of stacking sequence

Numerical analysis was performed with the commercial FE package ABAQUS to assess the effects of the fibre orientation angle of the laminates on failure prediction in DLS joint subjected to tensile loading. In this analysis, three DLS models using 0.2 mm adhesive thickness and the CFRP composite adherend with three different fibre orientation angles ($[0^\circ, 90^\circ]_6$, $[90^\circ, 0^\circ]_6$ and $[+45^\circ, -45^\circ]_6$) were used. Also nonlinear geometric deformation of the DLS model was taken into account. All three models have similar FEA meshes as shown in Figure 7.2. The selected paths of damage initiation and propagation were decided in

accordance with failure modes from experimental results for corresponding joints with a 75 mm overlap. For the $[0^\circ, 90^\circ]_6$ model, the failure predicted by the CZM was in the adhesive layer, see Figure 7.6. While for the $[90^\circ, 0^\circ]_6$ and $[+45^\circ, -45^\circ]_6$ models, the failure was predicted to take place either in the adhesive or composite laminate. The latter occurred between the first and second layer of laminate. Figure 7.8 and 7.9 illustrates the two modes of failure respectively.

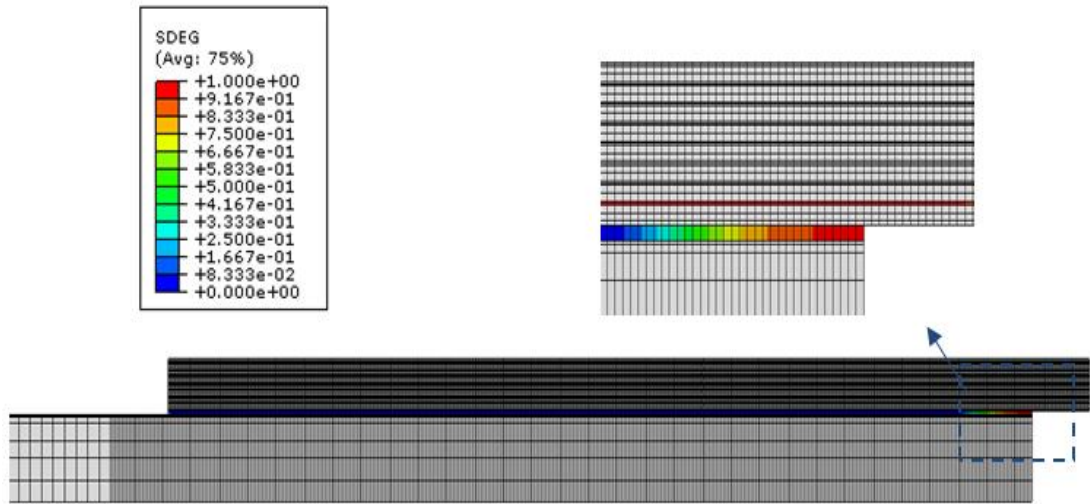


Figure 7.8: Contour, showing failure prediction of DLS joint in the adhesive and resin layers for the $[90^\circ, 0^\circ]_6$ model at load 48 kN

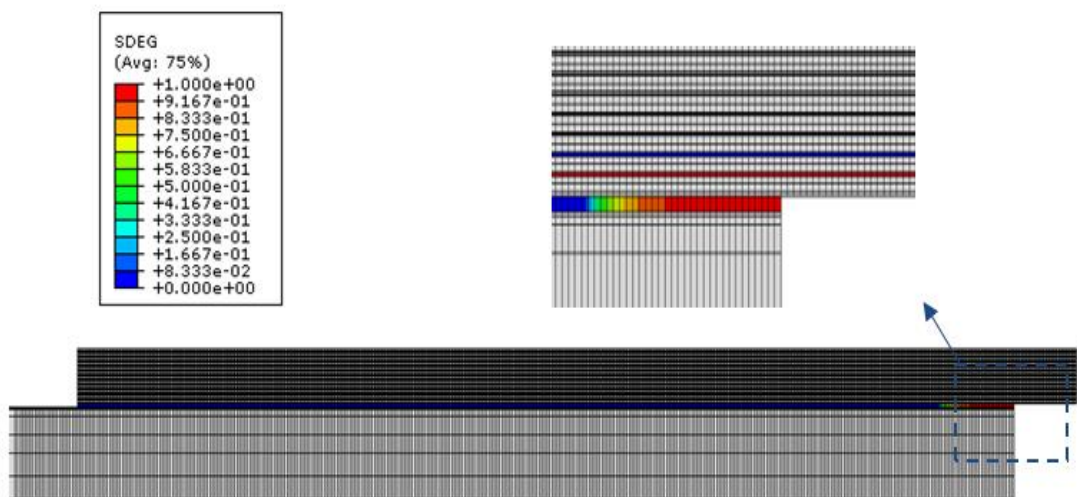


Figure 7.9: Contour, showing failure prediction of DLS joint in the adhesive and resin layers for the $[+45^\circ, -45^\circ]_6$ model at load 17 kN

7.6.2 Effect of adherend thickness

Figure 7.10 shows the growth of the damage variable or the stiffness degradation variable vs. displacement curves for the first element that reached ultimate failure, for the $[0^\circ, 90^\circ]_6$, $[0^\circ, 90^\circ]_{12}$ and $[0^\circ, 90^\circ]_{18}$ models with different laminate thicknesses, namely 3 mm, 6 mm and 9 mm. For each model, the first element along the interface reached the critical stress level which causes failure initiation.

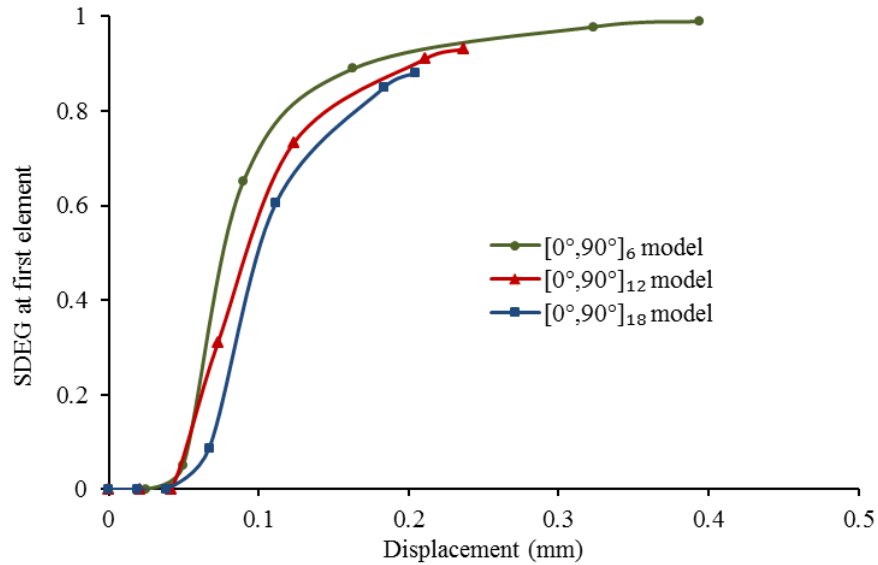


Figure 7.10: Stiffness degradation of the first element to fail in three models

The figure indicates that damage initiation started in the model with the thinnest laminate, i.e. 3 mm $[0^\circ, 90^\circ]_6$ and followed by $[0^\circ, 90^\circ]_{12}$ and $[0^\circ, 90^\circ]_{18}$ models. In addition, it should be noted that although $[0^\circ, 90^\circ]_{12}$ and $[0^\circ, 90^\circ]_{18}$ models produced interfacial debonding, these occurred at applied loads that are much larger than are required for debonding of the $[0^\circ, 90^\circ]_6$ model.

The load-displacement curves for each model are shown in Figure 7.11. The numerical and experimental methods indicate an increase of joint strength with an increase in laminate thickness. For example there is an 18% increase in joint strength as a result of increasing the thickness from 3 mm to 9 mm.

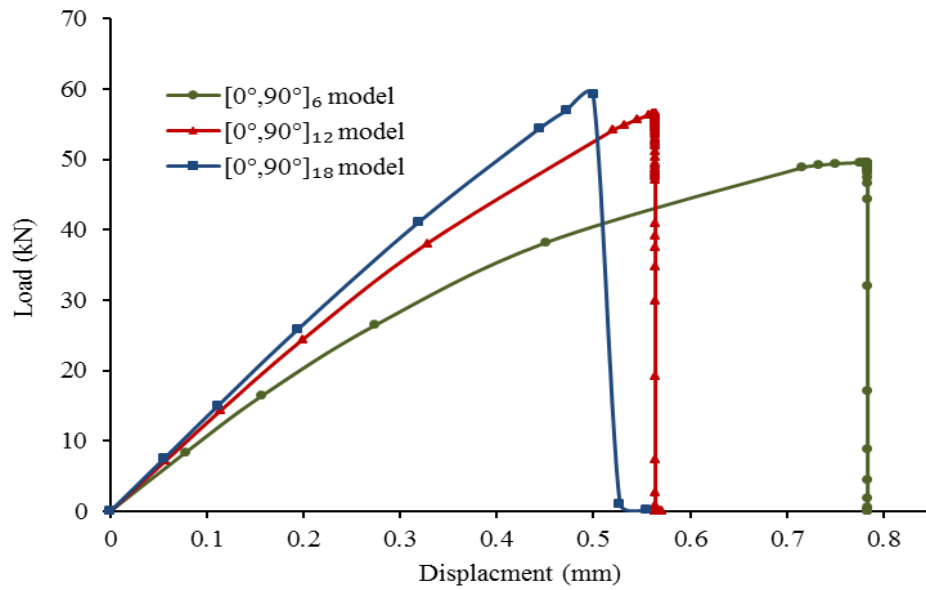


Figure 7.11: Numerical load displacement curves for models with different thickness

7.6.3 Effect of overlap length

One of the most important geometric parameters that influences the joint strength is the overlap length. The failure loads for joints obtained by applying the numerical modelling CZM approach on the geometry of DLS joint, the cohesive properties were kept fixed for all models, and the length of the bonded length only varied. The models were based on $[0^0,90^0]_6$ laminates with thickness value of 3 mm. In the parametric analysis seven different overlap lengths were considered, ranging from 25 mm to 200 mm.

In Figure 7.12 the change in the load-displacement curves with respect to the overlap lengths are represented. The effect of overlap length on the failure loads in the $[0^0,90^0]_6$ model are shown in Table 7.5. Figure 7.13 shows that failure loads predicted from the numerical models increase nonlinearly with the increase in the overlap length. The curve shows a plateau at 100 mm overlap which the joint load does not increase further.

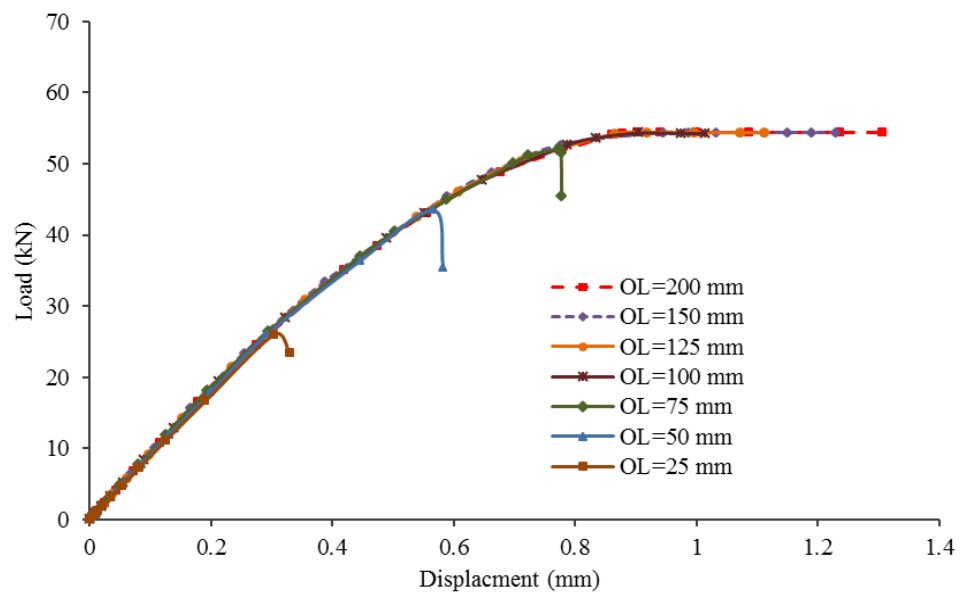


Figure 7.12: Influence of overlap length on the load-displacement curve
(Note: The overall length of the models are kept the same)

Table 7.5: Effect of overlap length on the failure load in the $[0^\circ, 90^\circ]_6$ model

Overlap length (mm)	25	50	75	100	125	150	200
Failure load prediction (kN)	25.89	43.47	50.08	54.31	54.36	54.38	54.38

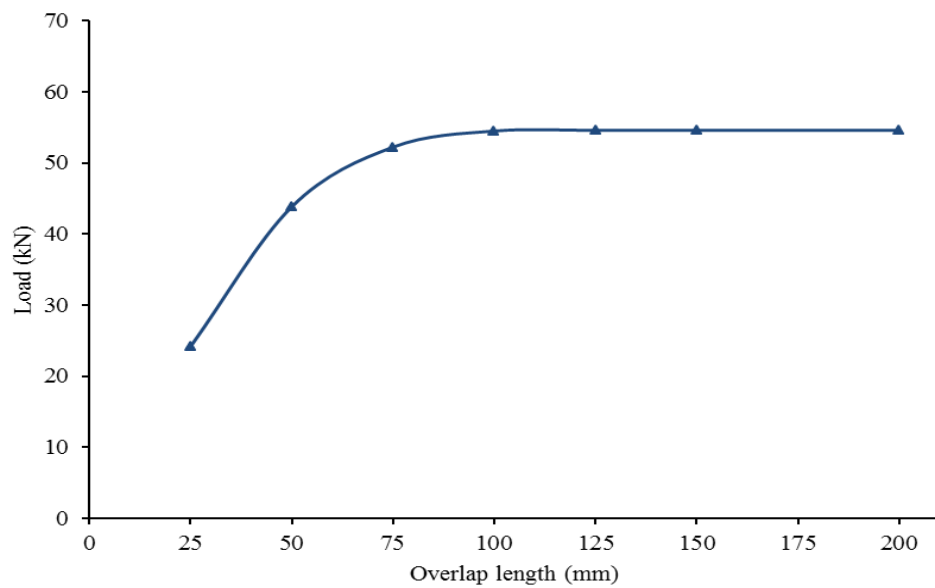


Figure 7.13: Numerical loads prediction for different overlap length

7.7 Conclusions

This chapter studied numerically, interaction of interface delamination in DLS joint under tensile load of steel adherends bonded by CFRP adherends. A cohesive zone model approach was adopted to simulate the interface rupture between steel and CFRP and between the layers in CFRP adherend. A cohesive element for adhesive and rich resin layers can be used to represent the propagation of pre-existing delamination, as well as the onset and propagation of delamination in modules that do not contain pre-existing cracks.

It was found that the convergence difficulties that are typical of cohesive laws can be mitigated with the use of viscoelastic stabilisation, or by reducing the interfacial strength to enlarge the process zone.

The main conclusions which arise from the present research can be summarised as follows:

- Different failure modes were observed for CFRP adherends with different orientation angles: adhesive layer failure (cohesive failure) for the $[0^\circ, 90^\circ]_6$ model, CFRP delamination, which occurred between the first and second layer of carbon fibre for the $[90^\circ, 0^\circ]_6$ model, and CFRP delamination and adhesive interface debonding for the $[+45^\circ, -45^\circ]_6$ model.
- A critical bond length may be evaluated, beyond which any increase in bond length cannot increase the failure load, but provides an increase of ductility to the joint.
- Increasing the thickness outer composite adherend leads to an increase in joint strength. A thickness increase from 3 mm to 9 mm resulted in an 18% increase in the failure load.

Chapter 8

8 Discussion, conclusions and future work

8.1 Discussion

8.1.1 Properties of materials

The structural adhesive used in this work to bond the specimens was two-part epoxy adhesive Araldite 2015. This type of adhesive was chosen based on many advantages such as; it allows excellent joint strength, exhibits good stability and assemblies of similar and dissimilar materials. According to research at University of Glasgow [203, 211], the adhesive has been found to provide an effective bond between the CFRP to steel material system.

The Araldite 2015 is known to have elasto-plastic properties, but this was not shown from the tests. Therefore, it was important to use elasto-plastic properties for the numerical analysis, using supplier data in conjunction with lab tests and engineering assumptions. The adhesive failed at 35 MPa obtained from the butt joint lab test. Huntsman quoted 30 MPa and also mentioned the true failure stress of 30 MPa with 0.044 strain (see Appendix B). In order to calculate the strain at the adhesive failure load, the true curve was extrapolated to 40 MPa. After interpolation in chapter 3 (see Section 3.3.3), the adhesive failure strain was 0.06 at 40 MPa. Therefore, the adhesive is in the elastic region between a strain of 0 and 0.022. After 0.022 the adhesive is in the plastic region, until 0.06, where it fails. There are still contradictory views about adhesive properties in general in much of the literature [211, 212, 213, 214].

Tensile butt joint specimens were used to verify and support strength data for the bulk adhesive. The specimens were prepared carefully using the jig to ensure alignment of the butt joint adherends. Three out of five specimens were selected for testing, those which were apparently bubble-free. Some of the results were also discarded due to high bubble contents, as this always compromises the failure strength and strain.

The thick adherend shear test (TAST) is also used to verify and determine the shear strength.

It is one of the most popular tests to identify the shear behavior of structural adhesive. When thick and very short metallic adherends are used, the adhesive is in a state of uniform shear. As regards specimen manufacture, ISO11003-2 recommends machining the specimens from two adherends bonded together. Overlap length in TAST joints was also controlled by the use of PTFE sheets. Specimens were also prepared carefully using the jig to ensure alignment of the shear test adherends. The TAST is probably the simplest and most reliable technique to use. The average shear stress for Araldite 2015 adhesive was 24 MPa obtained from the TAST specimen (see Section 3.3.4). On other hand, the shear stress can be converted into equivalent tensile values based on von Mises by multiplying by $\sqrt{3}$.

The cross ply composite laminates were produced and supplied by FFI, Norway. These were produced by infusion moulding of lightly stitched UD high strength carbon fibre mats/plies and epoxy resin. The mechanical properties of the composite material were obtained using Rule of mixtures [20], Tsai and Hahn equations [178] and the transversely isotropic materials assumption for better estimation. The mechanical properties were obtained from calculations based on the volume fraction of carbon fibre of 60%.

8.1.2 DCB and ENF tests

The mode I and mode II fracture parameters are partially successful in determination of values of G_{IC} and G_{IIC} which have been reported elsewhere [133, 185], and as such are a useful indicator of where the fracture energy of this specific thickness of Araldite 2015 and epoxy resin LY3505/XB3405 may be found. However, the range of values deduced via this method suggest that the mode I fracture energy becomes stable at around 400 N/m for Araldite 2015, and 160 N/m for epoxy resin LY3505/XB3405. However, more measurements would need to be recorded to confirm this. BS 7991:2001 followed stipulates that at least 15 crack propagation measurements should be recorded before a total of 65 mm in crack length has been reached (from the PTFE insert). All of these recommended values were obtained for the 0.2 mm test conducted, due to the stick-slip fracture behavior of polymers under constant applied extension rate loading conditions. Hence a coarser representation of the mode I fracture energy was apparent as a result.

In many fracture tests, the measured fracture energy (as seen on a typical R-curve, Figure 3.21) will reach a plateau region which signals that the measured fracture energy has reached a constant level. This is termed steady state fracture energy, which is when the related plastic zone ahead of the crack tip is fully developed [119]. The reasons for such non-

typical behavior reported in this work can largely be attributed to experimental error, as not only was the crack tip difficult to follow manually, but even when the tip was located, this may not have been the true location of the tip, due to plasticity effects [150].

Also, an improvement which could rectify a proportion of the discrepancies mentioned would be the use of a high magnification video camera. The recording could be replayed retrospectively and subsequently correlated with the measured load-displacement curve to accurately collate the load, displacement and crack propagation values in a more organised manner. The crack measurements should be within ± 0.5 mm of the crack tip, which is challenging when using manual visual inspection such as a microscope. Also, the crack measurements strain gauge would have been more valuable, but these were not envisaged at the time of experimentation

The BS 7991:2001 does not provide a stress-elongation relationship, which is usually a common feature of CZM fracture parameter identification. In this work however, this was acceptable, as the fracture parameters were identified via means of an inverse identification procedure. The SBT described the deflections of the beam due to bending and shear, but does not account for important effects of the beam root rotation. The root rotation affects the resulting values of the fracture energy G_{IC} . This is largely down to the fact that when using mild steel as a substrate material, the neglected crack roots rotation in the SBT method will lead to significant errors, and as such, these values are not indicative of the true fracture energy of the specimen [150]. Another feature of the BS 7991:2001 which could be improved is the fact that this technique relies upon the beam opening displacement being represented by the relative crosshead displacement of the testing machine. This could be improved by placing an extensometer across the neutral axis of each substrate as in [128], and subsequently this could also be used as an input for a more accurate methodology of obtaining the cohesive relation in mode I [119]. Another significant contributor to the discrepancies observed can be related to the system compliance effects of the testing equipment used. This is due to the componentry of the equipment having a finite compliance which can be seen to affect the measured values of G_{IC} [150], and in this instance an assumption was made for the magnitude of system compliance. However, a more in-depth study of the specific compliance of the machine used could yield more accuracy in the overall results. As is evident from the analysis, the most accurate set of results were obtained using CBT and ECM; it is commonly held that the ECM method yields the most accurate results [132].

The drawbacks with using SBT, ECM and CBT involve the simultaneous measurement of the applied force, load point displacement and subsequent crack length, but the crack length measurement can be dubious, as the fracture process zone (i.e. damaged zone ahead of the crack tip) is not very well defined and can extend several millimetres before a crack actually starts to propagate [215]. An alternative methodology to that of the BS 7991:2001 protocol involves use of the Compliance Based Beam Method (CBBM), which is based on beam theory, and utilises beam compliance in the data reduction scheme. As such, it does not require any crack length measurements to be recorded during the test. This is a relatively new approach and has promising signs for replacing the BS 7991:2001 protocol [216].

The end notched flexure (ENF) test was usually used for measuring mode II fracture toughness of adhesive bonding. One remaining challenge of this test method is monitoring the accurate crack length during its propagation as the load increases [217]. For the ductile adhesive failure process, it is very difficult if not impossible to identify the exact location of the crack tip. The employment of high resolution observation equipment gives more detail of the crack tip, while only making it even more confusing to tell where the “true” crack tip is. In order to overcome this difficulty, the equivalent crack method [217, 213] has been developed recently, in which the crack length is calculated using the experimental compliance and a beam theory based relation. On the base of the J-integral theory, Alfredsson [218] presented a novel approach to calculate the mode II energy release rate. This theory avoided the measurement of crack length, while the crack tip deformation needs to be continuously monitored. The equivalent crack method was initially developed by Moura et al. [213].

8.1.3 Numerical modelling of DCB and ENF

In the numerical investigation of this work, the intrinsic modelling technique was initially conducted on the DCB model and ENF model. These allowed for the adhesive and epoxy resin to be characterised by a tailored CZM, in the form of the bilinear relation. The experimental cohesive parameters of the DCB and ENF specimens were determined by an inverse method, fitting the numerical and experimental load-displacement curves of each specimen. An inverse identification procedure was conducted in order to iteratively ascertain the peak strength and fracture energy, to create a tailored bilinear CZM for this specific testing scenario. This was done by comparing the peak force of the experimental load-

displacement plot with the numerical output of the DCB model, until a minimum deviation between the two plots was observed. Using this procedure a good agreement between the numerical and experimental tests has been found, but one must note that by adopting this methodology that the resulting fracture parameters obtained via finely tuning the numerical response will be unique to that specific experimental test only. The peak strength was obtained by using a very fine cohesive element length (0.01 mm) in order to accurately capture the tractions in the cohesive zone of the numerical model. The procedure of tailoring the CZM implemented in this report serves as an illustration of how to deduce the relevant mode I fracture parameters using this commonly used technique. A much more in-depth analysis could be conducted by doing more DCB tests in order to accurately find the peak strength during the data fitting procedure, as each DCB test will be unique due to the difficulty in keeping such a thin layer perfectly constant (i.e. thickness deviation in substrates needing to be strictly controlled). The inverse identification procedure yields a unique solution for the respective mode I fracture energy and peak strength values, but serves as a useful illustration of this commonly implemented technique, and gives indicative magnitudes of what these values actually are.

Other methods used in the literature to obtain the CZM parameters can lead to a wide array of quoted fracture parameters for similar adhesives. More complex methods of obtaining the CZM parameters can be obtained via a J-integral approach using the DCB specimen [133]. This method involves the use of extensometers in order to measure the end opening displacement at the neutral axis on the beam at the initial crack tip, and by differentiating the resultant calculated J-integral found from the load used, in order to obtain a cohesive law (i.e. for mode I; this is defined as peel stress versus peel separation and for mode II; this is the shear stress verses the shear displacement) [119]. A noteworthy result of these methodologies is that the maximum peak strength value (or tripping traction) found was of the same order of magnitude as the yield stress of the bulk adhesive, which bears a similarity to the obtained value of peak strength found using the inverse identification procedure in this work, as the obtained magnitude of peak strength was 32 MPa; compared to the tensile yield strength for the bulk adhesive used (Figure 3.4). The mode II cohesive parameters used were deduced via the CBBM technique [216, 195] and show that the often quoted ratio of fracture energies, $G_{IIC}/G_{IC} = 2$, can be inaccurate, and as such, much higher ratios for this relation can be observed for Araldite 2015 [195].

8.1.4 Cohesive interface element technique

Damage problems in adhesive joints remain a difficult task, and therefore engineering structures are often designed to be tolerant to reasonably sized flaws. However, interface delamination is generally very complex in nature and difficult to solve, because it involves not only geometric and material discontinuities, but also the inherently coupled Mode I, II and III fracture in layered material. A valuable approach from this point of view is represented by linear elastic fracture mechanics (LEFM) [151]. LEFM has proven to be a useful tool and allowed for a more rapid extension of adhesives technology applications. The major advantage of LEFM is its simplicity. So far, the single parameter treatment based on the stress intensity factor has been extensively and successfully applied to tackle fracture events in adhesive joints [150]. However, LEFM requires pre-existing crack-like defects or notches and, therefore, crack initiation cannot be treated directly. A valid alternative to LEFM for those problems in which these conditions may not be met consists of using CZM. In this thesis, a CZM with bilinear traction separation law is proposed to represent progressive damage occurring within the interface during the fracture process. The CZM is represented by cohesive elements to connect the two surfaces of materials.

A built-in cohesive zone modelling capability is available in ABAQUS, which was employed in this research to predict the failure load of DLS joints under tensile loads. The cohesive zone model is implemented in FEA through the use of cohesive elements. A cohesive element may be considered as two faces separated by a distance, and the relative movement of the two faces is used to determine damage and failure. The geometric model development, problem setup and meshing of the 2D model was carried out using Abaqus/CAE. Two sets of parameters are required for application of the developed interface element, namely, interfacial strength and fracture toughness. The initiation of fracture is determined by the interfacial strength and the progression of fracture is determined by the interface fracture toughness. In the finite element modelling, these interface elements are positioned within the interface where potential delamination propagation is expected. Contact-type interface element is also developed to simulate contact behaviour in the delaminated region.

8.1.5 Verification of interface element model

A verification process applying the developed interface element is presented with numerical simulations of standard fracture test configurations, namely DCB and ENF specimens, under Mode I and Mode II respectively. For all the simulations, the finite element solutions are in good agreement with the experimental results. Typical computational issues related to modelling with interface elements are discussed. Issues of mesh sensitivity, effects of interfacial strength and viscous regularisation factor are investigated.

Generally, zone modelling does not require very fine mesh near the crack front, since no singularity is present. However, in order to obtain a relatively smooth solution, the mesh should be sufficiently fine in the evolving process zone at the delamination front, and the element size needs to be less than the cohesive zone length. Slightly lowering the interfacial strength can reduce the burden on mesh refinement without sacrificing the accuracy of the prediction. It is found that when a small value of the viscosity parameter is used, the viscous regularisation helps improve the rate of convergence without compromising results, as shown in Figure 6.21 and 6.22. A helpful experience from the current study is that simulations of stable crack growth events using the CZM approach require careful convergence studies, not just with respect to the standard finite element, but also with respect to the cohesive element length relative to the cohesive zone size. The cohesive zone length is directly related to the convergence issue that is the most crucial point for the CZM application [219]. The cohesive zone model implemented is distinctive of materials softening after their characteristic separation is reached, and practical applications in Abaqus/standard often come up with convergence problems. A common technique to overcome some of these convergence difficulties is the use of the viscous regularisation factor. Figure 6.19 and 6.20 show a comparison of the simulation prediction of the load-displacement curves for DCB and ENF models respectively. Based on this observation, simulation solutions with cohesive element length 0.2 mm for mode I and mode II are considered to be converged.

8.1.6 DLS joint modelling

A 2D finite element model was created in order to analyse the behaviour of DLS joints under tensile loading. The numerical modelling of the DLS joint was selected based on the symmetry in joint geometry and loading, as shown in Figure 5.1. The model consists of steel

adherend, adhesive layer and CFRP laminate adherend, and the CFRP laminate modelled at its constituent level i.e. unidirectional laminates and the resin rich layers, as shown in Figure 5.3. Thus, this modelling gives a good representation of the material properties and the overall joints' behaviour, especially when dealing with CZM of the resin within the laminate. A number of meshing methods are available in ABAQUS 6.9-1, and each geometric area was meshed based on the geometric shape. All the shapes were meshed with structured mesh, and used plane strain quadratic elements CPE8R (reduced integration). The minimum element size was at the overlap edges, and the coarse mesh was far from the overlap region, which was the region of interest during the analysis. These elements were to be joined by shared nodal points, which were used to create the mesh of the model. The stress and strain at each nodal point of each element can then be readily calculated. The strength of materials approach is the classical method. This aimed at providing the distributions of stresses and strains, and in particular the locus and value of maximal stresses and strains.

The CZM was used in all DLS joint simulations; as shown in Figure 7.2, the numerical analysis was carried out using non-linear geometry. Four-node plane strain reduced integration elements (CPE4R) were used for the steel adherend and the composite plies. The adhesive layer and resin-rich layers were modelled with a sweep mesh and four-node cohesive elements (COH2D4), with bilinear traction separation. The cohesive element was only one element through thickness of the adhesive layer, and of the rich resin zones between the unidirectional laminates. The CZM parameters were determined by experimental tests. It was found that the results from the FEA model were in good agreement with results from the experimental tests. Both results matched the load-strain curves. These agreements also demonstrated that the determination of CZM parameters is correct, and thus these parameters can be extended to other simulations.

The effects of cohesive zone position in 2D models were studied using the CZM technique for the adhesive-cohesive model and cohesive models, as shown in Figure 7.3. It was found that both models can be equivalent to each other, and did not affect the simulation results. This implies that the change of cohesive layer position does not affect the modelling results once the parameters of CZM are correct.

The CZM approach enabled a diagnostic of the current damage state and an update of the strength prediction. The damage initiation is automatically localised due to the use of the strength of material approach, while the damage propagation is controlled through fracture

mechanics concepts, without assuming any initial cracks. Another advantage of CZM for the failure prediction of bonded joints comes from the fact that the required experimental characterisation investigates directly the mechanical behaviour of the adhesive layer, such as employed in the final bonded joints. The cohesive elements are used in the DLS joint model for FEA simulation, these elements saving computation time by modelling the adhesive as a single element layer, and preserve results' accuracy. The numerical predictions are highly satisfactory, and validate the use of the constitutive model for FEA simulation of large industrial bonded structures [220]. Figure 8.1 shows the variation of CPU time with the overlap length for both the strength of material and the CZM models of the $[0^\circ, 90^\circ]_6$ joint. All the simulations were run using a CPU (DELL OptiPlex 780, Intel® Core 2 Quad Q8400 @ 2.66 GHz). In general, the strength of the material model and cohesive zone model are almost the same, indicating the potential critical region in the DLS joint.

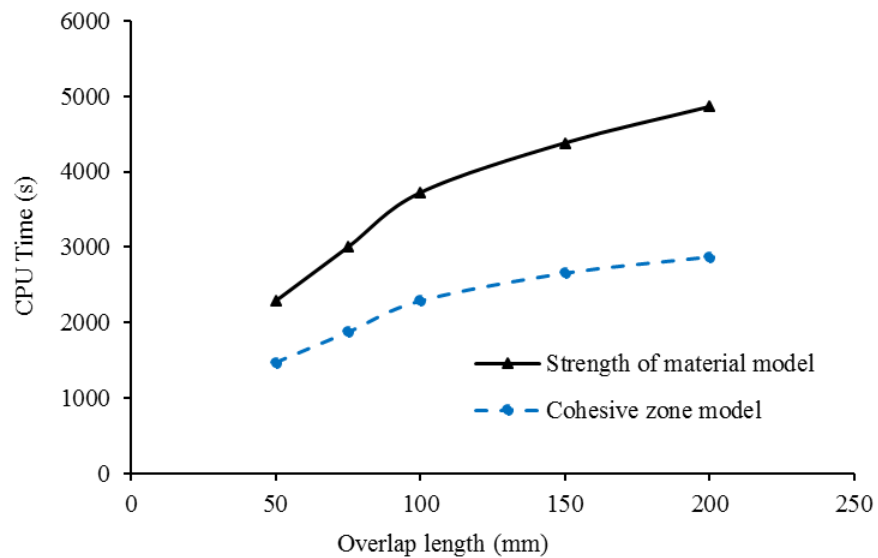


Figure 8.1: Variation of CPU time with overlap length of the $[0^\circ, 90^\circ]_6$ models for both the strength of material and the CZM approaches.

However, the 2D FEA based on the CZM model runs faster than the strength of material model. The computed time of CZM modelling saved about 34% to 40% of the computing time of the strength of material modelling, see Table 8.1.

Table 8.1: Percent saving in simulation time between strength of material and CZM approaches for the $[0^\circ, 90^\circ]_6$ models with different overlap lengths

Overlap length (mm)	CPU time (s)		Saving in simulation time (%)
	Strength of material	Cohesive zone model	
50	2250	1480	34%
75	3002	1873	37%
100	3723	2278	39%
150	4380	2626	40%
200	4861	2892	40%

8.1.7 Prediction of failure of DLS joints

In Chapters 4, 5 and 7, experimental and numerical results for hybrid (steel/composite) DLS joints were presented. In this chapter, predictions of the FEA numerical model are compared with the experimental results. A good agreement would increase confidence in the validity of the FEA model. Comparisons were made in terms of load-strain curves. However, due to instrumentation and measurement constraints, it was not possible to compare FEA predictions for adhesive response with experimental values. Nevertheless, good agreement in the quantities compared should be seen as a partial validation of the FEA models.

In the experiments, more detailed strain gauge instrumentation was attempted in order to compare results at strategic positions of the joint. Thus, strain gauges were bonded onto the CFRP and steel adherends at strategic positions, along the length at mid-width of joint, with strain gauge numbering corresponding to the diagram in Figure 4.17. Figure 8.2 compares the strain values for the $[0^\circ, 90^\circ]_6$ specimens and models, to validate the static response predicted by the 2D models in this study. The comparison provides good correlations for the numerical models with these experiments. According to this study there are two possible failure initiation modes in long DLS joints. One is in the adhesive, which includes cohesive or adhesive failure. The second mode is delamination failure of the outer composite adherend. The results from the numerical strength limit analysis showed that failure modes correspond well with the results from the experiments.

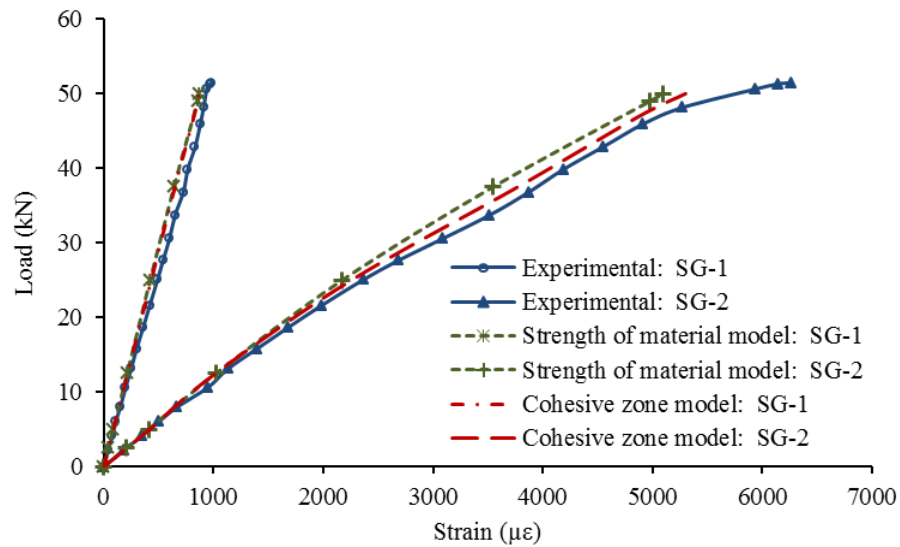


Figure 8.2: Comparison of the load versus strain curves for $[0^\circ, 90^\circ]_6$ specimens and models with overlap length of 75 mm

The degree of correlation depends on the geometry of the joints in terms of adherend thickness, fibre orientation and length of overlap. Among the failure criteria that have been employed in this study are maximum peel or principal stresses of the adhesive and adjacent resin at the RHS of the joint and model (see Table 5.3 and 5.4). These are compared to corresponding strength values for the adhesive and resin. Also, the longitudinal and transverse tensile strength of the UD composite may be used as measures of failure.

Another important measure of joint failure is the level of the plastic shear stress within a joint. Figure 5.21 showed the shear stress along the adhesive/composite interface for all joints $[0^\circ, 90^\circ]_6$ model with different overlap lengths, being high at the RHS near the centre of the joint. The length of plastic zone for the 25 mm and 50 mm overlap joints is about 50% of the overlap. For overlaps greater or equal to 75 mm, the maximum stress remained almost constant, the plastic zone length being about 30 mm. This has a good practical dimension; for example, structural joints (butt connection) in marine construction where overlaps are expected to be well in excess of a 100 mm (200 mm strap).

The CZM approach has also shown a good failure prediction. This however depends on the CZM parameters determined from the DCB and ENF specimens, which are dependent on the test method and materials used in order to obtain the critical strain energy release rates (G_{IC} and G_{IIC}) of the adhesive and resin. The obtained values of the strain energy release rate G_{IC} for experiments was 410 N/m, and the literature quoted value 430 N/m for the same

adhesive (Araldite 2015) [221] . Also, when the values of G_{IIC} are unknown, it is common in the literature to assume a ratio of G_{IIC}/G_{IIC} is 2, which is not realistic. However, the results presented here show a relation of approximately 9.5 for the adhesive. Another study [221] has shown a ratio of approximately 10 for G_{IIC}/G_{IIC} for this adhesive. Therefore, it is important to test not only in mode I but also test mode II for adhesive properties.

The location of the damage initiation and propagation also matched the results from the experiments. Figure 7.7 showed the stiffness degradation curves at various percentages of maximum failure load for the $[0^\circ, 90^\circ]_6$ model. The failure initiates at the RHS of the overlap at about 50% of the total failure load. The damage then begins to grow, and at around 90% of the failure load, damage begins to accumulate in the model at the LHS. The respective damage at the centre and end of the overlap begins to grow, with a higher damage magnitude apparent at the RHS.

8.1.7.1 Effect of fibre orientation

The influence of fibre orientation on the load-displacement response of the DLS joints is illustrated in Figure 4.11. This included three different stacking sequences of $[0^\circ, 90^\circ]_6$, $[90^\circ, 0^\circ]_6$ and $[+45^\circ, -45^\circ]_6$ specimens with 75 mm overlap length. It can be seen that the failure load for the $[0^\circ, 90^\circ]_6$ specimen is 5% and 70% higher than the $[90^\circ, 0^\circ]_6$ and $[+45^\circ, -45^\circ]_6$ specimens, respectively.

Figure 4.12 showed the experimental failure surfaces for the three different specimens. It can be seen that the $[0^\circ, 90^\circ]_6$ specimen suggests that failure initiated within the adhesive layer, see Figure 4.12a. But when the stacking sequences are based on the $[90^\circ, 0^\circ]_6$ or $[+45^\circ, -45^\circ]_6$ specimens, the fractures have taken place at the top ply. From Figure 4.12b and c it can be seen that both specimens showed delaminated composite at the left on the steel adherend surfaces.

In relation to numerical modelling, in the case of the $[0^\circ, 90^\circ]_6$ model the longitudinal tensile stress (S11) was very significant (911 MPa) and somewhat close to the tensile strength of the composite (1400 MPa). The failure initiation in this case was thought to be in the adhesive, where maximum principal stress and maximum shear stress (S12) at the RHS reached 54 MPa and 24.5 MPa respectively (see Table 5.3). In the case of the $[90^\circ, 0^\circ]_6$ model, the longitudinal stresses (S11) reached 71.6 MPa (Table 5.4), which is very close to the ultimate transverse tensile strength of the laminate (86 MPa) given in Table 5.1. Another possibility for the failure initiation in this case is in the adhesive, where maximum principal

stress at the RHS reached 50 MPa (Table 5.3). This means that the initial crack in the joint could have started either in the laminate or adhesive. Assuming this had started in the 90° ply as seen in Figure 4.12b, the crack is then extended to the resin rich interface between the 90° and 0° ply, leading to delamination.

The [+45°, -45°]₆ specimen and model clearly showed a significant drop in the failure load compared with the other two cases of fibre orientations (Figure 4.11). Nonetheless, the model produced significant stresses in the adhesive, resin and composite (Table 5.3 and 5.4). The maximum tensile strength of the resin is 85 MPa. As can be seen from Table 5.4, the resin tensile stress (S11) reached the failure limit. Also, the tensile stress of the top ply, which is 165 MPa, could have caused delamination failure due to in-plane shear stress, transverse stress, or both. The low global stiffness and strength of the outer adherend in comparison to the other specimens are main factors in this failure. Local stiffness is another factor which may influence joint strength. This is governed by the fibre orientation for the ply next to the adhesive. The effect of this seems small in comparison to the global stiffness, hence the small difference in the failure load between the [0°, 90°]₆ and [90°, 0°]₆ specimens and models. Perhaps having a thin ply (0.25 mm) next to the adhesive bondline (0.2 mm) does not affect joint strength significantly. However, thicker plies, e.g. in excess of 1 mm, may do so.

The tensile (S11), peel (S22) and shear (S12) stresses distributions through the thickness of adhesive and the laminate are illustrated in Figure 5.18-5.20. From these figures it can be observed that the ply stacking sequences appear to have considerable influence on stress distribution through the thickness of the adhesive and CFRP composite laminate at RHS. It can be seen from these figures that tensile stress (S11) distributions are higher at 0° layers, see Figure 5.18a and 5.19a. Also, the shear stress (S12) value in adhesive layer of the [0°, 90°]₆ model is higher than that in other models, as shown in Figure 5.18b and 5.19b.

8.1.7.2 Effect of overlap length

To investigate the influence of overlap length on load-displacement response, DLS joints with 5 overlap lengths (25 mm, 50 mm, 75 mm, 100 mm and 125 mm) were tested. In this group, all the joints have the same stacking sequence of [0°, 90°]₆ and the same overall length (Figure 4.8). The load-displacement curves of the specimens with different overlap lengths are shown in Figure 4.13. As can be seen, the load-displacement curves are linear until

respective point of failure. Also, Figure 4.15 shows the ultimate failure load of the specimens with different overlap lengths. It is obvious that the ultimate failure load of the joints increases with the increase of overlap length. When the overlap length is less than 50 mm, the relationship between the ultimate failure load and overlap length is approximately linear. However, the increasing rate gets slower as the overlap length exceeds 50 mm.

Figure 8.3 shows the experimental and numerical results from strength and CZM approaches for the $[0^\circ, 90^\circ]_6$ specimens and models with various overlaps. The agreements between the experimental and numerically predicated failure loads are very close. The average deviation from the measured load at failure is 7% and 5% for CZM and the strength of material approaches respectively.

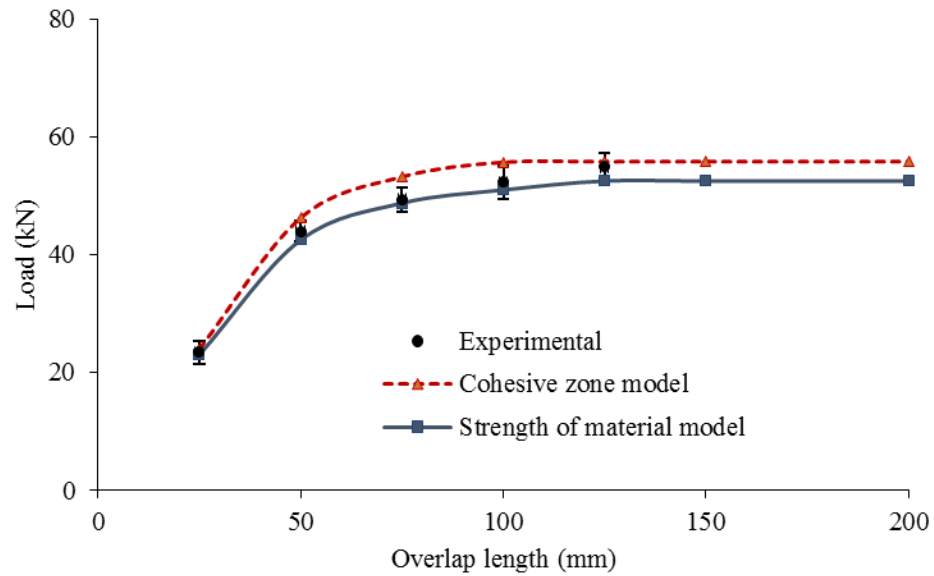


Figure 8.3: Comparison between the experimental and numerical curves for $[0^\circ, 90^\circ]_6$ joint with different overlap length, experimental from Figure 4.15 and numerical from Figure 7.13

8.1.7.3 Effect of adherend thickness

As for the outer composite adherend thickness, two different stacking sequences were considered. These are $[90^\circ, 0^\circ]_6$ and $[90^\circ, 0^\circ]_{12}$ specimens which represent 3 mm and 6 mm thickness, respectively and for 50 mm overlap. Figure 4.16 shows the load-displacement curves for specimens with different CFRP laminate adherend thickness. As can be seen, the load-displacement curves also behave linearly with increasing the adherend thicknesses.

However, when the thickness is doubled, the ultimate failure load only increased by 15%. This indicates that the ultimate failure load is not directly proportional to the thickness of the adherend. Figure 4.17 shows that failures for both specimens have taken place at the top ply. It can be seen that the 90° ply is normally the weak link for delamination between 90° and 0° plies. This can be found in all of the specimens.

The load-displacement curves of models with different adherend thicknesses are shown in Figure 7.11. As can be seen, the load-displacement curves were linear. It is obvious that the ultimate failure load of the models increases as the laminate thickness increases. On the other hand, it is obvious that the maximum principal stress at the upper RHS (Table 5.5) of the models decreases as the adhered thickness increases. Figure 5.22-5.24 show that with increase in the CFRP adherend thickness, reductions in the values of maximum principle, shear and peel stresses towards the centre of the joint RHS take place.

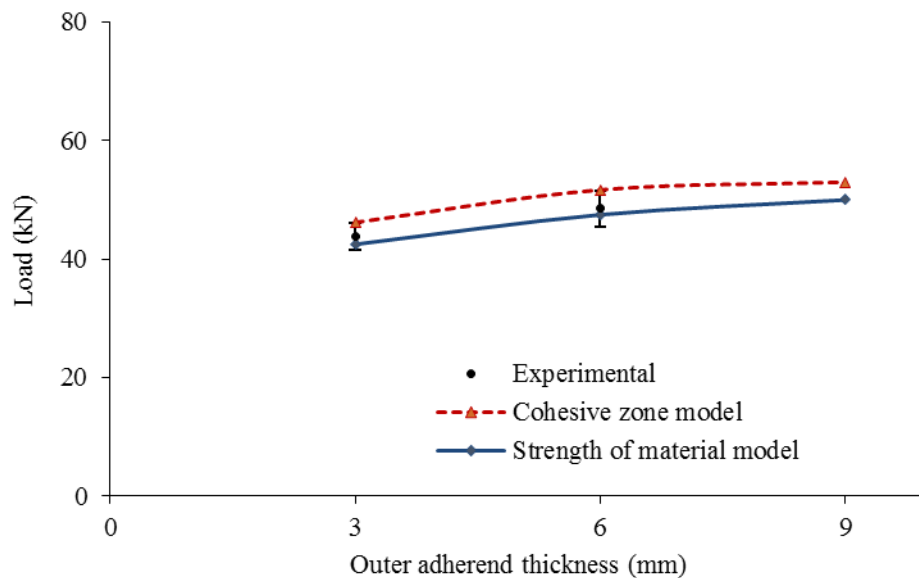


Figure 8.4: Comparison between the experimental and numerical curves for $[0^\circ, 90^\circ]$ joint with different laminate thickness

Figure 8.4 shows the failure load by both experimental and numerical techniques on increasing joint strength with an increase in laminate thickness. For example, there is an 18% increase in joint strength as a result of increasing the thickness from 3 mm to 9 mm.

8.1.8 General modelling and experimental issues

The differences between the FEA models and experimental results are possibly caused by a number of reasons:

- a) The CFRP material properties were not determined experimentally, but were taken from published literature and supplied by the manufacturer. Consequently, some errors in this deference could have produced inaccuracies in the FEA modelling.
- b) The overall 2D geometry of the hybrid DLS joints was modelled reasonably accurately. However, the corners of the steel adherend and the CFRP laminate were shaped, but simply modelled as right angled. Therefore, both the steel and the CFRP adherends, which were bonded DLS joints, were affected by this approximation. Again, this would have had an effect on the local behaviours and the response of the adhesive joints.
- c) In order to have an effective aspect ratio in the finite elements which model the thickness of the adhesive layer, in the FEA models the thickness was taken as 0.2 mm instead of the actual thickness in the experiments, which had some errors in the adhesive thickness from one specimen to another.
- d) The manufacturing technique applied in the fabrication of the DCB, ENF and DLS joints would invariably produce some non-uniformities and small deviations of the dimensions. This could possibly have produced slight differences when compared to the FEA model results.
- e) In the FEA models the boundary conditions were assumed to be perfect, which may not have been the case experimentally.

Numerical issues

- a) It may not be appropriate to use maximum stress as a criterion in conjunction with a detailed finite element analysis. If the ends of adherends and the adhesive layer are modelled as sharp corners then the stresses become singular. If these features are smoothed, the maximum values are a function of the rounding used. The joint strength can be predicted by comparing the respective equivalent stresses at critical regions obtained by stress based criteria, with the properties of the structure. These criteria are highly mesh dependent, as stress singularities are present at the end of the overlap regions, especially at sharp corners. Singularity issues at the interface of the

adhesive and laminate were dealt with according to the third-node stress consideration proposed in the research work by Gleich et al [222].

- b) The common difficulty encountered in FEA analysis to simulate the crack propagation with CZM is the convergence issue. The complex constraints such as connection and ties, together with nonlinearities including softening constitutive relations, mean that the FEA model is often discouraged with non-convergence. Many researchers have noted this problem and come up with several solutions [206]. This problem is still active in research, and demands more investigation. In this work the viscous regularisation method was applied to help with numerical difficulties. A stabilisation technique was used for unstable finite element computations. When using the small value of the viscosity parameter, the viscous regularisation helps recover the rate of convergence without compromising the results.

8.2 Summary and conclusions

Tests and analyses related to thick-adherend steel/carbon composite double lap shear joints have been carried out in this work. The structural failure of the joint, including delamination of the composites at different overlap length, fabric orientation and adherend thickness have been investigated, both experimentally and numerically. The experimental programme includes fabrication, mechanical testing and failure examinations of various joints. The analysis methods developed in this thesis may potentially be employed for the development and assessment of hybrid joints and advanced composite structures. The numerical methods are based on 2D models using the strength of materials and cohesive zone modelling methods.

There are two chapters presenting experiments in this work. Chapter 3 introduces the materials used in this research, and the rule of mixtures is used to determine the material properties of CFRP laminates. This chapter includes the test of a standard steel butt joint and thick adherend shear test to obtain the mechanical properties of an adhesive. Additionally, it describes the manufacture and fracture tests of steel DCB and ENF specimens, the results in this chapter being used to determine the parameters of cohesive zone model (CZM). Then, the CZM was applied to simulate DCB and ENF models in Chapter 6.

The cohesive parameters were determined by fitting the numerical results on the respective experimental data. These results were used to simulate the DLS model in Chapter 7. Chapter 4 describes the manufacture and tensile test of DLS joints. It is noted that the results of Chapter 4 were compared with FEA simulation of Chapter 5 and Chapter 7.

In this work, two failure tests were accomplished. These tests included the DCB test (mode I) and ENF test (mode II). The purpose of these tests was to determine the parameters in cohesive zone model applications. The bilinear cohesive zone model has been used, the critical strain energy release rate of which was the only parameter that was obtained from previous DCB tests and ENF tests. The cohesive strength values of the bonding materials were determined using the inverse method. This method includes fitting procedures for numerical and experimental load-displacement curves of fracture tests and models. Regarding the damage part of the model, the six parameters were also split into two groups. The three mode I parameters (G_{IC} , σ_0 and K_{nn}) were identified with the DCB specimen by fitting measured and computed load-displacement results. The same procedure was used for the three mode II parameters (G_{IIC} , τ_0 and K_{ss}) using the ENF specimen.

The bilinear CZM was proven to be able to predict the initiation of crack and crack propagation in a DLS joint, and also suitable for predicting multiple cracks by placing cohesive elements between every two neighbouring solid elements. The stress analysis highlighted the regions of critical stresses within the DLS model, and using the deduced mode I and mode II fracture parameters, progressive damage analysis was conducted. This analysis concluded that damage initiates at the centre of the overlap at approximately 50% of the failure load, when the CFRP are used as outer adherend. In addition the analysis of DLS joints indicated that failure is to be expected within the adhesive layer for $[0^\circ, 90^\circ]_6$ joint, and predicted a shift from adhesive failure to delamination failure in composite adherend for the $[90^\circ, 0^\circ]_6$ joint. Results obtained with the strength of material approach and cohesive zone model approach were found to be in good agreement with those obtained experimentally. The following main conclusions can be drawn in relation to this study:

- 1) Failure initiation in long overlap steel/composite joints starts at the RHS of the joint at about 50% of the failure load.
- 2) DLS joints made of thin ply laminates with $[0^\circ, 90^\circ]$ orientation produces only a slightly higher strength compared to the $[90^\circ, 0^\circ]$ equivalent. However, a joint with $[+45^\circ, -45^\circ]$ orientation produces a significantly lower strength than the other two.

- 3) The adhesive plastic shear zone at failure remains at about 30 mm in length when increasing the overlap length of the DLS joint beyond 75 mm. Damage tolerance, however, increases with the increase in overlap length.
- 4) Maximum principal, peel and shear stresses at the interface adhesive vary with fibre orientation, due to variation of local and global stiffness and strength.
- 5) Increasing the thickness of outer composite adherend leads to an increase in joint strength. A thickness increase from 3 mm to 9 mm resulted in an 18% increase in the failure load.
- 6) Joint failure mode depends on fibre orientation. While this is mainly cohesive failure in the adhesive for the $[0^\circ, 90^\circ]$ joint, it is largely interlaminar for the $[90^\circ, 0^\circ]$ joint. The failure for the $[+45^\circ, -45^\circ]$ joint is largely in-plane delamination of tope ply.
- 7) The cohesive zone modelling technique was found to be a powerful and economical analytical tool for the analysis of delamination in steel/CFRP laminated composite joints.
- 8) For the ENF test, the proposed traction separation model with linear softening function as produced from the CBBM scheme is very helpful in numerical simulations for Mode II fracture growth.
- 9) The computing time to simulate the numerical model of the DLS joint by the CZM approach can save 40% of simulation time when compared with the strength of materials approach.

8.3 Future work

Although the strength prediction of adhesively bonded between CFRP laminates and steel in double lap shear joints under tensile loading could already have been improved through this research, there are still areas for further research. More experimental and numerical work is recommended to optimise the material properties for adhesive and epoxy resin, to further understanding of the behaviour of adhesively bonded DLS joints. The study could be extended in future by considering the following important areas.

- Extend experimental and FEA work to obtain the cohesive parameters for mixed-mode fracture toughness.

- Extensive experimental work has been performed in this research, and future work should focus on further FEA analysis, including 3D modelling of the DLS joint, to investigate the effect of stresses which act through the width of the joint.
- Further investigation into damage shapes will be necessary to understand the damage development mechanisms.
- DLS joint tests in this work were subjected to in-plane deformation. In practice, many varieties of out-plane deformation, such as bending and torsion of adhesively bonded joints, exist; therefore joints under more complex loads should be investigated.
- The investigations presented in this thesis are only for specimens subjected to quasi-static loading conditions. Further investigation of the effect of stacking sequences in the performance of CFRP under different loading scenarios, such as fatigue and impact, may be of interest.
- The use of video microscopy to investigate the behaviour of the bond line in double lap joints could be more integrated, in a way where data can be recorded accurately and used as another means of measuring crack initiation strains in the adhesive layer.
- To carry out 3D stress analysis modelling of actual butt connection (DLS joint), e.g. in ship application, to compare the computing time need for the CZM approach versus strength limit approach, and in line with what is currently considered in automotive applications.

References

- [1] Velthuis R, Koetter MP, Geiss PL, Schlarb AK., “Lightweight structures made of metal and fibre-reinforced polymers,” *Kunststoffe International*, vol. 11, pp. 22-24, 2007.
- [2] Baldan A., “Adhesively-bonded joints and repairs in metallic alloys, polymers and composite materials: Adhesives, adhesion theories and surface pre-treatment,” *Journal of Materials Science*, vol. 39, p. 1– 49., 2004.
- [3] da Silva L.F.M., Adams R.D., “Adhesive joints at high and low temperatures using similar and dissimilar adherends and dual adhesives,” *International Journal of Adhesion and Adhesives*, vol. 27, pp. 216-226, 2007.
- [4] Vinson, J.K., “Adhesive Bonding of Polymer Composites,” *Polymer Engineering and Science*, vol. 29, no. 19, pp. 1325-1331, 1989.
- [5] Adams R.D., Comyn J. and Wake W.C., *Structural adhesive joints in engineering*, London: Chapman & Hall, 1997.
- [6] Hollaway LC and Cadei J., “Progress in the technique of upgrading metallic structures with advanced polymer composites,” *Progress in Structural Engineering and Materials*, vol. 4, no. 2, p. 131–148, 2002.
- [7] Zhao XL. and Zhang L., “State of the art review on FRP strengthened steel structures,” *Engineering Structures*, vol. 29, no. 8, p. 1808–1823, 2007.
- [8] Mahi A El, Berthelot JM and Brillaud J, “Stiffness reduction and energy release rate of cross-ply laminates during fatigue tests,” *Composite Structures*, vol. 30, no. 2, pp. 123-130, 1995.
- [9] Berglund L A, Varna J and Yuan J., “Transverse Cracking and Local Delamination in [04/90n]s, and [90n/04]s Carbon Fiber/Toughened Epoxy Laminates,” *Journal of Reinforced Plastics and Composites*, vol. 11, no. 6, pp. 643-660, 1992.
- [10] Guild F J, Ogin SL and Smith P A, “Modelling of 90° Ply Cracking in Crossply Laminates, Including Three-Dimensional Effects,” *Journal of Composite Materials*, vol. 27, pp. 646-667, 1993.

- [11] Fernlund G and Spelt JK, "Analytical method for calculating adhesive joint fracture parameters," *Engineering Fracture Mechanics*, vol. 40, pp. 119-132, 1991.
- [12] Fernlund G and Spelt JK, "Mixed-mode fracture characterization of adhesive joints," *Composites Science and Technology*, vol. 50, pp. 441-449, 1994.
- [13] Papini M Fernlund G and Spelt JK, "The effect of geometry on the fracture of adhesive joints," *International Journal of Adhesion and Adhesives*, vol. 14, pp. 5-13, 1994.
- [14] Gent AN and Hamed GR, "Peel mechanics for an elastic-plastic adherend," *Journal of Applied Polymer Science*, vol. 21, pp. 2817-2831, 1977.
- [15] Gent AN and Hamed GR, "Peel mechanics of adhesive joints," *Polymer Engineering and Science*, vol. 17, pp. 462-466, 1977.
- [16] Tvergaard V and Hutchinson JW, "On the toughness of ductile adhesive joints," *Journal of the Mechanics and Physics of Solids*, vol. 44, no. 5, pp. 789-800, 1996.
- [17] Tvergaard V. and Hutchinson J.W., "The influence of plasticity on mixed-mode interface toughness," *Journal of the Mechanics and Physics of Solids*, vol. 41, pp. 1119-1135, 1993.
- [18] Tvergaard V and Hutchinson LW, "The relation between crack growth resistance and fracture process parameters in elastic-plastic solids," *Journal of the Mechanics and Physics of Solids*, vol. 40, pp. 1377- 1397, 1992.
- [19] Tvergaard V and Hutchinson LW, "Toughness of an interface along a thin ductile joining elastic solids," *Philosophical Magazine A*, vol. 70, pp. 641-656, 1994.
- [20] Jones R.M., *Mechanics of composite materials*, 2nd edition, Taylor & Francis, Inc., 1999.
- [21] Swanson S.R., *Introduction to design and analysis with advanced composites materials*, Prentice Hall, 1997.
- [22] Edwards K.L., "An overview of the technology of fibre reinforced plastics for design purposes," *Materials and Design*, vol. 19, pp. 1-10, 1998.
- [23] Smith C.S., *Design of marine structures in composites materials*, Material Characteristics, Elsevier, 1990.

- [24] Xu L. and Drzal L.T., "Influence of matrix cure volume shrinkage on the adhesion between vinyl ester and carbon fibre," *Proceedings of the Adhesion Society*, pp. 415-417, 2003.
- [25] Gurdal Z., Haftka R.T. and Hajela P., *Design and Optimization of Laminated Composite Materials*, John Wiley & Sons, 1990.
- [26] "<http://www.umms.sav.sk/index.php?ID=1088>," [Online].
- [27] Smith S.T., Kaul R., Sri Ravindrarajah, R. and Ootom, O.M.A., *Durability considerations for FRP- Strengthened RC Structures in the Australian Environment*, 2005.
- [28] Pendhari S.S., Kant T. and Desai Y.M., "Application of polymer composites in civil construction: A general review," *Composite Structures*, vol. 84, pp. 114-124, 2008.
- [29] Hollaway L.C., "The evolution of and the way forward for advanced polymer composites in the civil infrastructure," *Construction and Building Materials*, vol. 17, pp. 365-378, 2003.
- [30] Shaat A. and Fam A., "Slender steel columns strengthened using high-modulus CFRP plates for buckling control," *Journal of Composites for Construction*, vol. 13, pp. 2-12, 2009.
- [31] Armstrong K.B., "Carbon Fibre Fabric Repairs to Metal Aircraft Structures. The third technology Conference on Engineering with Composites," in *London, England, SAMPE European, Chapter, 8.1-8.12*.
- [32] Karbhari V.M., and Shulley S.B., "Use of Composites for Rehabilitation of Steel Structures – Determination of Bond Durability," *Journal of Materials in Civil Engineering. ASCE*, vol. 7, no. 4, pp. 239-245, 1995.
- [33] Allan R.C., Bird J. and Clarke J.D., "Use of Adhesives in Repair of Cracks in Ship Structures," *Materials Science and Technology*, vol. 4, no. 10, pp. 853-859, 1988.
- [34] Hashim S.A., "Adhesive Bonding of Thick Steel Adherents for Marine Structures," *Marine Structures*, vol. 12, pp. 405-423, 1999.
- [35] Bocciarelli M., Colombi P., Fava G. and Poggi C., "Fatigue performance of tensile steel members strengthened with CFRP plates," *Composite Structures*, vol. 87, pp. 334-343, 2009.

- [36] Minford J.D., In : Kinloch A.J., Editor, *Durability of structural adhesives*, London, 1983, p. 135.
- [37] Kinloch A.J., *Durability of structural adhesives*, Elsevier Applied Science Publishers, ISBN 0 85334 214 8, Chap 1.
- [38] Kinloch A.J., "The science of adhesion part 1. Surface and interfacial aspects," *Journal of Material Science*, vol. 15, pp. 2141-2166, 1980.
- [39] Bikerman J.J., "The fundamentals of tackiness and adhesion," *Journal of Colloid Science*, vol. 2, pp. 163-175, 1947.
- [40] Voyutskii S.S., *Autohesion and adhesion of high polymers*, John Wiley & Inc., 1963.
- [41] Deryaguin B.V. and Smilga V.P., *Adhesion: fundamentals and practice*, London: McLaren & Son, 1969, p. 152.
- [42] Staverman A.J., *Adhesion and adhesives*, vol. 1, edited by Houwink R. and Salmon G., Elsevier, Amsterdam, 1965, p. 9.
- [43] Cagle, Charles V., *Handbook of adhesive bonding: wetting*, Kingsport Press, USA, 1973, pp. 1-12.
- [44] Johnson R.E. and Dettre R.H., "Surface properties of polymers: I. The surface tensions of some molten polyethylene," *Journal of Colloid and Interface Science*, vol. 21, no. 4, pp. 367-377, 1966.
- [45] Wenzel R.N., *Resistance of solid surfaces to wetting by water*, vol. 28, Ind. Eng. Chem., 1936, pp. 988-994.
- [46] Mays G.C. and Hutchinson A.R., *Adhesives in Civil Engineering*, Cambridge University Press, New York, 1992, p. 333.
- [47] Rudawska A., "Selected aspects of the effect of mechanical treatment on surface roughness and adhesive joint strength of steel sheets," *International Journal of Adhesion & Adhesives*, vol. 50, p. 235–243, 2014.
- [48] Baker F.S., "Effect of ultra clean stainless steel surfaces on the strength of epoxide-stainless steel butt joint," *Journal of Adhesion*, vol. 10, pp. 107-122, 1979.
- [49] Shahid M and Hashim SA, "Effect of surface roughness on the strength of cleavage joints," *International Journal of Adhesion and Adhesives*, vol. 22, pp. 235-244, 2002.

- [50] Harris A.F and Beevers A., "The effects of grit-blasting on surface properties for adhesion," *International Journal of Adhesion & Adhesives*, vol. 19, pp. 445-452, 1999.
- [51] Pocius A.V., *Adhesion and adhesive technology: An Introduction*, Hanser publishers, Munich, 1997.
- [52] Boone M.J., *Mechanical testing of epoxy adhesives for naval applications*, M.Sc. Thesis, University of Maine, 2002, p. 7.
- [53] Wingfield J.R.J., "Treatment of composite surfaces for adhesive bonding," *Int. J. Adhes. Adhes.*, vol. 13, no. 3, pp. 151-156, 1993.
- [54] Brockmann W.G., "The importance of surface pretreatment prior to bonding," *Proc. Conf. IMechE*, pp. 61-70, 1986.
- [55] Parker B.M., "Adhesive bonding of fibre reinforced composites," *International Journal of Adhesion and Adhesives*, vol. 14, pp. 137-143, 1994.
- [56] Guha P.K. and Epel J.N., "Adhesives for the bonding of graphite /glass composites," *Society of Automotive Engineers, Inc. 790149*, pp. 566-572, 1980.
- [57] Baker A., "Repair of cracked or defective metallic aircraft components wit advanced fibre composites- an overview of Australian work.," *Composite Structures*, vol. 2, pp. 153-181, 1984.
- [58] Taib A, Boukhili R, Achiou S, Gordon S, Boukehili H., "Bonded joints with composite adherends. Part I. Effect of specimen configuration, adhesive thickness, spew fillet and adherend stiffness on fracture," *International Journal of Adhesion and Adhesives*, vol. 26, no. 4, p. 226–236, 2006.
- [59] Schliekelmann R.J., "Past, present, and future of structural adhesive bonding in aerospace applications," *Transactions of the Japan Society for Composite Materials*, vol. 5, 1979.
- [60] Katsiropoulos C.V., Chamos A.N., Tserpes K.I. and Pantelakis S.G., "Fracture toughness and shear behaviour of composite bonded joints based on a novel aerospace adhesive," *Composites Part B: Engineering*, vol. 43, no. 3, pp. 240-248, 2012.
- [61] Mouritz A.P., Gellert E., Burchill P., Challis K., "Review of advanced composite structures for naval ships and submarines," *Composite Structures*, vol. 53, pp. 21-42, 2001.

- [62] Le Lan J.Y., Parneix P. and Gueguen P.L., “Composite material superstructures,” *International Conference on Nautical Construction with Composite Materials*, Paris, France, 1992.
- [63] Boyd S.W., Blake J.I.R., Shenoi R.A. and Kapadia A., “Integrity of hybrid steel-to-composite joints for marine application,” *Proceedings of the Institution of Mechanical Engineers, Part M: Engineering for the Marine Environment*, vol. 218, no. M4, pp. 235-246, 2004.
- [64] Nicholas G., Tsouvalis N. and Karatzas V.A., “An investigation of the tensile strength of a composite to metal adhesive joint,” *Applied Composite Materials*, vol. 18, no. 2, pp. 149-163, 2011.
- [65] Boyd S.W., Winkleb I.E. and Day A.H., “Bonded butt joints in pultruded GRP panels: an experimental study,” *International Journal of Adhesion & Adhesives*, vol. 24, pp. 263-275, 2004.
- [66] Cao J. and Grenestedt J.L., “Design and testing of joints for composite sandwich/steel hybrid ship hulls,” *Composites Part A: Applied Science and Manufacturing*, vol. 35, no. 9, p. 1091–1105, 2004.
- [67] Wright P. N. H., Wu Y. and Gibson A. G., “Fibre reinforced composite-steel connections for transverse ship bulkheads,” *Plastic, Rubber and Composites*, vol. 29, no. 10, p. 549–557, 2000.
- [68] Clifford S. M., Manger C. I. C. and Clyne T. W., “Characterisation of a glass-fibre reinforced vinylester to steel joint for use between a naval GRP superstructure and a steel hull,” *Composite Structs.*, vol. 57, p. 59–66, 2002.
- [69] “<http://www.dodmantech.com/dmc/achievement2005>,” [Online].
- [70] “http://www.composites.ugent.be/home_made_composites/HomMaCom.html,” [Online].
- [71] Maxwell D., and Bond D., “Principle and practices of adhesively bonded structural joints and repairs,” *International Journal of Adhesion & Adhesives*, vol. 19, pp. 91-105, 1999.
- [72] “<http://www.fibre-reinforced-plastic.com/2012/02/adhesive-joint-and-bonding-in-frp.html>,” [Online].
- [73] Hart-Smith L.J., “Analysis and design of advanced composite bonded joints,” 1974.

- [74] Hart Smith L.J., “Advances in the analysis and design of adhesive bonded joints in composite aerospace structures,” *SAMPLE Process Engineering Series*, vol. 19, pp. 722-737, 1974.
- [75] Lee J., Kim Y., Jung J., Kosmatka J., “Experimental characterisation of a pultruded GFRP bridge deck for light weight vehicles,” *Composite Structure*, vol. 80, pp. 141-151, 2007.
- [76] Mortensen, Flemming and Thybo Thomsen, Ole, , “Coupling effects in adhesive bonded joints,” *Composite Structures* , vol. 56, no. 2, p. 165 , 2002.
- [77] Meneghetti G., Quaresimin M., and Ricotta, M., , “Influence of the interface ply orientation on the fatigue behaviour of bonded joints in composite materials,” *International Journal of Fatigue*, vol. 32, pp. 82-93, 2010.
- [78] de Goeij W.C., van Tooren M.J.L. and Beukers A., “ Composite adhesive joints under cyclic loading,” *Materials & Design*, vol. 20 , no. 5, p. 213 , 1999.
- [79] Song M.G., Kweon J.H., Choi J.H., and Song M.H., “ Effect of manufacturing methods on the shear strength of composite single-lap bonded joints,” *Composite Structures*, vol. 92, pp. 2194-2202, 2010.
- [80] Ferreira J.A. M., Reis P.N., Costa J.D.M. and Richardson M.O.W., “ Fatigue behaviour of composite adhesive lap joints,” *Composites Science and Technology* , vol. 62 , no. 10, p. 1373 , 2002.
- [81] Godara A. and Raabe D., “Influence of fibre orientation on global mechanical behavior and mesoscale strain localization in a short glass-fibre-reinforced epoxy polymer composite during tensile deformation investigated using digital image correlation,” *Composites Science and Technology* , vol. 67 , no. 11-12, p. 2417 , 2007.
- [82] Mertz D.R. and Gillespie J.W., “Rehabilitation of steel bridge girders through the application of advanced composite materials,” Final Report to the Transportation Research Board for NCHRP-IDEA Project 11, University of Delaware, 1996.
- [83] Miller C., Michael J. Chajes, Dennis R. Mertz and Jason N. , “Strengthening of a steel bridge girder using CFRP plates,” *ASCE Journal of Bridge Engineering*, vol. 6, no. 6, pp. 514-522, 2001.

- [84] Lam C.C.A., Cheng J.J.R. and Yam C.H.M., "Study of the tensile strength of CFRP/steel double lap joints," *Advanced Composite Materials in Bridges and Structures*, July 20-23, 2004.
- [85] Fawzia S., Al-Mahaidi R. and Zhao X.L., "Experimental and finite element analysis of a double strap joint between steel plates and normal modulus CFRP," *Composite Structures*, vol. 75, pp. 156-162, 2006.
- [86] Lenwari A., Thepchatri T. and Albrecht P., "Debonding Strength of Steel Beams Strengthened with CFRP Plates.," *Journal of Composites for Construction, ASCE*, vol. 10, no. 1, pp. 69-78, 2006.
- [87] Liu H.B., Zhao X.L. and Al-Mahaidi R., "The Effect of Fatigue Loading on Bond Strength of CFRP Bonded Steel Plate Joints," *Proceedings of the International Symposium on Bond Behaviour of FRP in Structures*, Hong Kong, 2006.
- [88] Schnerch D.A., "Strengthening of Steel Structures with High Modulus Carbon Fibre Reinforced Polymer (CFRP) Materials," Ph.D. Dissertation, North Carolina State University, 2005.
- [89] Roy A.K., Donaldson S.L. and Schoeppner G.A., "Bonded joints of unidirectional and cross-ply laminates: An experimental study," *38th AIAA/ASME/ASCE/AHS/ASC Structures, Structural Dynamics and Material Conference and Exhibit, Part-3*, pp. 1994-2003, 1997.
- [90] Hashim S.A., Cowling M.J. and Lafferty S., "The integrity of bonded joints in large composite pipes," *International Journal of Adhesion and Adhesives*, vol. 18, pp. 421-429, 1998.
- [91] Altus E., "Three-Dimensional Singularities in Double Lap Joints.," *Engineering Fracture Mechanics*, vol. 21, no. 6, pp. 1097-1112, 1985.
- [92] McGeorge D., "Inelastic fracture of adhesively bonded over lap joints," *Engineering Fracture Mechanics*, vol. 77, no. 1, pp. 1-21, 2010.
- [93] Volkersen O., "Die Niekraftverteilung in Zugbeanspruchten mit Konstanten Laschenquerschnitten," *Luftfahrtforschung*, vol. 15, pp. 41-47, 1938.
- [94] Goland M. and Reissner E., "The stresses in cemented joints," *Journal of Applied Mechanics*, vol. 11, pp. 17-27, 1944.

- [95] De Bruyne N.A., "The strength of glued joints," *Aircraft Engineering*, vol. 16, pp. 115-118., 1944.
- [96] Hart-Smith L.J., "Adhesive-bonded double-lap joints," *NASA CR-112235, National Aeronautics and Space Administration.*, 1973.
- [97] da Silva L.F.M., Öchsner A. and Adams R.D., *Handbook of Adhesion Technology*, Springer, Heidelberg, 2011.
- [98] Crocombe A.D. and Adams R.D., "Influence of the spew fillet and other parameters on the stress distributions in the single-lap joint," *Journal of Adhesion*, vol. 13, pp. 141-155, 1981.
- [99] Ojalvo I.U. and Eidinoff H.L., "Bond thickness effects upon stresses in in single-lap adhesive joints," *Journal of the American Institute of Aeronautics and Astronautics* , vol. 16, pp. 204-211, 1978.
- [100] Tsai M.Y., Oplinger D.W., and Morton J., "An improved theoretical solutions for adhesive lap joints," *International Journal of Solids and Structures* , vol. 35, p. 1163–1185, 1998.
- [101] Jalali S.J. and Taheri F., "An analytical solution for cross-ply laminates under cylindrical bending based on through-the-thickness inextensibility, Part I: Static loading," *International Journal of Solids Structures*, vol. 35, p. 1559–1574, 1998.
- [102] Yang C., Huang H., Tomblin J.S. and Sun W., "Elastic–plastic model of adhesive-bonded single-lap composite joints," *Journal of Composite Materials* , vol. 38, p. 293–309, 2004.
- [103] Zou G.P., Shahin K. and Taheri F. , "An analytical solution for the analysis of symmetric composite adhesively bonded joints," *Composite Structures* , vol. 65, p. 499–510, 2004.
- [104] Frostig Y., Thomsen T.O. and Mortensen H., "Analysis of adhesive-bonded joints, squareend, and spew-fillet- high-order theory approach," *Journal of Engineering Mechanics*, vol. 125, pp. 1298-1307, 1999.
- [105] Luo Q. and Tong L., "Fully-coupled nonlinear analysis of single lap adhesive joints," *International Journal of Solids and Structures*, vol. 44, p. 2349–2370, 2007.
- [106] Adams R.D. and Peppiatt N.A., "Stress analysis of adhesive-bonded lap joints," *Journal of Strain Analysis for Engineering Design*, vol. 9, p. 185–196, 1974.

- [107] Adams R.D. and Harris J.A., “Strength prediction of bonded single lap joints by nonlinear finite element methods,” *International Journal of Adhesion and Adhesives*, vol. 4, p. 65–78, 1984.
- [108] Adams R.D. ,Atkins R.W. ,Harris J.A. and Kinloch A.J., “Stress analysis and failure properties of carbon-fibre-reinforced-plastic/steel double-lap joints,” *Journal of Adhesion* , vol. 20, p. 29–53, 1986.
- [109] Adams R.D. and Davies R., “Strength of lap shear joints,” in *The Mechanics of Adhesion* , ed. by Dillard D.A. and Pocius A.V., Elsevier, Amsterdam, 2002.
- [110] Ikegami K., Takeshita T., Matsuo K. and Sugibayashi T. , “Strength of adhesively bonded scarf joints between glass fibre-reinforced plastics and metals,” *International Journal of Adhesion and Adhesives*, vol. 10, pp. 385-400, 1990.
- [111] John S.J., Kinloch A.I. and Matthews F.L. , “Measuring and predicting the durability of bonded fibre/ epoxy composite joints,” *Composites*, vol. 22, pp. 121-127, 1991.
- [112] Lee S.J. and Lee D.G. , “Development of a failure model for the adhesively bonded tubular single lap joint,” *Journal of Adhesion* , vol. 40, pp. 1-14, 1992.
- [113] da Silva L.F.M., Carbas R.I.C., Critchlow G.W., Figueiredo M.A.V. and Brown K. , “Effect of material, geometry, surface treatment and environment on the shear strength of single lap joints,” *International Journal of Adhesion and Adhesives*, vol. 29, p. 32, 2009.
- [114] da Silva L.F.M., das Neves P.J.C., Adams R.D. and Spelt J.K., , “Analytical models of adhesively bonded joints- Part I: literature survey,” *International Journal of Adhesion and Adhesives* , vol. 29, pp. 319- 330, 2009.
- [115] Crocombe A.D., “Global yielding as a failure criteria for bonded joints,” *International Journal of Adhesion and Adhesives*, vol. 9, pp. 145- 153, 1989.
- [116] Clark J.D. and McGregor I.J., “Ultimate tensile stress over a zone - A new failure criterion for adhesive joints,” *Journal of Adhesion*, vol. 42, no. 4, pp. 227-245, 1993.
- [117] Mazars J. and Pijaudier G. , “From damage to fracture mechanics and conversely: A combined approach,” *International Journal of Solids and Structures*, vol. 33, no. 20, pp. 3327-3342, 1996.

- [118] Duan K., Hu X. and Mai Y.W., “Substrate constraint and adhesive thickness effects on fracture toughness of adhesive joints,” *Journal of Adhesion Science and Technology*, vol. 18, p. 39–53, 2004.
- [119] Liljedahl C.D.M., Crocombe A.D., Wahab M.A. and Ashcroft I.A., “Damage modelling of adhesively bonded joints,” *International Journal of Fracture*, vol. 141, p. 147–161, 2006.
- [120] Campilho R.D.S.G., Banea M.D., Pinto A.M.G., da Silva L.F.M. and de Jesus A.M.P., “Strength prediction of single- and double-lap joints by standard and extended finite element modelling,” *International Journal of Adhesion and Adhesives*, vol. 31, p. 363–372, 2011.
- [121] Yang Q.D., Thouless M.D. and Ward S.M., “Elastic-plastic mode-II fracture of adhesive joints,” *International Journal for Solids and Structures*, vol. 38, pp. 3251–3262, 2001.
- [122] Turon A., Costa J., Camanho P.P. and Davila C.G., “Simulation of delamination in composites under high-cycle fatigue,” *Composite Part A*, vol. 38, p. 2270–2282, 2007.
- [123] Chandra N., Li H., Shet C. and Ghonem H., “Some issues in the application of cohesive zone models for metal–ceramic interfaces,” *International Journal for Solids and Structures*, vol. 39, p. 2827–2855, 2002.
- [124] Song S.H., Paulino G.H. and Buttlar W.G., “A bilinear cohesive zone model tailored for fracture of asphalt concrete considering viscoelastic bulk material,” *Engineering Fracture Mechanics*, vol. 73, p. 2829–2848, 2006.
- [125] Kafkalidis M.S. and Thouless M.D., “The effects of geometry and material properties on the fracture of single lap-shear joints,” *International Journal for Solids and Structures*, vol. 39, p. 4367–4383, 2002.
- [126] Dugdale D.S. , “Yielding steel sheets containing slots,” *Journal of the Mechanics and Physics of Solids*, vol. 8, pp. 100–104, 1960.
- [127] Barenblatt G.I., “Mathematical theory of equilibrium cracks in brittle fracture,” *Advances in Applied Mechanics*, vol. 7, pp. 55–129, 1962.

- [128] Alfano M., Furgiele F., Leonardi A., Maletta C. and Paulino G.H., "Mode I fracture of adhesive joints using tailored cohesive zone models," *International Journal of Fracture*, vol. 157, pp. 193-204, 2009.
- [129] Blackman B., Hadavinia H., Kinloch AJ and Williams, J.G., "The use of a cohesive zone model to study the fracture of fibre composites and adhesively-bonded joints," *International Journal of Fracture*, vol. 119, no. 1, pp. 25-46, 2003.
- [130] Campilho R., de Moura M., Ramantani D. and Goncalves J., "Obtaining the cohesive laws of a trapezoidal mixed-mode damage model using an inverse method," *Ciencia e Tecnologia dos Materiais (Science & Technology of Materials)*, vol. 20, no. 1/2, 2008.
- [131] Andersson T. and Stigh U., "The stress-elongation relation for an adhesive layer loaded in peel using equilibrium of energetic forces," *International Journal for Solids and Structures*, vol. 41, pp. 413-434, 2004.
- [132] BS 7991:2001, "Determination of the mode I adhesive fracture energy GIC of structure adhesives using the double cantilever beam (DCB) and tapered double cantilever beam (TDCB) specimens," 2001.
- [133] Ji G., Ouyang Z., Li G., Ibekwe S., Pang S.S., "Effects of adhesive thickness on global and local Mode-I interfacial fracture of bonded joints," *International Journal of Solids and Structures*, vol. 47, pp. 2445- 2458, 2010.
- [134] Ji G., Ouyang Z., Li G., "Effects of bondline thickness on Mode-II interfacial laws of bonded laminated composite plate," *International Journal of Fracture*, vol. 168, p. 197-207, 2011.
- [135] Carberger T., Stigh U., "Influence of layer thickness on cohesive properties of an epoxy based adhesive-an experimental study," *Journal of Adhesion*, vol. 86, pp. 814-833, 2010.
- [136] Yang Q.D., Thouless M.D., Ward S.W., "Elastic-plastic mode-II fracture of adhesive joints," *International Journal of Solids and Structures*, vol. 38, pp. 3251-3262, 2001.
- [137] de Moura M.F.S.F., Oliveira J.M.Q., Morais J.J.L., Xavier J., "Mixed-mode I/II wood fracture characterization using the mixed-mode bending test," *Engineering Fracture Mechanics*, vol. 77, pp. 144-152, 2010.

- [138] Choupani N., “Interfacial mixed-mode fracture characterization of adhesively bonded joints,” *International Journal of Adhesion and Adhesives*, vol. 28, pp. 267-282, 2008.
- [139] Banea M.D., da Silva L.F.M., Campilho R.D.S.G. , “Mode I fracture toughness of adhesively bonded joints as a function of temperature: experimental and numerical study,” *Int. J. Adhes. Adhes.*, vol. 31, p. 273–279 , 2011.
- [140] Campilho R.D.S.G., de Moura M.F.S.F., Domingues J.J.M.S.,, “Numerical prediction on the tensile residual strength of repaired CFRP under different geometric changes,” *Int. J. Adhes. Adhes.*, vol. 29, p. 195–205, 2009.
- [141] de Moura, M.F.S.F., Goncalves, J.P.M., Chousal, J.A.G., Campilho R.D.S.G., “Cohesive and continuum mixed-mode damage models applied to the simulation of the mechanical behaviour of bonded joints,” *Int. J. Adhes. Adhes.*, vol. 28, pp. 419-426, 2008.
- [142] Mello A.V., Liechti K.M. , “The effect of self-assembled monolayers on interfacial fracture,” *J. Appl. Mech.* , vol. 73, p. 860–870, 2006.
- [143] Li S., Thouless M.D.,waas A.M., Schroeder J.A. and Zavattieri P.D., “Use of a cohesive-zone model to analyse the fracture of a fibre reinforced polymer–matrix composite,” *Compos. Sci. Technol.*, vol. 65, p. 537–549, 2005.
- [144] Harris JA, Adams RD. , “Strength prediction of bonded single-lap joints by non-linear finite element methods,” *International Journal of Adhesion & Adhesives* , vol. 4, p. 65–78, 1984.
- [145] Bigwood DA, Crocombe AD., “Non-linear adhesive bonded joint design analyses,” *International Journal of Adhesion & Adhesives*, vol. 10, p. 31–41, 1990.
- [146] Crocombe AD, Adams RD.,, “An elasto plastic investigation of the peel test,” *The Journal of Adhesion*, vol. 13, p. 241–267 , 1982.
- [147] Qian ZQ and Akisanya AR., “An investigation of the stress singularity near the free edge of scarf joints,” *European Journal of Mechanics A/Solids* , vol. 18, p. 443–463, 1999.
- [148] Dragoni E. and Mauri P., “Intrinsic static strength of friction interfaces augmented with anaerobic adhesives,” *International Journal of Adhesion & Adhesives*, vol. 20, p. 315–321, 2000 .

- [149] Feih S. and Shercliff HR., “Adhesive and composite failure prediction of single joint structures under tensile loading,” *International Journal of Adhesion & Adhesives*, vol. 25, p. 47–59, 2005.
- [150] Blackman B, Kinloch AJ, Paraschi M., “Measuring the mode I adhesive fracture energy, GIC, of structural adhesive joints: the results of an international round-robin,” *International Journal of Adhesion & Adhesives*, vol. 23, no. 4, pp. 293-305, 2003.
- [151] Blackman B, Hadavinia H, Kinloch AJ.,, “The calculation of adhesive fracture energies in mode I revisiting the tapered double cantilever beam (TDCB) test,” *Engineering Fracture Mechanics*, vol. 70, no. 2, p. 233–248, 2003.
- [152] Cavalli M.N. and Thouless M.D., “The effect of damage nucleation on the toughness of an adhesive joint,” *The Journal of Adhesion*, vol. 76, p. 75–92, 2001.
- [153] Campilho R.D.S.G., de Moura M.F.S.F., Domingues J.J.M.S., “Stress and failure analyses of scarf repaired CFRP laminates using a cohesive damage model,” *Journal of Adhesion Science and Technology*, vol. 21, p. 855–970, 2007.
- [154] Alvarez D., Blackman B.R.K., Guid F.J., Kinloch A.J., “Mode I fracture in adhesively bonded joints: A mesh size independent modelling approach using cohesive elements,” *Engineering Fracture Mechanics*, vol. 115, pp. 73-95, 2014.
- [155] Song S.H., Paulino G.H., Buttlar W.G., “Simulation of crack propagation in asphalt concrete using an intrinsic cohesive zone mode,” *Journal of Engineering Mechanics*, vol. 132, no. 11, p. 1215–1223, 2006.
- [156] Park K., Paulino G.H., Roesler J.R., “Determination of the kink point in the bilinear softening model for concrete,” *Engineering Fracture Mechanics*, vol. 75, no. 13, p. 3806–3818, 2008.
- [157] Zhang Ye, Vassilopoulos A. and Keller T., “Modes I and II fracture behaviour of adhesively-bonded pultruded composite joints,” *Engineering Fracture Mechanics*, vol. 77, no. 1, p. 128–43, 2010.
- [158] Zhao X.L. and Zhang L., “State of the art review on FRP strengthened steel structures,” *Engineering Structures*, vol. 29, pp. 1808-1823, 2007.

- [159] Hayashi T., "Analytical study of interlaminar shear stresses in a laminae composite plate," *Transaction of Japanese Society for Aeronautics and Space Science*, vol. 10, pp. 43-48, 1967.
- [160] Pagano N.J. (editor), *Interlaminar response of composite materials*, Elsevier Science Publisher B. V., 1989.
- [161] Kim R.Y. and Soni S. R., "Experimental and analytical studies on the onset of delamination in laminated composites," *Jounial of Composite Materials*, vol. 18, pp. 70-80, 1984.
- [162] Sun C.T. and Zhou S.G., "Failure of quasi-isotropic composite laminates with free edges," *Journal of Reinforced Plastics and Composites*, vol. 7, pp. 515-557, 1988.
- [163] Whitney J.M. and Nuismer RJ., "Stress fracture criteria for laminated composites containing stress," *Journal of Composite Materials*, vol. 8, pp. 253-265, 1974.
- [164] Chang F.K., Scott RA. and Springer C.S., "The Effect of Laminate Configuration on Characteristic Lengths and Rail Shear Strength," *Journal of Composite Materials*, vol. 18, pp. 290-296, 1984.
- [165] Rybicki E.F., Schmueser D.W. and Fox J., "An energy release rate approach for stable crack growth in the fiber-edge delamination problem," *Journal of Composite Materials*, vol. 11, pp. 470-487, 1977.
- [166] Wang A.S.D., Slomiana M. and Bucinell R B., "Delamination crack growth in composite laminates," *Delamination and Debonding of Materials, ASTM STP*, 876, pp. 135-167, 1985.
- [167] Law G.E., "A mixed-mode fracture analysis of ("25/90)s Graphite/epoxy composite laminates," *Effects of Defects in Composite Materials, ASTM STP* 836, pp. 143-160, 1984.
- [168] Zhou S.G. and Sun C.T., "Failure analysis of composite laminates with free edges," *Journal of Composite Technology and Research*, vol. 12, pp. 91-97, 1990.
- [169] Soni S.R. and Kim R.Y., "Delamination of composite laminates stimulated by interlarninar shear," *Composite Materials: Testing and Design, ASTM STP* 893, pp. 286-307, 1986.
- [170] Lagace P.A and Brewer J.C., "Studies of delamination growth and final failure tensile loading," *ICCM-6*, vol. 5, pp. 262-273, 1987.

- [171] O'Brien T. K., "Characterization of delamination onset and growth in a composite laminate," *Damage in Composite Materials, ASTM STP 775*, pp. 140-167, 1982.
- [172] Jurf R A. and Pipes R B., "Interlaminar fracture of composite materials," *Journal of Composite Materials*, vol. 16, pp. 386-394, 1982.
- [173] Lee S.M., "Failure mechanism of delamination fracture," *Composite Materials: Testing and Design, ASTM STP 972*, pp. 356-365, 1988 .
- [174] Kenane M., "Delamination growth in unidirectional Glass/epoxy composite under static and fatigue loads," *Physics Procedia* , pp. 1195-1203, 2009.
- [175] Nisar, J. A., Modelling the interfaces of bondable pultrusions, PhD thesis, University of Glasgow, 2010.
- [176] Huntsman Advanced Materials, "www.huntsman.com," 2004.
- [177] Soden PD Hinton MJ and Kaddour AS, "Lamina properties, lay-up configurations and loading conditions for a range of fibre reinforced composite laminates," *Compos. Sci. Technol*, vol. 58, no. 7, pp. 1011-1022, 1998.
- [178] Tsai SW and Hahn HT, Introduction to composite materials, Pennsylvania: Technomic Publishing Company, 1980.
- [179] BS 5350-C3: Methods of test for adhesives: Determination of bond strength in direct tension, 1989.
- [180] Andersson TL, Fracture Mechanics: Fundamentals and Applications, 3rd edition, Taylor & Francis, Boca Raton, 2005.
- [181] Kinloch AJ, Adhesion and Adhesives: Science and Technology, Chapman and Hall, London, 1987.
- [182] Afendi M Banks WM and Kirkwood D, "Bubble free resin for infusion process," *Composites: Part A*, vol. 36, pp. 739-746, 2005.
- [183] Jousset P. and Rachik M., "Implementation, identification and validation of an elastoplastic damage model for the finite-element simulation of structural bonded joints," *International Journal of Adhesion and Adhesives*, vol. 50, pp. 107-118, 2014.
- [184] Kinloch AJ, Shaw J and Tod DA, "Deformation and fracture behaviour of a rubber-toughened-epoxy: 1. Microstructure and fracture studies," *Polymer*, vol. 24, pp. 1341-1354, 1983.

- [185] Carlsson LA, Gillespie JW and Pipes B, "On the analysis and design of the end notched flexure (ENF) specimen for mode II testing," *Journal of Composite Materials*, vol. 20, pp. 594-604, 1986.
- [186] Chai H and Mall S, "Design aspects of the end-notch adhesive joint specimen," *International Journal of Fracture*, vol. 36, pp. R3-R8, 1988.
- [187] Leffler K and Stigh U, "On the existence of a unique stress-deformation relation for an adhesive layer loaded in shear," in *In the 11th International Conference on Fracture-ICF11, turin*, 2005.
- [188] de Moura M.F.S.F. and de Morais A.B., "Equivalent crack based analyses of ENF and ELS," *Eng. Fract. Mech*, vol. 75, p. 2584–2596, 2008.
- [189] Grant L.D.R., Adams R.D., and da Silva L.F.M, "Experimental and numerical analysis of single-lap joints for the automotive industry," *International Journal of Adhesion and Adhesives*, vol. 29, no. 4, pp. 405-413, 2009.
- [190] You M., Yan Z.M., Zheng X.L., Yu H.Z., and Li Z., "A numerical and experimental study of adhesively bonded aluminium single lap joints with an inner chamfer on the adherends," *International Journal of Adhesion and Adhesives*, vol. 27, no. 7, pp. 65-78, 2007.
- [191] Kim K.S., Yi Y.M., Cho G.R. and C.-G. Kim C.G., "Failure prediction and strength improvement of uni-directional composite single lap bonded joints," *Composite Structures*, vol. 82, no. 4, pp. 513-520, 2008.
- [192] Panigrahi S.K. and Pradhan B., "Through-the-width delamination damage propagation characteristics in single-lap laminated FRP composite joints," *International Journal of Adhesion and Adhesives*, vol. 29, pp. 114-124, 2009.
- [193] Wu Z., "Stress concentration analyses of bi-material bonded joints without inplane stress singularities," *International Journal of Mechanical Sciences*, vol. 50, pp. 641-648, 2008.
- [194] Kaw AK, *Mechanics of composite materials*, 2nd Edition, Taylor & Francis, New York, 2006.
- [195] da Silva L.F.M. de Magalhaes F.A.C.R.G. Chaves F.J.P and de Moura M.F.S.F., "ModeII fracture toughness of a brittle and a ductile adhesive as a function of the adhesive thickness," *Journal of Adhesion*, vol. 86, pp. 891-905, 2010.

- [196] Clarke JD and McGregor J, "Ultimate tensile stress over a zone: a new failure criterion for adhesive joints," *Journal of Adhesion*, vol. 42, pp. 227-245, 1993.
- [197] Gleich DM Tooren V and Beukers A, "Analysis and evaluation of bond line thickness effects on failure load in adhesively bonded structures," *Journal of Adhesion Science and Technology*, vol. 15, no. 9, pp. 1091-1101, 2001.
- [198] Hillerborg A, Mode'er M, Petersson PE, " Analysis of crack formation and crack growth in concrete by means of fracture mechanics and finite elements," *Cement and Concrete Research*, vol. 6, no. 6, pp. 773-781, 1976.
- [199] de Silva LFM, "Progressive Damage Modelling," in *Modelling of Adhesively Bonded Joints*, Springer Verlag Berlin Heidelberg, 2008.
- [200] Kinloch AJ, *Adhesion and adhesives, science and technology*, London: Chapman and Hall , 1986.
- [201] ABAQUS V6.9, Abaqus Analysis User's Manual, Section 28.5 Cohesive elements.
- [202] Camanho PP and Davila CG, "Mixed mode decohesion finite elements or the simulation of delamination in composite materials," *NASA/TM*, pp. 211737,1-37, 2002.
- [203] Yahya NA and Hashim SA, "Delamination of thick adherend steel/CFRP laminate connections," in *The European Adhesion Conference (9th EURADH)* , Friedrichshafen/Germany, September 2012.
- [204] Turon AT, *Simulation of delamination in composites under quasi-static and fatigue loading using cohesive zone models*, PhD Thesis, University of Girona, Spain, 2006.
- [205] Turon A, Davila CG, Camanho PP and Costa J, "An engineering solution for mesh size effects in the simulation of delamination using cohesive zone models, Eng Fract Mech, 74 (2007), pp.,," *Eng Fract Mech*, vol. 74, p. 1665–1682, 2007.
- [206] Khoramishad H., Crocombe A.D., Katnam K.B. and Ashcroft I.A., "Predicting fatigue damage in adhesively bonded joints using a cohesive zone model," *International Journal of Fatigue*, vol. 32, p. 1146–1158, 2010.
- [207] Benzeggagh M.L. and Kenane M., "Measurement of mixed-mode delamination fracture toughness of unidirectional glass/epoxy composites with mixed-mode bending apparatus.," *Journal of Composite Science and Technology*, vol. 56, pp. 439-449, 1996.

- [208] Campilho R.D.S.G., de Moura M.F.S.F. and Domingues J.J.M.S., “Using a cohesive damage model to predict the tensile behaviour of CFRP single-strap repairs,” *International Journal of Solids and Structures*, vol. 45, p. 1497–1512, 2008.
- [209] Pardoen T., Ferracin T., Landis C.M., and Delannay F., “Constraint effects in adhesive joint fracture,” *Journal of the Mechanics and Physics of Solids*, vol. 53, p. 1951–1983, 2005.
- [210] Xie D. and Waas A.M., “Discrete cohesive zone model for mixed-mode fracture using finite element analysis,” *Engineering Fracture Mechanics*, vol. 73, p. 1783–1796, 2006.
- [211] Hashim S., Berggreen C., Tsouvalis N., McGeorge D., Chirica I., Moore P., Boyd S., Nisar J., Anyfantis K., Misirlis K., Juin E., Hayman B., Dow R. and Orsolini A., “Fabrication, testing and analysis of steel/composite DLS adhesive joints,” *Ships and Offshore Structures*, vol. 6, no. 1-2, pp. 115-126, 2011.
- [212] da Silva L.F.M., da Silva RAM, Chousala J.A.G. and Pinto A.M.G., “Alternative methods to measure the adhesive shear displacement in the thick adherend shear test,” *Journal of Adhesion Science and Technology*, vol. 22, no. 1, pp. 15-29, 2008.
- [213] de Moura M.F.S.F., Campilho R.D.S.G. and Gonçalves J.P.M., “Pure mode II fracture characterization of composite bonded joints,” *International Journal of Solids and Structures*, vol. 46, pp. 1589-1595, 2009.
- [214] Campilho R.D.S.G., Pinto A.M.G., Banea M.D., Silva R.F. and da Silva L.F.M., “Strength improvement of adhesively bonded joints using a reverse bent geometry,” *Journal of Adhesion Science and Technology*, vol. 25, no. 18, pp. 2351-2368, 2011.
- [215] Gustafson P.A. and Waas A.M., “The influence of adhesive constitutive parameters in cohesive zone finite elements models of adhesively bonded joints,” *International Journal of Solids and Structures*, vol. 46, pp. 2201-2215, 2009.
- [216] de Moura M.F.S.F., “Progressive Damage Modelling. Modelling of Adhesively Bonded Joints. , Chapter 6,” Springer-Verlag, 2008.
- [217] Blackman B.R.K., Kinloch A.J. and Paraschi, “The determination of the mode II adhesive fracture resistance, GIIC, of structural adhesive joints: an effective crack length approach,” *Engineering Fracture Mechanics*, vol. 72, pp. 877-897, 2005.

- [218] Alfredsson K.S., “On the instantaneous energy release rate of the end-notch flexure adhesive joint specimen,” *International Journal of Solids and Structures*, vol. 41, pp. 4787-4807, 2004.
- [219] Jousset P. and Rachik M., “Comparison and evaluation of two types of cohesive zone models for the finite element analysis of fracture propagation in industrial bonded structures,” *Engineering Fracture Mechanics*, vol. 132, p. 48–69, 2014.
- [220] Jousset P. and Rachik M., “Pressure dependent plasticity for structural adhesive constitutive modeling,” *Journal of Adhesion Science and Technology*, vol. 24, no. 11, pp. 1999-2010, 2010.
- [221] Campilho RDSG, de Moura MFSF, Ramantani DA, Morais JJL and Domingues JJMS, “Tensile behaviour of three-dimensional carbon-epoxy adhesively bonded single and double-strap repairs,” *International Journal of Adhesion and Adhesives*, vol. 29, pp. 678-686, 2009.
- [222] Gleich D.M., Tooren V., Beukers A., “Analysis and evaluation of bond line thickness effects on failure load in adhesively bonded structures,” *Journal of Adhesion Science and Technology*, vol. 15, pp. 1091-1101, 2001.
- [223] Herakovich CT, *Mechanics of fibrous composites*, New York: Wiley, 1998.
- [224] Hashin Z., “Failure criteria for unidirectional fibre composites,” *Journal of Applied Mechanics*, vol. 47, pp. 329-334, 1980.
- [225] Chandler HD., Campbell IMD., “An assessment of failure criteria for fibre-reinforced composite laminates,” *International Journal of Fatigue*, vol. 17, no. 7, pp. 513-518, 1995.

Appendices

Appendix A: Technical data sheet (Araldite LY3505/Hardeners XB3405)



Advanced Materials

Araldite® LY 3505* / Hardeners XB 3403* / XB 3404* / Aradur® 3405*

WARM CURING EPOXY SYSTEMS

Araldite® LY 3505 is an epoxy resin
Hardeners XB 3403, XB 3404 and Aradur® 3405 are based on aliphatic polyamines

APPLICATIONS	Industrial composites, repair of composites.		
PROPERTIES	Laminating systems without reactive diluent. The reactivity of the systems may easily be adjusted to demands through the combination of the three hardeners of different reactivity. The long possible pot life facilitates the production of very large industrial parts. The systems are qualified by Germanischer Lloyd.		
PROCESSING	<ul style="list-style-type: none"> • Wet lay-up • Filament Winding • Resin Transfer Moulding (RTM) • Pressure Moulding 		
KEY DATA	Araldite® LY 3505		
	Aspect (visual)	clear liquid	
	Colour (Gardner, ISO 4630)	≤ 3	
	Viscosity at 25 °C (ISO 12058-1)	6500 - 8000	[mPa s]
	Density at 25 °C (ISO 1675)	1.15 - 1.20	[g/cm³]
	Flash point (ISO 2719)	> 200	[°C]
	Storage temperature (see expiry date on original container)	2 - 40	[°C]
	Hardener XB 3403		
	Aspect (visual)	transparent liquid	
	Viscosity at 25 °C (ISO 12058-1)	5 - 20	[mPa s]
	Density at 25 °C (ISO 1675)	0.95 - 1.0	[g/cm³]
	Flash point (ISO 2719)	124	[°C]
	Storage temperature (see expiry date on original container)	2 - 40	[°C]
	Hardener XB 3404		
	Aspect (visual)	clear, blue liquid	
	Viscosity at 25 °C (ISO 12058-1)	20 - 40	[mPa s]
	Density at 25 °C (ISO 1675)	0.95 - 1.0	[g/cm³]
	Flash point (ISO 2719)	121	[°C]
	Storage temperature (see expiry date on original container)	2 - 40	[°C]
KEY DATA	Hardener XB 3405		
	Aspect (visual)	clear, red liquid	
	Viscosity at 25 °C (ISO 12058-1)	70 - 90	[mPa s]
	Density at 25 °C (ISO 1675)	0.95 - 1.0	[g/cm³]
	Flash point (ISO 2719)	109	[°C]
	Storage temperature (see expiry date on original container)	2 - 40	[°C]

* In addition to the brand name product denomination may show different appendices, which allows us to differentiate between our production sites: e.g., BD = Germany, US = United States, IN = India, CI = China, etc. These appendices are in use on packaging, transport and invoicing documents. Generally the same specifications apply for all versions. Please address any additional need for clarification to the appropriate Huntsman contact.

PROCESSING DATA			
MIX RATIO	Components	Parts by weight	Parts by volume
	Araldite® LY 3505	100	100
	Hardener XB 3403	35	42
	Araldite® LY 3505	100	100
	Hardener XB 3404	35	42
	Araldite® LY 3505	100	100
	Hardener XB 3405	35	42
<p>We recommend that the components are weighed with an accurate balance to prevent mixing inaccuracies which can affect the properties of the matrix system. The components should be mixed thoroughly to ensure homogeneity. It is important that the side and the bottom of the vessel are incorporated into the mixing process.</p> <p>When processing large quantities of mixture the pot life will decrease due to exothermic reaction. It is advisable to divide large mixes into several smaller containers.</p>			
INITIAL MIX VISCOSITY (HOEPLER, ISO 12058-1)		[°C]	[mPa s]
	LY 3505/XB 3403	at 25	300 - 400
	LY 3505/XB 3404	at 25	550 - 800
	LY 3505/XB 3405	at 25	1000 - 1200
POT LIFE (TECAM, 100 ML, 65 % RH)		[°C]	[min]
	LY 3505/XB 3403	at 23	600 - 720
		at 30	430 - 510
	LY 3505/XB 3404	at 23	80 - 100
	LY 3505/XB 3405	at 23	26 - 36
GEL TIME (HOT PLATE)		[°C]	[min]
	LY 3505/XB 3403	at 60	105 - 125
		at 80	36 - 48
		at 100	14 - 18
	LY 3505/XB 3404	at 60	60 - 70
		at 80	11 - 18
		at 100	3 - 7
	LY 3505/XB 3405	at 60	18 - 26
		at 80	5 - 11
		at 100	1 - 6
<p>The values shown are for small amounts of pure resin/hardener mix. In composite structures the gel time can differ significantly from the given values depending on the fibre content and the laminate thickness.</p>			
GELATION AT 23 °C (IN THIN LAYERS: 0.4 - 0.7 MM)			[h]
	LY 3505/XB 3403	Start	14 - 16
		End	19 - 21
	LY 3505/XB 3404	Start	5 - 7
		End	9 - 11
	LY 3505/XB 3405	Start	2 - 3
		End	4 - 5
TYPICAL CURE CYCLES	<p>15 h at 50 °C or 8 - 10 h at 60 °C or 6 - 8 h at 80 °C</p> <p>Optimum properties cannot be reached with room temperature cure. The optimum cure cycle has to be determined case by case depending on the processing and the economic requirements.</p>		
RECOMMENDATIONS TO GET SHORTEST CURING TIME	at 50 °C with XB 3403 = 10 h	with XB 3404 = 7 h	with XB 3405 = 6 h
	at 60 °C with XB 3403 = 8 h	with XB 3404 = 6 h	with XB 3405 = 4 h
<p>Araldite® LY3505 Hardener XB3403 XB3404 Page 2 of 5 03/07/2007</p>			

		at 80 °C with XB 3403 = 6 h	with XB 3404 = 3 h	with XB 3405 = 1 h
PROPERTIES OF THE CURED, NEAT FORMULATION				
GLASS TRANSITION TEMPERATURE	Cure:	T _g	LY 3505 XB 3403	LY 3505 XB 3404 XB 3405
(IEC 1006, DSC, 10 K/MIN)	8 days 23 °C	[°C]	49 - 53	55 - 60
	1 day 23 °C + 15 h 50 °C	[°C]	63 - 68	68 - 73
	8 h 60 °C	[°C]	66 - 72	71 - 76
	6 h 80 °C	[°C]	75 - 80	86 - 91
	4 h 60 °C + 6 h 80 °C	[°C]	78 - 83	87 - 92
	8 h 100 °C	[°C]	81 - 86	85 - 89
TENSILE TEST		Cure: 4 h 60 °C	LY 3505	LY 3505
(ISO 527)		+ 6 h 80 °C	XB 3403	XB 3404 XB 3405
	Tensile strength	[MPa]	70 - 74	85 - 90
	Elongation at tensile strength	[%]	3.8 - 4.2	4.4 - 4.9
	Ultimate strength	[MPa]	46 - 50	83 - 89
	Ultimate elongation	[%]	10 - 13	5.0 - 6.2
	Tensile modulus	[MPa]	3180 - 3280	3500 - 3900
FLEXURAL TEST		Cure: 7 days	LY 3505	LY 3505
(ISO 178)		23 °C	XB 3403	XB 3404 XB 3405
	Flexural strength	[MPa]	85 - 93	90 - 100
	Elongation at flexural strength	[%]	2.4 - 2.8	2.2 - 2.6
	Ultimate strength	[MPa]	85 - 93	90 - 100
	Ultimate elongation	[%]	2.4 - 2.8	2.2 - 2.6
	Flexural modulus	[MPa]	3450 - 3600	3800 - 4000
		Cure: 24 h 23 °C	LY 3505	LY 3505
		+ 15 h 50 °C	XB 3403	XB 3404 XB 3405
	Flexural strength	[MPa]	120 - 135	140 - 155
	Elongation at flexural strength	[%]	4.4 - 4.8	5.0 - 6.0
	Ultimate strength	[MPa]	64 - 72	125 - 140
	Ultimate elongation	[%]	11.0 - 13.0	7.0 - 8.5
	Flexural modulus	[MPa]	3400 - 3550	3600 - 3750
		Cure: 4 h 60 °C	LY 3505	LY 3505
		+ 6 h 80 °C	XB 3403	XB 3404 XB 3405
	Flexural strength	[MPa]	110 - 130	135 - 155
	Elongation at flexural strength	[%]	4.8 - 5.5	5.2 - 6.2
	Ultimate strength	[MPa]	70 - 85	125 - 145
	Ultimate elongation	[%]	10.5 - 13.0	7.0 - 9.0
	Flexural modulus	[MPa]	3100 - 3300	3450 - 3650
FRACTURE PROPERTIES		Cure: 4 h 60 °C	LY 3505	LY 3505
BEND NOTCH TEST		+ 6 h 80 °C	XB 3403	XB 3404 XB 3405
(PM 258-0/90)	Fracture toughness K _{1c}	[MPa√m]	0.95 - 1.05	0.8 - 0.9
	Fracture energy G _{1c}	[J/m ²]	250 - 280	150 - 190
WATER ABSORPTION	Immersion:	Cure: 4 h 60 °C	LY 3505	LY 3505
(ISO 62)		+ 6 h 80 °C	XB 3403	XB 3404 XB 3405
	10 days H ₂ O 23 °C	[%]	0.38 - 0.42	0.30 - 0.35

PROPERTIES OF THE CURED, REINFORCED FORMULATION				
INTERLAMINAR SHEAR STRENGTH (ASTM D 2344)	Short beam: Laminate comprising 12 layers unidirectional E-glass fabric (425 g/m ²) Laminate thickness t = 3.0 - 3.2 mm Fibre volume content: 63 - 65 %			
	Cure: 4 h 60 °C + 6 h 80 °C			
		LY 3505 XB 3403	LY 3505 XB 3404	LY 3505 XB 3405
	Shear strength	[MPa]	53 - 57	59 - 62 54 - 58
STORAGE				
Provided that Araldite LY 3505 and Hardeners XB 3403, XB 3404 and XB 3405 are stored in a dry place in their original, properly closed containers at the above mentioned storage temperatures they will have the shelf lives indicated on the labels. Partly emptied containers should be closed immediately after use.				
HANDLING PRECAUTIONS				
Personal hygiene				
Safety precautions at workplace				
protective clothing				
gloves				
arm protectors				
goggles/safety glasses				
Skin protection				
before starting work				
after washing				
Cleansing of contaminated skin				
Dab off with absorbent paper, wash with warm water and alkali-free soap, then dry with disposable towels. Do not use solvents				
Disposal of spillage				
Soak up with sawdust or cotton waste and deposit in plastic-lined bin				
Ventilation				
of workshop				
of workplaces				
Renew air 3 to 5 times an hour Exhaust fans. Operatives should avoid inhaling vapours				
FIRST AID				
Contamination of the eyes by resin, hardener or mix should be treated immediately by flushing with clean, running water for 10 to 15 minutes. A doctor should then be consulted.				
Material smeared or splashed on the skin should be dabbed off, and the contaminated area then washed and treated with a cleansing cream (see above). A doctor should be consulted in the event of severe irritation or burns. Contaminated clothing should be changed immediately.				
Anyone taken ill after inhaling vapours should be moved out of doors immediately. In all cases of doubt call for medical assistance.				

IMPORTANT LEGAL NOTICE

Huntsman Advanced Materials warrants only that its products meet the specifications agreed with the user. Typical properties, where stated, are to be considered as representative of current production and should not be treated as specifications.

The manufacture of materials is the subject of granted patents and patent applications; freedom to operate patented processes is not implied by this publication.

While all the information and recommendations in this publication are, to the best of Huntsman Advanced Material's knowledge, information and belief, accurate at the date of publication, NOTHING HEREIN IS TO BE CONSTRUED AS A WARRANTY, WHETHER EXPRESS OR IMPLIED, INCLUDING BUT WITHOUT LIMITATION, AS TO MERCHANTABILITY OR FITNESS FOR A PARTICULAR PURPOSE. IN ALL CASES, IT IS THE RESPONSIBILITY OF THE USER TO DETERMINE THE APPLICABILITY OF SUCH INFORMATION AND RECOMMENDATIONS AND THE SUITABILITY OF ANY PRODUCT FOR ITS OWN PARTICULAR PURPOSE.

The behaviour of the products referred to in this publication in manufacturing processes and their suitability in any given end-use environment are dependent upon various conditions such as chemical compatibility, temperature, and other variables, which are not known to Huntsman Advanced Materials. It is the responsibility of the user to evaluate the manufacturing circumstances and the final product under actual end-use requirements and to adequately advise and warn purchasers and users thereof.

Products may be toxic and require special precautions in handling. The user should obtain Safety Data Sheets from Huntsman Advanced Materials containing detailed information on toxicity, together with proper shipping, handling and storage procedures, and should comply with all applicable safety and environmental standards.

Hazards, toxicity and behaviour of the products may differ when used with other materials and are dependent on manufacturing circumstances or other processes. Such hazards, toxicity and behaviour should be determined by the user and made known to handlers, processors and end users.

Except where explicitly agreed otherwise, the sale of products referred to in this publication is subject to the general terms and conditions of sale of Huntsman Advanced Materials LLC or of its affiliated companies including without limitation, Huntsman Advanced Materials (Europe) BVBA, Huntsman Advanced Materials Americas Inc., and Huntsman Advanced Materials (Hong Kong) Ltd. Huntsman Advanced Materials is an international business unit of Huntsman Corporation. Huntsman Advanced Materials trades through Huntsman affiliated companies in different countries including but not limited to Huntsman Advanced Materials LLC in the USA and Huntsman Advanced Materials (Europe) BVBA in Europe.

Araldite and Aradur are registered trademarks of Huntsman Corporation or an affiliate thereof.

Copyright © 2007 Huntsman Corporation or an affiliate thereof. All rights reserved.

Main Office :
Huntsman Advanced Materials (Switzerland) GmbH
Klybeckstrasse 200
4057 BASEL
Switzerland
+41 61 966 3333

Appendix B: Technical data sheet (Araldite 2015)



Advanced Materials

Araldite® 2015

Structural Adhesives

TECHNICAL DATA SHEET

Araldite® 2015

Two component epoxy paste adhesive

Key properties

- Toughened paste
- Ideal for bonding GRP, SMC and dissimilar substrates
- Low shrinkage
- Gap filling, non sagging up to 10mm thickness
- High shear and peel strength

Description

Araldite 2015 is a two component, room temperature curing paste adhesive giving a resilient bond. It is thixotropic and non sagging up to 10mm thickness. It is particularly suitable for SMC and GRP bonding.

Product data

Property	2015 A	2015 B	Mixed Adhesive
Colour (visual)	neutral paste	neutral paste	neutral paste
Specific gravity	1.4	1.4	1.4
Viscosity at 25°C (Pas)	thixotropic	thixotropic	thixotropic
Pot Life (100 gm at 25°C)	-	-	30 - 40 minutes

Processing

Pretreatment

The strength and durability of a bonded joint are dependent on proper treatment of the surfaces to be bonded. At the very least, joint surfaces should be cleaned with a good degreasing agent such as acetone, iso-propanol (for plastics) or other proprietary degreasing agents in order to remove all traces of oil, grease and dirt. Low grade alcohol, gasoline (petrol) or paint thinners should never be used. The strongest and most durable joints are obtained by either mechanically abrading or chemically etching ("pickling") the degreased surfaces. Abrading should be followed by a second degreasing treatment.

Mix ratio	Parts by weight	Parts by volume
Araldite 2015/A	100	100
Araldite 2015/B	100	100

Araldite 2015 is available in cartridges incorporating mixers and can be applied as ready to use adhesive with the aid of the tool recommended by Huntsman Advanced Materials.

Application of adhesive

The resin/hardener mix may be applied manually or robotically to the pretreated and dry joint surfaces. Huntsman's technical support group can assist the user in the selection of an suitable application method as well as suggest a variety of reputable companies that manufacture and service adhesive dispensing equipment.

A layer of adhesive 0.05 to 0.10 mm thick will normally impart the greatest lap shear strength to the joint. Huntsman stresses that proper adhesive joint design is also critical for a durable bond. The joint components should be assembled and secured in a fixed position as soon as the adhesive has been applied.

For more detailed explanations regarding surface preparation and pretreatment, adhesive joint design, and the dual syringe dispensing system, visit www.araldite2000plus.com.

Equipment maintenance

All tools should be cleaned with hot water and soap before adhesives residues have had time to cure. The removal of cured residues is a difficult and time-consuming operation.

If solvents such as acetone are used for cleaning, operatives should take the appropriate precautions and, in addition, avoid skin and eye contact.

Times to minimum shear strength

Temperature	°C	10	15	23	40	60	100
Cure time to reach	hours	12	7.5	4	1	-	-
LSS > 1MPa	minutes	-	-	-	-	17	6
Cure time to reach	hours	21	13	6	2	-	-
LSS > 10MPa	minutes	-	-	-	-	35	7

LSS = Lap shear strength.

Typical cured properties

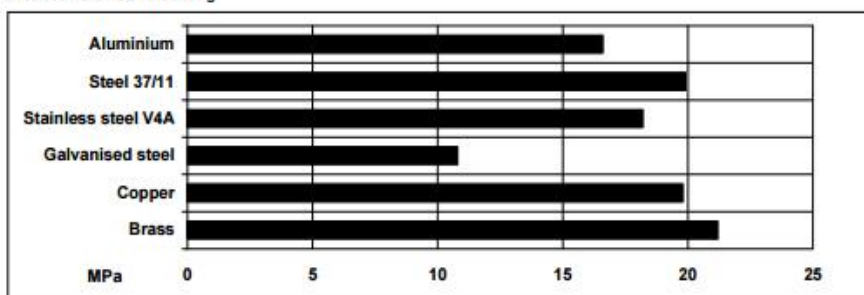
Unless otherwise stated, the figures given below were all determined by testing standard specimens made by lap-jointing 114 x 25 x 1.6 mm strips of aluminium alloy. The joint area was 12.5 x 25 mm in each case.

The figures were determined with typical production batches using standard testing methods. They are provided solely as technical information and do not constitute a product specification.

Average lap shear strengths of typical metal-to-metal joints (ISO 4587)

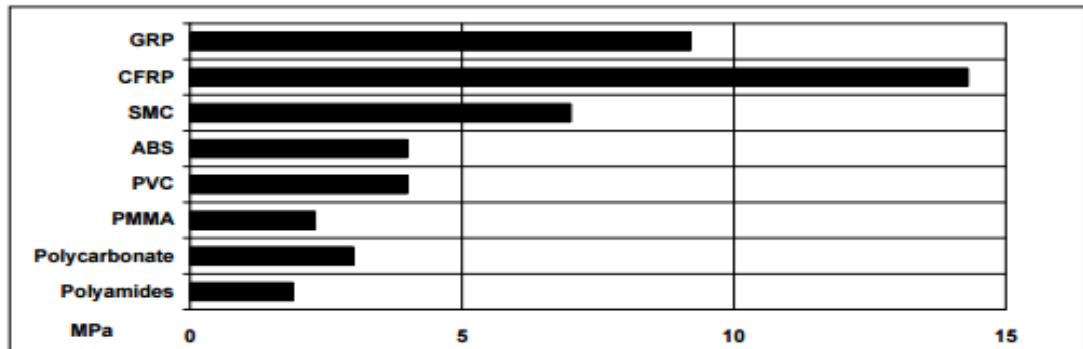
Cured for 16 hours at 40°C and tested at 23°C

Pretreatment - Sand blasting



Average lap shear strengths of typical plastic-to-plastic joints (ISO 4587)

Cured for 16 hours at 40°C and tested at 23°C. Pretreatment – Lightly abrade and alcohol degrease.



Tensile strength at 23°C (ISO 527)

30 MPa

Tensile modulus

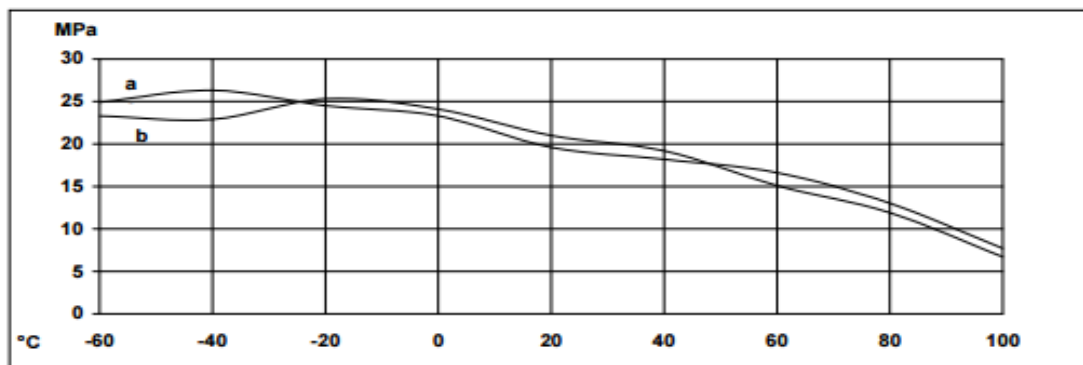
2 GPa

Elongation at break

4.4 %

Lap shear strength versus temperature (ISO 4587) (typical average values)

Cure: (a) = 7 days at 23°C; (b) = 24 hours at 23°C + 30 minutes at 80°C



Roller peel test (ISO 4578)

Cured: 16 hours at 40°C

4 N/mm

Glass transition temperature

Cure: 16 hours at 40°C

67°C by DSC

Cure: 1 hour at 80°C

87 by shear modulus

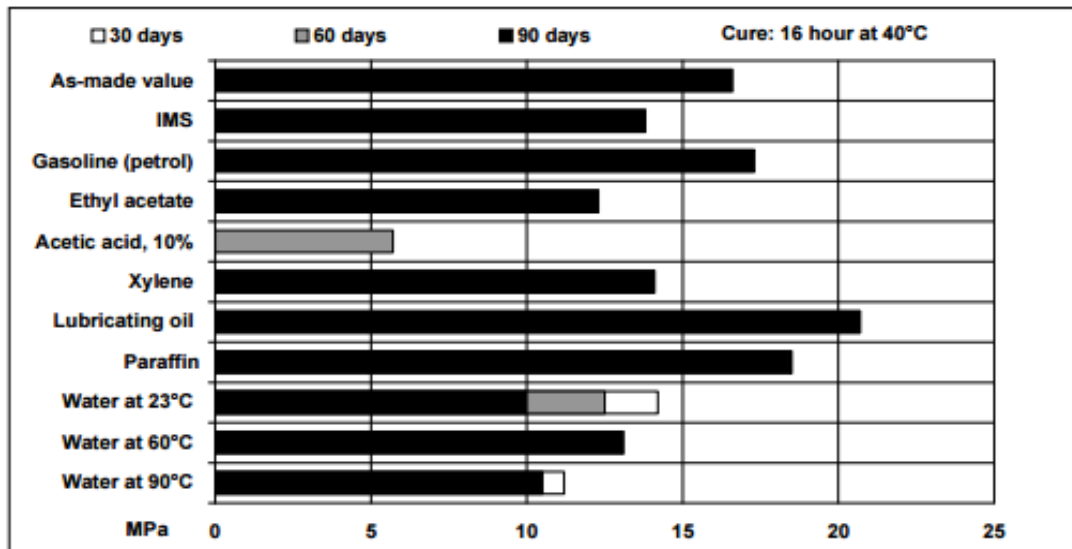
DIN 53445

Dielectric constant (500v at 25°C)

5.6 at 1 kHz

Lap shear strength versus immersion in various media (typical average values)

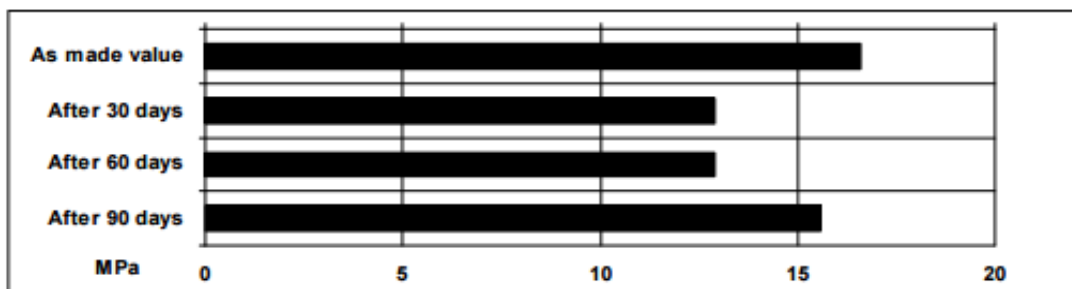
Unless otherwise stated, L.S.S. was determined after immersion for 90 days at 23°C



Lap shear strength versus tropical weathering

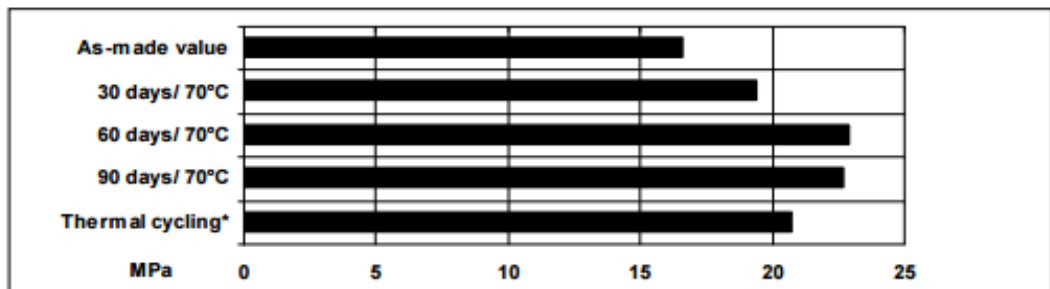
(40/92, DIN 50015; typical average values)

Cure: 16 hours at 40°C Test: at 23°C



Lap shear strength versus heat ageing

Cure: 16 hours at 40°C



*25 cycles -30°C to + 70°C

Shear modulus (DIN 53445)

Cure: 1 hour at 80°C

Temperature	G'	Δ
0°C	1.0 Gpa	0.25
25°C	0.9 Gpa	0.25
50°C	0.8 Gpa	0.35
75°C	0.2 Gpa	1.9
100°C	2 MPa	0.5

Flexural Properties (ISO 178) Cure 16 hours/ 40°C

tested at 23°C

Flexural Strength

42.7 MPa

Flexural Modulus

1813.6 MPa

Resistance to fatigue (40 Hz at 23°C) (quoted as cycles to failure)

Maximum applied load	Sandblasted aluminium	Chromate pickled aluminium
20% of static failing load	>10 ⁷	>10 ⁷
25% of static failing load	>10 ⁷	10 ⁷
30% of static failing load	3 x 10 ⁶	8 x 10 ⁵

(Static failing load 16 MPa)

Storage

Araldite 2015/A and Araldite 2015/B may be stored for up to 3 years at room temperature provided the components are stored in sealed containers. The expiry date is indicated on the label.

Handling precautions

Caution

Our products are generally quite harmless to handle provided that certain precautions normally taken when handling chemicals are observed. The uncured materials must not, for instance, be allowed to come into contact with foodstuffs or food utensils, and measures should be taken to prevent the uncured materials from coming in contact with the skin, since people with particularly sensitive skin may be affected. The wearing of impervious rubber or plastic gloves will normally be necessary; likewise the use of eye protection. The skin should be thoroughly cleansed at the end of each working period by washing with soap and warm water. The use of solvents is to be avoided. Disposable paper - not cloth towels - should be used to dry the skin. Adequate ventilation of the working area is recommended. These precautions are described in greater detail in the Material Safety Data sheets for the individual products and should be referred to for fuller information.

Huntsman Advanced Materials

All recommendations for the use of our products, whether given by us in writing, verbally, or to be implied from the results of tests carried out by us, are based on the current state of our knowledge. Notwithstanding any such recommendations the Buyer shall remain responsible for satisfying himself that the products as supplied by us are suitable for his intended process or purpose. Since we cannot control the application, use or processing of the products, we cannot accept responsibility therefor. The Buyer shall ensure that the intended use of the products will not infringe any third party's intellectual property rights. We warrant that our products are free from defects in accordance with and subject to our general conditions of supply.



Huntsman Advanced Materials
(Switzerland) GmbH
Klybeckstrasse 200
4057 Basel
Switzerland

Tel: +41 (0)61 966 33 33
Fax: +41 (0)61 966 35 19
www.huntsman.com/advanced_materials

Huntsman Advanced Materials warrants only that its products meet the specifications agreed with the buyer. Typical properties, where stated, are to be considered as representative of current production and should not be treated as specifications.

The manufacture of materials is the subject of granted patents and patent applications; freedom to operate patented processes is not implied by this publication.

While all the information and recommendations in this publication are, to the best of our knowledge, information and belief, accurate at the date of publication, NOTHING HEREIN IS TO BE CONSTRUED AS A WARRANTY, EXPRESS OR OTHERWISE. IN ALL CASES, IT IS THE RESPONSIBILITY OF THE USER TO DETERMINE THE APPLICABILITY OF SUCH INFORMATION AND RECOMMENDATIONS AND THE SUITABILITY OF ANY PRODUCT FOR ITS OWN PARTICULAR PURPOSE.

The behaviour of the products referred to in this publication in manufacturing processes and their suitability in any given end-use environment are dependent upon various conditions such as chemical compatibility, temperature, and other variables, which are not known to Huntsman Advanced Materials. It is the responsibility of the user to evaluate the manufacturing circumstances and the final product under actual end-use requirements and to adequately advise and warn purchasers and users thereof.

Products may be toxic and require special precautions in handling. The user should obtain Safety Data Sheets from Huntsman Advanced Materials containing detailed information on toxicity, together with proper shipping, handling and storage procedures, and should comply with all applicable safety and environmental standards.

Hazards, toxicity and behaviour of the products may differ when used with other materials and are dependent on manufacturing circumstances or other processes. Such hazards, toxicity and behaviour should be determined by the user and made known to handlers, processors and end users.

Except where explicitly agreed otherwise, the sale of products referred to in this publication is subject to the general terms and conditions of sale of Huntsman Advanced Materials LLC or of its affiliated companies including without limitation, Huntsman Advanced Materials (Europe) BVBA, Huntsman Advanced Materials Americas Inc., and Huntsman Advanced Materials (Hong Kong) Ltd. Huntsman Advanced Materials is an international business unit of Huntsman Corporation. Huntsman Advanced Materials trades through Huntsman affiliated companies in different countries including but not limited to Huntsman Advanced Materials LLC in the USA and Huntsman Advanced Materials (Europe) BVBA in Europe.

[Araldite® 2015] is a registered trademark of Huntsman Corporation or an affiliate thereof.

Copyright © 2007 Huntsman Corporation or an affiliate thereof. All rights reserved.

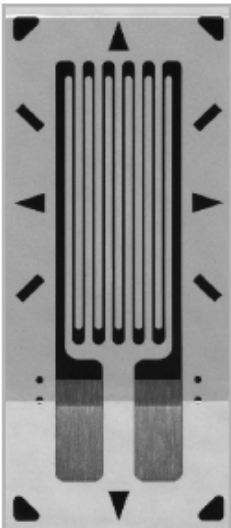
Appendix C: Technical specification of Vishay strain gauges

250UN

Vishay Micro-Measurements



General Purpose Strain Gages - Linear Pattern

GAGE PATTERN DATA					
			GAGE DESIGNATION	RESISTANCE (OHMS)	OPTIONS AVAILABLE
			See Note 1		See Note 2
			CEA-XX-250UN-120 CEA-XX-250UN-350	120 \pm 0.3% 350 \pm 0.3%	P2 P2
			DESCRIPTION General-purpose gage with narrow geometry. Exposed solder tab area 0.08 x 0.05 in [2.0 x 1.1 mm]. See also 250UW pattern.		
GAGE DIMENSIONS			Legend:	ES = Each Section S = Section (S1 = Sec 1)	CP = Complete Pattern M = Matrix
					<div>inch</div> <div>millimeter</div>
Gage Length	Overall Length	Grid Width	Overall Width	Matrix Length	Matrix Width
0.250	0.415	0.120	0.120	0.52	0.22
6.35	10.54	3.05	3.05	13.2	5.6
GAGE SERIES DATA					
See Gage Series data sheet for complete specifications.					
Series	Description	Strain Range	Temperature Range		
CEA	Universal general-purpose strain gages.	\pm 5%	-100° to +350°F [-75° to +175°C]		

Note 1: Insert desired S-T-C number in spaces marked XX.

Note 2: Products with designations and options shown in bold are not RoHS compliant.

Appendix D: Technical data sheet of strain gauge adhesive (M-bond AE-10)



M-Bond AE-10

Vishay Micro-Measurements

Strain Gage Adhesive



OTHER ACCESSORIES USED IN AN M-BOND AE-10 INSTALLATION:

- CSM Degreaser or GC-6 Isopropyl Alcohol
- Silicon-Carbide Paper
- M-Prep Conditioner A
- M-Prep Neutralizer 5A
- GSP-1 Gauze Sponges
- CSP-1 Cotton Applicators
- PCT-2M Gage Installation Tape
- HSC Spring Clamp
- GT-14 Pressure Pads and Backup Plates



DESCRIPTION

Two-component, 100%-solids epoxy system for general-purpose stress analysis. Transparent, medium viscosity. Cure time as low as six hours at +75°F [+24°C] may be used. Elevated-temperature postcure is recommended for maximum stability, and/or tests above room temperature.

Highly resistant to moisture and most chemicals, particularly when postcured. For maximum elongation, bonding surface must be roughened. Cryogenic applications require very thin gluelines.

CHARACTERISTICS

Operating Temperature Range:

Long Term: -320° to +200°F [-195° to +95°C].

Elongation Capabilities:

1% at -320°F [-195°C];
6% to 10% at +75°F [+24°C];
15% at +200°F [+95°C].

Shelf Life:

12 months at +75°F [+24°C]; 18 months at +40°F [+5°C]. If crystals form in resin jar, heat to +120°F [+50°C] for 30 minutes. Cool before mixing.

Pot Life:

15 to 20 minutes at +75°F [+24°C]. Can be extended by cooling jar or by spreading adhesive on clean aluminum plate.

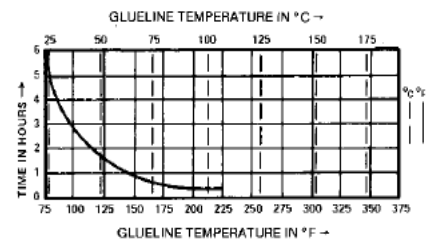
Clamping Pressure:

5 to 20psi [35 to 140kN/m²].

Cure Requirements:

Preferred Room-Temperature Cure: 24-48 hours at +75°F [+24°C].

Recommended Postcure: 2 hours at 25°F [15°C] above maximum operating temperature.



Appendix E: Failure Criteria

Principal stresses failure criterion

Failure takes place in any isotropic material like an adhesive, coating resin and matrix resin, when the maximum in plane principal stress is greater than the material's yield stress.

$$SP_{1,2} = \frac{(\sigma_{11} + \sigma_{22})}{2} \pm \sqrt{\frac{(\sigma_{11} - \sigma_{22})^2}{4} + \tau_{12}^2} \geq S_y$$

Maximum Stresses failure criterion

Maximum stress failure criterion has been used for isotropic material failure [223] without the interaction of other stress components. Failure takes place when any of the stress components reaches its corresponding limits. i.e.

$$|\sigma_{11}| \geq X_t \text{ or } X_c$$

$$|\sigma_{22}| \geq Y_t \text{ or } Y_c$$

$$|\tau_{12}| \geq S_c$$

Hashin Failure Criterion. [Hashin, 1973]

Hashin failure criterion [224] identifies that failure takes place when the failure index exceeds unity for the subsequent failure modes as long as that the materials are elastic. Let us assume that σ_{11} (Longitudinal), σ_{22} (Transverse), and τ_{12} (In-plane shear) are the in-plane stresses within the lamina and in-plane strength along longitudinal (X_t , X_c), transverse (Y_t , Y_c) and shear S_c with T and C represents tension and compression respectively.

1. Fibre failure:

$$\text{(Tensile)} \quad \left(\frac{\sigma_{11}}{X_t} \right)^2 + \left(\frac{\tau_{12}}{S_c} \right)^2 = 1.0 \quad \text{Fibre breakage} \quad (\sigma_{11} \geq 0)$$

$$\text{(Compressive)} \quad -\frac{\sigma_{11}}{X_c} = 1.0 \quad \text{Fibre buckling} \quad (\sigma_{11} < 0)$$

2. Matrix failure:

$$\text{(Tensile)} \quad \left(\frac{\sigma_{22}}{Y_t} \right)^2 + \left(\frac{\tau_{12}}{S_c} \right)^2 = 1.0 \quad \text{Matrix creaking} \quad (\sigma_{22} \geq 0)$$

$$\text{(Compressive)} \quad \left(\frac{\sigma_{22}}{Y_c} \right)^2 + \left(\frac{\tau_{12}}{S_c} \right)^2 = 1.0 \quad \text{Matrix creaking} \quad (\sigma_{22} < 0)$$

Tsai-Hill failure criterion [225]

Failure takes place within uni-directional lamina when the calculated value equals, or exceeds 1.

$$\left(\frac{\sigma_{11}}{X_t} \right)^2 + \left(\frac{\sigma_{22}}{X_c} \right)^2 - \left(\frac{\sigma_{11} \cdot \sigma_{22}}{X_t^2} \right) + \left(\frac{\tau_{12}}{S_c} \right)^2 \geq 1$$

Where X_t , X_c , S_c are the tensile, compressive and shear strength of lamina.

Damage initiation criterion for cohesive element [201]

Damage initiation refers to the beginning of degradation of the response of a material point. For cohesive model, it indicates the start of the delamination damage. The process of damage begins when the stresses or strains satisfy certain damage initiation criteria that are specified. Abaqus provides several different criteria, which can be chosen by the users, such as maximum nominal stress or strain criterion, and quadratic nominal stress or strain criterion. In this study, the quadratic nominal stress criterion (QUADS) is used:

$$\left(\frac{\langle \sigma \rangle}{\sigma_0} \right)^2 + \left(\frac{\tau}{\tau_0} \right)^2 = 1$$

Where $\langle \rangle$ represents that compressive (negative) normal stress does not initiate any delamination damage. And the σ is the component of normal to the likely debonding surface,

while τ is the shear component on the likely debonding surface. Damage is assumed to initiate when the above quadratic interaction criterion is satisfied.

Benzeggagh-Kenane (BK) criterion [B&K 1996]

The Benzeggagh-Kenane fracture criterion [207] is particularly useful when the critical fracture energies during deformation purely along the first and the second shear directions are the same; i.e., $G_{II}^C = G_{III}^C$ it is given by,

$$G_{IC} + (G_{IIC} - G_{IC}) \left(\frac{G_{II}}{G_T} \right)^\eta = G_{TC}$$

Where:

$G_T = G_I + G_{II}$, and η is a material parameter.

- G_I and G_{II} are the energies released by the traction due to the respective separation in the normal and shear directions.
- G_{IC} and G_{IIC} are the critical energy release rates in modes I and II.

Publications

- Yahya N.A. and Hashim S.A., “Delamination of thick-adherend steel/CFRP laminate connections”, The European Adhesion Conference (9th EURADH), Friedrichshafen/Germany, September 2012.
- Yahya N.A. and Hashim S.A., “Stress analysis of steel/carbon composite double lap shear joints under tensile loading”, Proc. IMechE Part L: Journal of Materials: Design and Applications, IMechE 2014, DOI: 10.1177/1464420714547223.

Delamination of thick-adherend steel/CFRP laminate connections

Najeeb Yahya, Safa Hashim, University of Glasgow, Glasgow, UK

Summary

The paper deals with the failure of bonded double lap shear (DLS) joints where the inner adherend is steel and the outer adherend is cross-ply unidirectional (UD) CFRP Composite. Overlap lengths of 25-200 mm and laminate thicknesses of 3-9 mm were considered. There are different ways for such joints to fail, which makes predicting failure difficult. The relatively low interlaminar tensile strength of the composite/resin system cause failure before that of the adhesive. The overall objective of the paper is to investigate the delamination of the CFRP laminates within the DLS joints under quasi-static loading. Both experimental and numerical techniques were used. The numerical study was based on 2-D models, taking into consideration the UD properties of the plies and the resin layers separating these. Both strength-limit FEA stress analysis and cohesive zone modelling (CZM) were used, with continuum and cohesive elements respectively. The CZM was based on bilinear traction separation laws in pure modes I and II to account for the behaviour of the adhesive and the resin separating the plies. The separation laws are determined by the inverse method of the cohesive parameters with a fitting procedure of the experimental and numerical load-displacement curves of the respective fracture characterization test. The paper shows that both strength limit and CZM methods can provide satisfactory prediction of failure of CFRP within the joint. The effect of increased laminate thickness shows a significant reduction in the stress levels occurring at the joint centre, especially for the peel stress.

1. Introduction

Adhesive bonding applications are used widely in industry because of the advantages such as uniform stress distribution, the ability to join different materials and design flexibility. Adhesive bonding provides several advantages over riveting and bolting, such as reduction of stress concentrations, reduced weight penalty and easy manufacturing [1]. The use of CFRP for the repair of steel structure is also advantageous, for example to avoid welding or bolting which can weaken structure and add fire risk. Any successful applications of steel/composite connections, however, require understanding the structural behaviour and failure of these connections. This study is based on adhesive bonded DLS joints where the inner adherend is steel and the outer adherend is unidirectional CFRP. Different approaches were employed in the past to predict the mechanical behaviour of bonded assemblies. In the FEA work on bonded assemblies research dates back to the 1970s when Wooley and Carver [2] conducted a stress analysis on single lap joint. On the strength prediction of bonded assemblies, two different lines of analyses were developed: the strength of materials and fracture mechanics based methods. The strength of materials approach is based on the evaluation of allowable stresses [3] or strains [4] by theoretical formulations or the FEA. The assemblies strength can be predicted by comparing the respective equivalent stresses or strains at critical regions obtained by stress or strain-based criteria, with the properties of the structure. These criteria are highly mesh dependent, as stress singularities are present at the end of the overlap regions especially at sharp corners [5]. As for

Stress analysis of steel/carbon composite double lap shear joints under tensile loading

NA Yahya and SA Hashim

Proc IMechE Part L:
J Materials: Design and Applications
0(0) 1–17
© IMechE 2014
Reprints and permissions:
sagepub.co.uk/journalsPermissions.nav
DOI: 10.1177/1464420714547223
jml.sagepub.com
SAGE

Abstract

The study is related to adhesive-bonded long overlap double lap shear joints with thick adherends. The outer adherend is based on crossply carbon fibre/epoxy composite laminate and the inner adherend is mild steel. The paper aims to predict and assess the structural failure of the joint, including delamination of the composite and to determine the effects of the design parameters of adherend thickness, overlap length and fabric orientation on the joint's failure. Both experimental and numerical methods were used for the analysis. The experimental programme includes fabrication, mechanical testing and failure examinations of various joints. The numerical methods are based on 2-D models using strength-limit and cohesive zone modelling methods, taking into consideration the composite properties of the plies and the resin layers separating them. The study showed a good agreement between the numerical and experimental results. Key conclusions in relation to the failure and design parameters of the joints are made.

Keywords

Adhesive joints, thick adherend, composite, delamination, finite element analysis, cohesive models

Date received: 11 July 2013; accepted: 21 July 2014

Introduction

Hybrid connections are becoming more desirable in many areas of engineering applications including large construction and repair work. In the former, this is necessary for high stiffness requirements in composites, e.g. ships, aircrafts and wind turbine blades, where the stiffness of the composite on its own is not adequate. Adhesive bonding is used widely in industry because of its advantages over fastening. The advantages include uniform stress distribution, the ability to join different materials and design flexibility. The absence of holes and fasteners eliminates stress concentration and makes manufacturing more cost-effective.¹ The use of carbon fibre composite for the repair of steel structures is also advantageous, for example to avoid welding or bolting which can weaken the structure and add a fire risk, e.g. in an explosive-proof environment.² Any successful application of steel/composite connections, however, requires understanding of the structural behaviour and failure of these connections.

This study is based on adhesive bonded double lap shear (DLS) joints where the inner adherend is steel and the outer one is carbon fibre reinforced polymer (CFRP) laminate. Different approaches have been employed in the past to predict the mechanical behaviour of bonded assemblies. The finite element analysis

(FEA) work on bonded assemblies research dates back to the 1970s when Wooley et al.³ conducted a stress analysis on a single lap joint. Adams et al.^{4,5} are among the first to have used the FEA for analysing adhesive joint stresses. On the strength prediction of bonded assemblies, two different lines of analyses were developed: the strength of materials and fracture mechanics-based methods. The strength of materials approach is based on the evaluation of allowable stresses⁶ or strains⁷ by theoretical formulations or the FEA. The joint strength can be predicted by comparing the respective equivalent stresses or strains at critical regions obtained by stress or strain-based criteria, with the properties of the structure. These criteria are highly mesh dependent, as stress singularities are present at the end of the overlap regions especially at sharp corners.⁸

Most analyses of delamination growth initially applied a fracture mechanics approach and, to evaluate energy release rates, G using the virtual crack closure technique (VCCT).^{9,10} However the use of

School of Engineering, University of Glasgow, Glasgow, UK

Corresponding author:

Safa Hashim, School of Engineering, University of Glasgow, James Watt Building, Glasgow G12 8QQ, UK.
Email: safa.hashim@glasgow.ac.uk